Synthesis and optimization of the transition metal boride nanoparticles and their possible magnetic/hybrid composite applications

A Dissertation submitted to the
Graduate School of Science and Engineering
in partial satisfaction of the requirements for
the degree of

Doctor of Philosophy

in

Materials Science and Engineering

By

Sina Khoshsima

KOÇ
UNIVERSITY

November 26th, 2020

Koç University

Graduate School of Sciences and Engineering

This is to certify that I have examined this copy of a Doctoral dissertation by

Sina Khoshsima

and have found that it is complete and satisfactory in all respects,
and that any and all revisions required by the final
examining committee have been made.

Committee Members:

Prof. Dr. Mehmet S. Somer (Advisor, Koç University)

Res. Asst. Prof. Dr. Özge Balcı (Co-Advisor, Koç University)

Assoc. Prof. Dr. Uğur Ünal (Koç University)

Assoc. Prof. Dr. Bora Derin ((İstanbul Technical University)

Prof. Dr. İsmail Lazoğlu (Koç University)

Assoc. Prof. Dr. Güldem Kartal Şireli (İstanbul Technical University)

Date: 26.11.2020

ABSTRACT

The main objective of this study is to synthesize nanoparticles of transition metal borides adopting a low-temperature method and explore and optimize their magnetic and hybrid reinforcement properties and enhance their mechanical properties towards targeted application areas, both in scientific and in industrial fronts. This thesis reports the synthesis conditions of crystalline cobalt-metal-boron (Co-M-B (M = Fe, Ti)) based boride systems: Investigations of Co-Fe-B systems as effective magnets and Co-Ti-B as effective reinforcement agents in hybrid composite production have been targeted. In the scope of the thesis, synthesis studies were carried out by inorganic molten salt and reduction at autogenic pressure techniques using the anhydrous/hydrous metal chloride and sodium borohydride mixtures. The results of the experiments as well as their possible applications are described in detail within each chapter.

Chapter two focuses on the in-situ synthesis of Co-Fe-B crystalline nanoparticles via a new approach utilizing the optimized low-temperature method, metal chlorides, and NaBH4 as precursors and, incorporating inorganic molten environment. The effect of the reaction systems and synthesis conditions on the phase formation, microstructure, purity, and magnetic properties of the obtained samples were investigated. The use of an inorganic molten environment helped reduce the melting point of the precursor materials. Following the reaction of $CoCl_2$, $FeCl_3$ and $NaBH_4$ at 850 °C in sealed stainless-steel tubes, CoB and Fe_3B phases formed separately. After a reaction under Ar flow; however, $CoFeB_2$ solid solution nano powders were obtained in one step at 850 °C with an average size of 60 nm.

After annealing at 1100 °C, stable and highly crystalline $(CoFe)B_2$ solid solution phase with a Co:Fe molar ratio of 1:1 was achieved. As-synthesized particles exhibited ferromagnetic property and possessed a narrow hysteresis curve characteristic of soft magnetic materials. Extended reaction temperature from 650 to 850 °C is seen to produce coercivity enhancement up to 500 Oe without a significant reduction in saturation magnetization. On the other hand, after an annealing process and subsequent phase and chemical change, crystalline $(CoFe)B_2$ particles exhibited superparamagnetic property.

Chapter three describes research performed on the chemical synthesis of crystalline and nanoscale cobalt-iron metal boride powders using hydrous metal chlorides and $NaBH_4$ and also reveals the effect of application of optimization steps to the reaction systems and synthesis conditions. The effects of precursor concentration and optimized synthesis conditions on the phase formation, microstructure, and magnetic properties were investigated. After applying a reaction of $CoCl_2 \cdot 6H_2O$-$FeCl_3 \cdot 6H_2O$-$NaBH_4$ at 850°C, $(CoFe)B_2$, (CoFe)B, Co_2B, Fe_3B, and $Fe_{0.91}B_{0.09}$ boride phases were obtained from different synthesis conditions applied under autogenic pressure or Ar flow atmosphere. Oxychloride impurities were the reason for the reduced magnetization values, and it was revealed that the ternary solid solution phase forms when synthesized under active Ar flow. The highest saturation magnetization of 183 emu/g belongs to obtained nanoparticles containing $(CoFe)B_2$ and (CoFe)B pure phases. After implementing the optimization steps acquired from our previous experiences, the obtained saturation magnetization of the samples was increased 9-fold which emphasizes the importance of purity of the powders and the role of

oxygen. High temperature magnetic measurements marked synthesized powders as soft magnetic materials up to 795 K while no T_c was reached for the obtained phases.

The focus of chapter four shifts toward nanoparticles synthesized to be used as a reinforcement agent. In this chapter, a novel low-temperature approach was adopted for the synthesis of cobalt-titanium-boron based crystalline powders. The method was based on the single-step direct reaction of $CoCl_{2(s)}$, $TiCl_{4(l)}$, and $NaBH_{4(s)}$ in a sealed reactor under autogenic pressure. After the reaction of the precursors at 850 °C, with molar ratios of metal chlorides to $NaBH_4$ as 1:3, CoB and TiB_2 phases were formed in-situ. The subsequent annealing process at 1100 °C achieved a full conversion of metal chlorides to CoB-TiB_2 composite nanostructures. It was concluded that the binary forms of the borides tend to form as separate phases, which is illustrated in the SEM/EDS analyses with different morphologies. The amorphous boron layer surrounded TiB_2 particles with an average particle size of 60 nm, whereas the CoB particles formed agglomerates with an average size of 450 nm. The use of 1 wt. % of the synthesized composite powders as reinforcement in metal matrices resulted in enhanced hardness (506 Hv) and compressive strength (1682 MPa) of the Ti6Al4V bulk samples.

ÖZET

Bu çalışmanın temel amacı, geçiş metali borürlerin nanoparçacıklarını sentezlemek ve düşük sıcaklık yöntemini kullanarak manyetik ve hibrit takviye özelliklerini hem bilimsel hem de endüstriyel alanlarda hedeflenen uygulama alanlarına doğru araştırmak ve optimize etmektir. Bu kapsamda, kristalin kobalt-metal-bor (Co-M-B (M = Fe, Ti)) esaslı borür sistemleri incelenmiştir. Tez kapsamında inorganik ergimiş tuz tekniği ve otojenik basınçta redüksiyon tekniği ile sentez çalışmaları susuz/sulu metal klorür ve sodyumborhidrür karışımları kullanımı ile gerçekleştirilmiştir. Deney sonuçlarının yanı sıra bu malzemeler ile yapılabilecek olası uygulamalar her bölüm içerisinde ayrıntılı olarak açıklanmaktadır.

İkinci bölüm, optimize edilmiş düşük sıcaklık yöntemini, metal klorürleri ve öncü olarak $NaBH_4$'ü kullanan ve inorganik ergimiş tuz ortamı içeren yeni bir yaklaşımla Co-Fe-B kristalin nanopartiküllerin yerinde sentezine odaklanmaktadır. Reaksiyon sistemlerinin ve sentez koşullarının, elde edilen örneklerin faz oluşumu, mikro yapısı, saflığı ve manyetik özellikleri üzerindeki etkisi araştırılmıştır. İnorganik ergimiş tuz ortamının kullanılmasının, öncü maddelerin ergime noktasının azaltılmasına yardımcı olduğu gözlemlenmiştir. $CoCl_2$, $FeCl_3$ ve $NaBH_4$'ün 850 °C'de kapalı paslanmaz çelik borularda reaksiyonunu takiben CoB ve Fe_3B fazları ayrı olarak elde edilmiştir. Ar akışı altında gerçekleşen reaksiyondan sonra ise, $(CoFe)B_2$ katı çözelti nano tozları ortalama 60 nm boyutunda 850°C'de tek adımda sentezlenmiştir. Aynı tozların 1100 °C'deki tavlama işleminden sonra, 1: 1 Co: Fe mol oranına sahip kararlı ve oldukça kristalin $(CoFe)B_2$ katı çözelti fazı elde edilmiştir. Sentezlenen parçacıkların ferromanyetik özellik sergilediği ve elde edilen yumuşak manyetik

malzemelerin karakteristik dar bir histerezis eğrisine sahip olduğu gözlemlenmiştir. 650 - 850 °C arasındaki reaksiyon sıcaklığı aralığında sentezlenen tozların manyetik ölçümleri, doyma magnetizasyonunda önemli bir azalma olmadan 500 Oe'ye kadar koersivite artışı sağlandığını göstermiştir. Öte yandan, tavlama işlemi ardından elde edilen faz ve kimyasal değişimden sonra, kristalin $(CoFe)B_2$ parçacıkların süperparamanyetik özellik sergilediği tespit edilmiştir.

Üçüncü bölüm, sulu metal klorürler ve $NaBH_4$ kullanarak kristalin ve nano boyuttaki kobalt-demir metal borür tozlarının kimyasal sentezi üzerinde yapılan araştırmaları açıklamakta ve ayrıca reaksiyon sistemlerine ve sentez koşullarına optimizasyon adımlarının uygulanmasının etkisini ortaya koymaktadır. Başlangıç malzeme konsantrasyonunun ve optimize edilmiş sentez koşullarının faz oluşumu, mikroyapı ve manyetik özellikler üzerindeki etkileri araştırılmıştır. 850 °C'de $CoCl_2 \cdot 6H_2O$ - $FeCl_3 \cdot 6H_2O$ - $NaBH_4$ arası reaksiyon uygulandıktan sonra, uygulanan farklı sentez koşullarından $(CoFe)B_2$, (CoFe)B, Co_2B, Fe_3B ve $Fe_{0.91}B_{0.09}$ borür fazları elde edilmiştir. Otojenik basınçta oluşan oksiklorür empüritelerinin, azaltılmış manyetizasyon değerlerinin sebebi olduğu; öte yandan aktif Ar akışı altında sentez gerçekleştiğinde üçlü katı çözelti fazının oluştuğu ortaya çıkmıştır. 183 emu/g ile en yüksek doygunluk manyetizasyonu, $(CoFe)B_2$ ve (CoFe)B saf fazlarını içeren nanoparçacıklarda elde edilmiştir. Bir önceki bölümdeki deneyimlerimizden elde edilen optimizasyon adımlarını uyguladıktan sonra, numunelerin elde edilen doygunluk manyetizasyonu 9 kat arttırılmıştır. Bu da tozların saflığının önemini ve oksijenin rolünü vurgulamaktadır. Yüksek sıcaklık manyetik ölçümleri, sentezlenmiş tozların 795 K'ye kadar

yumuşak manyetik malzemeler olarak kararlı olduğuna işaret ederken, elde edilen fazlar için T_c değerine ulaşılmamıştır.

Dördüncü bölümün odağı, takviye maddesi olarak kullanılmak üzere sentezlenen nanoparçacıklara doğru kaymaktadır. Bu bölümde, kobalt-titanyum-bor bazlı kristal tozların sentezi için yeni düşük sıcaklık yaklaşımı benimsenmiştir. Yöntem, otojenik basınç altında kapalı bir reaktör içinde $CoCl_{2(s)}$, $TiCl_{4(1)}$ ve $NaBH_{4(s)}$ in tek aşamalı doğrudan reaksiyonuna dayanmaktadır. Öncüllerin 850 °C'de reaksiyonundan sonra, metal klorürlerin 1:3 olarak $NaBH_4$'e molar oranları ile CoB ve TiB_2 fazları yerinde sentez yöntemi ile oluşturulmuştur. 1100 °C'de müteakip tavlama işlemi, metal klorürlerin CoB-TiB_2 kompozit yapılara tam bir dönüşümünü sağlamıştır. Borürlerin ikili formlarının, farklı morfolojilerle SEM/EDS analizlerinde gösterilen ayrı fazlar oluşturma eğiliminde olduğu sonucuna varılmıştır. Amorf bor tabakası, ortalama partikül boyutu 60 nm olan TiB_2 partiküllerini kuşatırken, CoB partikülleri ortalama 450 nm'lik bir boyutta aglomeratlar oluşturmuştur. Sentezlenen tozların metal matrislerde takviye elemanı olarak kullanımı, Ti6Al4V yığın numunelerinde yükseltilmiş sertlik (506 Hv) ve basınç mukavemeti (1682 MPa) değerleri ile sonuçlanmıştır.

ACKNOWLEDGEMENTS

No words will cover the depth of my gratitude and appreciation towards my advisor Prof. Dr. Mehmet S. Somer, who has encouraged and guided me throughout my research with his patience and knowledge, supported me in the times of need and cheered me up when I was down. He has inspired me to become an independent researcher and helped me realize the power of critical reasoning. He also taught me about life, about art and many other aspects of life that make us human. It was an absolute honor for me to have been his student and I will never forget the long discussions and laughs we had together.

I want to express my sincere appreciation to my co-advisor, friend and mentor, Asst. Prof. Dr. Özge Balcı. There is nothing that can explain the value of the experience of working with her. She taught me dedication and determination and the ability to work under pressure. She taught me to think above and beyond, and helped me become a better version of myself, supported me when I needed it and helped me through my tough times. I will forever be grateful to her.

Special thanks to Prof. Dr. Uğur Ünal and Prof. Dr. Bora Derin for their valuable insight on this work. I also want to thank the members of my jury committee for their valuable time and experience they have allocated to me.

Special thanks must go to my dear friend and colleague Dr. Zerrin Altıntaş. She is the most kind and forgiving person I have met during the course of my studies. I would not have been able to overcome the overwhelming load of this work if it was not for her. She is the closest I will ever get to have a big sister who guides me, holds me accountable when I am wrong and pushes me when I am lazy.

My thanks and appreciation goes to Dr. Barış Yağcı, Dr. Ali Bateni, Kamil Kiraz and Cansu Yıldırım for the stimulating discussions and patiently teaching me how to use instruments.

This thesis was supported by “The Scientific and Technological Research Council of Turkey (TUBITAK)” with the project name "*Novel Low Temperature Synthesis of Cobalt–Metal–Boron (Metal=Ni, Fe, Ti) Based Ternary Metal Borides from Metal Chlorides:*

Characterization and Application Oriented Investigations on Catalyzer/Magnet/Hybrid Composite Fabrication" and number of 117F178. My sincere thanks go to the TUBITAK for granting me the opportunity to work on this project. I would like to thank Graduate School of Sciences and Engineering and Koç University Surface Science and Technology Center (KUYTAM) for providing me support during my thesis studies.

There is no way to express how much it meant to me for being a member of Koç University Boron and Advanced Materials Application and Research Center (KUBAM). I was lucky to have brilliant friends and fellow lab mates who inspired me over the many years whom I extend my sincere thanks and appreciation to them for the many amazing memories and friendships we had.

In addition, I would like to thank Prof. Dr. Yuri Grin for his support in using the facilities of Max Planck Institute in Dresden, Germany. I want to acknowledge Dr. Ulrich Burkhardt, Dr. Marcus Schmidt and Dr. Matej Bobnar from Max Planck Institute for their support during microstructural, thermal and magnetic analyses. I would like to thank Prof. Dr. K. G. Prashanth for granting me the opportunity to visit Tallinn University, Estonia.

Finally and above all, I would like to extend my utmost gratitude to my family for their continuous and unconditional love, help and support. I believe that family is the most important possession one can have in this finite world. Their love and support, even from a far, and at my most vulnerable moments, helped me get back on my feet whenever I was down and shaped my personality. There are no words that can describe my appreciation, so the only thing left would be to say thank you from the bottom of my heart. I would not have been the person who I am and where I am today, if it were not for them. To them I say, I love you with all my heart.

In memory of my beloved grandmother Malekeh,

Table of Contents

List of Tables

List of Figures

Chapter 1. Introduction and Review

1.1. Elemental Boron and Its Modifications

After nearly 200 years of its discovery, still much remains undisclosed about the chemistry of elemental Boron. Being a nonmetallic light element [1], boron showcases properties such as high strength (stronger than steel) and melting point (2450 °C), electron deficiency, structural intricacy, and unconventional chemical bonds which enables formation of numerous compounds. It is used in superconductors (MgB_2, T_c = 39 K) [2], in high power electronics (LaB_6) [3], as dopants or as alternatives to carbon systems, for coatings in nuclear reactor walls, and as a constituent in hydrogen storage materials (e.g. $LiBH_4$) [4]. Additionally, it showcases small reactivity at room temperature. All of the mentioned properties are closely related to boron's ability to form complex structures. Elemental boron has two well-known crystalline modifications that are stable at room temperature: α-rhombohedral boron (α-B) and β-rhombohedral boron (β-B) shown in figures 1 and 2. The β-B is known to be thermodynamically stable at elevated temperatures given the fact that T > 1400 K is required for its synthesis, while α-B is synthesized at T < 1300 K. The fact that calculated energy levels of α-B modification is lower than that of the β-B modification also suggests this classification [5,6]. Other modifications of boron also exist such as tetragonal boron I, tetragonal boron II, and γ-B_{28}; however, the tetragonal modifications are known to

be stabilized by foreign atoms and γ-B_{28} is known to be a high pressure modification [7–9]. Amorphous boron, black or brown, was first synthesized from boric acid (H_3BO_3) or boron oxide (B_2O_3) and potassium or via electrolysis at 1808 [10]. This modification of boron was discovered later in 1892 by Moissan through magnesiothermic reduction of B_2O_3 with magnesium [11].

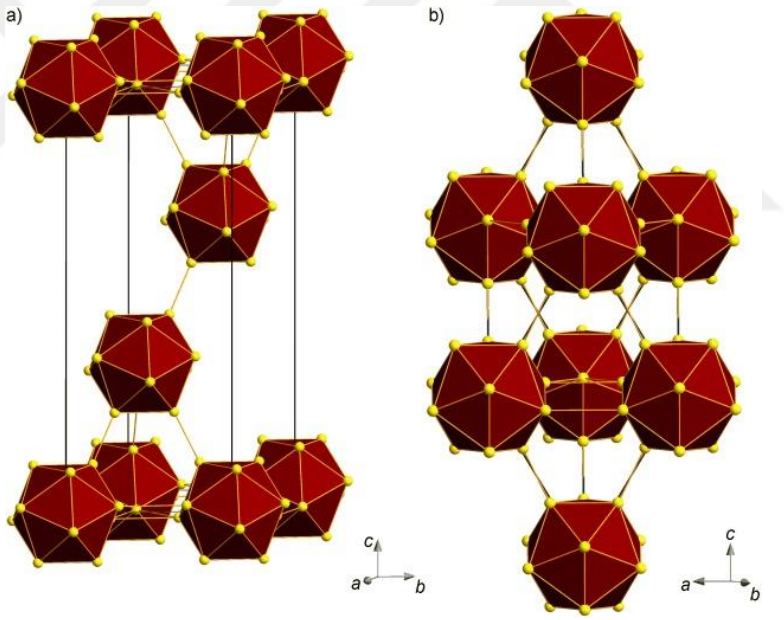

Figure 1. Unit cells of α-B: a) hexagonal setting, b) rhombohedral setting (Adopted from Albert et al.) [12].

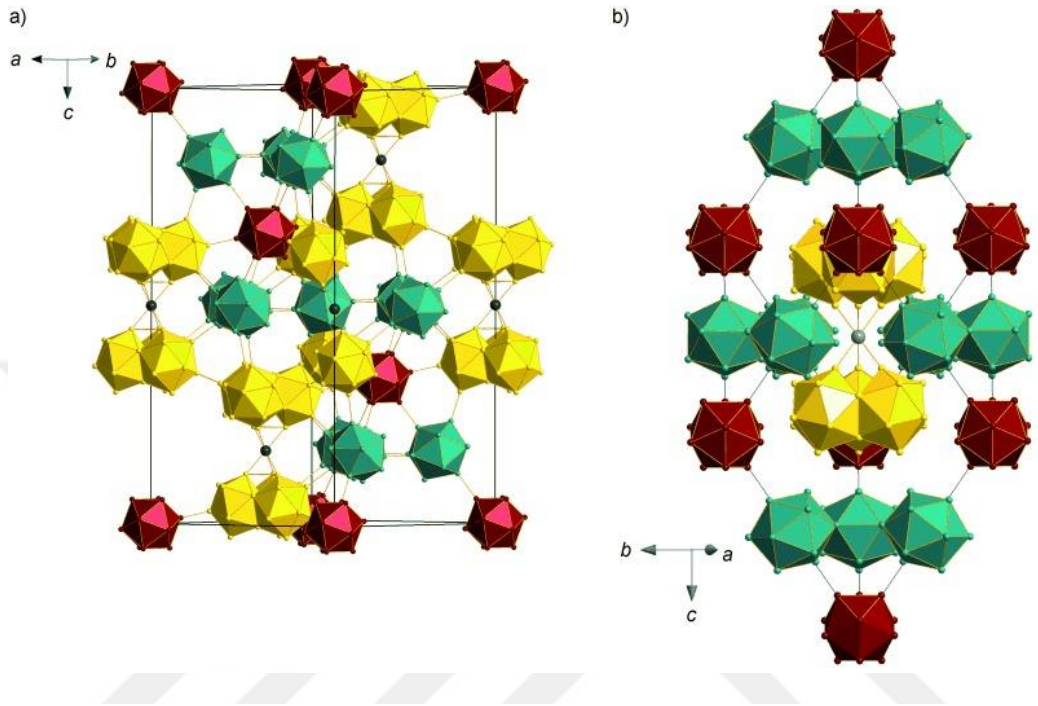

Figure 2. Unit cells of β-B: a) hexagonal setting, b) rhombohedral setting (Adopted from Albert et al.) [12].

Interestingly, within the complex crystalline modification of boron, α-B can be obtained through crystallization of amorphous boron in a platinum melt [12]. On the other hand, an alternative route to produce α-B is to decompose halogenides of boron in presence of hydrogen gas on tantalum surfaces via pyrolysis [13,14]. α-Boron is of red or dark red color and exhibits both non- or semi-conductive behavior [6]. In contrast, β-B possesses a grayish black color, is a semi-conductor, and has a melting point above 2400 K [15]. β modification can be produced through a boron melt and purified via zone melting [16,17]. Despite a number of recent studies and reports, the existence of tetragonal boron I allotrope of pure

boron is debatable [18–21]. In addition, the existence and synthesis conditions of tetragonal boron II has been reported. A recent study claimed that - according to density function theory calculations - these modifications can exist and be more stable than the α and β rhombohedral modifications if only the surface energy is accounted for [22,23]. Moreover, Oganov et al. reported that if β-B is subjected to 2000 K and 20 GPa, a new boron phase is obtained which - given its meta-stability and structural complexity - is known as high-pressure modification or ionic boron [8,9]. Considering the aforementioned allotropic forms - with its ability to form electron deficient multicenter bonds - boron and its compounds can be utilized in many industrial and scientific applications such as airbag igniters, semi-conductors, nuclear and medical fronts (boron neutron capture therapy), and as reinforcement fibers in light metals and synthetic materials i.e. aerospace industry [24,25].

1.2. Metal Borides

Metal borides are compounds consisting of boron and one or more metals less electronegative than boron (M_xB_y, $M_xM'_yB_z$, etc.; M, M' = metals) [26]. The first reports on metal boride date back to early 19th century with the formation of platinum and iron boride as a result of carbo-reduction of metallic powders and boric acid. Many of the elements of the periodic table - with some exceptions such as cadmium, mercury, gallium etc.- can form binary metal borides in different compositions that extend from M_3B to MB_{66} [27]. In

addition, ternary and quaternary metal borides are also known [28–30]. However, the aforementioned exceptions for the binary metal borides which are considered an exception due to low affinity with boron, can be incorporated into ternary boride structures (e.g. cadmium and gallium) [28,30,31].

Nano-scaled crystalline metal borides have not been investigated much in the literature due to problems and challenges that scientists face to synthesize and purify them. Amorphous metal borides have been addressed via the colloidal routes but their conversion to crystalline materials requires much detailed investigation [32–36]. Many scientists have adopted difficult and expensive means and methods such as high energy ball mill, pressurized vessels etc. which are very costly [37,38]. Another challenge that scientists face in order to obtain crystalline nano metal borides is tunable stoichiometry and thus tunable properties.

The reason why nano-scaled metal borides are not investigated as much as other nano materials can be classified into two categories, namely bonding situation and boron source. Metal boride possess very strong M-B and B-B (M = metal, B = boron) covalent bonds which prevents it from forming long range orders that are usually observed in the glassy state, unless severe synthesis conditions - e.g. high temperatures - are adopted for their crystallization [39]. On the other hand, this pathway is impractical in case of nanostructured compounds that are intrinsically metastable i.e. it would be near impossible to isolate them. The other challenge is the lack of boron source capable of providing boron atoms in high efficiency via a simple route. One example is the α-B. This covalent solid, has a reluctance towards solubility and is highly inert [40]. For better understanding of the variety and

complexity of metal boride structures and their wide range of application, one has to look to the interaction of the metal lattice, the strong covalent boron framework within the metal borides and, inspect the bonding situation in more detail. It is observed that in both metal-rich (MB_x, $x \leq 2$) and boron-rich (MB_x, $x \geq 2$) configurations as the ratio of boron to metal increases, the complexity of the boron network evolves from dispersed boron atom clusters to three dimensional boron frameworks (e.g. yttrium boride for boron-rich and nickel boride for metal-rich systems) [41,42]. This results in various crystal structures for metal borides ranging from hexagonal sheet-like structures to complex B_{12} icosahedra based ones [43]. The structure also depends on the metal - as in the case for transition metal borides - where changing the metal (i.e. the group number) results in changing of the ionicity of the M-B bond which in turn changes the crystal structure for the same stoichiometry (e.g. MB_x, x = Ti, Re, Os) [44–46]. Conclusively, with increasing boron to metal ratio, the B-B bond distance decreases as the covalency in the B sublattice increases and is very close to the B-B bond distance in elemental boron. With increasing attraction between boron atoms in the structure, the coordination number of the metal atom decreases. Subsequently electron delocalization takes place in the metal sublattice which results in an elongation of M-M bond distances through the boron sheets. This increase corresponds to an increase in the number of inter-sheet M-M antibonding orbital with increasing number of electrons in the d orbitals [47–50]. Figures 3 and 4 illustrates different boride structures formed due to difference in bond structures of each one.

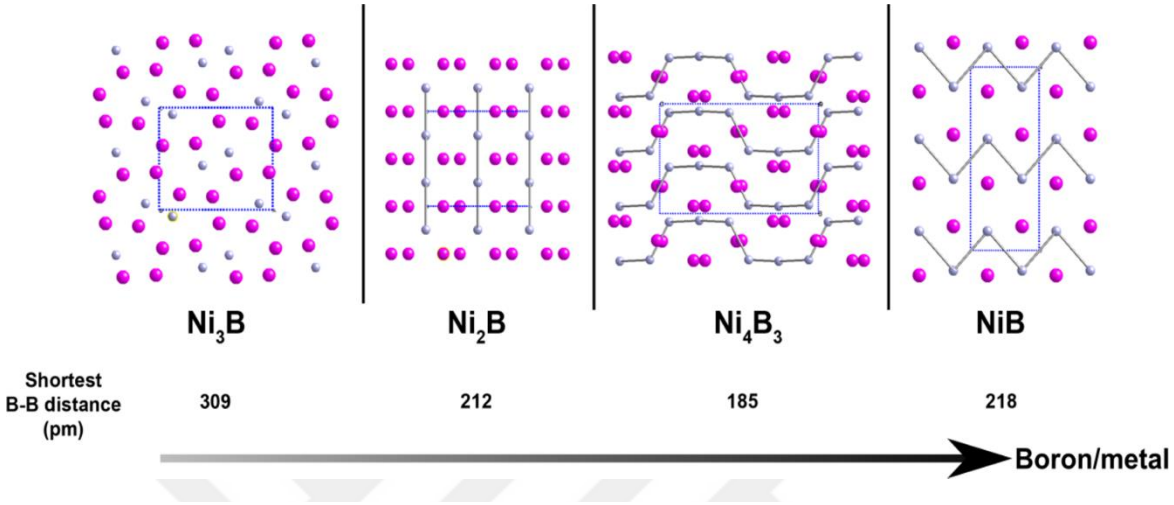

Figure 3. Crystal structures and compositions of nickel borides as an example of metal-rich borides. Small spheres represent boron atoms; large spheres represent nickel atoms (Adopted from Carenco et al.) [39].

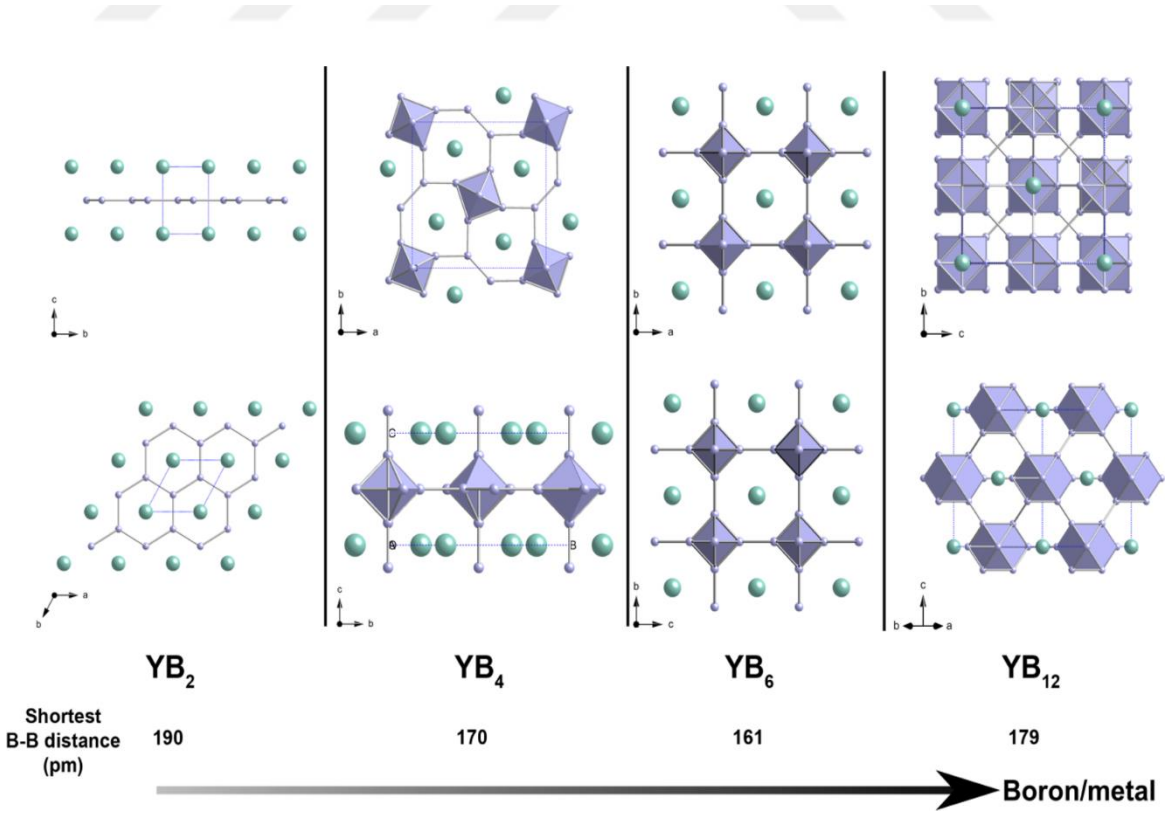

Figure 4. Crystal structures, compositions of yttrium borides YB_2, YB_4, YB_6, and YB_{12}. Small spheres (polyhedra) represent boron atoms (boron polyhedra); big spheres represent yttrium atoms. (Adopted from Carenco et al.) [39].

1.3. Properties and Applications of Metal Borides

The diversity and complexity of the structures of metal borides and fluctuations of bonding situation in both metal and boron sublattices discussed above have resulted in variety of fascinating properties; however, the arduous challenges in obtaining these borides, namely harsh synthesis conditions and lack of an efficient boron source has limited their commercial applications. The following are the discussion for some of the alluring properties of metal borides - within the scope of this thesis - for different applications in both scientific and industrial fronts.

1.3.1. Magnetism

The metal borides performance in the field of magnetism and magnetic materials is more focused on the stabilizing role of boron in terms of a facilitator for the functional structures that leads to alluring magnetic properties of that structure, in this case the metal borides. This is particularly important because metal borides exhibit considerable magnetism only when present in a compound [51]. The bulk $Nd_2Fe_{14}B$ is the strongest magnetic material known yet which has the highest remnant magnetization amongst others [52,53]. Thus, it finds quite a wide range of applications such as speakers, hard drives, electronics and any field that requires a strong magnetic operation field. Given the outstanding properties of these borides, efforts has been made towards downscaling of these materials in hopes of finding new behaviors or enhancing the existing ones [54,55]. For instance, a narrower coercive field was

observed for aggregated nanoparticles of $Nd_2Fe_{14}B$ that are bigger than 100 nm in comparison to its bulk form, and for amorphous iron boride nanoparticles coated with silica [54–57]. In the case of $Nd_2Fe_{14}B$, the root of the magnetism is coming from the ferromagnetic metals, Nd and Fe. However, boron plays a crucial role by coordinating to six Fe atoms which, in turn, results in the alignment of the magnetic moment of Fe atoms along the long axis (c-axis), which causes strong magnetic anisotropy [58]. On the other hand, the magnetic exchange coupling is also effective in enhancing the strength of the magnetic field [54,59]. Some studies in the literature have investigated the relationship of magnetic behavior of Co-B with their particle size. It was observed that for Co-B aggregates of 50-100 nm consisted of 5 nm particles, there exists a strong magnetic exchange coupling interaction between the constituents [60]. On the other hand, the soft magnetic properties of metal borides are very desirable for biomedical applications. Iron boride (FeB) and its derivatives are among the well-known species of borides in that class. Contrary to iron oxide, the research of iron boride nanoparticles for their role in curing cancer and hyperthermia has attracted attention recently [61]. Iron boride also in a very desirable material due to its' outstanding metal anti-corrosion, its's performance in electrochemistry and catalytic performance [62–64]. For instance, the <002> orientation of Fe_2B showcases an enormous energy barrier against chemical corrosion and thus finds application as corrosion-resistance coatings [65,66]. Moreover, Fe_2B was branded as efficiency catalyst for hydrogen evolution reaction consequent to having high adsorption for hydrogen on boron-rich surfaces [63]. All in all, one can say that introduction

of boron can induce (e.g. $Nd_2Fe_{14}B$) or suppress (e.g. nickel borides) the coercivity of the nanoparticles, thus tune the properties of the obtained product [67].

1.3.2. Mechanical properties

The boron based compounds and especially metal borides have been the center of attention in the hard and super hard materials and ultrahigh temperature ceramics fields [68–70]. Because of the bias that boron has towards forming chemical bonds series, it has a tendency to form 3 dimensional covalent frameworks of strong B-B bonds. Presence of this phenomena in the structure of metal borides results in a compound with high modulus of rigidity as dislocations are incapable of traversing through strong directional boron bonds [43]. The hardness of borides has induced numerous studies into their machining and machinability properties while other properties that result from this network of bonds such as wear resistance has been overlooked to some extend that can be useful in biomedical applications [71,72]. Using a method such as borodizing which is a boron diffusion method, one can form a metal rich boride layer on the surface of a metal prosthetic or implant and thus, increase its life span. This, in turn, will eliminate the need for extra surgery and reduce the complications of having an implant, especially for elderly people. The boron atoms in the structure of these lower borides follows the interstitial diffusion path forming strong covalent bonds with the metal matrix [73]. These bonds inhibit the sliding of metal planes resulting in increased hardness and wear resistance of the compound. The Hall-Petch equation states that

with decreasing size of the grains and thus increasing the grain boundaries, dislocation motion becomes harder yielding a much stronger material. Consequently, the effort for nano-scaling of metal borides have been the focus of many studies [73]. It was observed that crystalline nano-scale films of HfB_2, exhibited high modulus of elasticity, high hardness and wear resistance [74,75]. Also, an increase in the nanoindentation values obtained from amorphous cobalt borides showed increased hardness values compared to their bulk forms [76]. On the other hand, considering that boron has the second highest melting point among the elements of the periodic table, it is not surprising that borides are capable of withstanding extreme temperatures. Zirconium diboride, being one of the known refractory borides, possess a melting point of 3230 °C and crystalizes with a two dimensional hexagonal AlB_2 type of structure [77]. The combination of these two properties enables ZrB_2 to withstand extreme and harsh temperatures (cycles up to 2700 °C in air) and grants it outstanding oxidation resistance [78]. This material was investigated by the United States Army branches for use in re-entry vehicles, hypersonic flight and, space applications [79].

1.3.3. Superconductivity

Superconductors have been the focal point of research in the past few years given their promise of transfer of power without any loss of energy as ohmic heat, which enables generation of large and strong magnetic fields required in devices such as NMR, MRI and super magnets [80]. Magnesium diboride is one of metal borides that has been in the center

of attention due to its higher critical temperature (T_c) of 39 K compared to other conventional superconductors [2,81]. The reason for this can be related to the p orbital overlap in addition to the s orbital overlap which is the case in traditional type-I superconductors [82]. It was reported that MgB_2 has one of the longest c-axis among metal borides. It was validated by calculations and modeling that on extension of the c-axis of MgB_2 - and compression of its a-axis - the T_c is expected to experience an increase. Other studies were carried out on different diborides that superconductivity can be induced in materials that do not exhibit this behavior by using excess amount of boron. Given the complex network of boron bonds in metal borides, there are many borides that exhibit superconductive behavior such as Mo_2B, W_2B, TaB, NbB, ScB_{12}, YB_{12}, YB_6, ThB_6, LaB_6, ZrB_{12} and LuB_{12} ; however, none of them possesses a higher T_c than that of MgB_2 [51,83,84].

1.3.4.Electrical, thermal and optical properties

Metal borides possess other properties given their complex structure and strong bonding network that make them important in electrochemical and photoelectrochemical applications. For instance, the catalytic activity of palladium boride compounds was investigated and exhibited a better activity rate in the electro-oxidation of formic acid compared to commercial palladium carbon catalyst under the same conditions [85]. The reason for the enhanced activity rate and poison resistance was imputed to the transfer of electron between Pd and B, expansion of the Pd lattice and, increased number of active sites

[85]. On the other hand, it might be surprising to talk about the optical properties of the metal boride due to the fact that they are metallic conductors and they do not show interesting results in the visible spectrum; however, they have remarkable interactions with other wavelengths [86]. For instance, metal borides interact with the photons of ultra violet range, thus, they have been used as UV light filters that can be employed in deep space applications [87]. As other optical applications of metal borides one can refer to lanthanum hexaboride as X-ray standard, hot cathodes, near infrared absorbers for windows and the isotopically enriched lanthanum hexaboride for neutron diffraction. Also, the use of YB_{66} as X-ray monochromator and synchrotron radiation is noteworthy. Moreover, metal borides have attracted attention due to their interesting electrical properties. For instance, the discovery of the bulk MgB_2 with an interestingly high critical temperature (39 K) was a promising step forward toward a solution for energy that is wasted as heat [2]. According to the estimated energy use in 2019 for USA diagram, 24.2 % of the generated electricity is wasted as heat. In light of this discovery, efforts have been made to investigate the conductive properties of nanoscale MgB_2 with a focus on measuring the critical temperature in hopes of obtaining a higher one [88,89]. Some studies reported a similar value of critical temperature for nanocrystalline structures compared to the bulk values [90,91]. Metal borides have also been suggested as an alternative material for electrodes in solar cells. Binary borides such as ZrB_2, HfB_2 and, TiB_2 have illustrated promising properties as a barrier for Cu diffusion in electrical circuits due to their chemical stability, electrical conductivity and low thermal dilatation [92]. There exist various other applications for metal borides such as being an alternative for

fabrication of metal nitride semi-conductors as a result of similar crystal structure and thermal expansion coefficient. They are also well-known amongst scientists for their fame as field electron emitters such as LaB_6 which helps provide a stable electron beam [93,94]. Metal borides are considered suitable materials for thermoelectric applications due their refractory properties and thermal conductivity. Most of the investigated metal borides for this context are p-type materials that at higher temperatures possess high ZT values [95,96]. There are other metal borides that when doped with β-rhombohedral illustrate n-type properties e.g. Fe, Cr, or V [97,98]. Superior p-n control was observed by Mori et al. in high-temperature borides [99]. Binary alkaline earth hexaborides were investigated by Takeda et al. who reported high negative seebeck coefficients for SrB_6, CaB_6 and, BaB_6 [100].

1.3.5.Catalysis

The application of metal borides in the field of catalysis started around the second half of the 19th century with the recognition of their high efficiency in selectivity and activity during hydrogenation and reduction of a range of organic reactions [101]. This was in the interim with the discovery of amorphous metal borides via precipitation from solution [102,103]. Upon investigation of different alloy compositions of nanoparticles obtained from aqueous solutions for their catalytic activity, the amorphous form of Co-B and Ni-B exhibited outstanding performance in terms of efficiency with respect to selectivity, activity rate and, resistance to poisoning (i.e. inhabitation of active metal sites). Thus making them a better choice compared to their metallic form for hydrogenation of a number of organic substrates such as alkenes, aldehydes, ketones etc. [104–107]. It was observed that presence of a metalloid atom in the structure of the catalyst enhanced their superior efficiency as they boost the thermal stability of the catalyst by causing a homogeneous distribution uninhibited active metal sites [108]. Considering the aforementioned, it was observed that ternary and quaternary boride systems exhibit outstanding catalytic performance which is due to better stability of the amorphous phase obtained as a result of smaller particle size and thus enhanced local disorder. Furthermore, increasing the number of Lewis acidic sites, both as a result of introduction of additional metals in the structure of metal borides was designed for the purpose of catalysis [109,110].

1.4. Synthesis Methods for Metal Borides

There are many ways and techniques to synthesize and obtain metal boride compounds each of which requires different conditions and equipment. To mention only a few are experimental ovens and media that the reaction takes place and result in different forms of obtained boride in terms of structure (e.g. polycrystalline powders, amorphous powders etc.) and reaction yield and purity of the obtained boride phase. Moreover, it is well known that most of the boride synthesis methods require highly elevated temperatures to take place. So far, metal oxide reduction using boron is known to be the most scalable and the synthesis from metals and elemental boron is known to yield metal borides with highest purity. Additionally, chemical vapor deposition and molten mixture electrolysis are known to result in production of a protective, resistant and, refractory layer on the surface of the materials. Some examples of obtained boride phases and their references are depicted in Table 1.

Table 1. Various metal borides and their respective crystal structure information.

Metal	*Boride*	*Lattice*	*Structure Type*	*Space Group*	*Density* [g cm^{-3}]	*Ref*
Mg	MgB_2	Hexagonal	AlB_2	*P6/mmm*	2.63	[111]
Ca	CaB_6	Cubic	CaB_6	*Pm$\bar{3}$m*	2.45	[112]
Sr	SrB_6	Cubic	CaB_6	*Pm$\bar{3}$m*	3.42	[113]
Ba	BaB_6	Cubic	CaB_6	*Pm$\bar{3}$m*	4.32	[113]
Al	AlB_2	Hexagonal	AlB_2	*P6/mmm*	3.16	[114]
	α-AlB_{12}	Tetragonal	$Al_{1.67}B_{22}$	*P4$_1$2$_1$2*	2.55	[115]
Y	YB_{66}	Cubic	YB_{66}	*Fm$\bar{3}$c*	2.50	[116]
La	LaB_6	Cubic	CaB_6	*Pm$\bar{3}$m*	4.71	[117]
Ce	CeB_6	Cubic	CaB_6	*Pm$\bar{3}$m*	4.71	[118]
Nd	NdB_6	Cubic	CaB_6	*Pm$\bar{3}$m*	4.94	[119]
Ti	TiB	Orthorhombic	FeB	*Pnma*	4.57	[120]
	Ti_3B_4	Orthorhombic	Ta_3B_4	*Immm*	4.56	[121]
	TiB_2	Hexagonal	AlB_2	*P6/mmm*	4.46	[122]
Zr	ZrB_2	Hexagonal	AlB_2	*P6/mmm*	6.1	[77]
Hf	HfB_2	Hexagonal	AlB_2	*P6/mmm*	11.16	[123]
V	VB	Orthorhombic	CrB	*Cmcm*	5.44	[124]
	VB_2	Hexagonal	AlB_2	*P6/mmm*	5.07	[124]
Nb	NbB	Orthorhombic	CrB	*Cmcm*	7.57	[125]
	NbB_2	Hexagonal	AlB_2	*P6/mmm*	6.95	[125]
Ta	TaB	Orthorhombic	CrB	*Cmcm*	14.21	[126]
	Ta_2B	Tetragonal	$CuAl_2$	*I4/mcm*	15.21	[126]
	TaB_2	Hexagonal	AlB_2	*P6/mmm*	12.53	[127]
Cr	CrB	Orthorhombic	CrB	*Cmcm*	6.07	[128]

Metal	*Boride*	*Lattice*	*Structure Type*	*Space Group*	*Density* [g cm^{-3}]	*Ref*
	Cr_2B	Orthorhombic	Mn_4B	*Fddd*	6.47	[124]
	CrB_2	Hexagonal	AlB_2	*P6/mmm*	5.21	[124]
Mo	Mo_2B	Tetragonal	$CuAl_2$	*I4/mcm*	9.23	[124]
	α-MoB	Tetragonal	MoB	*I4$_1$/amd*	8.67	[124]
	β-MoB_2	Hexagonal	AlB_2	*P6/mmm*	7.87	[129]
W	W_2B	Tetragonal	$CuAl_2$	*I4/mcm*	17.09	[130]
	WB_4	Hexagonal	$W_{1.83}B_9$	*P6$_3$/mmc*	8.4	[131]
Mn	MnB	Orthorhombic	FeB	*Pnma*	6.37	[132]
	MnB_2	Hexagonal	AlB_2	*P6/mmm*	5.35	[132]
	MnB_4	Monoclinic	MnB_4	*C2/m*	4.45	[132]
Re	ReB_2	Hexagonal	ReB_2	*P6$_3$/mmc*	12.67	[133]
	Re_3B	Orthorhombic	Re_3B	*Cmcm*	19.36	[134]
Fe	FeB	Orthorhombic	FeB	*Pnma*	6.75	[124]
	Fe_2B	Tetragonal	$CuAl_2$	*I4/mcm*	7.34	[124]
Co	CoB	Orthorhombic	FeB	*Pnma*	7.37	[135]
	Co_2B	Tetragonal	$CuAl_2$	*I4/mcm*	8.05	[135]
	Co_3B	Orthorhombic	Fe_3C	*Pnma*	8.11	[135]
Ni	NiB	Orthorhombic	CrB	*Cmcm*	7.2	[124]
	Ni_2B	Tetragonal	$CuAl_2$	*I4/mcm*	8.06	[124]
	Ni_3B	Orthorhombic	Fe_3C	*Pnma*	8.18	[124]
	Ni_4B_3	Orthorhombic	Ni_4B_3	*Pnma*	7.58	[124]
Pd	Pd_2B	Orthorhombic	$CaCl_2$	*Pnnm*	9.93	[136]
Pt	Pt_2B	Hexagonal	MoS_2	*P6$_3$/mmc*	18.79	[137]

The first conventional method uses elemental metal powders and boron as precursors and is carried out through the reaction presented in Eq.1:

$$xM + yB \rightarrow M_xB_y \quad (1)$$

In this method the precursors are either melted by usage of an arc melting furnace, a high temperature furnace or an induction furnace or are sintered in an inert atmosphere or under vacuum. Considering the relative melting point of the selected metal to boron, a small amount of excess boron (≈10 at%) is added to the reaction due to the possible boron loss by sublimation during the heating process to maintain the stoichiometry of the obtained product [77,123,138]. Moreover, formation of some borides requires presence of excess amount of boron because otherwise, the boride form that is thermodynamically more stable will form, such as WB_4 compared to WB_2. The formation of WB_4 is only possible with a metal to boron ratio of 1:12 [131,139,140]. Synthesis via arc melting is the conventional method for obtaining poly crystalline borides which is normally carried out in an arc melting oven sealed under argon or helium gas atmosphere by using pellets of metal and boron powders. There are many classes of metal borides that can be obtained via synthesis of pure precursors in an arc melting device including:

1) Lower metal borides and their alloys such as TiB; ReB_2; NbB_2; WB_2; Ru_2B_3; $Sc_{1-x}W_xB_2$; $W_{1-x}Ta_xB$ and $Sc_{1-x}Re_xB_2$ [120,133,141,142].

2) Tungsten tetraboride (WB_4) and its alloys with transition metals (Zr, Ti, V, Hf, Ta, Nb, Mn, Cr, Mo and Re) [139,140,143,144].

3) Metal dodecaborides (MB_{12}) and their alloys: $Zr_{1-x}Sc_xB_{12}$; $Zr_{0.6}Y_{0.4}B_{12}$; $Th_{1-x}Zr_xB_{12}$; $Y_{1-x}Hf_xB_{12}$; ErB_{12}; ScB_{12}; $Y_{1-x}Sc_xB_{12}$; $Zr_{1-x}Y_xB_{12}$; YB_{12}; UB_{12} and ZrB_{12} [71,145–147].

4) β-rhombohedral boron and its transition metal doping phases (HfB_{50}, ScB_{50}) [148,149].

5) $YPtB_{50}$ [150].

Hot pressing of the precursor powder mixtures is another common method of synthesizing metal borides which is mainly used for making boride tools [151]. Acquiring a single crystal of a crystalline material is crucial for characterization and understanding of its properties and behavior. In case of metal borides, a high frequency induction furnace is commonly utilized to obtain single crystals of ScB_{12}, ZrB_{12}, YB_{66}, UB_{12}, TmB_{12}, ErB_{12} etc. [152–154]. Furthermore, flux growth method is commonly used to produce single crystals of lower metal borides with Bi, Sn and Al as flux reagents, such as in the case of ReB_2 and AlB_2 [114,155]. Another method to obtain lower boride single crystals is to use pressed pure metal and boron powders sealed in a quartz ampule in presence of a mineralizer such as iodine at high temperatures (i.e. 1000 °C), such as in the case of MnB_4 and CrB_4 [156,157]. Spark plasma sintering and high temperature furnaces can also be used to synthesize metal borides, for instance HfB_2, Y_2ReB_6, ReB_2 and ZrB_2 can be synthesized via this route [133,134,158]. Obtaining metal borides from the reaction of elemental boron and metal sulfide, hydride or nitride is also considered among the mentioned methods [159].

One of the other well-known methods used in synthesis of metal borides is self-propagating high-temperature synthesis (SHS) [160]. In this method the heat produced by the exothermic reaction of the precursors is the solely driving force and the only requirement

is an initiation step to activate the reaction. The efficiency of the reaction and the composition of the final product is relying on how dense the formed pellet is and the initial stoichiometry of the precursor powders respectively. Due to the fast propagation speed of these reactions and the fact that no additional energy sources are required for its transpiring, this method is considered to be advantageous amongst others. However, given the fast pace of this reaction the control of the stoichiometry of the final product is very difficult and requires precision in sample preparation steps. This method has been utilized in synthesizing lower borides of Ti, V, Zr, Nb, Hf, Ta, Mo and Cr [161].

Reduction of metal oxide and boron using carbon, or carbothermal reduction, is one of the oldest methods of obtaining metal borides that dates back to 1936 [162]. The theoretical reaction is presented in Eq. 2 as follows:

$$MeO(s) + B_2O_3(l) + C(s) \rightarrow MeB(s) + CO(g)\uparrow \quad (2)$$

One disadvantage of this method is the formation of side products and impurity in the form of boron carbide and/or metal. Obtaining a phase pure product by this technique has proved to be difficult because of the required high temperatures (1900 °C) and the application of excess boron oxide (due to loss by sublimation). The latter two are the main limiting factors which have impeded the universal use of this method.

Borocarbothermal reaction is the case where pure boron is used as the boron source instead of boron oxide; however, given that boron is a stronger reducing agent than carbon, the obtained metal borides contain up to 6 wt% carbon in their structure which is a huge

disadvantage [163]. The metal borides obtained via reduction by boron carbides yields the least amount of carbon impurity in the final product. This happens due to the formation of the gaseous carbon monoxide (CO) which ensures the completion of the reaction and the vacuum atmosphere preventing the further oxidation of the products.

One of the most common industrial methods used for synthesis and obtaining metal borides is known as the borothermal reaction and takes place through reduction of metal oxides by boron and yields boron oxide as a by-product [164]. The boron plays two roles in this reaction as boron source and as reducing agent, and in order to remove the final oxide ~~version~~ the reaction is carried out under vacuum which, in turn, reduces the necessary purification steps for the final product [165]. The method can be used for synthesis of transition metal borides of group IV–VI and depending on the conditions of the reaction and used precursors can result in various boride structures ranging from monoborides (MB) to MB_{12} [165].

A further alternative route of obtaining metal borides is the reaction of metal oxides with boron oxide in the presence of reducing metals such as magnesium, calcium, aluminum, sodium, potassium or silicon [166]. This method is based on a set of solid state oxidation and reduction reactions with metals whereby magnesium being the most commonly used one naming the reaction magnesiothermic reduction reaction [167]. This technique is also considered to be a cost effective one considering that it allows the usage of boric acid as the boron source instead of boron oxide [167]. Diborides of some transition metals such as Ti,

Cr, Nb etc. and hexaborides of rare-earth and alkali metals are some of the metal boride examples produced via this method [167].

Metal borides can also be synthesized via precipitation of the products from the gaseous phase, also known as chemical vapor deposition (CVD). The general theoretical reaction is presented in Eq. 3 as follows:

$$MeCl_4\,(s/l) + 2BCl_3(l) + 5H_2\,(g) \rightarrow MeB_2(s) + 10HCl(g) \quad (3)$$

Where the reaction moves forward through the reduction of the reactants to their elemental forms by hydrogen gas, followed by the reaction to form the metal borides and the side products. This method has been utilized to obtain films and coatings of metal boride for applications such as combustion chambers, refractory coating for re-entry vehicles, turbine blades, cutting tools etc. and in some cases growth of metal boride single crystals (e.g. TiB_2) [168,169]. However, optimization of the reaction parameters to obtain borides with the desired stoichiometry and properties is one of the main handicaps of this method [170,171]. Another route for metal boride surface coatings is the preparation via electrolysis. Herein, molten salts of strong electrolytes are mixed and subjected to a current and the final product is deposited on the cathode or anode via electrochemical deposition reaction that takes place. The reaction parameters such as applied voltage, temperature of the mixture and current density can vary based on the desired composition and quality of the product. Lower borides of chromium are examples of metal borides synthesized via this method. Other methods used for the synthesis of metal borides also include mechanochemical synthesis and mechanical alloying [172,173].

One of the biggest obstacles of synthesizing pure metal borides has been the refractory nature of them requiring the use of high-temperature furnaces, expensive equipment and purification of the final product. This in turn has triggered the tendency towards alternative synthesis methods such as solid-state metathesis (SSM) where two reactants capable of forming a salt are mixed and reacted in double displacement reactions. As a result of the initiation, self-sustaining heat is produced which acts as the driving force to yield metal boride and a side product (generally a salt). The latter is removed via a solvent after the reaction. OsB_2 and ReB_2 are the two examples synthesized by this method [133,174,175].

This thesis investigates a low-temperature synthesis route both with and without the help of an inorganic molten salt environment, investigating the feasibility of obtaining ternary and/or binary transition metal borides in detail. The properties of the obtained metal borides are investigated in detail according to the intrinsic character of the transition element used. The following three chapters' exhibit the obtained results of this study classified based on application areas and synthesis conditions according to the ideal reactions provided below:

$$CoCl_2 + FeCl_3 + xNaBH_4 \rightarrow CoFeB_x + xNaCl + H_2 \quad (4)$$

$$CoCl_2 \cdot 6H_2O + FeCl_3 \cdot 6H_2O + xNaBH_4 \rightarrow CoFeB_x + xNaCl + NaOH + H_2 \quad (5)$$

$$CoCl_2 + TiCl_4 + xNaBH_4 \rightarrow CoTiB_x + xNaCl + H_2 \quad (6)$$

The reaction takes place upon decomposition of $NaBH_4$ to NaH and BH_3 which then reduces the chlorides, triggering the formation of metal boride and salt as a result [39]. Further investigations into the properties of the obtained boride samples are required to achieve a

better and deeper understanding of the applicability and compatibility of the boride nanoparticles in various aspects of industry and life.

Chapter 2. Crystalline Co-Fe-B Nanoparticles: Synthesis, Microstructure and Magnetic Properties

2.1. Introduction

Due to their superior properties like high melting point, chemical stability, hardness and wear resistance, magnetic behavior and biocompatibility, synthesis and characterization of binary and ternary metal boride nanoparticle powders has been of dire importance in recent years [32,176]. These properties make various transition element borides desirable for many applications like catalysis reactions, magnetic materials, biomaterials and reinforcement agents [32,176–178]. Given their magnetic nature, iron and its alloys and compounds have application in various scientific and industrial fronts and products. They are also used in biomedical applications such as cancer detection and therapy, magnetic resonance imaging (MRI), magnetic drug targeting and delivery, cell and tissue repair, catalysis, hyperthermia and xerography [32,176–178].

It has been reported that the performance of cobalt boride-based composites or cobalt boron-based alloys was improved with various additives such as Co-metal-boron alloys or Co-boron based composite nanoparticles. They were found to be suitable for use as catalysts, magnetic materials and coating materials with high corrosion or abrasion resistance in hydrogen storage applications [76,179,180]. Also, it has been reported that cobalt-iron-boron compounds (Co-Fe-B) formed with the addition of Fe promise superior properties to the

binary structures in their respective application areas [181–184]. The properties of the Co-Fe-B based powders, such as larger active surface area and improved ability of absorption obtained with a second metal contribution, led to greater interest in their catalytic effect [184,185]. Also, these powders have been intensively investigated for their soft magnetic behavior in microwave and medical domains [61,186]. The compatible electronic interaction between Co and Fe atoms has led to use of these metal combinations to develop boron alloys with various properties. Some CoFeB amorphous alloys have been proposed for use in fine and ductile magnetic coating material or water electrolysis [187–189]. The wear properties of CoFeB magnetic thin films suitable for use with various substrates and the magnetic orientation behaviors of CoFeB alloys, which are suitable for use in modern electronic equipment, are investigated in the literature [190,191]. CoFeB thin films of ferro-magnetic properties have been reported to have low remanence and high saturation magnetization properties [192].

Binary borides of cobalt and iron are generally produced via chemical reduction processes using different forms of starting materials [32,176,177,193–195]. In addition, electric arc method, thermal plasma method, melt-spinning, sol-gel method, auto ignition, co-precipitation processes, self-propagating high temperature synthesis (SHS), chemical vapor deposition method (CVD) are the other production routes for iron borides [57,196–199]. Solid-state processes are also utilized for the synthesis of iron borides [197,200,201].

On the other hand, the production methods of ternary borides are much less known than their binary compounds and are still being investigated. The ternary borides have

conventionally been obtained by direct reaction of pure elemental metals and boron in an inert atmosphere or under vacuum (> 1500 °C) [39,193]. Since these processes require a very high reaction temperature and time, it is difficult to avoid impurities of oxygen, carbon or other elements in the final product [193]. One of the methods developed later involves milling the binary metal boride and metallic powder mixtures in a ball mill followed by pressing and sintering under high temperature vacuum (~1300 °C) [202,203]. Furthermore, reduction techniques have been applied such as inorganic molten salt or aqueous solutions for the production of ternary metal-boron compounds or alloys developed as catalyst or magnet [39]. As the chemicals obtained by these methods are amorphous or complex compounds, their characterization is quite difficult [204]. Additionally, these techniques are not suitable as a general and effective synthesis method, since the final products are mostly of low surface area and low purity [39,204].

As discussed above, there are numerous studies investigating different synthesis methods of metal boride composites which are mainly using elemental powders for precursor and implement high temperature techniques [187,205]. This study; however, focuses on the synthesis of nano crystalline metal borides using metal chlorides as precursors via low temperature routes and studies of their structures with investigations of chemical and physical properties.

2.2. Experimental Procedure

2.2.1. Precursor Materials

The synthesis was carried out using $CoCl_2$ (Anhydrous Cobalt Chloride, Alfa Aesar, 99.7 % purity), $FeCl_3$ (Anhydrous Iron Chloride, Alfa Aesar, 98 % purity) and $NaBH_4$ (Sodium Borohydride, Alfa Aesar, 98 % purity) powders as starting materials. The mixture of LiCl (Lithium Chloride, Alfa Aesar, 99% purity) and KCl (Potassium Chloride, Merck, 99.5% purity) powders with eutectic composition (LiCl/KCl with 45:55 wt. % ratio) was melted in quartz tube using oxygen torch and then cooled to room temperature. The prepared mixture was used to obtain a water soluble inorganic molten environment with a low melting point. XRD patterns of the precursor powders are given in Figures A1 (a)-(c) (Appendix A). The broad peak observed at 2θ=15-20° belongs to the Kapton file used to prevent oxidation, whereas the other peaks belong to the powders ($FeCl_3$ ICDD Card No: 04-007-2291, $CoCl_2$ ICDD Card No: 00-001-0173, $NaBH_4$ ICDD Card No: 01-075-0208). DSC heating and cooling curve of the LiCl/KCl eutectic mixture is given in Figure A1 (d) (Appendix A). The endothermic and exothermic peaks observed respectively during heating and cooling curves indicate that the eutectic mixture melts at about 350 °C in accordance with the theoretical temperature which in turn proved the suitability of the mixture.

2.2.2. Reaction Systems

Two different reaction systems were used in experiments: The first one is the synthesis in sealed steel tubes placed in a chamber furnace to which we refer as "close system" hereafter. Stainless steel tubes were sealed under Ar using arc welding and then transferred to the furnace for reaction at 850 °C for 2 h. The second reaction system is the synthesis in an alumina crucible placed in a quartz tube which was carried out in a vertical tube furnace at 650-850 °C for 2 h under controlled Ar flow. To this system, we refer as "open system" hereafter. The purpose of the open system is to get rid of unwanted gaseous by-products in the flow of Ar which protects the prepared powder mixtures from oxidation or decomposition. In both experimental systems, for complete decomposition of $NaBH_4$ to happen, the reaction was put on hold at the temperature of 550 °C for 2 h and then heated up to reaction temperature with a holding time of 2 h. To study the effect of reaction time on the microstructure, additional experiment was done at 850 °C for 6 h. All powder preparations were carried out in a glovebox under Argon (Ar) gas atmosphere.

The ideal reaction between $CoCl_2$, $FeCl_3$ and $NaBH_4$ should result in a formation of ternary metal boride and NaCl compounds, and H_2 gas. Based on previous studies and our preliminary investigations, optimum results were obtained with a molar ratio between 1:2 – 1:3 of metal chlorides to $NaBH_4$ [32,39,206]. Thus, the powders were put in furnaces for synthesis by using a total of 2 mmol $CoCl_2$, 2 mmol $FeCl_3$ and 12 mmol $NaBH_4$. The eutectic composition of KCl/LiCl was used with a 10:1 weight ratio to reactants, to create the molten salt medium in which the reaction would take place [207]. The powders and eutectic mixture

were subjected to roll milling for 10 min in order to achieve a more homogeneous mixture. Process flow chart is summarized in Figure 5. Only one experiment in close system was done without eutectic mixture to reveal the effect of molten salt environment on the phase and microstructure. For comparing purposes, the synthesis of binary borides (CoB, FeB) were studied in identical conditions by using $CoCl_2$-$NaBH_4$ or $FeCl_3$-$NaBH_4$ mixtures, respectively and were investigated in terms of phase formation and thermal behavior.

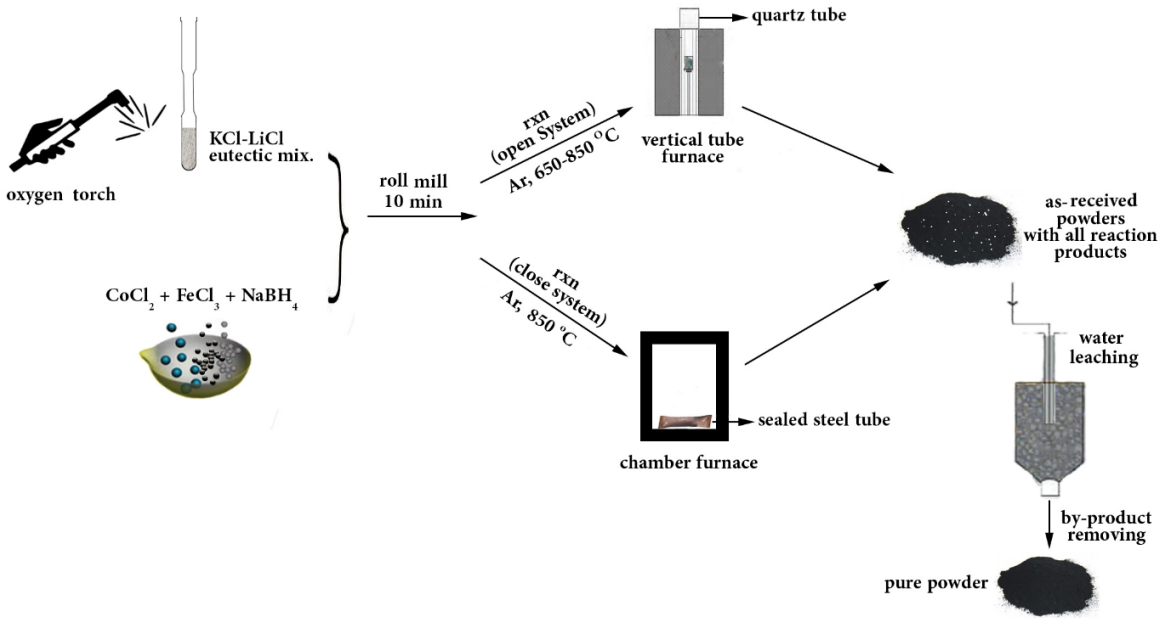

Figure 5. Process flow chart used in the experiments.

Some of the powder mixtures were pressed into pellets using hydraulic press with maximum load of 10 tons and then placed in quartz tubes, subjected to vacuum for 15 min

and then sealed using oxygen torch. The pressed and sealed powders were annealed at 1100 °C for 2 h to confirm presence of desired phases and to investigate their crystalline structure. In order to remove the by-products (NaCl, LiCl and KCl), the obtained powders were repeatedly leached with distilled water at 70 °C, then centrifuged at 3500 rpm for 15 min to precipitate the powders and finally placed overnight into a vacuum oven at 70-200 °C to dry. The obtained powders are composed of nanoparticles, which are very hygroscopic, hence making the leaching and drying step of importance.

2.2.3. Characterization

Phase analysis and microstructural characterization of the powders were performed by Rigaku Miniflex X-Ray diffractometer (XRD, CuKα). The phases were determined using the International Center for Diffraction Data (ICDD) database. A common problem during XRD measurements of powders containing cobalt with CuKα rays is the lack of uniformity of the patterns due to the fluorescent effect of the cobalt. This problem was solved using the XRF reduction mode of the Rigaku device and by changing the detector angle to reduce the fluorescence effect. Microstructural and morphological characterizations of the powders were performed using Zeiss Ultra Plus field emission scanning electron microscope (FE-SEM) equipped with energy dispersive X-Ray spectrometer (EDS). Structure of the powders and the phase distribution in the structure were analyzed and supported via XRD and SEM/EDS analysis. Thermal analyses were performed using differential scanning calorimetry (DSC, TASC 414/3 A, Netzsch) and differential thermal analysis/thermogravimetric (DTA/TG, STA449F3, Netzsch) apparatuses. DTA/TG analyses

were conducted in an alumina crucible up to a heating temperature of 1500 °C with a heating rate of 10 K/min under Ar atmosphere. Elemental analysis up to ppm level was conducted using Bruker Tiger S8 XRF device. Particle size and distribution analyses were carried out using particle size measuring device (Malvern ZS - Zetasizer) incorporating dynamic light scattering (DLS) technique. Surface area measurements of some powders were done with BET surface area analysis (Micromeritics ASAP 2020 HD) supporting particle size measurements. For surface analysis, X-ray photoelectron spectrometer (XPS, Thermo K-Alpha) and attenuated total reflection - Fourier transform infrared spectrometer (ATR-FTIR, Thermo Scientific IS10) were used. Magnetic properties of synthesized powders were measured on a SQUID magnetometer (MPMS-XL7, Quantum Design) at room temperature.

2.3. RESULTS AND DISCUSSION

2.3.1. Nanoparticles synthesized in close system

2.3.1.1 Effect of eutectic salt mixture on the phase formation

XRD patterns of the powders obtained from the reaction of $CoCl_2$-$FeCl_3$-$NaBH_4$ at 850 ˚C with and without eutectic salt mixture are presented in Figure 6 comparatively. In both cases the phase structure of the powders is the same and the XRD patterns show only the presence of the binary CoB (ICDD Card No: 04-003-2122, orthorhombic, *a = 3.948* Å, *b = 5.243* Å, *c = 3.037* Å – Refined lattice parameters: *a = 3.949(2), b = 5.263(4), c = 3.044(2)*) and Fe_3B (ICDD Card No: 04-001 -3343 orthorhombic, *a = 5.428* Å, *b = 6.699* Å and *c = 4.439* Å) phases. Alongside formation of CoB phase, (CoB_{MP} = 1460 °C) which is thermodynamically most stable phase of the cobalt boride, iron boride has been formed also in a thermodynamically known phase [208].

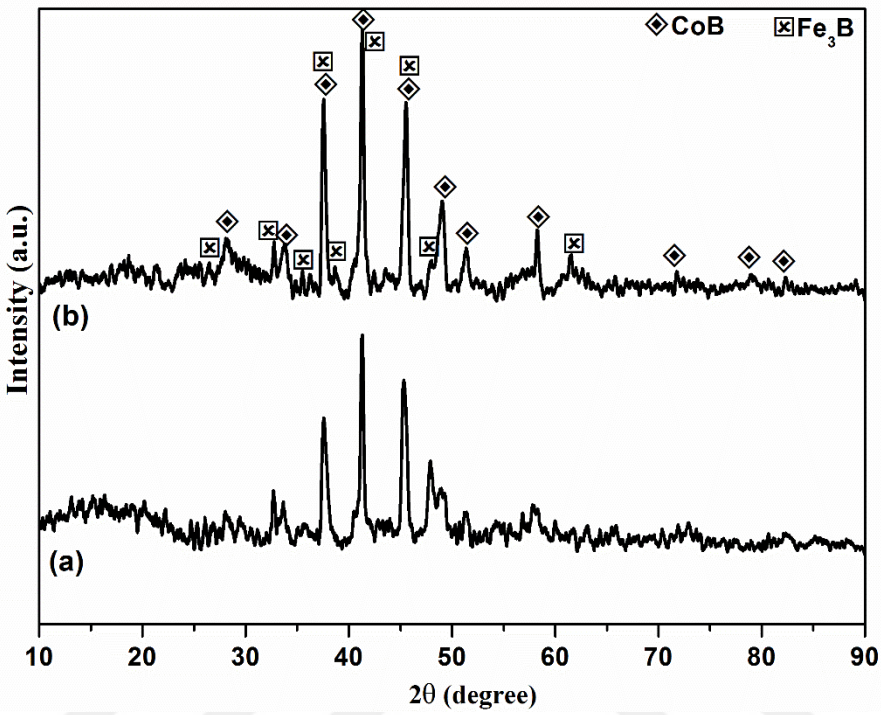

Figure 6. XRD patterns of the powders obtained by reaction of a mixture of $CoCl_2$-$FeCl_3$-$NaBH_4$ at 850 °C in the close system: (a) without eutectic salt mixture and (b) with eutectic salt mixture (See appendix A2 for comparison with reference peaks).

Figure A3 (Appendix A) and Table 2 respectively present the FTIR and chemical analyses of the powders obtained from the reaction of $CoCl_2$-$FeCl_3$-$NaBH_4$ in the close system at 850 ˚C. Figure A3 (a) suggests the presence of B-H bonds in the reaction products obtained without eutectic salt mixture, which indicates the presence of unreacted $NaBH_4$ in the powder. The chemical analysis given in Table 2 also supports this situation: While the powder does not contain any Cl element, presence of 4.2 wt. % Na element shows that either $NaBH_4$ remains unreacted or elemental Na remained in the powder after being vaporized during $NaBH_4$ decomposition [208,209]. The broad peak observed around wave number

3300 cm^{-1} is corresponding to the well-known O-H vibration which exists in the structure of water and moisture. It is known that $NaBH_4$ is decomposed to NaH and BH_3 at 550 °C; however, a recent study showed that decomposition of $NaBH_4$ continued even after 600 °C [208,209]. The presence of $NaBH_4$ in the powder obtained from the reaction at 850 °C can be explained either by the difficulty in the formation of gas products due to the high pressure in the close system and inability of all of $NaBH_4$ to decompose or as a result of very high vapor pressure of Na metal at elevated temperatures. Also, it could be attributed to early decomposition of $NaBH_4$ as a result of presence of chlorides which act as catalysts for $NaBH_4$ dehydrogenation by bringing the decomposition activation energy to lower values, thus reducing the peak decomposition temperature to 470 °C [209]. According to the yield calculations, the efficiency of the $CoCl_2$ conversion in the eutectic salt mixture was found to be 10 % higher than in the eutectic-free mixture, which can be also attributed to better decomposition of $NaBH_4$ as a result of presence of substantial amount of chlorides in the mixture [208,209]. In addition, very small amount of K and/or Cl elements in the composition of the powder (Table 2) can be attributed to a small amount of KCl phase which cannot be removed during water leaching (in case of using eutectic mixture), or a K impurity coming from the precursors. Water-leaching was applied to this powder for a second time and after XRF analysis, KCl was completely removed. Repeated trials have shown that second leaching process applied to powders after drying removes unwanted chloride phases completely. This indicates to the importance of purification processes. As a result, there is no Na impurity in the powder obtained from the reaction performed in the close system with

eutectic mixture environment (Table 2) and the FTIR spectra does not present any peaks corresponding to B-H, B-OH or B-O bonds (Figure A2(b)).

Table 2. Chemical analysis of powders obtained by reaction of $CoCl_2$-$FeCl_3$-$NaBH_4$ in the close system at 850 °C.

Element (wt. %)	*Co*	*Fe*	*Na*	*Si*	*Cl*	*K*
Without Eutectic Salt Mixture	34.64	39.38	4.2	-	-	0.60
With Eutectic Salt Mixture	47.47	36.19	-	0.32	0.11	0.16

2.3.1.2 Microstructural evolution

Figure 7 shows the SEM images of the powders obtained by reaction of $CoCl_2$-$FeCl_3$-$NaBH_4$ in the close system at 850 °C. The microstructure shows particles with dimensions ranging from 30 to 80 nm and clearly, the gas pressure in the close system decreases the particle size considerably. However, when the eutectic mixture is not used, the microstructure shows a heterogeneous appearance: As seen in Figure 7 (b), the microstructure in the lower magnification SEM analysis shows agglomerated particles of sizes up to 6 µm. On the other hand, the molten media created by the eutectic mixture provided a more homogenous appearance of the powders after the reaction (Figure 7 (c)). These results can be attributed to the two-fold effect of the eutectic particles on

recrystallization kinetics: particles (<0.1μm) that are well distributed inhibit recrystallization while others (>1μm) promote recrystallization through particle stimulated nucleation [210,211,220,212–219]. It can be concluded that eutectic environment triggers a uniform particle size distribution in the final powder morphology, while particle size distribution for powders synthesized without it, have a broader range from nano to micron scale. In addition, according to SEM images, it is observed that there are no other forms of morphology in the structure.

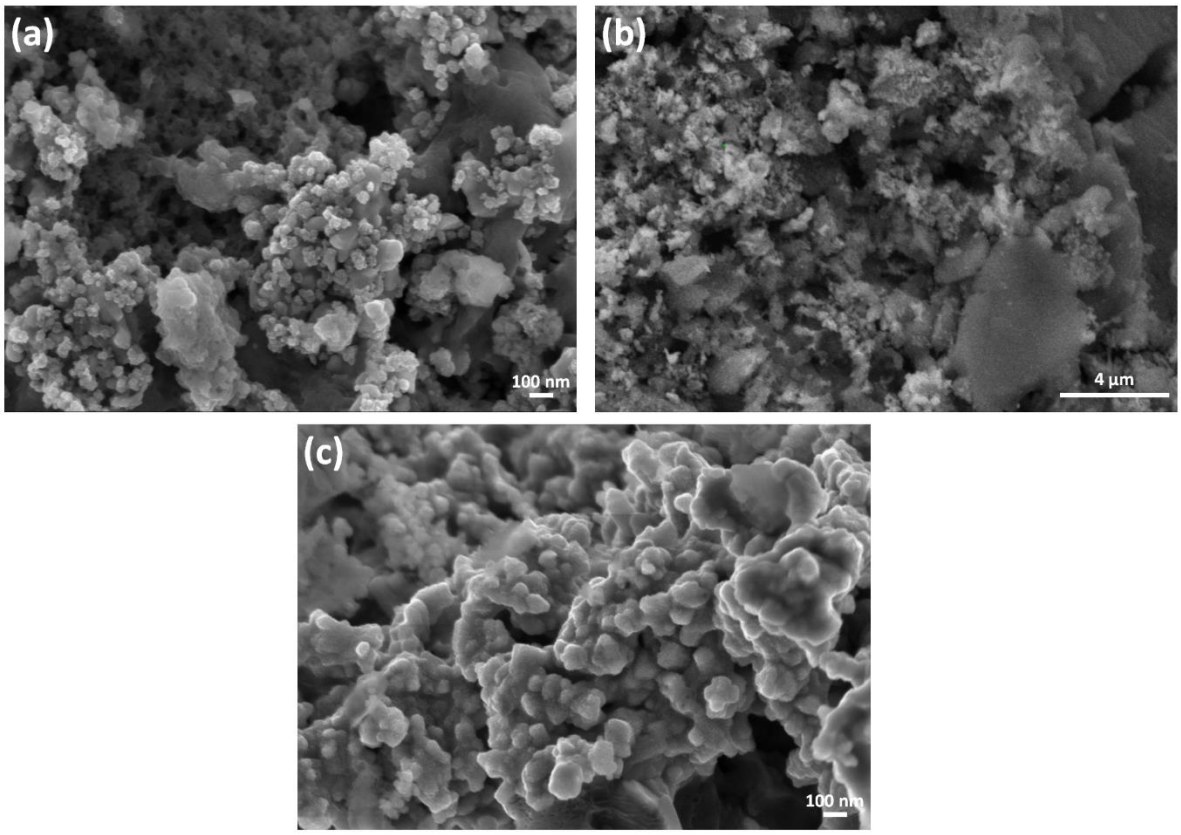

Figure 7. SEM images of powders obtained by reaction of $CoCl_2$-$FeCl_3$-$NaBH_4$ in the close system at 850 °C: (a) and (b) without eutectic salt mixture and (c) in eutectic salt mixture medium.

After the powders were dispersed in the ultrasonic bath, particle size measurements were made using DLS analysis method. The average particle sizes of the powders prepared with and without of the eutectic salt mixture medium were measured as 222 and 100 nm, respectively. However, since agglomerated particles with sizes up to 6 µm observed in SEM images (Figure 7 (b)) were not detected in the DLS technique due to fast precipitation, the value obtained from the DLS analysis does not reflect an accurate measurement. On the other

hand, powders presented in Figure 7 (c) is homogeneous and of submicron size which is confirmed by SEM and DLS analyses.

2.3.2. Nanoparticles synthesized in open system

2.3.2.1 Phase analysis

Figure 8 shows the XRD patterns of the powders obtained from reaction of $CoCl_2$-$FeCl_3$-$NaBH_4$ with eutectic salt mixture in the open system at 650-850 °C, comparatively. As illustrated in Figure 8, $CoFeB_2$ (ICDD Card No: 01-079-2846, orthorhombic, *a = 5.430* Å, *b = 2.985* and *c = 4.020* Å – Refined lattice parameters: *a = 5.26(7)*, *b = 2.97(2)*, *c = 4.05(3)*) phase was determined in the XRD patterns. When the temperature rises from 650 to 850 °C, a significant increase in the peak intensity of the $CoFeB_2$ phase is observed, which results from further crystallization of this phase with the increasing temperature. When the XRD patterns in Figures 6 and 8 are compared, it is understood that the peaks formed between 2θ = 70-85° in Figure 8 originate from the $CoFeB_2$ phase [221]. In addition, it should be noted that peaks of CoB and FeB (ICDD Card No: 04-013-1637, orthorhombic, *a = 5.504* Å, *b = 2.945* and *c = 4.056* Å – Refined lattice parameters: *a = 5.5(5)*, *b = 2.7(1)*, *c = 4.3(4)*) overlap with some peaks of the ternary boride in XRD patterns. Having the same crystal structure with CoB and FeB, it is also possible to observe binary phases with the $CoFeB_2$ solid solution formed in between the CoB and FeB phases. This indicates that the powders obtained are mixed phases (solid solutions) in equilibrium, which agrees with previous studies in both

metal rich and boron rich cases [184]. Comparing the phase formations in close and open systems (Figures 6 and 8), it was observed that CoB and Fe_3B phases formed separately as a result of a reaction in sealed tubes, whereas $CoFeB_2$ solid solution nano powders were obtained in one step at 850 °C after a reaction under Ar flow. This can be attributed to two different reaction mechanisms originating from autogenous pressure or gas flow conditions in close and open systems, respectively. This probably affects the reaction between $CoCl_2$ and $FeCl_3$, and hence accelerates the inter-diffusion between two binary phases and results in a formation of a solid solution in open system.

Formation of a solid solution between borides of transition elements is a known fact. It happens because of either a change in number of valance electron number per formula unit of the crystal, also known as valence electron concentration (VEC) or movement of dislocation kinks (small sections of material that move stepwise, parallel to the direction of the normal of the plane), which in case of covalently bonded crystals such as borides, is determined via bonding interactions between the kinks and near neighbor atoms. Mobility of these kinks in a crystalline material are relatively easy as a result of equivalent electrostatic forces on each side of the kink, which is disturbed when a second element is introduced to the structure. In the present case, formation of a solid solution is attributed to change in VEC, since cobalt and iron are not in the same periodic group, hence having different VECs [222,223]. CoB and FeB have the same structure, similar atomic radii and similar lattice constants, resulting in a matching XRD patterns, which is in agreement with other studies of binary and ternary borides [222,223]. In addition, there is no undesirable phase, impurity or

intermetallic compound in the XRD patterns of the purified powders showing that the reaction between $CoCl_2$-$FeCl_3$-$NaBH_4$ is complete and that the NaCl reaction by product and the eutectic mixture are thoroughly removed by water leaching. Thus, high purity powders are obtained.

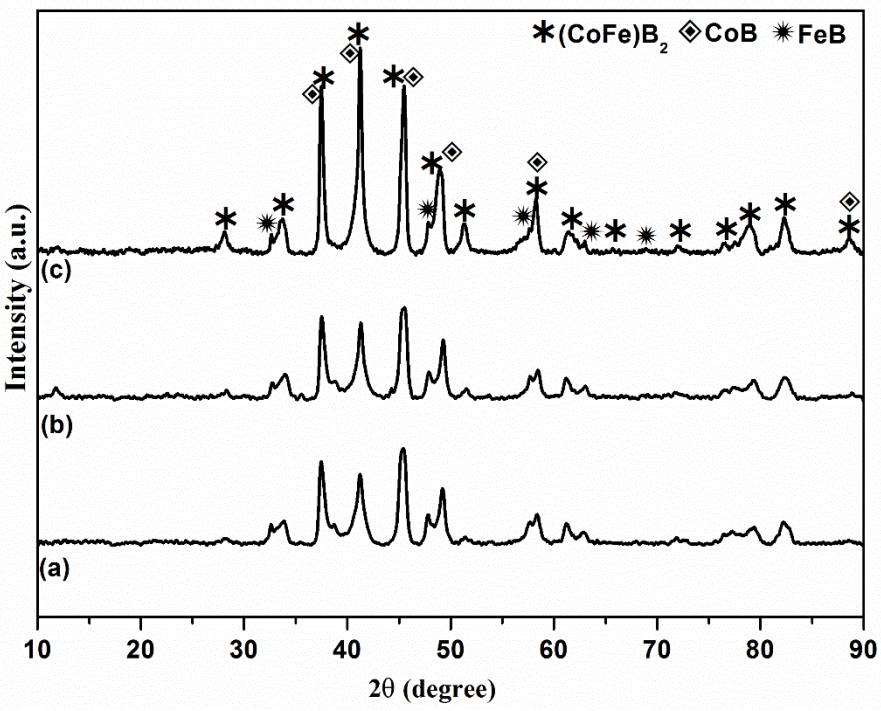

Figure 8. XRD patterns of the powders obtained from reaction of $CoCl_2$-$FeCl_3$-$NaBH_4$ (with eutectic salt mixture in the open system) at: (a) 650, (b) 750 and (c) 850 °C (See appendix A4 for comparison with reference peaks).

Figure 9(a) presents the XRD patterns of the CoB, FeB and $CoFeB_2$ powders obtained from the reaction of $CoCl_2$-$NaBH_4$, $FeCl_3$-$NaBH_4$, $CoCl_2$-$FeCl_3$-$NaBH_4$, respectively. Figure 9(b) shows the DTA curves of the binary powders (eutectic salt mixture in the open system at 850 °C). When compared with their XRD reference patterns (Figure 9(a)), all obtained phases are pure with no impurity present in their composition. Combining the obtained CoB and FeB peaks, results in the measured $CoFeB_2$ peaks, which happens due to the very similar radii of Co and Fe, making it very hard to distinguish between the ternary phase and a solid solution. The asymmetric and broad reflection observed at approximately $2\theta=40^{o}$ in the XRD pattern of the binary FeB exists as a result of large number of stacking faults present in the α-FeB modification [224]. These are also thermodynamically stable phases, which is confirmed by the DTA curves in case of the binary phases (Figure 9(b)). DTA curves of the binary phases show presence of no impurity or unstable phase in the obtained powders and puts melting points of CoB and FeB at 1400-1500 °C.

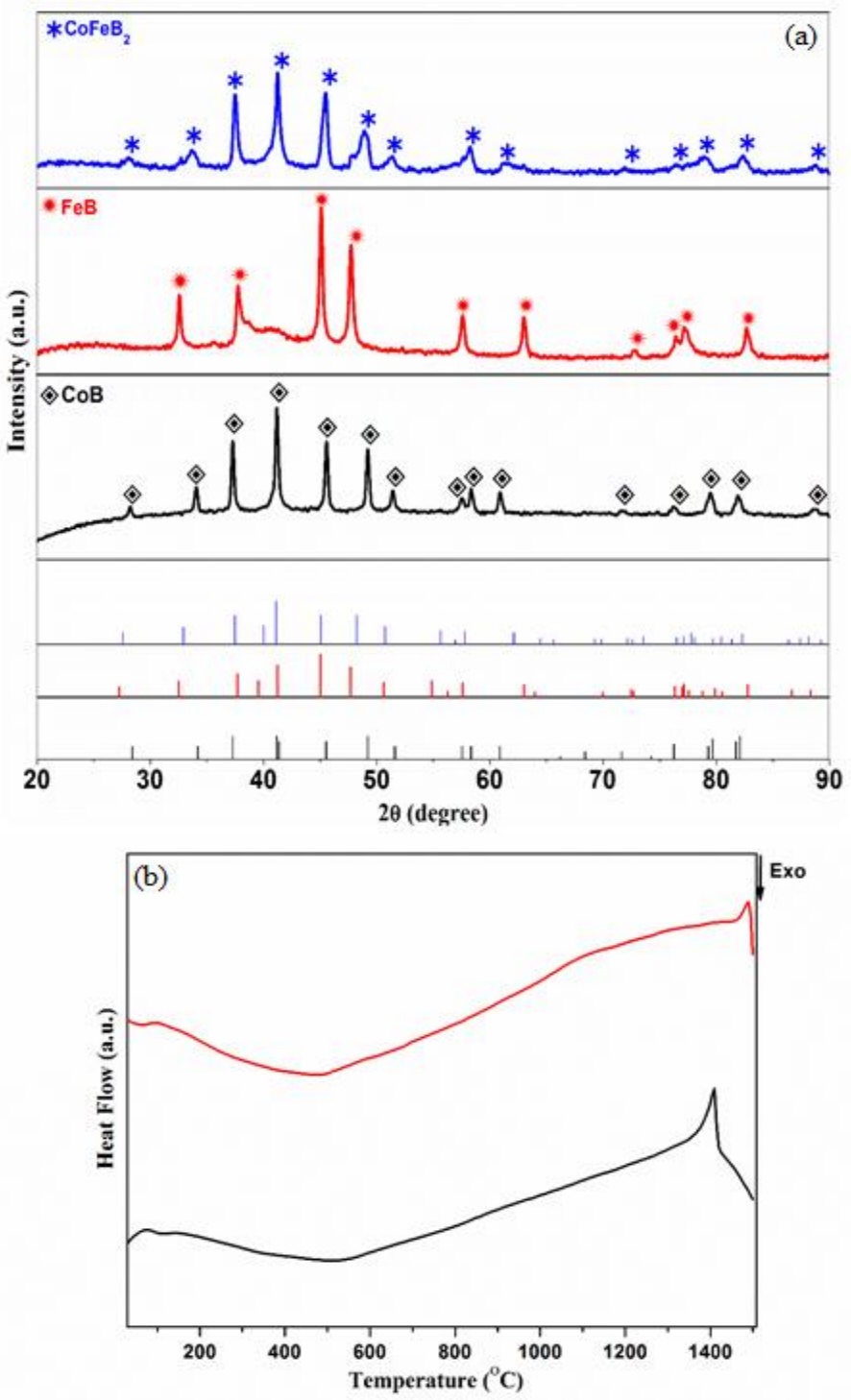

Figure 9. (a) XRD patterns of the CoB, FeB and $CoFeB_2$ powders obtained from reaction of $CoCl_2$-$NaBH_4$, $FeCl_3$-$NaBH_4$, and $CoCl_2$-$FeCl_3$-$NaBH_4$, respectively (with eutectic salt mixture in the open system at 850 °C and (b) DTA curves of the CoB and FeB powders obtained

Figure A5 (Appendix A) shows the FTIR spectra of the $CoFeB_2$ powders, obtained by reaction of $CoCl_2$-$FeCl_3$-$NaBH_4$ with eutectic salt mixture in the open system at different temperatures. As shown in Figure A5, no peaks corresponding to B-H, B-OH or B-O bonds are observed in the FTIR spectra. This shows that $NaBH_4$ decomposed and reacted completely during the 2 h hold period at 550 °C. Also, according to the chemical analysis, no impurities exist in the powder composition.

2.3.2.2 Thermal analysis

Figures 10 and A6 (Appendix A) show the DTA and TG curves of the $CoFeB_2$ powders, obtained by reaction of $CoCl_2$-$FeCl_3$-$NaBH_4$ with eutectic salt mixture in the open system at different temperatures, respectively. The sharp and low endothermic peaks observed at about 1465 °C in the DTA curve shown in Figures 10 (a) and (b) belong to the melting of the CoB phase (CoB_{MP} = 1460 °C). It was observed that some amount of the powders was stuck to the bottom of the pot after DTA analysis. Unlike these two powders, the DTA curve of the powder synthesized at 850 °C (Fig. 10 (c)) did not show melting effect and no adhesion to the crucible was observed after analysis. By interpreting the DTA analyses together with the XRD patterns of the powders (Figure 8), it may be concluded that with the increasing temperature of the reaction and thus with the increasing peak intensity of the $CoFeB_2$ phase in Figure 8 (c), the products side dominates in the chemical equilibrium. The absence of CoB phase in this powder is supported by DTA analysis (Figure 10 (c)) where no sharp

endothermic peak for the melting of the CoB phase was observed [225]. The DTA curve in Figure 10 (c) has a non-sharp broad endothermic peak at about 1340 °C. This endothermic peak corresponds to the sublimation of boron oxide [172].

On the other hand, the TG experiments on all samples show a 2-5 % initial weight loss on heating up to about 250 °C, which results from the evaporation of moisture from the samples (Figure A4(a)-(c)). On further heating, an additional weight loss is observed at high temperatures, totaling 13 wt. % at 1500 °C for the samples prepared at 650 and 750 °C and 7 wt. % at 1500 °C for the sample prepared at 850 °C shown in Figure A4 (a), (b) and (c), respectively. This effect results from the evaporation of boron oxide. The fact that boron oxide was not detected via XRD but its sublimation was observed during DTA/TG measurement can be due to low amount of amorphous boron oxidizing as a result of exposure to air during characterization steps [226]. This suggests that the powders are highly affected by atmospheric conditions like moisture and oxygen due to their nano-sized particles. Figure A7 (Appendix A) presents the corresponding Fe-B, Co-B and Co-Fe-B phase diagrams for further clarity [227].

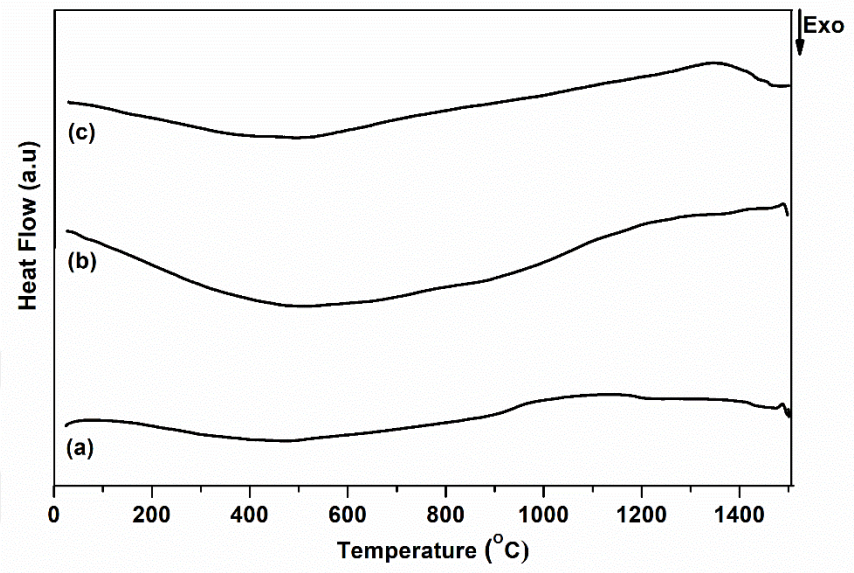

Figure 10. DTA curves of the powders obtained by reaction of $CoCl_2$-$FeCl_3$-$NaBH_4$ (with eutectic salt mixture in the open system) at: (a) 650, (b) 750 and (c) 850 °C.

2.3.2.3 Surface analysis

Previous studies for binary systems have reported that CoB crystalline nanoparticles have formed in an amorphous matrix of Cobalt (II) and partially oxidized boron and that oxygen is expected to be in the amorphous matrix [32,177]. Surface analysis was performed to prove that the powders were affected by atmospheric conditions and to investigate the source of oxygen in the structure. XPS analyses of the $CoFeB_2$ powders obtained by reaction of $CoCl_2$-$FeCl_3$-$NaBH_4$ with eutectic salt mixture in the open system are presented in Figure 11 indicating that a high percentage of oxygen is present on the surface of the particles. Thus, XPS results confirm that the weight loss in TG curves is indeed due to the evaporation of the

surface oxides. The O 1s peak at 533.0 eV, being the most intense one, corresponds to oxidized boron, which is in turn coherent with B 1s contribution at 193.0 eV confirming the partially oxidized boron (II). The formation of the oxide on the surface has been attributed to the presence of the superficial amorphous B layer encapsulating core boride particles [177]. Furthermore, the Co $2p_{3/2}$ and Fe $2p_{3/2}$ peaks in XPS spectra at 780.0 and 712.0 eV can be attributed to cobalt(II) and iron(II) species, respectively [177]. Figure A8 (Appendix A) presents the Fe and Co regions for further clarity.

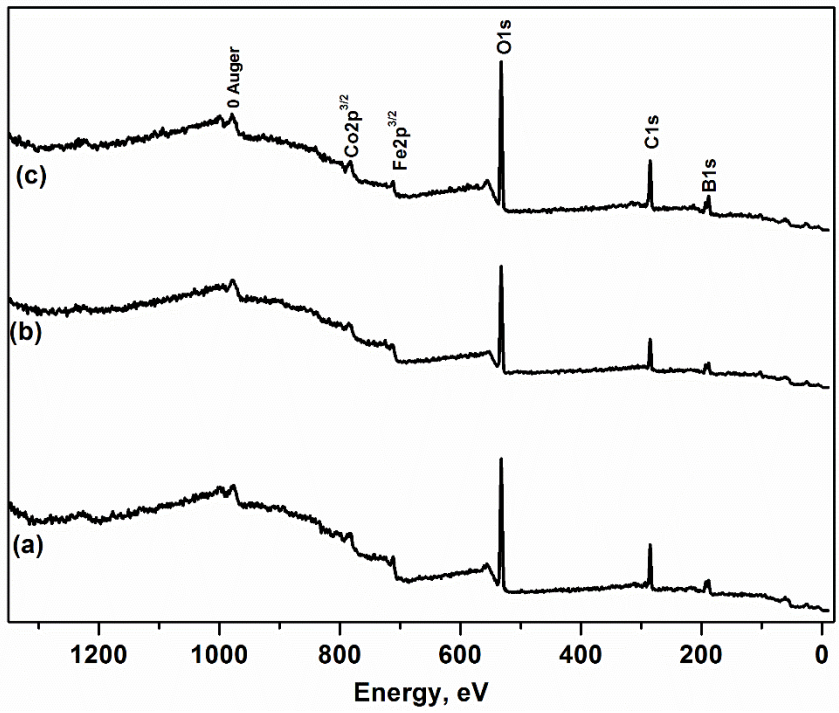

Figure 11. XPS analysis of the powders obtained by reaction of $CoCl_2$-$FeCl_3$-$NaBH_4$ (with eutectic salt mixture in the open system) at: (a) 650, (b) 750 and (c) 850 °C.

2.3.2.4 Microstructural evolution and particle size measurement

SEM / EDS and DLS images and analyses of the powders obtained by reaction of $CoCl_2$-$FeCl_3$-$NaBH_4$ with eutectic salt mixture in the open system are given in Figure 12. Figures 12 (a), (b) and (c) show an increase in particle size with increasing temperature. According to the BET surface area measurements on the same powders, the surface area was reduced from 15.28 to 14.99 m^2 /g with increasing reaction temperature from 650 to 750 °C, respectively. This indicates that 100 °C increase in temperature did not have a significant effect on the particle size of powders. As shown in the DLS analysis in Figure 12 (d), the average particle size of the powder obtained at 850 °C is 60 nm and the size distribution of the particles is homogeneous in the microstructure (Figure 7 (e)). The resulting powder morphology comprises of particles with spherical, coaxial and rod-like structures. Given the low temperature regime used in this synthesis method, formation of nano size particles was expected. The synthesized powders had a particle size distribution of 20-100 nm. Various studies conducted to obtain binary metal boride particles aimed towards different application areas have reported a general particle size distribution of 4-200 nm using different synthesis methods [177,228,237–239,229–236]. It was observed in literature that morphology of the powders are generally spherical with a tendency towards agglomeration [236]. Furthermore, as seen in the EDS analysis given in Figure 12 (f), oxygen was detected besides Co, Fe and B elements. This confirms the surface oxidation of the nanoparticles, which was already supported by XPS analysis (Figure 11).

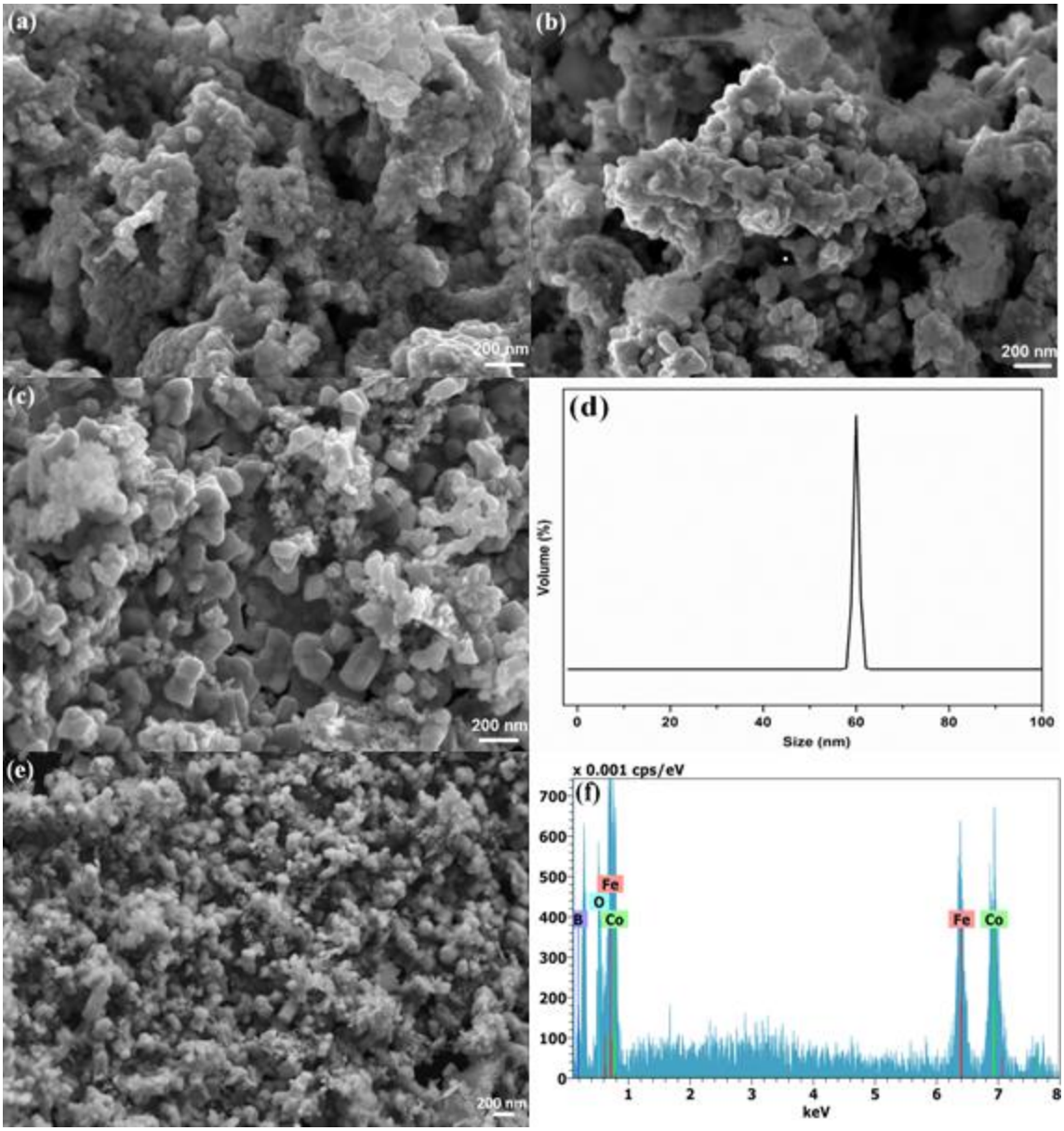

Figure 12. SEM /EDS and DLS analysis of powders obtained by reaction of $CoCl_2$-$FeCl_3$-$NaBH_4$ (with eutectic salt mixture in open system) at: (a) 650, (b) 750 and (c) (d) (e) (f) 850 °C.

To observe the effect of the reaction time, powders were reacted under the same conditions for 6 h. Only $CoFeB_2$ phase was observed in the samples. Increasing the reaction time from 2 to 6 h did not change the sample composition but increased the conversion yield of $CoCl_2$ slightly. According to the calculations, when compared under the same conditions, increasing the dwell time of the reaction from 2 to 6 h provides a 9-10 % increase in conversion yield. Figure 13 presents SEM / EDS and DLS analyses of the powder obtained by reaction of $CoCl_2$-$FeCl_3$-$NaBH_4$ with eutectic salt mixture in open system at 850 °C for 6 h. SEM images show that increase in reaction time leads to a morphological change. SEM image in Figure 13 shows that generally spherical or rod-shape particles, which were observed in all other experiments above, transform into thin long rod particles with the increase of the reaction time to 6 h, which agrees with morphologies observed for Fe_2B particles synthesized in the literature [196]. According to DLS analysis, the average particle size is 80 nm and homogeneous throughout the microstructure. The increase in reaction time caused a slight increase in particle size.

The inorganic molten salt technique applied in the scope of this study makes possible the removal of the impurities stemming from the system. This is achieved by changing the reaction parameters, which is allowed by the low temperature and the method being based on metal chlorides. In current literature, Fe-B and some other binary borides were obtained and reported in high purity by applying this technique [177,196]. The present work is the first one that reports successful synthesis process of crystalline Co-Fe-B ternary metal boride nanoparticles using the low temperature method and inorganic molten salt environment.

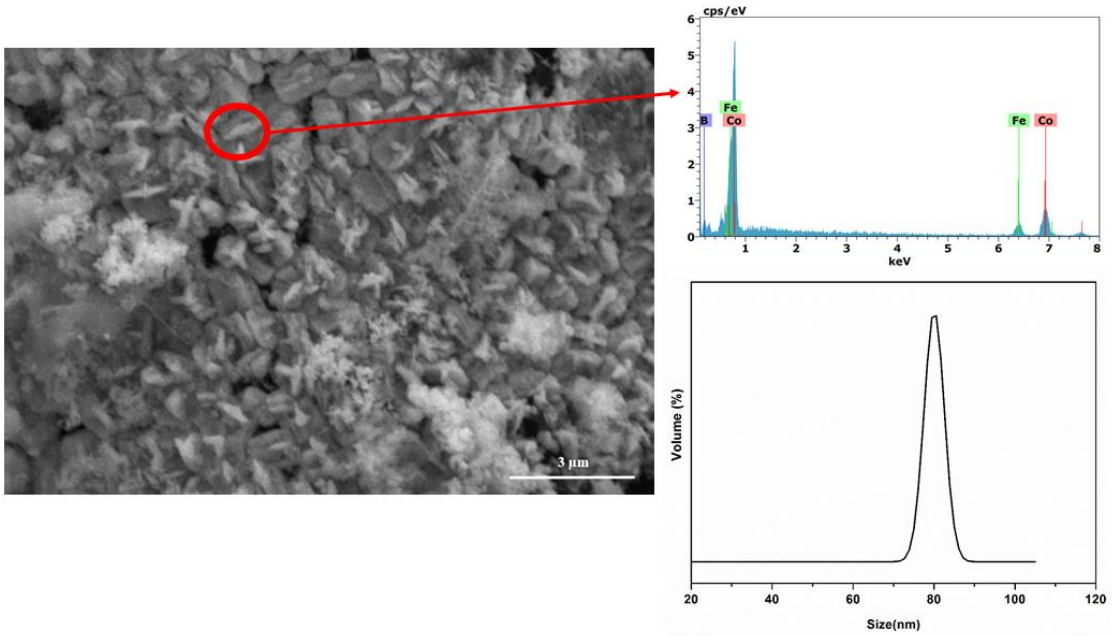

Figure 13. SEM / EDS and DLS analysis of powder obtained by reaction of $CoCl_2$-$FeCl_3$-$NaBH_4$ (with eutectic salt mixture in open system) at 850 °C for 6 h.

2.3.2.5 Effect of annealing on the phase formation

To observe the effect of annealing on the phase change, the powders synthesized at 850 °C for 2 h were annealed at 1100 °C for 2 h. The resulting XRD pattern and the DTA curve are presented in Figure 14. As seen from the XRD pattern, the $CoFeB_2$ phase has indeed formed in situ and, in agreement with earlier explanation, the increased temperature forces the reaction towards a highly crystalline $CoFeB_2$ phase. The smaller characteristic peaks of $CoFeB_2$ are present at $2\theta = 70\text{-}85°$. Using the inorganic molten salt and subsequent annealing techniques, $CoFeB_2$ phase was obtained in crystalline form well below the temperature

reported in the literature. As seen from the DTA curve after annealing (Figure 14(b)), the obtained phase is a pure one with the exception of a very minute endothermic effect at around 1300 °C, which corresponds to trace amounts of boron oxide in the powder. Given that the boron present in the obtained powder is of nano scale and also amorphous, it is oxidized very easily. Comparing Figure 10 (c) and 14 (b) shows that all major effects caused by moisture and evaporation of boron oxide disappeared. This indicates that annealing the samples successfully removes moisture and surface oxides from the composition of the powder. In addition, the missing endothermic effects corresponding to CoB and FeB melting points, which were observed in Figure 9 (b), prove the formation of the ternary Co-Fe-B phase, which has a very high melting point in comparison to the two binary phases. The combined study of the XRD pattern and the DTA curve of the annealed powder makes it clear that the obtained $CoFeB_2$ powder is crystalline and of very high purity.

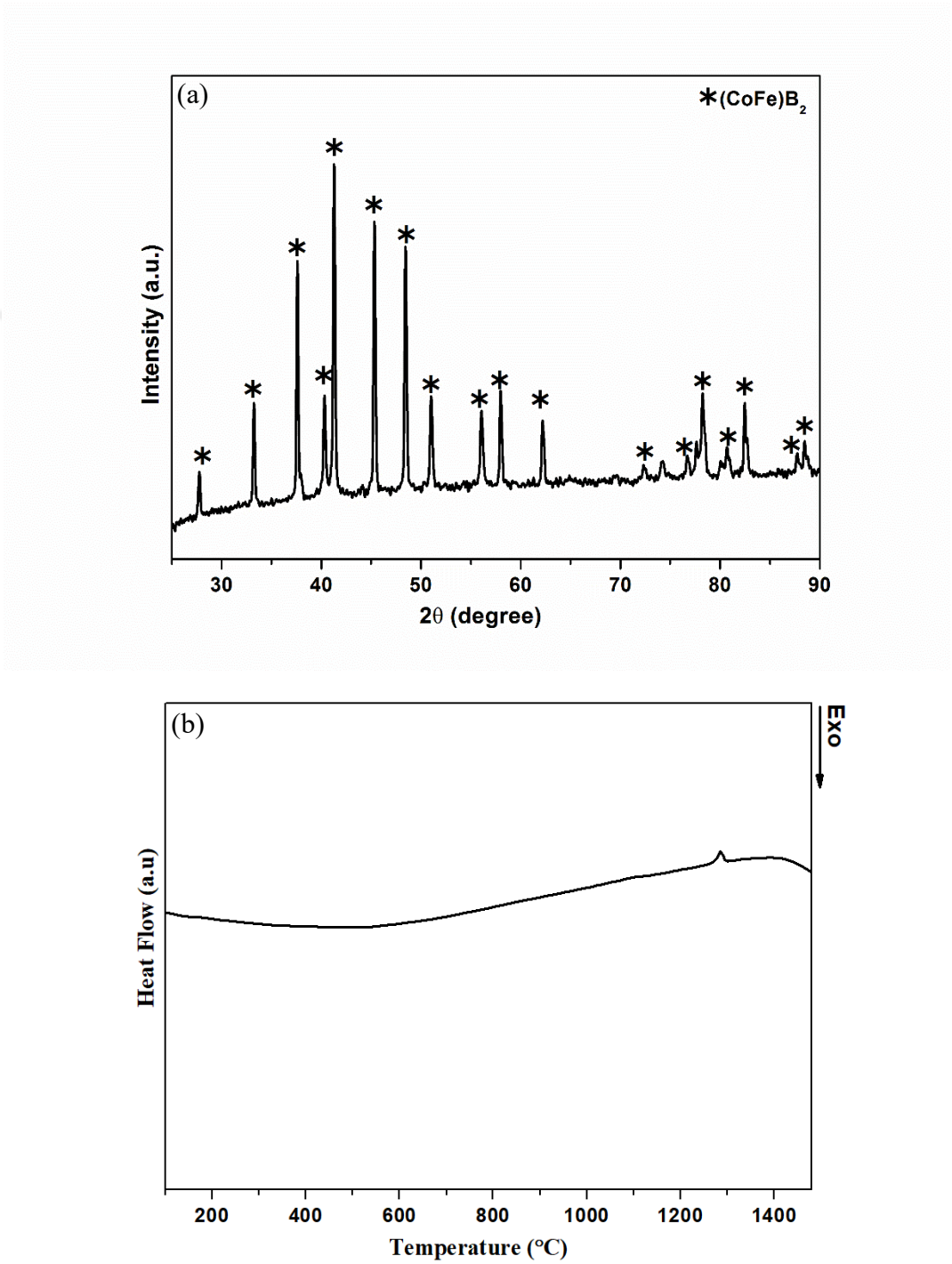

Figure 14. (a) XRD pattern and (b) DTA curve of the powders obtained by reaction of $CoCl_2$-$FeCl_3$-$NaBH_4$ (with eutectic salt mixture in open system at 850 °C) and annealed at 1100 °C (See appendix A9 for comparison with reference peaks).

Table 3 presents the chemical analysis results of the synthesized and annealed $CoFeB_2$ powders at 850 °C and 1100 °C, respectively. As seen from the results, Co to Fe ratio of the obtained powders changed from 1.5 to 1.03 indicating elimination of the thermodynamically unstable phases and formation of the stable $CoFeB_2$ phase. Thus, chemical analyses of annealed $CoFeB_2$ powders gives the molar ratio of Co and Fe to be approximately 1:1 and this value agrees with the determined stoichiometry in the powder structure.

Table 3. Chemical analysis of powders obtained by reaction of $CoCl_2$-$FeCl_3$-$NaBH_4$ in open system at 850 °C, before and after annealing at 1100 °C.

Element (wt. %)	***Co***	***Fe***
$CoFeB_2$	44.98	29.79
Annealed $CoFeB_2$	33.73	32.56

2.3.2.6 Magnetic Measurements

Figure 15 presents the magnetic hysteresis curves of CoB, FeB and $CoFeB_2$ powders at room temperature (25 °C). CoB is expected to be paramagnetic at room temperature and as seen from Figure 15 (a), the synthesized CoB exhibited the saturation magnetization (M_s) of only 0.8 emu/g, which suggests that about 0.4 % of Co in the sample might be found in elemental form. The ferromagnetic FeB powders exhibited saturation magnetization (M_s) of 44.6 emu/g. On the other hand, as seen in Figure 15(b), synthesized $CoFeB_2$ powders exhibited an average saturation magnetization of 21.1 emu/g, which is a value between those of two binary borides. As all powders obtained at different reaction temperatures contain the same phase (Figure 15(b)), they yield similar hysteresis curves and show a ferromagnetic property. Because of the small coercive field (H_c), the hysteresis curves are quite narrow, and the powders can be classified as soft magnetic material. Other studies implementing various synthesis methods have investigated magnetic properties of Co-Fe-B nano particles [186,192,234,240], including a study reporting a saturation magnetization (M_s) of the synthesized powders of about 83.5 emu/g [186]. They also observed that the coercivity (H_c) of the samples increased with increasing Fe/Co ratio and showed a maximum of 148 Oe in some cases [186]. In comparison, the magnetic measurements of the nano particles synthesized in this study showed an average saturation magnetization of 21.1 emu/g at the magnetic field of 70 kOe. However, the samples were handled in air and thus the mass of the sample might have increased slightly due to oxygen and moisture intake. Furthermore, in the present study, before the measurements, no surface modification was applied on the powders

to protect the surface. Repeating the magnetic measurement with a sample reacting at 850 °C and never exposed to air resulted in an increase of saturation magnetization by 20 %. The hysteresis curve at high fields continues to increase slowly, indicating that the magnetization does not completely saturate. This most likely originates from the paramagnetic CoB, which was shown by the XRD to be present in the samples. As indicated in the inset of Figure 15, the samples show an average coercivity value of about 500 Oe, except for the sample reacting at 650 °C, where the coercivity of only about 130 Oe is observed. Thus, extended reaction temperature is seen to produce coercivity enhancement without significant reduction in saturation magnetization. With the decreasing size of the particles, the reduction of saturation magnetization and an increase of coercivity are typically observed until a single domain limit is reached [61]. Thus, in case of FeB, a kind of minimum in saturation magnetization and a maximum in coercivity was found for the average crystallite size of 30 nm [61]. Soft magnetic behavior with small coercivity lowers the amounts of energy loss for alternating current applications [186].

Figure 15(c) shows the magnetic hysteresis curves of the annealed $CoFeB_2$ powders. As the result of the powders synthesized at 850 °C (Figure 15(b)) is compared to that of annealed powders at 1100 °C (Figure 15(c)), it is seen that the ferromagnetic property changed to superparamagnetic with the magnetization reaching a value of 13 emu/g at the magnetic field of 7 T and with the tendency of further increase. This can be explained by the phase and chemical change in the powder structure after annealing at 1100 °C: As mentioned above, annealed powders comprised of a single-phase $(CoFe)B_2$ solid solution (Figure 15) without

any CoB or FeB present in the structure. Due to the ferromagnetic FeB phase existing in the powders synthesized at 850 °C (Figure 8(c)), a ferromagnetic property is observed in the hysteresis curve of the powders before annealing (Figure 15(b)). However, after the formation of stable and highly crystalline $(CoFe)B_2$ solid solution phase with a Co:Fe molar ratio of 1:1 and removal of all impurity and oxide phases in the structure, a superparamagnetic property was obtained, as seen in Figure 15(c). It is worth to mention that the ferromagnetic property of the amorphous Co-Fe-B nanoparticles, already reported in the literature, may be related to the remaining FeB phase, which could not be detected in XRD analysis due to the amorphous structure. Thus, it is clear in the present study that the crystalline single-phase $(CoFe)B_2$ particles possess superparamagnetic behavior at room temperature.

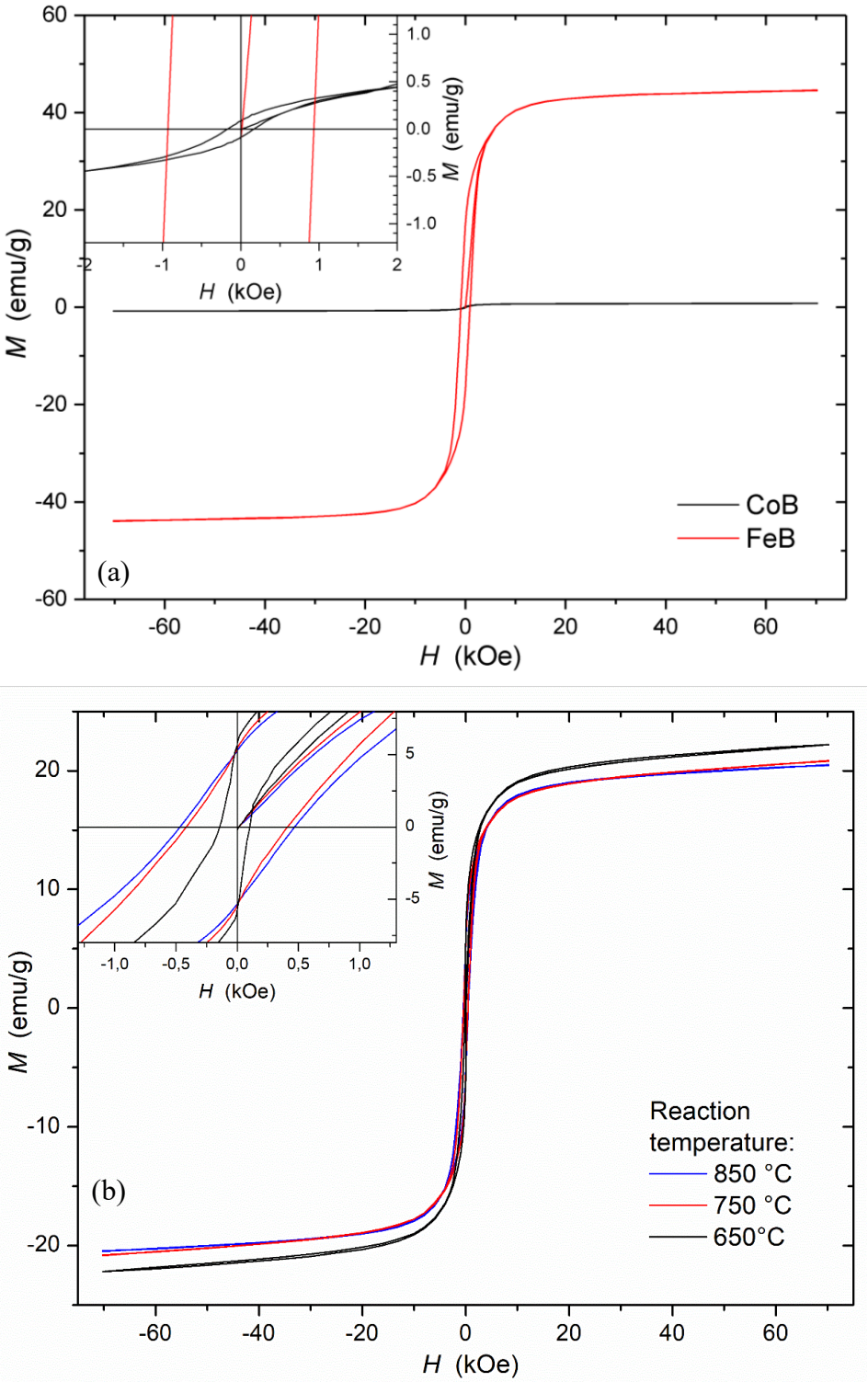
M (emu/g)
H (kOe)
CoB
FeB
(a)
Reaction temperature:
850 °C
750 °C
650°C
(b)

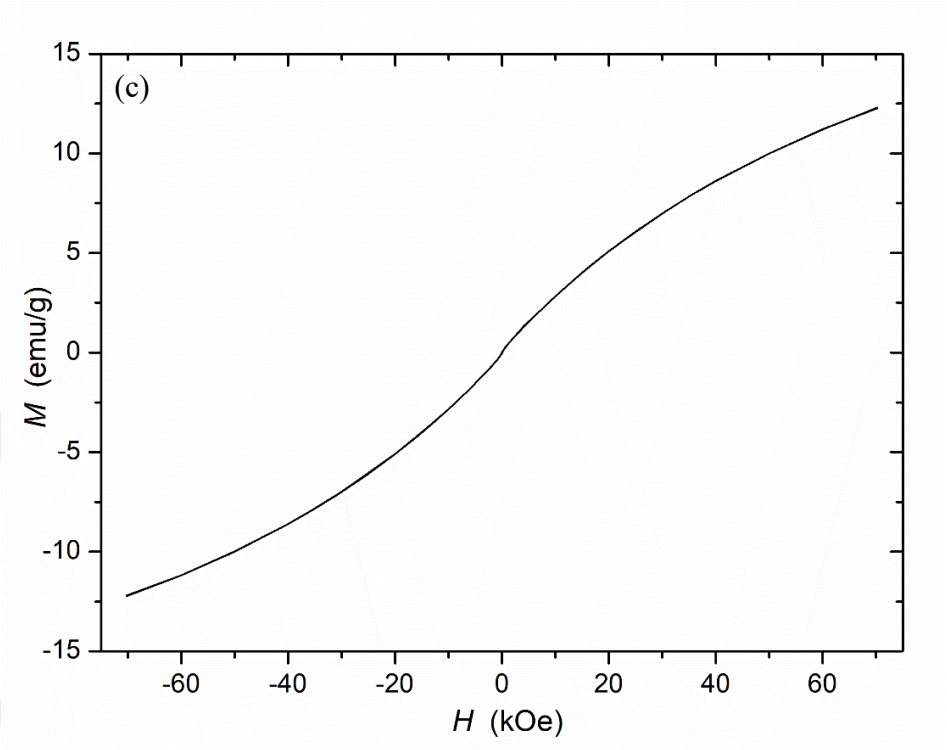

Figure 15. Magnetic hysteresis curves of CoB, FeB and $CoFeB_2$ powders: (a) CoB and FeB powders respectively obtained from $CoCl_2$-$NaBH_4$ or $FeCl_3$-$NaBH_4$ reaction with eutectic salt mixture in the open system at 850 °C, (b) $CoFeB_2$ powders obtained from $CoCl_2$-$FeCl_3$-$NaBH_4$.

2.4. Conclusion

The usage of molten salt synthesis method reduced the melting point of reactants and the impurities in final powders, ensuring that the powders had a more homogenous appearance and particle size. After the reaction of $CoCl_2$-$FeCl_3$-$NaBH_4$ with eutectic salt mixture in close system at 850 °C, CoB and Fe_3B stable phases formed separately in-situ. The reactions of binary systems $CoCl_2$-$NaBH_4$ and $FeCl_3$-$NaBH_4$ respectively resulted in pure CoB and FeB formation in open system at 850 °C under Ar flow. On the other hand, after the reaction of the $CoCl_2$-$FeCl_3$-$NaBH_4$ with eutectic salt mixture under identical conditions, $CoFeB_2$ solid solution nano powders were obtained in one step via a strong diffusion between two binary phases of CoB and FeB. Purity of the obtained Co-Fe-B phase was supported via FTIR and DTA data showing no B-O, B-H and/or B-OH bonds and no endothermic peaks corresponding to the melting point of the binary phases. $CoFeB_2$ powders possess crystalline structure, with a high purity and an average particle size of 60 nm, which comprised of crystalline particles with spherical, coaxial and rod-like structures. Due to nano sized particles and possible superficial amorphous boron layer, the powders oxidized during the leaching or storing while exposed to air. These effects were reduced significantly after optimization of the leaching step and completely removed after annealing, making it possible to obtain pure crystalline powder. Thus, following annealing at 1100 °C, $CoFeB_2$ solid solution powder was stable, high crystalline and all impurity and oxide phases were removed. Chemical analysis data of the annealed powders confirmed obtaining pure $CoFeB_2$ phase and

also gave a Co:Fe molar ratio of approximately 1:1 which agreed with the XRD results. As-synthesized particles exhibited ferromagnetic property and possessed a narrow hysteresis curve characteristic of soft magnetic materials. They also showed an average saturation magnetization of 21.1 emu/g and an average coercivity of 500 Oe. Extended reaction temperature in the open system from 650 to 850 °C is seen to produce coercivity enhancement without significant reduction in saturation magnetization. On the other hand, after an annealing process and subsequent phase and chemical change, crystalline $(CoFe)B_2$ particles exhibited superparamagnetic property, which resulted from the absence of binary FeB phase as the source of ferromagnetic property.

Chapter 3. Evolution of magnetic properties of crystalline cobalt-iron boride nanoparticles via optimization of synthesis conditions using hydrous metal chlorides

3.1. Introduction

Transition element borides have attracted noticeable attention due to various desired properties including major applications in industry such as hard magnets ($Nd_2Fe_{14}B$), hard materials (TiB_2), conductive and bulk refractory ceramics (ZrB_2 , HfB_2), and superconductors (MgB_2) [27,32,43,176]. The combination of a very strong covalent bond and a partially full d orbital has led to numerous binary and ternary combinations of transition metal borides. Consequently, the ability to combine multiple properties such as magnetism, catalysis, biomedical applications alongside outstanding mechanical and chemical stability, hardness, and corrosion resistance, etc. of different elements has triggered wide-spread utilization attempts in both scientific and industrial fronts. For example, crystalline nano particles of iron boride (FeB), cobalt boride (CoB), and cobalt iron boride ($CoFeB_2$) for magnetic behavior [184,186], nickel and cobalt boride (NiB, CoB) as catalyst for hydro-desulfurization and dehydrogenation reaction [241,242], iron boride (FeB), vanadium diboride (VB_2), and CoB as multi electron transfer anode materials for battery applications [243], iron diboride (FeB_2) and molybdenum borides as electro-catalysts for hydrogen evolution reaction [63,244]. Other studies have investigated the role of cobalt iron boride-

based nanoparticles for applications such as for brakes [245], sealing [246], lubricating [247], sensors [248], targeted drug delivery [249], and so forth. All of these different properties are associated with the boron covalent framework present in metal-boron alloys [32]. Most of the aforementioned are bulk properties; however, scaling down to nano scale has proven beneficial by yielding modified, improved and, in some cases, novel properties and behaviors that the bulk form of those materials do not possess [32].

Reducing the particle size has been very effective and useful in various application fields, especially in biomedical and therapeutic applications such as magnetic drug targeting, magnetic particle imaging, and magnetic hyperthermia [250–255]. Furthermore, nanoscale cobalt-iron boride particles are promising materials in electromagnetic devices and high frequency applications due to their high chemical stability [256]. However, in such applications, alloys and compounds with soft magnetic behavior e.g. high magnetization, low coercivity, and magnetic permeability are desirable [186]. Among the potential candidates, borides of iron play an important role given their magnetic properties [61]. The literature reports that the presence of additional third elements such as iron in the structure of cobalt iron boride (Co-Fe-B) compounds complements and enhances the properties of these compounds such as by providing larger surface area and improving catalytic activity compared to their binary counterparts [76,180,184,185]. In our earlier study, magnetic properties of iron boride (FeB), cobalt boride (CoB), and cobalt iron boride ($CoFeB_2$) were investigated. The saturation magnetization (Ms) values of 44.6 emu/g, 0.8 emu/g and 21.1 emu/g were reported, respectively [257].

Presently, there are not many studies investigating metal borides, especially their ternary compounds, due to the challenges existing in conventional methods [258]. Conventional method for the synthesis of transition metal borides uses elemental powders and high temperature and/or pressures (e.g. higher than 2500 °C via arc melting) or a chemical or physical method which proves impractical to produce such material in nanoscale [32,176,177,194,195]. Previous studies, have reported the formation of various species of boron oxide encapsulating the synthesized crystalline core particles [177,242]. The aim of this study is to investigate the possibility of obtaining nanoscale cobalt-iron metal boride powders employing hydrous metal chlorides as precursors and sodium borohydride ($NaBH_4$) playing both roles of boron source and reducing agent. To this purpose, the final phases were investigated, and their magnetic properties were examined in order to improve the synthesis condition and also to study the role of oxidation on magnetic properties.

3.2. Experimental Procedure

3.2.1.Precursor Materials

$CoCl_2 \cdot 6H_2O$ (99.9 % purity, metals basis, Alfa Aesar), $FeCl_3 \cdot 6H_2O$ (>99 % purity, Honeywell), and $NaBH_4$ (98 % purity, Alfa Aesar) powders were used as precursor materials. These powders were mixed in a mortar inside a glove box under Argon gas (Ar). The resulting powder after the reaction was a black powder with small white sodium chloride particles, which were removed by repeated leaching with hot distilled water. Two samples with different stoichiometry were selected considering the molar ratios of the $FeCl_3.6H_2O$ to $NaBH_4$, mentioned hereafter as 1:1 and 1:2 samples.

3.2.2. Reaction Systems

To investigate the effects of the synthesis condition parameters on the final product, two different routes for the reaction of $CoCl_2 \cdot 6H_2O$-$FeCl_3 \cdot 6H_2O$-$NaBH_4$ were adopted in this study. The first one, which we hereafter designate as the ‘open system’ was comprised of an alumina crucible that includes the sample powders and is put into a silica tube. This setup was then installed in a vertical furnace, and the reaction was performed at 850 °C for 2 h under controlled Ar flow. The second route is hereafter referred to as ‘closed system’. In this route, the sample powders were sealed inside a hydrothermal reactor (316-L stainless steel) and then put inside a chamber furnace operating under Ar gas atmosphere to react in a single-step process under autogenic pressure at 850 °C for 2 h. The idea behind the open system is

to remove all the gaseous by-products via Ar flow, in order to protect the products and reactants from oxidation and/or decomposition. Additionally, the effects of the autogenic pressure are investigated by comparison of both systems. Since $NaBH_4$ is playing two roles in this experiment, one as the reducing agent and the other as the boron source, it is vital for us to optimize the decomposition step of this reactant carefully. There are many studies investigating the mechanisms of the decomposition of $NaBH_4$. While two studies report that $NaBH_4$ decomposes into NaH and BH_3 at 550 °C [259,260], another one reported that this decomposition step continues even above 600 °C [209]. In an earlier study, we discovered that the decomposition step starts at 550 °C, therefore, we implemented a hold step in our reaction heating regime for 2 h at 550 °C in order to bring the decomposition reaction to completion [242,257]. The flow chart of the process is summarized in Figure 16.

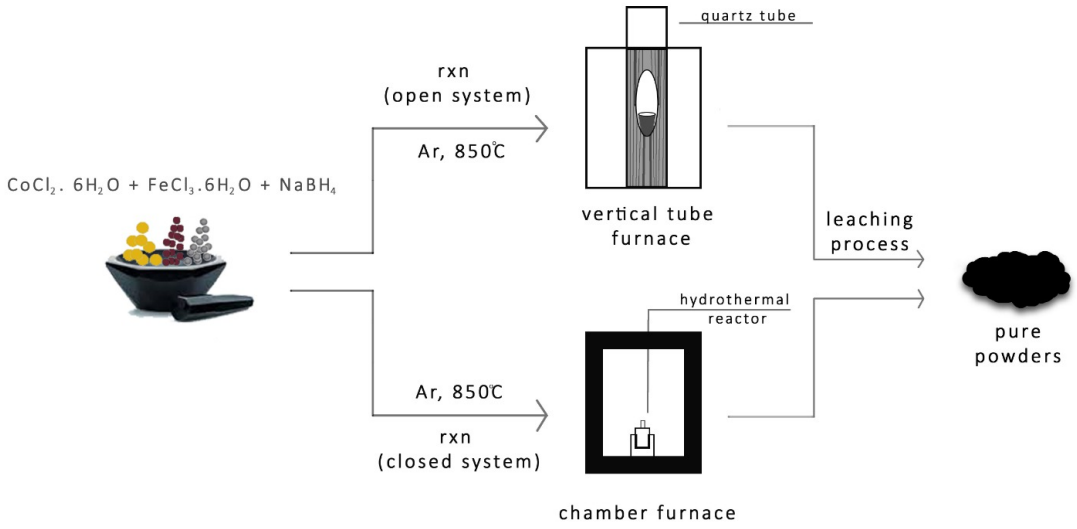

Figure 16. Flow chart of the process used in the experiments.

3.2.3. Characterization

The investigation of the obtained phases and the microstructural characterization of the powders were carried out on Rigaku Miniflex X-Ray diffractometer (XRD, CuKα). The phases were identified using the International Center for Diffraction Data (ICDD) database. A known obstacle during XRD measurements with CuKα rays of samples containing cobalt is the lack of uniformity of the patterns due to the fluorescent effect of the cobalt. To prevent this from happening, the detector was set to XRF reduction mode to reduce the fluorescence effect. Rietveld refinement was achieved utilizing a TOPAS total pattern solution software (Bruker Corp., Karlsruhe, Germany). The intensity of the XRD profile is represented by:

$$I_{rietveld}(2\theta) = b(2\theta) + S\sum_k Lk\,|Fk|^2\,\Phi\,(2\theta_i - 2\theta_k)\,P_kA_k \quad (4)$$

Where b(2θ) is the background intensity, S is the scale factor, L_k contains the Lorentz polarization and multiplicity factors, Φ is the profile function, P_k is the preferred orientation function, A_k is the absorption factor and F_k is the structure factor. The index K represents Miller indices for Bragg reflections. The Zeiss Ultra Plus field emission scanning electron microscope (FE-SEM) was used to carry out the microstructural and morphological characterizations of the powders. Both XRD and SEM/EDS analysis were utilized to analyze the composition and the phase distribution in the structure of the powders. Differential thermal analysis/thermogravimetric (DTA/TG, STA449F3, Netzsch) apparatuses were used to carry out the thermal analyses, which were performed using an alumina crucible up to the

temperature of 1500 °C with a 10 K/min heating rate under Ar atmosphere. The Bruker Tiger S8 XRF device was utilized to carry out the elemental analysis. A SQUID magnetometer (MPMS-XL7, Quantum Design) was used to measure the magnetic properties of synthesized powders at room and high temperatures. To prevent this from happening, the detector was set to XRF reduction mode to reduce the fluorescence effect. The Zeiss Ultra Plus field emission scanning electron microscope (FE-SEM) was used to carry out the microstructural and morphological characterizations of the powders. Both XRD and SEM/EDS analysis were utilized to analyze the composition and the phase distribution in the structure of the powders. Differential thermal analysis/thermogravimetric (DTA/TG, STA449F3, Netzsch) apparatuses were used to carry out the thermal analyses, which were performed using an alumina crucible up to the temperature of 1500 °C with a 10 K/min heating rate under Ar atmosphere. The Bruker Tiger S8 XRF device was utilized to carry out the elemental analysis. A SQUID magnetometer (MPMS-XL7, Quantum Design) was used to measure the magnetic properties of synthesized powders at room and high temperatures.

3.3. Results and Discussion

3.3.1. Analyses of the synthesized powders

The XRD patterns of the synthesized powders in the open system are presented in Figure 17 comparatively. The XRD patterns of the 1:2 batch yielded ternary $(CoFe)B_2$ (ICDD: 01-079-2846, orthorhombic, *a=5.430* Å, *b=2.985* Å, *c=4.020* Å – Refined lattice parameters: *a=5.436(2)* Å, *b=2.981(1)* Å, *c=4.025(2)* Å) and CoFeB (ICDD: 01-082-5452, tetragonal, *a=5.09* Å, *c=4.24* Å – Refined lattice parameters: *a=5.091(3)* Å, *c=4.237(1)* Å) phases while the 1:1 batch yielded Co_2B (ICDD: 04-001-0996, tetragonal, *a=5.015*Å, *c=4.220* Å – Refined lattice parameters: *a=5.017(1)* Å, *c=4.22(1)* Å) and Fe_3B (ICDD:04-001-3343, orthorhombic, *a=5.43* Å, *b=6.69* Å, *c=4.43* Å – Refined lattice parameters: *a=5.424(2)* Å, *b=6.699(3)* Å, *c=4.439(3)* Å) phases. The results suggest that the 1:2 batch is comprised of a solid solution of cobalt-iron boride. On the other hand, the presence of an excess amount of iron chloride hexahydrate in the 1:1 batch triggered the formation of the metal rich form of iron boride (Fe_3B) which, in turn, effected the magnetic properties of the produced powder discussed later on [208,257]. Chemical analysis of the samples revealed a presence of slight aluminum impurity (0.97 wt. %) in the 1:2 batch, originating from the reaction crucible; small amounts of chlorine (0.23 wt. %) also exist which are considered to be remnants of the chloride reactants which were not washed away during the leaching process.

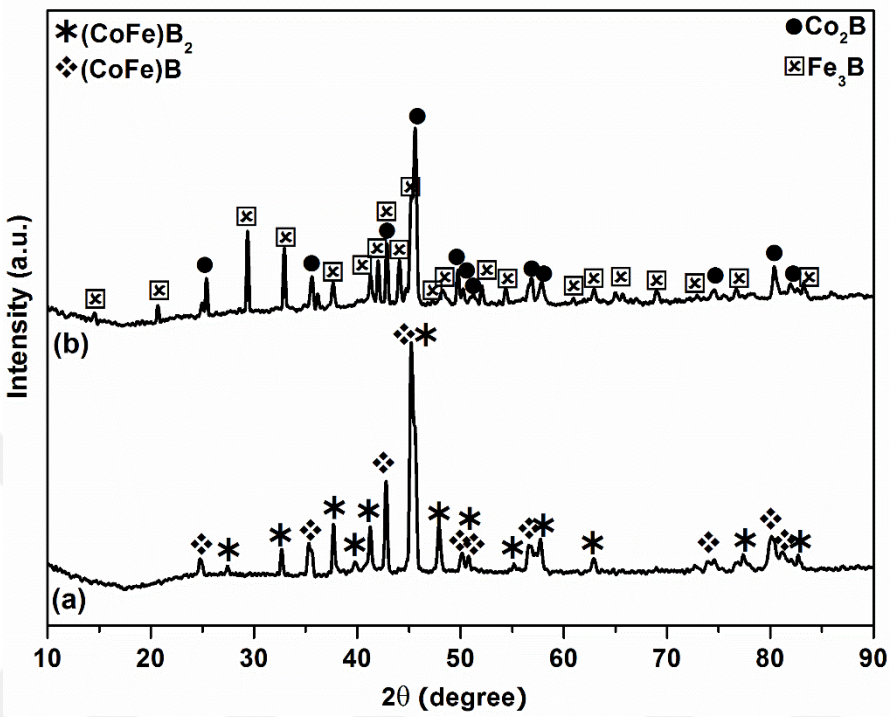

Figure 17. XRD patterns of the synthesized powders in the open system: (a) 1:2 and (b) 1:1 batch (See appendix B1 for comparison with reference peaks).

Figure 18 shows the XRD patterns of the synthesized powders in the closed system. As illustrated in Figure 18, (CoFe)B (ICDD: 01-082-5452, tetragonal, *a=5.09*Å, *c=4.24* Å – Refined lattice parameters: *a=5.079(4)* Å, *c=4.227(2)* Å) alongside $Fe_{0.71}Co_{0.29}$ (ICDD: 04-018-4135, cubic, *a=2.86* Å, – Refined lattice parameters: *a=2.862 (1)* Å) and $Fe_3B_7ClO_{13}$ (ICDD: 04-010-2555, Rhombohedral, *a=8.623* Å, *c=21.050* Å – Refined lattice parameters: *a=8.608(2)* Å, *c=21.050(4)* Å) phases were obtained from the 1:2 batch while the results from the 1:1 batch yielded (CoFe)B (ICDD: 01-082-5452, tetragonal, *a=5.09* Å, *c=4.24* Å – Refined lattice parameters: *a=5.100(2)* Å, *c=4.238(3)* Å) alongside $Fe_{0.71}Co_{0.29}$ (ICDD: 04-

018-4135, cubic, *a=2.86* Å, – Refined lattice parameters: *a=2.864 (2)* Å) and $Co_3B_7ClO_{13}$ (ICDD: 04-015-9718, Rhombohedral, a=8.54 Å, c=20.96 Å – Refined lattice parameters: *a=8.578 (3)* Å, *c=20.973 (2)* Å) phase. The intermetallic $Fe_{0.71}Co_{0.29}$ is a cubic phase and is stable at room temperature according to the Co-Fe phase diagram and has a nominal composition of $Fe_{1-x}Co_x$ which can change as a result of substitutional diffusion between Co and Fe due to similar atomic radii [261–263]. One key factor affecting the outcome of the aforementioned products is pressure occurring during the reaction. Reactions of the closed system are carried out inside a specially constructed stainless-steel reactor designed to withstand corrosion and also to contain the pressure produced by the gaseous products. The results obtained from the 1:1 and 1:2 batches confirm the formation of the (CoFe)B solid solution phase under autogenic pressure. Chemical analysis was performed on the synthesized powders of the closed system. The authors believe that the difference between the phases obtained from the two systems i.e. the presence of oxide species in the products of the closed system compared to that of the open system, can be attributed to presence of an Ar blanket in the setup of the open system and flow of Ar gas inside the reaction vessel. This helps facilitate the removal of minute amount of oxygen (if any) alongside the water vapor coming from the hydrous precursors. However, that is not the case for the closed system, where the Ar gas flows outside the reaction vessel and the water vapor originated from the precursors remains inside the vessel which at higher temperature and pressure results in formation of the oxide species in the products of the closed system. The results showed minute impurities originating from the reactor, namely, magnesium and chromium at ppm

level, which most probably exist due to the corrosion taking place as a consequence of using chloride precursors. Similar to the products of the open system, the presence of minute amounts of chlorine in the structure of the final powder suggests that additional leaching steps are required. Table B1 (Appendix B) summarizes the theoretical and refined lattice parameters for the open and closed systems. The reported refined lattice parameters of the obtained phases can have very close values due to the fact that Co and Fe elements possess very close radii and thus are diffused into each other through substitution. This in turn, alters the lattice parameters slightly compared to a case where interstitial replacement would be the case. Moreover, the existing difference between refined lattice parameters and the associated compounds is believed to be due to substitution of Fe and Co with each other in the structure of the compound. Considering the different radii of the Co and Fe elements, this substitution will result in variation of the void space in the lattice structure, bond lengths etc. that causes strain in the lattice. This strain will in turn change the nominal composition of the bulk for the obtained phases and also the position of the corresponding XRD peaks obtained from the samples to shift a bit from the standard positions, thus making refinement of the patterns necessary for correct identification of the phases which will be addressed in the magnetic characterization part.

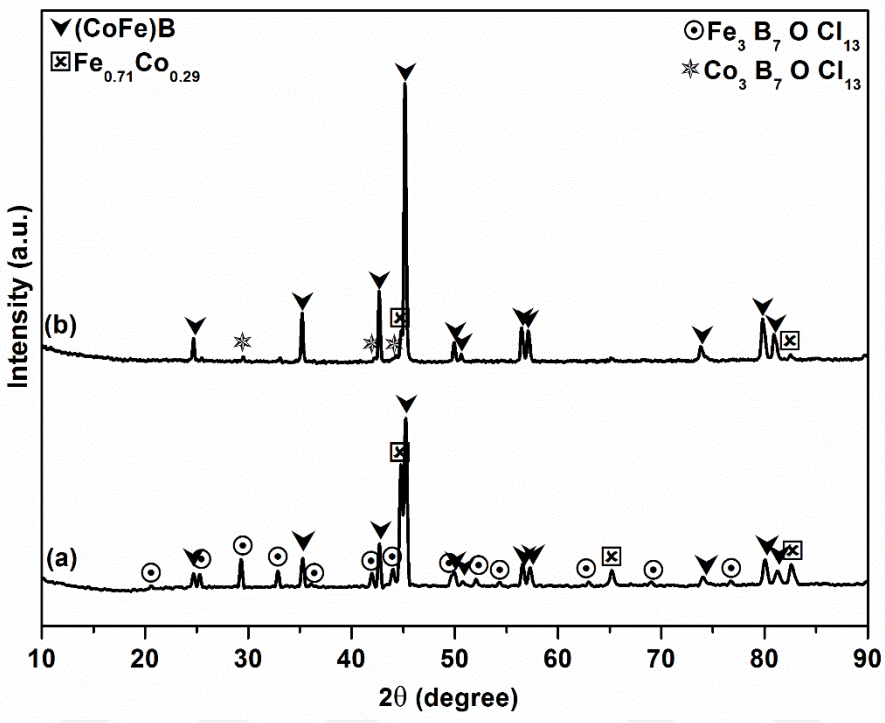

Figure 18. XRD patterns of the synthesized powders in the closed system: (a) 1:2 and (b) 1:1 batch (See appendix B2 for comparison with reference peaks).

Figure 19 illustrates the secondary electron SEM images of the synthesized powders in the open system at 850 °C. As seen from Figure 19a and 19c, the microstructure of the obtained powders possesses irregular and mostly aggregated shapes with a homogeneous distribution throughout the sample (< 2 μm). The particles obtained from the 1:1 batch possess an additional needle shape morphology as well (Figure 19d and Figure B3). One visible difference between these two batches is that the 1:1 batch containing an excess amount of iron chloride tends to form bigger particles compared to the interconnected sponge-like morphology of the 1:2 batch. On the other hand, at higher magnifications, the formation of much smaller particles, with an average size of about 80 nm, of the synthesized

particles obtained from the 1:2 batch is observed (Figure 19b). However, there is a slight difference between the images obtained from the 1:2 batch and the 1:1 batch, in that, this particular structure is abundant and of much smaller scale on the surface of the particles originating from the 1:2 batch. A similar phenomenon was reported by Palani et al. [264].

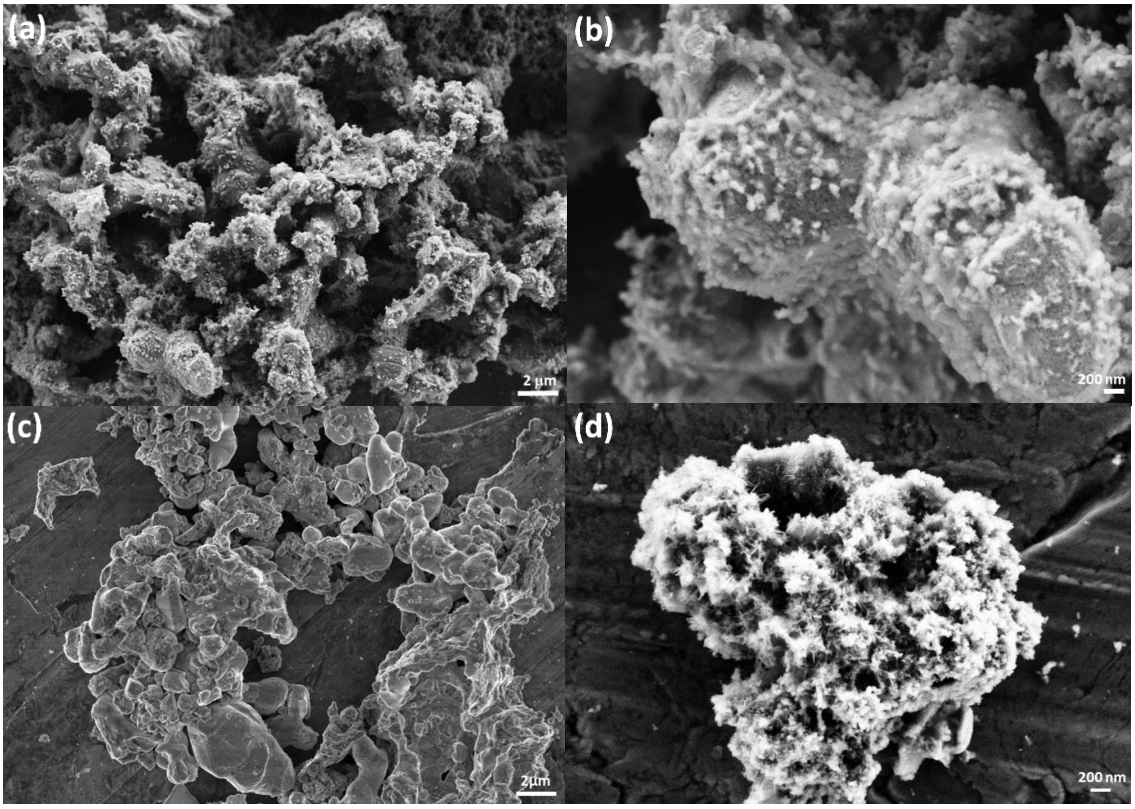

Figure 19. SEM images of synthesized powders in the open system: (a)-(b) 1:2 and (c)-(d) 1:1 batch.

Figure 20 presents the secondary electron SEM images of the synthesized samples in the closed system at 850 °C. It is observed that particles formed in the closed system possess a spherical morphology, which is attributed to the autogenic pressure present inside of the reaction vessel. The particles possess an average size of 20 nm. Formation of nanoscale

particles, discussed in the SEM images of the open system, is observed in particles of the closed system as well, but they are noticeably smaller in size. The main difference between particles obtained from the open and closed system is the morphology and average particle size. Particles obtained from the closed system possess spherical morphology and are on average 4 times smaller than the ones obtained from the open system, which is most likely due to the presence of pressure in the reaction vessel of the closed system.

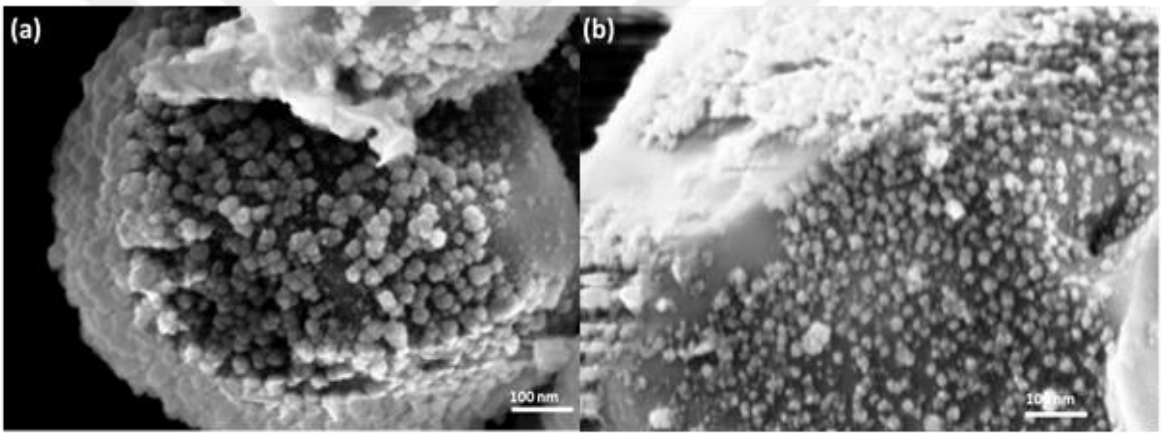

Figure 20. SEM images of synthesized powders in the closed system: (a) 1:2 and (b) 1:1 batch.

DTA/TG analysis was carried out on the select powders to examine the purity of the powders and also to observe possible phase transformations. Figure 21 illustrates the DTA measurement results for the 1:2 and 1:1 batches of the reaction products in the open system. The DTA curve of the 1:1 batch reveals a minute endothermic effect at 965 °C which, according to the iron-boride phase diagram, corresponds to the transformation of α-Fe to Fe_2B phase [262]. Additionally, two sharp endothermic effects were observed at 1115 °C

and 1133 °C. The effect occurring at 1115 °C is attributed to the Co_3B-B eutectic phase transformation, and the following endothermic effect occurring at 1133 °C is believed to result from another phase transformation taking place between Co_3B, Co_2B, and liquid CoB according to the Co-B phase diagram [262]. In an earlier study, we found that given the adopted low synthesis temperatures, the formation of amorphous shell-like nano sized boron structures, encapsulating the crystalline core boride particles was almost inevitable [177,257]. This amorphous layer would oxidize rapidly upon exposure to air during characterization steps and handling time. To avoid the complications of removing this oxide layer and obtaining a pure phase product, precautions were taken to keep the air exposure time to a minimum. On the other hand, the DTA curve of the 1:2 batch reveals a large endothermic effect at 1323 °C which most likely corresponds to the phase transformation between $(CoFe)B_2$ and (CoFe)B and free boron according to the Co-Fe-B phase diagram. This amorphous boron phase is seen as a broad peak in the XRD pattern visible between $2\theta = 20° – 32°$ presented in Figure B4 (Appendix B). Additionally, the presence of $(CoFe)B_2$ and (CoFe)B compounds in the XRD pattern obtained after DTA measurements supports this idea even further (Figure B2) [225,265].

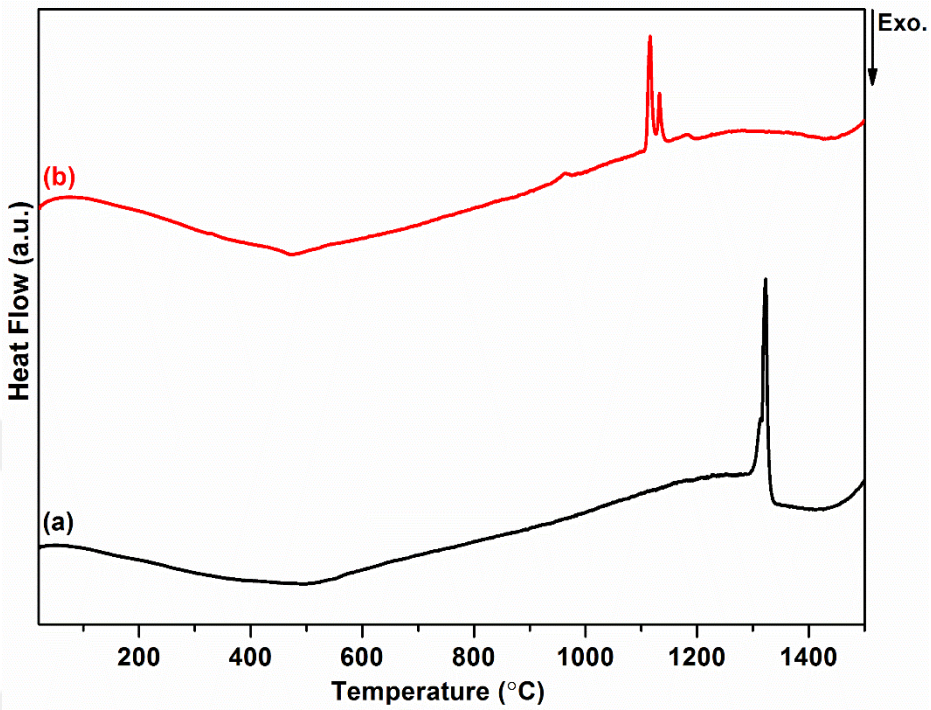

Figure 21. DTA curves of the synthesized powders in the open system: (a) 1:2 and (b) 1:1 batch.

Figure 22 presents the thermogravimetric (TG) results of the open system. In comparison to the previous studies, it reveals a significant reduction of the % mass loss, which was 0.87 % for the 1:2 batch and 3.4 % for the 1:1 batch, while results reported in previous studies have a range of 5 to 15 % mass loss [242,257]. The difference in the % mass loss between 1:2 and 1:1 batch corresponds to the evaporation of the slightly higher amount of formed boron oxide layer on the particles obtained from the 1:1 batch, comparatively (Figure 22a and 22b).

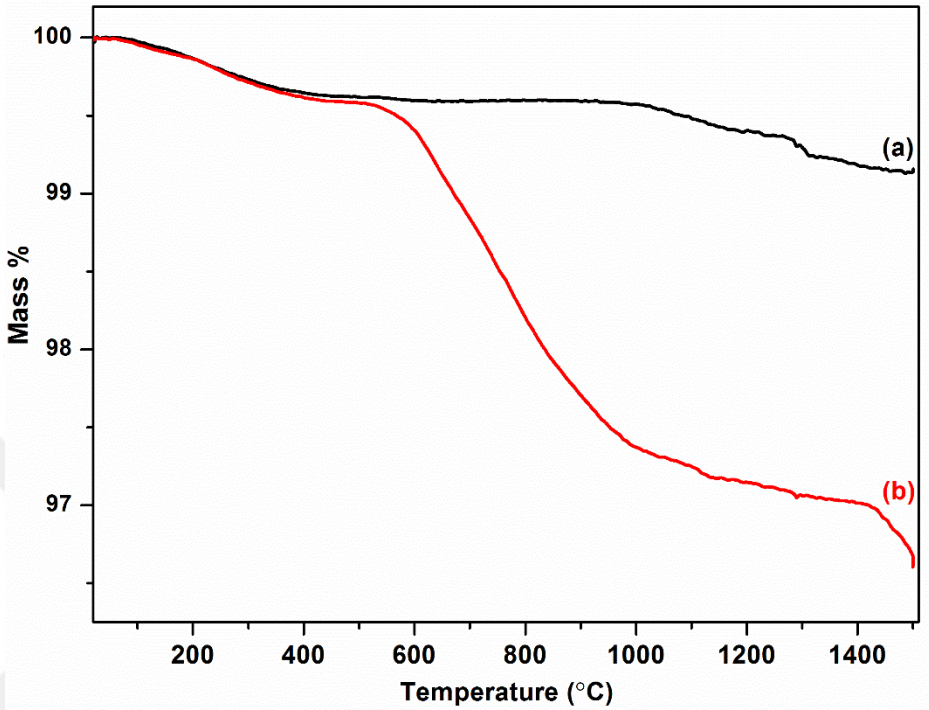

Figure 22. TG curves of the synthesized powders in the open system: (a) 1:2 and (b) 1:1 batch.

3.3.2. Magnetic Measurements

The magnetic hysteresis curves of all obtained samples at room temperature (25 °C) are presented in Figure 23. A number of studies have examined the magnetic properties of Co-Fe-B nano particles synthesized via different routes [186,192,196,266]. In our earlier study, we synthesized and measured the magnetic properties of binary CoB and FeB compounds, and the highest reported saturation magnetization was 44.6 emu/g for FeB nanoparticles [257]. Significantly higher saturation magnetization of the synthesized samples are observed in this study and amount to 183 emu/g and 146 emu/g for 1:2 and 1:1 batches of the open

system and 111 emu/g and 104 emu/g for the 1:1 and 1:2 batches of the closed system, respectively (Figure 23). The difference of magnetization values for the samples of the open system that exhibited a decrease of magnetization from 180 to 140 emu/g is believed to originate from the different final compositions. The 1:1 batch of the open system yields a mixture of Co_2B and Fe_3B phases (58.22 % for Co_2B and 41.78 % for Fe_3B according to the Rietveld analysis). Both phases are ferromagnetic with their saturated magnetization values of approximately 70 emu/g and 197 emu/g (theoretical), respectively [267,268]. It appears that the solid solution of the two ternary phases in the 1:2 batch of the open system has a large positive effect on the magnetization of the obtained sample. According to the Rietveld analysis the samples obtained from this batch is comprised of 70.79 % of the $(CoFe)B_2$ phase and 29.21 % of the (CoFe)B phase. The magnetization value of 183 emu/g is substantially higher than e.g. 83.5 emu/g measured on Co-Fe-B nano particles [186] or our previous measured value of about 21 emu/g for pure $CoFeB_2$ [257]. According to these findings, two possibilities can be considered for the magnetization value of the (CoFe)B phase. First, if the existence of a constructive magnetic behavior is ignored, then the calculations suggest that the individual magnetization of the (CoFe)B phase is about 168 emu/g. Second, is that there exists an additional constructive magnetic behavior that amplifies the magnetization value of the obtained products (both 1:1 and 1:2 batches of the open system). This surprising result requires further investigation, which is beyond the goals of this study. In the case of the samples obtained from the closed system, two ferromagnetic phases are present, (CoFe)B and $Fe_{0.71}Co_{0.29}$. The saturation magnetization of the $Fe_{0.71}Co_{0.29}$ phase has already been

measured to be 231.46 emu/g [263], but unfortunately, no definite magnetization values of the (CoFe)B compound exist. However, a trend of increased magnetization values with the increased concentration of the magnetic atoms within compounds is observed. Thus, higher concentration of $Fe_{0.71}Co_{0.29}$ enhances the magnetization of the sample and we may conclude that the relative concentration of the $Fe_{0.71}Co_{0.29}$ phase and the (CoFe)B phase determines the magnetization of the sample as a whole. To further analyze this, the Rietveld refinement results of the powders revealed the quantitative amounts for the obtained phases of the closed system. According to the refinement results the 1:2 batch is consisted of 93.56 % (CoFe)B, 5.38 % $Fe_3B_7ClO_{13}$ and, 1.06 % of the $Fe_{0.71}Co_{0.29}$ phase, while the 1:1 batch contained 89.01 % (CoFe)B, 8.44 % $Co_3B_7ClO_{13}$ and, 2.55 % of the $Fe_{0.71}Co_{0.29}$ phase. This means that for the 1:2 batch of the closed system which exhibited a magnetization value of 104 emu/g, the mathematical expected value (Appendix B), contributing to the overall magnetization of the sample is 1.10 emu/g and 2.83 emu/g for the 1:1 batch. Given the low amount of the $Fe_{0.71}Co_{0.29}$ phase, its contribution to the overall magnetization values of the obtained phases is not of statistical significance.

The paramagnetic nature of these oxide species reduces the potential saturation magnetization values in the products of the closed system by preventing some of the iron and cobalt to obtain ferromagnetic property [269]. Moreover, as stated in our previous work, the presence of the boron oxide species in the structure of the final powder also hinders magnetism by increasing the mass ratio of the nonmagnetic part of the sample [257]. The same study reported that by implementing precautions to avoid oxidation of the samples,

saturation magnetization of the mentioned samples was enhanced by 20 % [257]. The discussed precautions were implemented in the synthesis of the samples in this study as well, with more optimization. As seen in Figure 23, all samples investigated herein, possess a very narrow coercive field with an average coercivity in the range of 20 – 100 Oe, classifying these materials as soft ferromagnets. As observed in the TG curves (Figure 22), the reduction of the air exposure time (e.g. during characterization steps) resulted in reduced mass loss and thus also enhanced the magnetic properties of these samples significantly. Among all the samples, the 1:2 batch synthesized using the open system has the highest saturation magnetization at 183 emu/g which, to the best of the authors' knowledge, has not been reported in the literature for the Co-Fe-B based particles. This finding, in turn, emphasizes the importance of the absence of oxide species and their effect on the magnetic properties of boride nanoparticles. However, the main reason for this increased saturation magnetization is thought to be the simultaneous presence of crystalline (CoFe)B and (CoFe)B_2 phases (Figure 17(a)) [224]. Additionally, obtained magnetization values are most probably connected to the low temperature synthesis method adopted in this study which, in turn, resulted in the formation of all phases in nanoscale crystalline structures (Figure 19 and 20).

To further investigate the magnetic properties of the obtained powders, the 1:2 batches from both the open and closed systems were chosen, and their magnetic behavior with changing temperature was investigated (up to the temperature limit of the device being 795 K with a 4K/min rate at 10 kOe). Figure 24 presents the high temperature magnetic behavior of the select samples from the open and closed systems. It was observed that both samples

exhibit the expected reduction in magnetization at increasing temperature. However, the Curie temperature was not reached up to 795 K for the tested samples, which marks them as stable ferromagnets in the measured temperature range. At 10 kOe, the magnetization of the samples is close to complete (as observed in the hysteresis loops) and thus no significant difference between heating and cooling is observed. The magnetization of the sample from the closed system only drops from 171 emu/g at 300 K to 152 emu/g at 795 K, while the drop for the open system sample is much more pronounced, going from 105 emu/g at 300 K to 56 emu/g at 795 K. This suggests that the Curie temperature is somewhat higher in the former than in the latter sample.

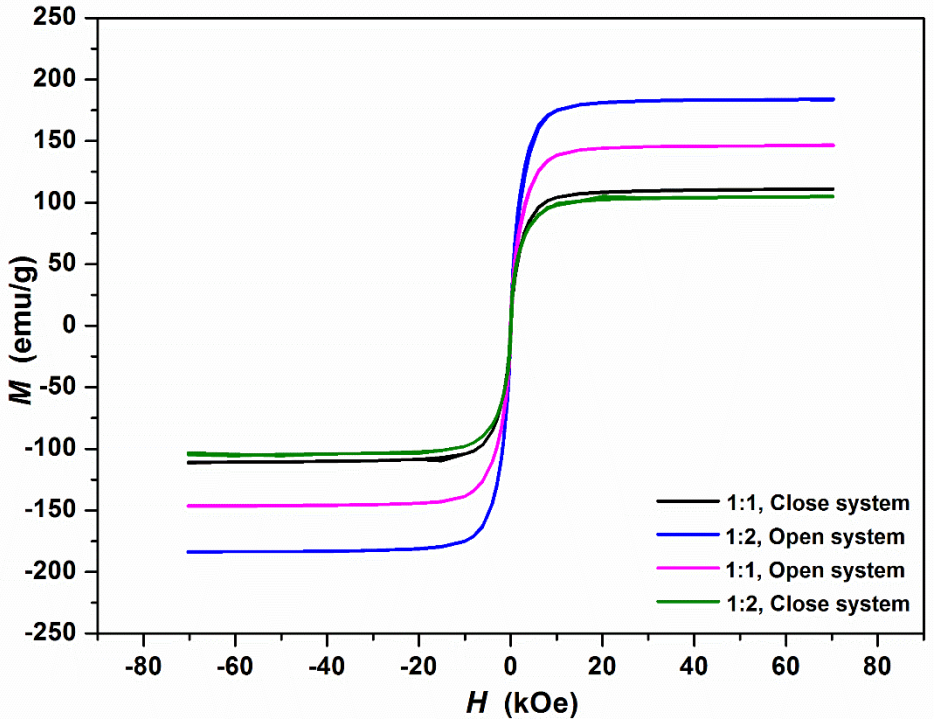

Figure 23. Magnetic hysteresis curves of obtained samples of both open and closed systems.

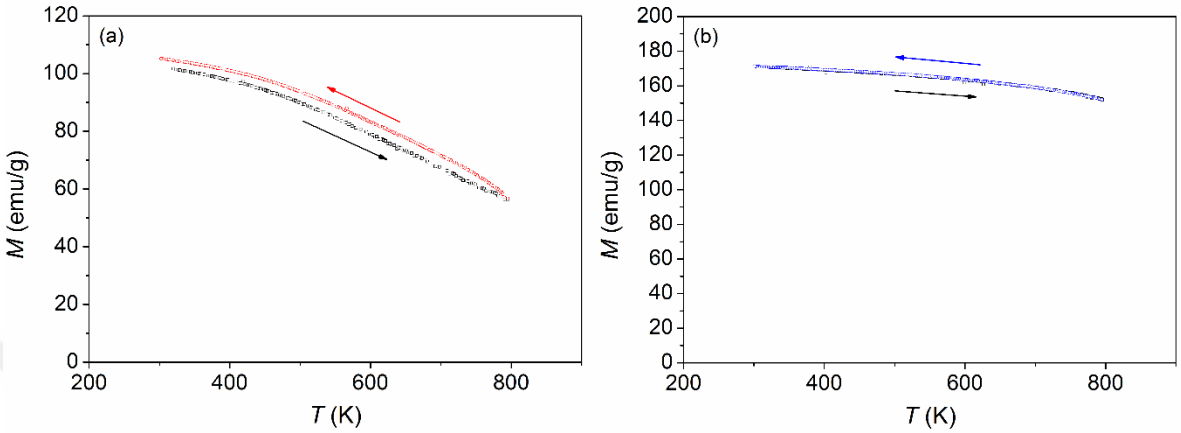

Figure 24. High temperature magnetic measurements of 1:2 synthesized samples: (a) open and (b) closed system.

3.4. Conclusion

Nanoscale and crystalline cobalt-iron metal boride powders were obtained using different reaction systems and optimized synthesis conditions. After reaction of $CoCl_2 \cdot 6H_2O$-$FeCl_3 \cdot 6H_2O$-$NaBH_4$ at 850 °C under autogenic pressure, (CoFe)B-$Fe_{0.71}Co_{0.29}$-$Fe_3B_7ClO_{13}$ and (CoFe)B-$Fe_{0.71}Co_{0.29}$-$Co_3B_7ClO_{13}$ phases were obtained. On the other hand, (CoFe)B-$(CoFe)B_2$ and Co_2B-Fe_3B phases were obtained in the open system under Ar flow. The crystalline nanoparticles had a homogenous microstructure with irregular shapes for the agglomerated particles obtained under Ar flow with an average particle size of 2 µm; however, at higher magnifications, smaller particles were observed with an average size of about 80 nm. Spherical particles were obtained under autogenic pressure (closed system) with an average particle size of 20 nm. The thermal analysis of the obtained powder showed that the precautions taken to avoid oxidation were effective and reduced the % mass loss

significantly. The synthesized powders exhibited a saturation magnetization range of 104-183 emu/g and a coercivity range of 20-100 Oe, marking these materials as soft magnets with very high magnetization values. It was observed that the precautions taken to avoid oxidation were indeed effective and increased the saturation magnetization up to 183 emu/g for the powders containing $(CoFe)B_2$ and (CoFe)B pure phases. The high temperature measurements of magnetization at 10 kOe revealed that the obtained samples were stable ferromagnets up to 795 K as no transition temperature (T_c) was observed.

Chapter 4. CoB-TiB_2 crystalline powders: Synthesis, microstructural analysis and their utilization as reinforcement agent

4.1. Introduction

Having a combination of superior chemical, physical, and mechanical properties have made transition metal borides of dire importance in various scientific and industrial fields [270–272]. Transition metal borides, thus, are utilized in automotive and aerospace industries and applied in numerous applications such as wear resistant coatings, magnets, catalyzers, cutting tools, and reinforcement agents in metal matrix composites or ceramics [272–277]. Numerous studies investigating properties of various binary and ternary boride ceramics have been conducted to obtain and/or improve the ceramics to meet the needs of industry and science. Co-based boride compounds have been used in various alloys as a coating material with high wear and corrosion resistance. There have been studies in the literature on significant improvements in the mechanical properties (elastic modulus, fracture toughness, etc.) of cobalt boride coated or impregnated alloys [176,278,279]. It is thought that Co-B based compounds developed by doping Ti will give superior properties compared to the binary system in terms of their mechanical properties [76]. On the other hand, being a well-known high temperature ceramic and possessing a set of highly desirable properties such as high melting point, strength, elastic modulus (>500 GPa), and hardness (>20 GPa), TiB_2 has

attracted much attention in science and industry due in part to heavy duty wear applications and, thus, is considered amongst the most advanced and prominent ceramics [272,280–285]. Various studies have investigated binary boride compounds, and many synthesis methods have been applied to obtain them such as self-propagating high temperature synthesis (SHS), carbothermal reduction, borothermal reduction, and mechanochemical synthesis [27,39,286–289]. A comparison of various synthesis methods including the effect of the synthesis conditions and parameters on the feasibility of the method is illustrated in Table C1 (Appendix C). However, the production of binary/ternary composite borides have been investigated less frequently. The conventional method for simultaneous production of these ternary materials uses pure elemental precursors and takes place at elevated temperatures (> 2000 °C) [39,193]. The elevated temperatures and long synthesis steps used in the mentioned reaction methods make obtaining pure phases somewhat difficult, and impurities such as carbon and oxygen are almost inevitable in the final product [193]. Moreover, such high temperature methods are not ideal for the synthesis of the desired composite borides as they deliver final products of large particles [39]. Hence, the most efficient and optimal method for obtaining transition element composite powders with fine particles requires further investigation and research. One important application where the synthesized nano/sub-micron particles can be used is as reinforcement particles in metal matrices (e.g. Ti-based alloys) that can target various scientific fronts. Some of the conventional methods for fabrication of Ti-based components include powder metallurgy, casting and forging [290,291]. These methods also require post processing steps such as heat treatment or

machining to obtain the desired component; however, it becomes a very tedious process in the case of Ti metal as a result of impediments such as high levels of chemical affinity and relative low thermal conductivity. These obstacles are highly undesired as they may result in unwanted chemical reactions and products, and they significantly deteriorate the machinability of the components, which renders these conventional methods inefficient as they require substantial material, energy, and time, which adds to the cost and difficulty of the fabrication of Ti-based components [292]. As a consequence, novel methods such as selective laser melting (SLM) based on a layer by layer approach (additive manufacturing) has attracted significant interest given its ability to fabricate near net shape geometries very efficiently which require very little post processing if not at all. This makes the process much simpler and much faster compared to conventional methods [293]. Overall, the focus of this research is on introducing a better and more efficient alternative path to obtain the mentioned composite metal borides via low temperature methods. Another important benefit of this low temperature synthesis method resides in the microstructure of the obtained powder. Smaller particle size, which is achieved by exercising low temperature synthesis routes, will have positive effects in the sintering steps of these powders as reducing sintering time and/or temperature [294]. In addition, the eligibility of the synthesized nano powders to be used as reinforcement particles is studied. In order to do this, metal matrix composites (MMC) in bulk form were fabricated by SLM method using synthesized composite powders as reinforcement agents and Ti6Al4V powder as the matrix.

4.2. Experimental Procedure

4.2.1. Precursor Materials

$CoCl_2$ (Alfa Aesar, 99.7 % purity) and liquid $TiCl_4$ (Honeywell, ≥ 99 % purity), and $NaBH_4$ (Alfa Aesar, 98 % purity) powders were used as precursors. The amount of the precursors was determined according to the ideal reaction between $CoCl_{2(s)}$, $TiCl_{4\ (l)}$ and $NaBH_{4(s)}$ that should prompt the formation of solid ternary metal boride and NaCl compound, and H_2 gas. Three different compositions were studied based on the balanced reaction being: stoichiometric amount of the starting materials, 50 wt. % excess amount of $NaBH_4$, and 50 wt. % excess amount of $TiCl_4$. These samples were prepared using the molar ratios of metal chlorides to $NaBH_4$ as 1:3, 1:4.5, and 1:2.4, respectively. The process flow chart of the experiment is given in Figure 25. To obtain a homogenous powder blend the powder mixtures were grinded in a mortar. Considering that $TiCl_4$ is in the liquid form in room temperature (it has a very low melting point -24 °C), to introduce it to the reaction mixture a Hamilton™ syringe was used. All samples were prepared in a glovebox operating with Ar gas atmosphere. The prepared mixture was then placed in a sealed 316-L stainless steel hydrothermal reactor and put in a chamber furnace to be synthesized in a single-step process at 850 °C for 2 h under autogenic pressure with a heating rate of 5 °C/min. Previous studies on kinetics of decomposition of $NaBH_4$ reported that decomposition of $NaBH_4$ at 550 °C yields NaH and BH_3 [259,260]; however, a recent study claimed that decomposition of $NaBH_4$ was not completed even after 600 °C [209]. Our previous investigation revealed that

complete decomposition of $NaBH_4$ takes place at 550 °C but it is not instantaneous, so to achieve complete decomposition, an 2 h interval at constant temperature was introduced to the reaction heating regime and then the temperature was increased to 850 °C [242,257]. The obtained powders were leached with hot deionized water for 15 min and then centrifuged at 3900 rpm for 15 min to remove the byproducts of the reaction (NaCl). This step was repeated three times to completely remove all of NaCl from the powder and then the powders were vacuum dried overnight at 110 °C. After the purification step, samples were pressed to form pellets using a manual hydraulic press and a maximum load of 10 tons, and then placed in quartz tubes and sealed via an oxygen torch. These samples were subjected to an annealing process at 1100 °C for 2 h. The effect of the amount of precursors on the phase formation was investigated.

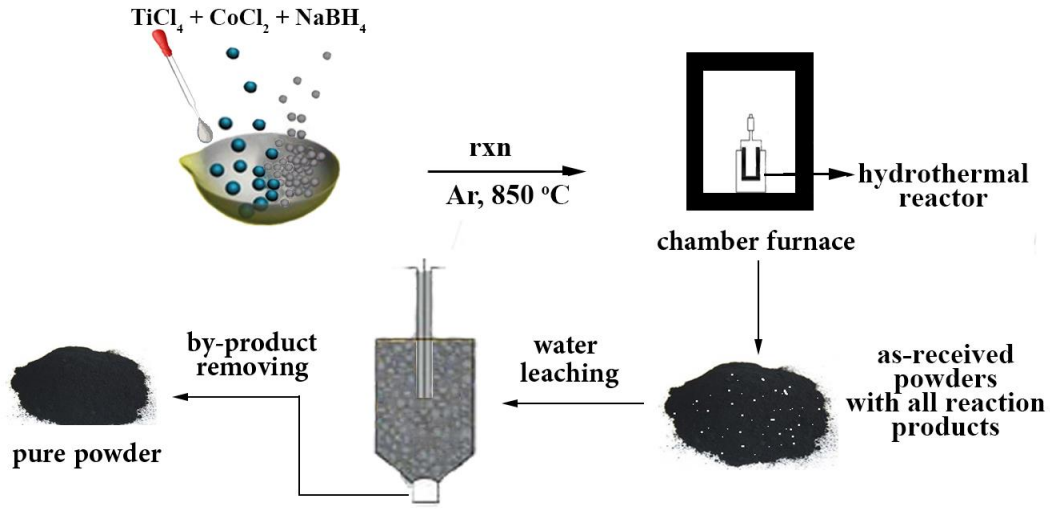

Figure 25. Process flow chart of the experiment.

4.2.2. Characterization of the powders

Rigaku Miniflex X-Ray diffractometer (XRD, CuK_α) and International Center for Diffraction Data (ICDD) database was used to analyze the phase structure of the samples. A common obstacle for the phase analysis of the powders containing Cobalt while using a CuKα source, is known as the fluorescent effect, which both deforms and reduces the quality and uniformity of the obtained XRD diagram. To address this issue, the detector set up was changed to XRF reduction mode. Differential thermal analysis/thermogravimetric (DTA/TG, STA 449C Jupiter, Netzsch) apparatus was used for thermal analysis. The DTA/TG analyses were carried out using an alumina crucible and via a heating rate of 10 K/min, under Ar atmosphere up to 1500 °C. Attenuated total reflection - Fourier transform infrared spectrometer (ATR-FTIR, Thermo Scientific IS10) was utilized to investigate surface properties and have better understanding of reaction mechanisms. Zeiss Ultra Plus field emission scanning electron microscope (FE-SEM) equipped with energy dispersive X-Ray spectrometer (EDS) was used for microstructural and morphological investigation, and also for measuring the particle size and distribution. Secondary electron detector was used to obtain the SEM images with an acceleration voltage of 10 kV and setting the working distance at 5 mm. Bruker XFlash 5010 EDS detector with 123 eV resolution was used for EDS measurements. To investigate the elemental and phase distribution, and to better understand the interaction of the coexisting phases with each other, the powders were incorporated into bakelite, then carefully polished to obtain a smooth surface. Electron backscattered diffraction (EBSD) analysis was performed on these polished powders with a

Bruker CrystAlign 400 system, connected to a scanning electron microscope JSM 7800 F (JEOL).

4.2.3. Bulk properties

4.2.3.1 Preparation of the bulk samples

In order to investigate the effect of the synthesized powders on the properties of the bulk samples, they were embedded in Ti6Al4V (SLM Solutions, ELI Grade 23) which is a Ti-based alloy and considered to be a suitable matrix material. Ti6Al4V was chosen as matrix powder given its wide range of applications in aerospace and biomedical engineering fields due to properties such as high strength (1070 MPa), high hardness (350HV), high fracture toughness, high corrosion resistance, and light weight. Samples were prepared by addition of 1 wt. % of the reinforcement powder to the matrix powder. The as received commercially pure TiB_2 (Titanium Boride - Metals Basis, Alfa Aesar, 99.5% purity, -325 mesh) hereafter referred to as (CP- TiB_2) and in house synthesized TiB_2 [282] hereafter referred to as (S-TiB_2) with particle size range of micron and submicron scale, were also incorporated into this matrix for the purpose of comparison. Powder mixtures were roll milled to achieve a homogenous distribution of the reinforcement particles and to ensure their proper attachment to the matrix particles. The milling step was done using a tumbler mixer with a speed of 75 rpm and a ball to powder ratio of 3:1 for 24 h. The resulting powders were then utilized to fabricate bulk samples via SLM method. SLM is a sub branch of additive manufacturing (AM) developed as an answer to the need of producing fully dense or porous metal

components (bulk) from powders, which are capable of competing with the components fabricated via conventional methods in terms of mechanical and structural properties [295]. In a SLM process, the high energy density laser, scans and selectively melts and fuses specific parts of the powder with a very high precision and resolution. The SLM (Realizer SLM 50 – Realizer GmbH) machine containing a 120 W laser was used for fabrication of the bulk parts under flow of high purity Ar gas. Manufacturing process was carried out with a scanning speed of 0.33 mm s^{-1}, hatching distance of 0.08 mm and layer thickness of 25 µm. The process was done via a continuous laser mode adopting a 60º rotation in the direction of melting. In order to compare the improvements in the mechanical behavior of the fabricated samples, a reference sample made of only Ti6Al4V was prepared using the same parameters and condition. Figure C9 (Appendix C) provides the schematic SLM procedure for further clarity.

4.2.3.2 Characterization of the bulk samples

To investigate the mechanical properties of the SLM fabricated components, compression and hardness tests were performed on the samples. Fabricated cylindrical samples were polished to obtain parallel and smooth surfaces using a Phoenix 4000 metallographic lapping/polishing machine (BUEHLER) and then subjected to compression strength test via an Instron 8516 machine with a load cell of 100 kN operating at a fixed crosshead speed of 5mm min^{-1}. To measure the hardness of the fabricated bulk samples, they were incorporated

into black phenolic resin via Simpliment 3000 automatic mounting device (BUEHLER) and then their surfaces were polished to obtain a smooth surface. Hardness tests were carried out using a Shimadzu HMV–G 21D micro hardness device with optical microscope. An average of 15 indents was taken for each measurement with a force of 98.07 mN and a 10 s dwell time. To investigate the microstructure of the samples, a Zeiss Ultra Plus FE-SEM equipped with EDS was used.

4.3. RESULTS AND DISCUSSION

4.3.1. Phase and thermal analyses

Phase formation of the powders obtained from the reaction of $CoCl_2$-$TiCl_4$-$NaBH_4$ at 850 ˚C with different stoichiometry were investigated. An XRD diagram of the obtained powders are presented in Figure 26 comparatively. XRD diagrams obtained from the reaction matched CoB (ICDD Card No: 04-003-2122, orthorhombic, a = 3.948 Å, b = 5.243 Å, c = 3.037 Å) and TiB_2 (ICDD Card No: 04-001-3239, hexagonal, a = 3.03100 Å, b = 3.03100 Å, c = 3.22900 Å) and are present in all tested stoichiometry, which happen to be thermodynamically stable as well. Nonetheless, different stoichiometry of Ti-B phases (i.e. named as TiB_x) were also observed in both cases with excess amounts of precursors (Figure 26(b) and (c)). The mechanism of the conversion of the chlorides to the obtained composite products in this study is based on reduction of the chloride precursors with decomposition of the $NaBH_4$ which is both the reducing agent and the boron source. The produced BH_3 and NaH react with and reduce the metal chlorides yielding NaCl and H_2 gas as by products and

the freed boron atoms attach to metal atoms yielding metal boride composite of CoB-TiB_2. The detailed mechanism of conversion of binary systems of metal chlorides and $NaBH_4$ to metal borides was investigated both in our previous work and also in the literature [32,39,177,257]. Thermal analysis was done on the as-synthesized powders obtained from the reaction of $CoCl_2$-$TiCl_4$-$NaBH_4$ at 850 ˚C. Figure C1 (Appendix C) presents the DTA curves of the as-synthesized powders. The broad endothermic effects seen at about 140-150 ˚C (peak max.) for all samples corresponds to the evaporation of the moisture present in the structure of the powders due to handling in air after synthesis. Since the temperature regime used in this study is lower in comparison to other conventional methods, the resulting powders tend to form particles of nano size which, in turn, increase the possibility of surface oxidation due to significant increase in surface area in these powders after synthesis. The sharp endothermic effect observed at around 1350 °C is attributed to the melting point of the eutectic phase between CoB and B whose melting point is defined at 1350 °C according to the Co-B phase diagram [262]. Furthermore, additional evaporation or sublimation of the boron oxide species formed during leaching and/or air handling time could also be contributed to this endothermic effect. The XRD pattern of the DTA sample (Figure C1(a)) after heating it up to 1500 °C resulted in the B_7O/B_6O phases in addition to the major CoB and TiB_2 phases indicating oxidation of the B phase. Previous studies on binary boride systems have reported the presence of an amorphous boron layer surrounding the synthesized boride particles, which oxidizes after synthesis and during leaching and/or air handling time, thus, validating our claim [39,177,277]. Figure C2 presents the TG curves of the samples and

shows a 12 – 15 % initial weight loss during heating up to 200 °C which agrees with the broad endothermic effect seen in DTA curves and is assigned to moisture elimination. The presence of trace amounts of surface oxide in the structure of the powders is in agreement with previous studies in the literature [177,257]. There is an additional weight loss of 4.69 % and 4.36 % for samples (b) and (c) and 2.92 % for sample (a) observed at 1300 – 1500 °C, which also supports the evaporation of boron oxide species. The corresponding Co-B and Ti-B phase diagrams are presented in Figure C3 (Appendix C) for further clarity.

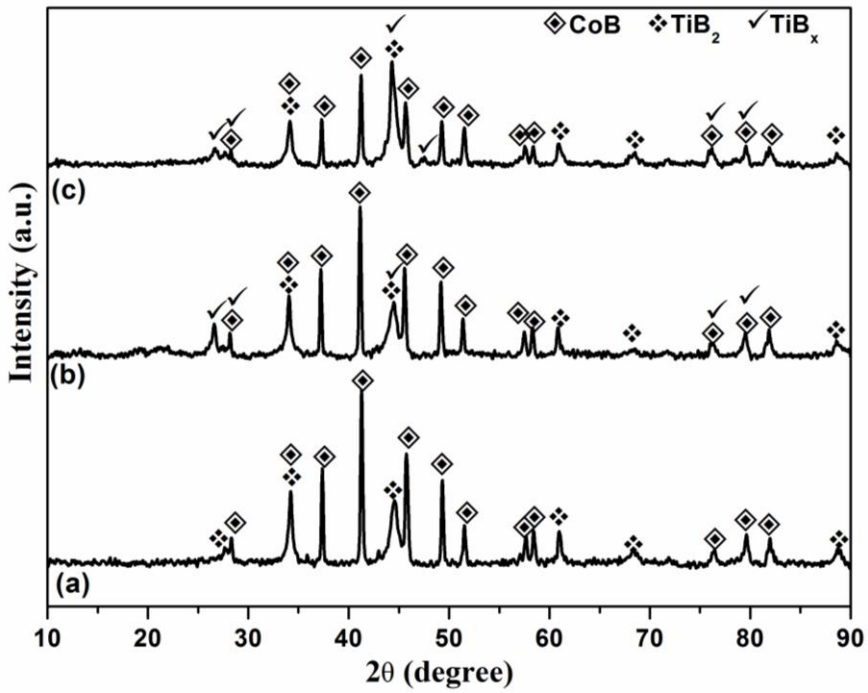

Figure 26. XRD patterns of the powders obtained from the reaction of $CoCl_2$-$TiCl_4$-$NaBH_4$ at 850 ˚C: (a) stoichiometric, (b) 50 wt. % excess $NaBH_4$ and (c) 50 wt. % excess $TiCl_4$.

4.3.2. Effect of annealing on the phase formation

Obtained powders were annealed at 1100 °C for 2 h to investigate the effect of annealing on the phase change, possibly improving the crystallinity of the powder and also to remove the undesired TiB_x phase. Figure 27 presents the XRD patterns of the stoichiometric powders obtained (a) from reaction of $CoCl_2$-$TiCl_4$-$NaBH_4$ and (b) after annealing at 1100 °C. It was observed that the crystallinity of the TiB_2 phase was increased compared to the as-synthesized sample. Considering the fact that the formation of the TiB_2 phase in this study takes place at relatively lower temperatures compared to conventional methods, one can say that the reason for this is because lower reaction temperature between $TiCl_{4(l)}$-$NaBH_{4(s)}$ was sufficient for the formation of this phase. Nevertheless, since TiB_2 is thermodynamically stable (TiB_{2mp} = 3230 °C), higher temperatures were necessary to initiate its recrystallization, which was provided during the annealing process and gave rise to increased crystallinity. However, it was not enough to continue the recrystallization, which is explained later on. It was observed that samples with excess amounts of $TiCl_4$ or $NaBH_4$ still had the unwanted TiB_x phase after annealing process. Figure C4 illustrates the XRD patterns of CoB-TiB_2-TiB_x composite powders after annealing at 1100 °C for 2 h. Thus, we chose the stoichiometric version as the optimum option.

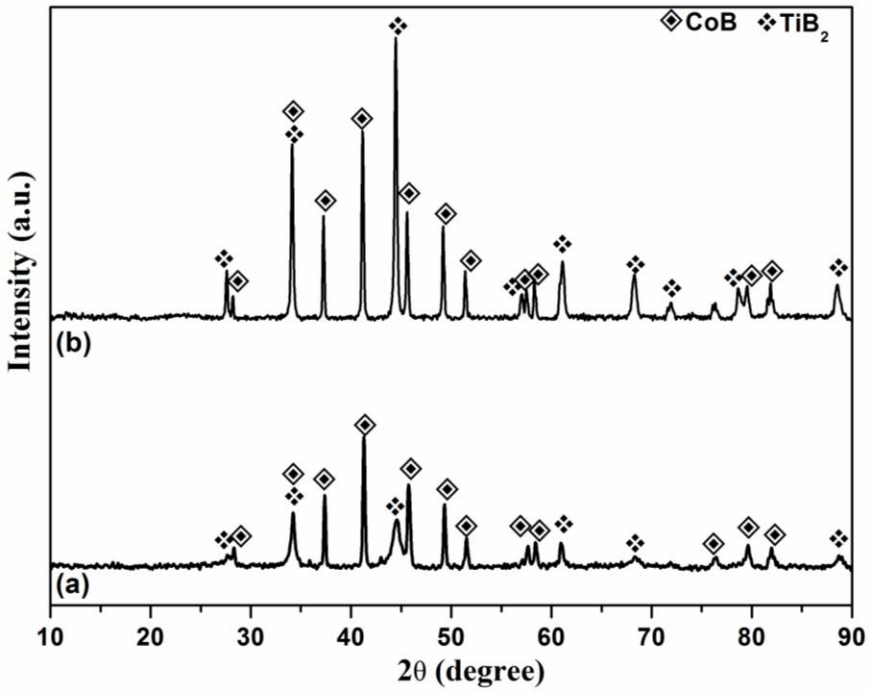

Figure 27. XRD patterns of the powders obtained from the stoichiometric reaction of $CoCl_2$-$TiCl_4$-$NaBH_4$: (a) obtained at 850 ˚C and (b) after annealing at 1100 ˚C (See appendix C10 for comparison with reference peaks).

To investigate phase purity and possible phase transformations, DTA/TG and FTIR analysis were implemented on the annealed powders. Figures 28 and 29 present the results obtained from stoichiometric samples. As seen in Figure 27, CoB–TiB_2 composite powder, has indeed formed from the reaction of $CoCl_2$-$TiCl_4$-$NaBH_4$ at 850 ˚C, and no further phase transformation was observed during the annealing process at 1100 ˚C. As seen in Figure 28 (b), all major endothermic effects belonging to moisture and evaporation/sublimation of boron oxide derivatives (Figure C1) no longer exist, meaning a pure phase has formed. The small endothermic effect at 1460 ˚C shows the melting of the CoB phase. This indicates a

partial melting of the powder which consists of CoB (MP: 1460 °C) and TiB_2 having a melting temperature higher than 3000 °C. The TG curve presented in Figure C5 exhibits no weight loss up to 1200 ˚C. However, a 4 % weight loss was noted after 1200 ˚C corresponding to the evaporation of trace amounts of remnant boron oxide. As seen from the FTIR spectra in Figure 29, B-OH, B-O, and B-H vibrations (vibration of the attached hydrogen or oxygen) are observed in the as-synthesized powder; however, all mentioned vibrations were absent for the annealed powders, which also validates the claim of purity for the products that were subjected to annealing at 1100 ˚C for 2 h.

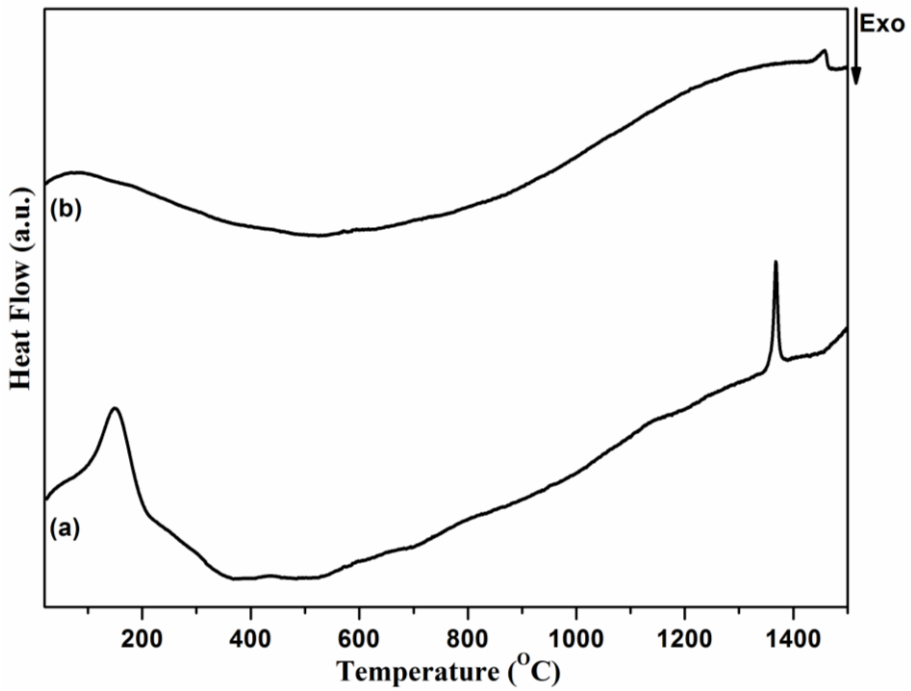

Figure 28. DTA curves of the powders obtained from the stoichiometric reaction of $CoCl_2$-$TiCl_4$-$NaBH_4$: (a) obtained at 850 ˚C and (b) after annealing at 1100 ˚C.

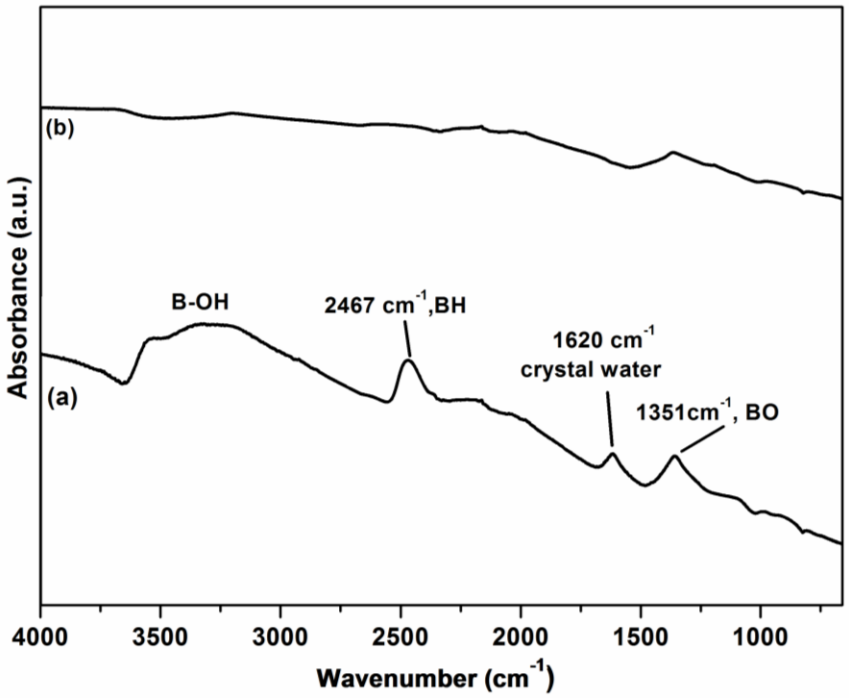

Figure 29. FTIR spectra of the powders obtained from the stoichiometric reaction of CoCl2-TiCl4-NaBH4: (a) obtained at 850˚C and (b) after annealing at 1100˚C.

4.3.3. Microstructural and chemical analyses of the powders

Figure 31 presents the SEM image of the powders obtained from the reaction of $CoCl_2$-$TiCl_4$-$NaBH_4$ at 850 ˚C. It was observed that the resulting powders possess particles with spherical-like morphology with some agglomerations, which are homogenously distributed between 300 – 500 nm. To have a deeper understanding of the relationship between morphology and elemental distribution and to investigate the presence of two distinctive phases, elemental mapping was performed on the annealed samples. Figure 31 illustrates the SEM/EDS images of the $CoCl_2$-$TiCl_4$-$NaBH_4$ powders after annealing at 1100 ˚C for 2 h. The

elemental mapping results clearly show that agglomerates are comprised of Cobalt element while other nano size particles are made of Titanium element. Observing nano particles was expected; however, their distribution is not homogenous within the powder, as CoB particles recrystallize and tend to form agglomerates while the reaction temperature is not high enough to trigger the recrystallization of the TiB_2 particles. Hence, two distinctively different morphologies are observed. The average particle size of different phases in the powders was measured using the screen measurement tool during SEM analysis. On the one hand, cobalt boride particles are frequently observed forming agglomerates with an average particle size of ~ 450 nm in homogenous distribution. On the other hand, TiB_2 particles have an average particle size of ~ 60 nm, which is also homogenous within TiB_2 particles. Table C2 and Figure C6 (Appendix C) summarize the average particle size measurement results for the CoB and TiB_2 phases for the particles after annealing in comparison to the particle size distribution of the powders before annealing. The results agreed with our hypothesis stating that CoB particles form agglomerates and TiB_2 particles remain in the nano scale and do not recrystallize as explained above.

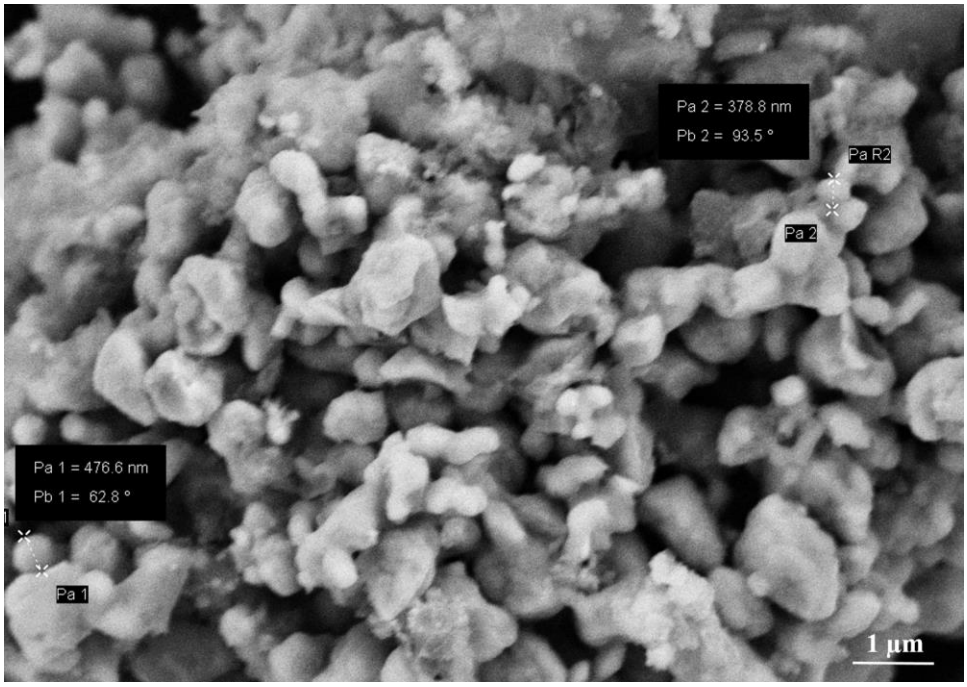

Figure 30. SEM image of the powders obtained from the stoichiometric reaction of $CoCl_2$-$TiCl_4$-$NaBH_4$.

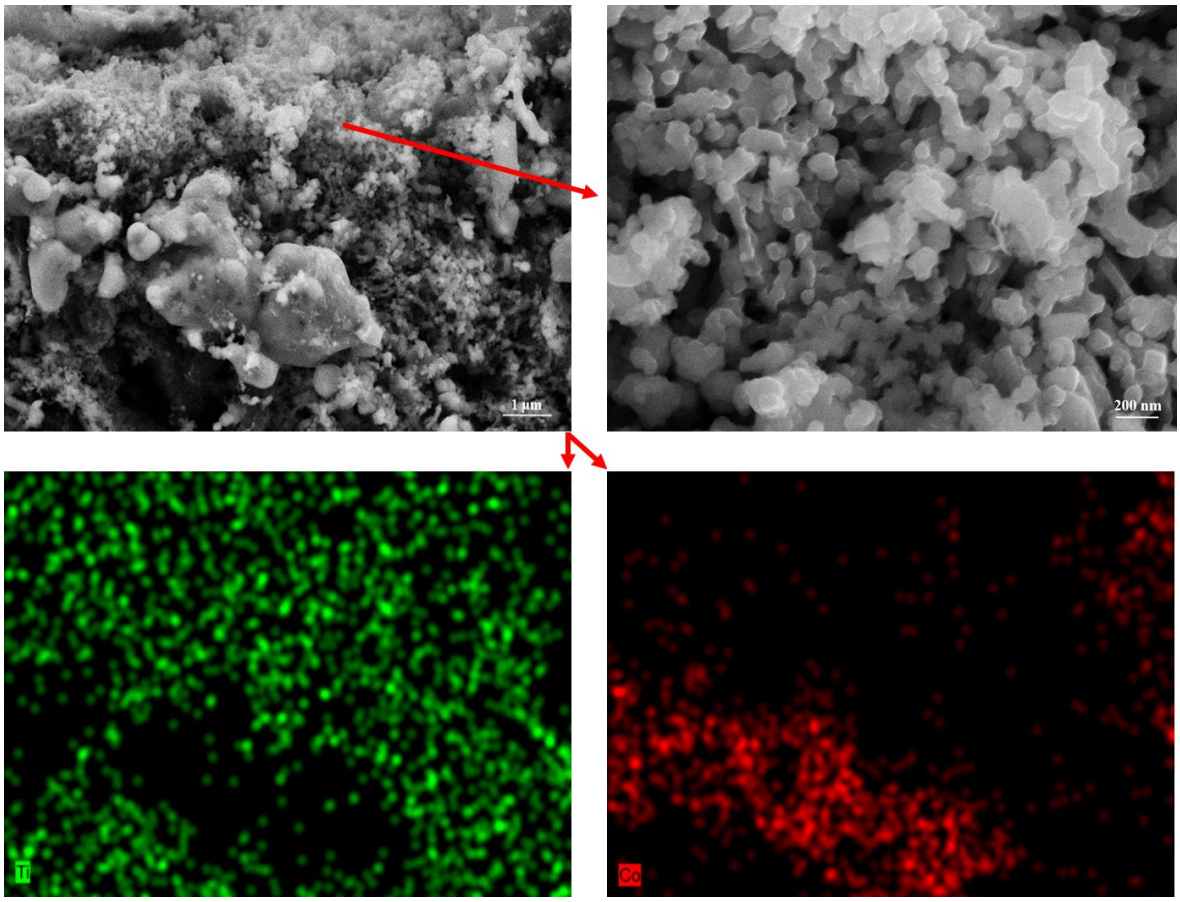

Figure 31. SEM images and EDS analysis of the powders obtained from the stoichiometric reaction of $CoCl_2$-$TiCl_4$-$NaBH_4$ and subsequent annealing: Secondary electron SEM images at different magnifications with corresponding elemental mapping (10 kV).

It is known that the oxidation rate of TiB_2 depends on temperature, composition, and oxygen partial pressure. For instance, monolithic TiB_2 starts oxidation by forming $TiBO_3$ first at temperatures below 400 ˚C and is further oxidized to form B_2O_3 [296]. In order to detect the oxidized areas, the polished samples were subjected to SEM/EDX analysis at low magnification. Figure 32 presents the elemental distribution map of the polished powders

obtained by the reaction of $CoCl_2$-$TiCl_4$-$NaBH_4$ powders after synthesis at 850 ˚C and subsequent annealing at 1100 ˚C. It is observed that the oxygen element is present alongside elemental Ti, which corresponds to minute TiB_2 particles with an average size of 60 nm illustrated in Figure 31. This, in turn, exposes a higher surface area of the material and facilitates the oxidation of the TiB_2 phase. The boron oxide is evaporated at temperatures above 900 ˚C leaving behind a porous TiO_2 layer [282,297–299]. Presence of elemental Ti, B, and O in the same place validate this claim.

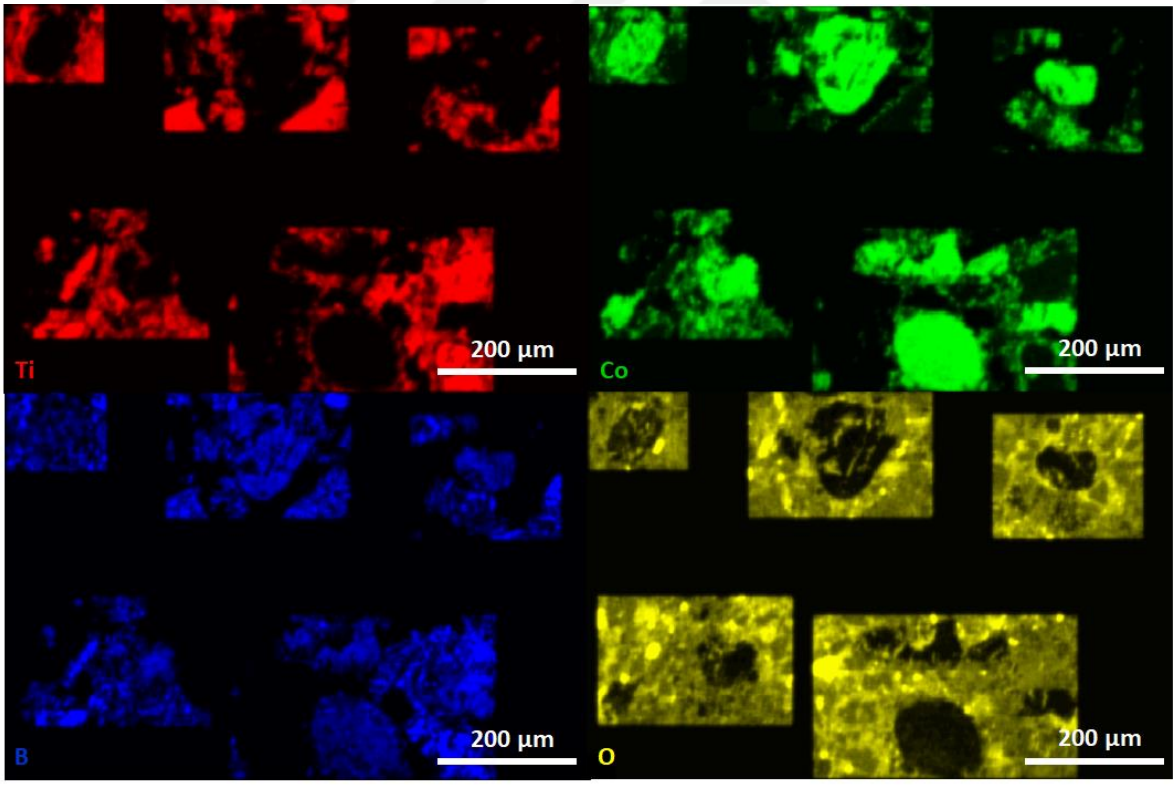

Figure 32. Low magnification SEM/EDX analysis (15 kV, elemental distribution map) of the polished powders obtained from the stoichiometric reaction of $CoCl_2$-$TiCl_4$-$NaBH_4$ and subsequent annealing.

Figure 33(a) and (b) show the quality and CoB phase maps taken from the same polished samples during EBSD analyses. The visualization of the phase mapping in Figure 33(b) was possible due to the single diffraction of CoB phase from the samples. It is notable that electron backscattered patterns could only be generated because neither a non-crystalline nor an intermediate phase was detected. The EDS analysis results taken from the BSE-SEM image in Figure 33(c) are presented in Figure 33(d) and Table 4. According to the EDS analysis results, it is clear that the green and red areas in Figure 33(d) correspond to the CoB and TiB_2 phases, respectively. However, TiB_2 phase could not be detected in the quality map during EBSD analysis most likely due to an amorphous layer surrounding the surface of the crystalline boride particles. The EDS analysis results taken from the marked regions 3, 4, and 5 present an excess amount of B which can be related to the amorphous boron layer and/or non-crystalline boron oxide species. Moreover, the EDS analysis results taken from the marked regions 1 and 2 show the CoB phase without any excess amount of boron. This also explains the reason of the detection of oxygen element alongside elemental Ti throughout the microstructure as seen in Figure 7. It can be concluded that nano sized TiB_2 particles were surrounded by an amorphous boron layer. This layer is thought to be oxidized at a later stage during handling steps. To the best of the authors' knowledge, formation of separate boride phases in this study can be attributed to a couple factors including low solubility of the reaction precursors in each other, slow rate of cation diffusion, and a difference in the reactivity of the chloride precursors with the reducing agent ($NaBH_4$). This can trigger formation of the binary borides at different time points during the overall course

of reaction. This promotes the formation of two separate phases, which is in agreement with previous works in the literature [277,300]. Studies in the literature have tried to solve this issue via incorporation of a diffusion promoter such as Cu element powder or by increasing the temperature of the reaction and the annealing step. However, doing so would contradict the goals that this study by means of introducing impurity and/or possible undesired by products [277]. Hence, the results of the present study will be useful and important for optimizing the synthesis conditions of the binary boride compounds in terms of in-situ reactions of the metal chlorides at low temperatures, as well as for obtaining crystalline and nano-scaled composite powders while keeping the focus on the purity of the final products.

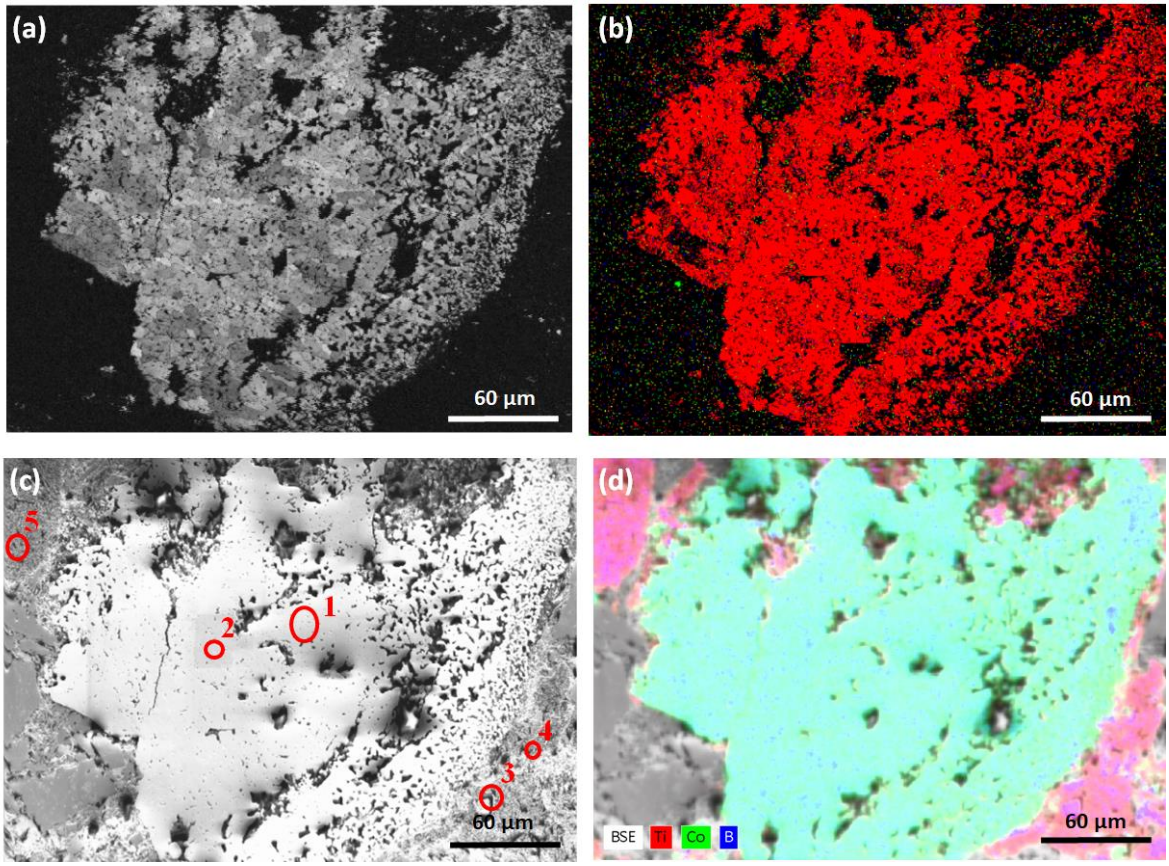

Figure 33. EBSD and SEM/EDS analyses of the polished powders obtained from the stoichiometric reaction of $CoCl_2$-$TiCl_4$-$NaBH_4$ and subsequent annealing: (a) quality map.

Table 4. EDS point analysis of the marked regions taken from the polished powders obtained from the stoichiometric reaction of $CoCl_2$-$TiCl_4$-$NaBH_4$ and subsequent annealing.

Marked regions	***Amounts of elements detected by EDS analyses (at. %)***		
	B	*Ti*	*Co*
1	50.22	0.05	49.73
2	50.69	1.23	48.08
3	70.71	26.48	2.81
4	71.73	25.44	2.83
5	72.42	25.76	1.82

4.3.4. Properties of the bulk samples

4.3.4.1 Microstructure of the bulk samples

The bulk samples fabricated by incorporating the synthesized nano-scaled composite powder (CoB-TiB_2) were studied in comparison with those reinforced with the binary TiB_2 powders. The SLM fabricated parts were incorporated into phenolic resin and then polished following the standard polishing procedures, and their mechanical and microstructural properties were studied. Figure C7 (Appendix C) presents the SEM analysis results of the polished samples. It was observed in the secondary electron SEM images that, other than minute porosity, the surface of the samples was smooth. The observed porosities can exist due to a variety of reasons such as balling or keyhole effects or as a result of a rapid heating/cooling rate of the SLM process (10^3-10^8 K/s). Moreover, the fact that TiB_2 has a higher melting point (3225 ºC) compared to Ti6Al4V (1933 ºC) renders simultaneous

melting of the matrix and reinforcement difficult [301]. Processing metallic systems containing intermetallic compounds and ceramics via laser-based manufacturing techniques is challenging due to the high melting point of these compounds and can result in increased viscosity of the melt, thus, causing defects [302]. The dynamic viscosity of the molten layer should be low enough to allow proper spreading of the melt yet also high enough to prevent the balling effect from happening [303,304]. The elements present in the matrix powder were detected (Ti, Al, and V) in the EDX analysis with the exception of boron because it is a lightweight element. Co and Ti were detected in the samples reinforced with the synthesized CoB-TiB_2 powder, which was also present in the structure of the reinforcement powder. On the other hand, the observation of reinforcement particles was not possible in the secondary electron SEM images most likely due to the fine and homogeneous distribution of the low number of particles (1 wt. %) in the matrix. The Fe present in the EDX results of this sample corresponds to trace amounts of impurities coming from the machine during the SLM process.

4.3.4.2 Hardness and compression evaluations

Figure 34 reveals the Vickers microhardness values and indent shapes taken from the SLM fabricated samples. It is observed that Ti6Al4V matrix reinforced with CoB-TiB_2 particles have the highest hardness value compared to S-TiB_2 and CP-TiB_2. The reason for the improvement in the hardness values of the samples compared to that of those reinforced

with CP-TiB_2 is the smaller particle size of these powders, comparatively. The average particle size for the CP-TiB_2 is 44 µm (325 mesh), for the S-TiB_2 it is 500 nm, and 300-500 nm for CoB-TiB_2 composite powder. The corresponding average Vickers micro hardness values are 420±11, 497±13, and 506±10 HV, respectively. It is thought that as a result of the smaller particle size of the S-TiB_2 in comparison to that of CP-TiB_2, the S-TiB_2 particles induce additional grain boundary hardening and inhibit dislocation motion in the structure of the sample. This eventually increases the hardness by 18.5 % in comparison to that of CP-TiB_2 reinforced matrix. In the case of the CoB-TiB_2 reinforced samples, this increase goes up to 20.5 % compared to the CP-TiB_2 reinforced sample. Figure C8 (Appendix C) illustrates the indentation marks left on the surface of the bulk CoB-TiB_2 reinforced sample, which is proof of homogeneity of the indents and, hence, the hardness values. Furthermore, an average hardness value of 410±30 HV was measured for the prepared Ti6Al4V reference sample. Thus, a significant improvement (506±10 HV) is achieved for the CoB-TiB_2 reinforced sample by comparison to unreinforced sample and the others.

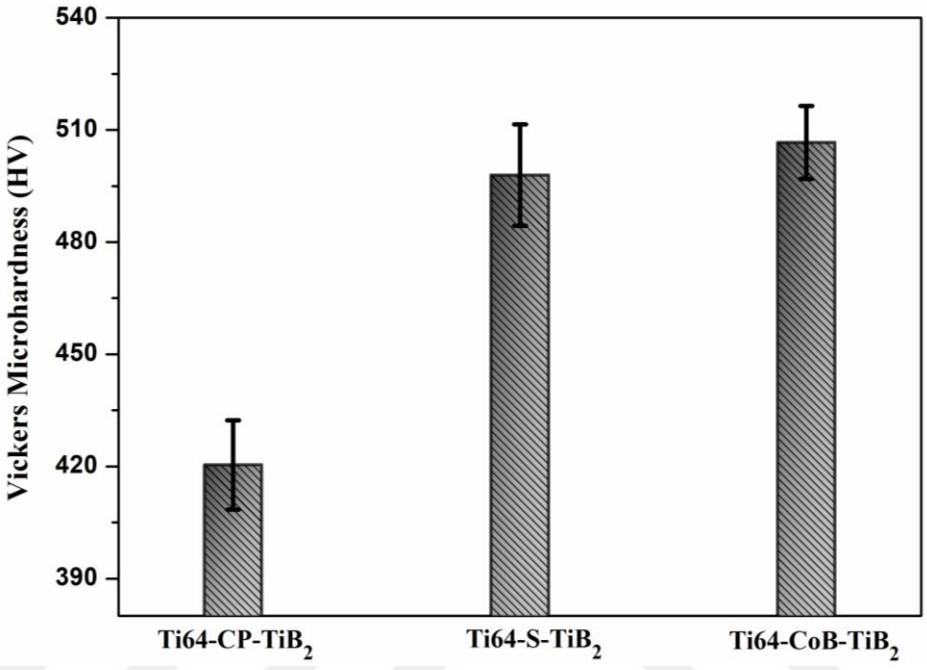

Figure 34. Vickers micro hardness values for SLM fabricated parts (Ti64 stands for Ti6Al4V).

Figure 35 presents the compression stress vs. strain diagrams of the reinforced bulk samples. It was observed that among the SLM fabricated bulk samples, the CoB-TiB_2 reinforced sample withstood the highest compressive stress at 1682 MPa followed by that of S-TiB_2 reinforced sample at 1617 MPa, and CP-TiB_2 at 1605 MPa. Simultaneously, the prepared Ti6Al4V reference sample could only bear a compressive strength of 1320 MPa. The reason behind the enhancement of the mechanical properties of the reinforced bulk samples observed both in hardness (Figure 34) and compression tests (Figure 35) is likely due to dislocations and strengthening mechanisms. It can be concluded that the smaller the grain size of a material, the higher the grain boundary area, hence the improvements in

hardness and compressive strength [305]. The relationship between the grain size and the mechanical properties of the materials (Hall-Petch Equation) is described in the literature [306]. The authors believe that such is the case in this study: The smaller the size of the TiB_2 particles (60 nm) in the synthesized composite powder (Figure 31 and Table C2), the more improved are the obtained results. Given that TiB_2 is a much harder material than CoB, and higher hardness values would be expected from TiB_2 reinforced samples, the authors believe that the presence of CoB particles could have enhanced the mechanical properties of CoB-TiB_2 reinforced samples even more by increasing the average grain boundary area. Other studies have reported the hardness and compressive strength values of the monolithic Ti6Al4V sample as 396 HV and 1070 MPa, respectively [307]. However, the prepared Ti6Al4V reference sample showed hardness and compressive strength values of 410 HV and 1320 MPa in the present study, which is considered the result of the different parameters used during the SLM process. Consequently, the incorporation of CoB-TiB_2 reinforcement particles in this work clearly illustrates the further enhancement and improvement of the discussed properties (506 HV and 1682 MPa).

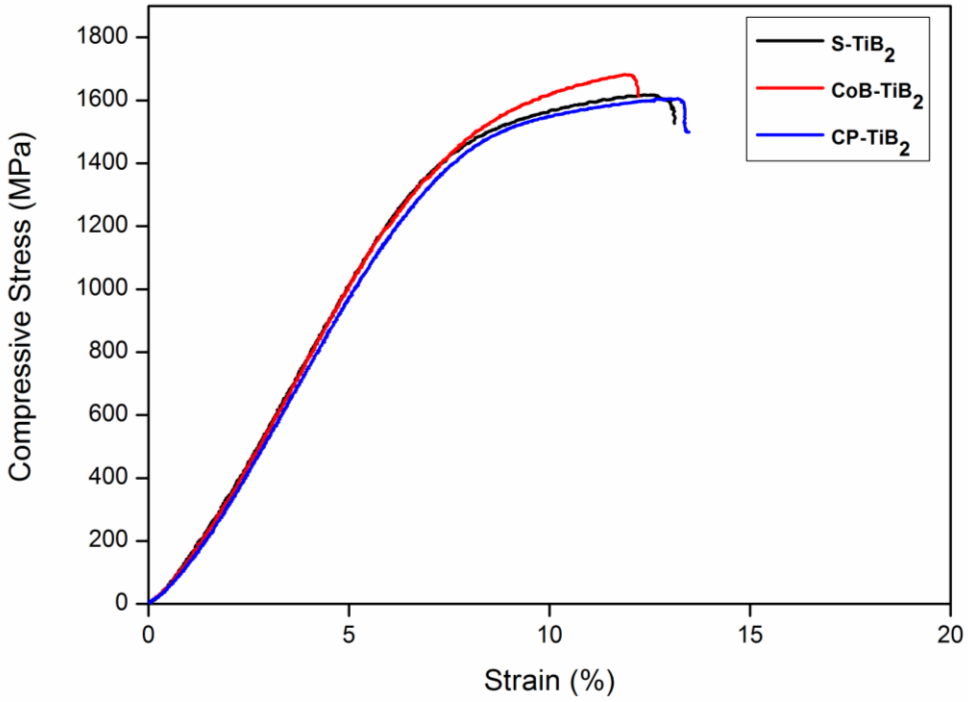

Figure 35. Compressive stress-strain curves for SLM fabricated parts. Legend indicates the reinforcement powders used in Ti6Al4V matrix.

4.4. Conclusion

In this study, we successfully synthesized cobalt-titanium-boron based composite nanostructures in a single-step process using metal chloride powder blends via a low temperature synthesis method, in a sealed reactor, under autogenic pressure. Stoichiometric excess amounts of precursors reacted at 850 ˚C yielded CoB, TiB_2, and unstable TiB_x phases. However, after a reaction of the stoichiometric amounts of precursors at 850 ˚C, we were able to achieve the conversion of metal chlorides to nanocrystalline CoB-TiB_2 composite powders with an average particle size of 300-500 nm. DTA/TG and FTIR analyses showed that water, moisture, and boron oxide species present in the structure of the powder were successfully removed after annealing at 1100 ˚C. SEM images of the annealed powders revealed that CoB and TiB_2 phases possess particles of distinguishably different morphologies and sizes. TiB_2 particles having an average size of 60 nm were surrounded by an amorphous boron layer, which could be oxidized later, whereas the CoB particles formed agglomerates with an average size of 450 nm without any surface oxidation. This is considered an interesting result for further investigation on the sintering processes of these nanocrystalline powders or their incorporation in metal matrix composite structures. Thus, recrystallized CoB particles with higher sizes would prevent further oxidation during the sintering of the composite powders at elevated temperatures. Bulk samples were fabricated via the SLM method using Ti6Al4V powder as matrix and synthesized CoB-TiB_2 composite powder, in house synthesized TiB_2, and CP-TiB_2 powders as reinforcements. It was observed that both hardness and compressive strength were enhanced in all of the produced Ti6Al4V

samples, and the CoB-TiB_2 reinforced sample exhibited the highest values, being 506 HV and 1682 MPa, respectively, in comparison with the unreinforced sample (410 HV and 1320 MPa) and the others (420-497 HV and 1605-1617 MPa). Consequently, investigations on the reinforced samples revealed that mechanical properties of Ti6Al4V sample could be significantly improved by incorporating composite powders consisting of sub-micron CoB, and nano-size TiB_2 particles.

Chapter 5. Prospectus

The summary of the achievements and results obtained during the course of this thesis are presented in this chapter. The powder samples in this work were synthesized via two different methods implementing low-temperature heating regime known as inorganic molten salt and reduction at autogenic pressure techniques. The obtained final materials were targeted towards various application fronts and optimized respectively. Following is the summary of what was accomplished over the course of this thesis.

The $CoFeB_2$, CoFeB, CoB-Fe_3B, Co_2B-Fe_3B, CoB-TiB_2 phases obtained in this study were synthesized utilizing the optimized low-temperature synthesis method. Within the context of this work, the conventional synthesis temperature of composites/ternary borides of Co-Fe-B and Co-Ti-B was reduced significantly (from about 2000 °C to T_{max}=850 °C) and nano or submicron size crystalline powder samples were obtained thanks to the optimized synthesis methods in a single-step reaction. Results showed that the synthesized $CoFeB_2$ powder (obtained from the anhydrous precursors) is suitable for use as a soft magnet with ferromagnetic properties and exhibits a superparamagnetic tendency after annealing and obtaining the high stability phase. The synthesized $CoFeB_2$ powder (obtained from the hydrous precursors) is also suitable for use as a soft magnet with ferromagnetic properties; however, after optimization of the synthesis conditions, the saturation magnetization of the obtained powders was increased 9 times. On the other hand, the synthesized CoB-TiB_2 powders were introduced as reinforcement to Ti6Al4V matrices by powder metallurgy methods and improved combination of microstructure-mechanical property was achieved.

Summary of the most important achievements are as follows:

- The nano-crystalline ternary $CoFeB_2$ phase was successfully synthesized from the single-step reaction of anhydrous $CoCl_2$-$FeCl_3$-$NaBH_4$ in presence of inorganic eutectic mixture (LiCl/KCl) following a reaction at 850 °C via the open system route.
- The nano-crystalline CoB and Fe_3B phases were obtained from the single-step reaction of anhydrous $CoCl_2$-$FeCl_3$-$NaBH_4$ in presence of inorganic eutectic mixture (LiCl/KCl) following a reaction at 850 °C via the closed system route.
- A pure $(CoFe)B_2$ solid solution was obtained after annealing the samples obtained from the reaction of anhydrous $CoCl_2$-$FeCl_3$-$NaBH_4$ via the open system at 1100 °C.
- An average particle size of 60 nm was successfully obtained (for the samples obtained from the reaction of anhydrous $CoCl_2$-$FeCl_3$-$NaBH_4$ at 850 °C via the open system), where the particles were homogeneously distributed throughout the sample containing spherical, co-axial and, rod-like morphologies.
- The as-synthesized samples obtained from the reaction of anhydrous $CoCl_2$-$FeCl_3$-$NaBH_4$ at 850 °C via the open system are classified as soft magnetic materials exhibiting a narrow hysteresis curve and an average coercivity value of 500 Oe and an average magnetization of 21.1 emu/g.
- Superparamagnetic behavior was observed after annealing the samples obtained from the reaction of anhydrous $CoCl_2$-$FeCl_3$-$NaBH_4$ at 850 °C via the open system at 1100 °C as a result of the absence of the FeB phase as the source of the ferromagnetism.
- The nano-crystalline cobalt iron metal boride powders were successfully synthesized as a result of the reaction of $CoCl_2 \cdot 6H_2O$-$FeCl_3 \cdot 6H_2O$-$NaBH_4$ at 850

°C, using different reaction systems and optimized synthesis conditions according to the results of the first chapter.

- After the reaction of $CoCl_2 \cdot 6H_2O$-$FeCl_3 \cdot 6H_2O$-$NaBH_4$ at 850 °C under autogenic pressure, the (CoFe)B - $Fe_{0.71}Co_{0.29}$ - $Fe_3B_7ClO_{13}$ and (CoFe)B - $Fe_{0.71}Co_{0.29}$ - $Co_3B_7ClO_{13}$ phases were obtained.
- After the reaction of $CoCl_2 \cdot 6H_2O$-$FeCl_3 \cdot 6H_2O$-$NaBH_4$ at 850 °C in the open system under Ar flow, (CoFe)B - $(CoFe)B_2$ and Co_2B - Fe_3B phases were obtained.
- The crystalline nano-particles obtained from the reaction of $CoCl_2 \cdot 6H_2O$-$FeCl_3 \cdot 6H_2O$-$NaBH_4$ at 850 °C in the open system under Ar flow had a homogenous microstructure with irregular shapes for the agglomerated particles obtained under Ar flow with an average particle size of 2 µm; however, at higher magnifications, smaller particles were observed with an average size of about 80 nm.
- The optimization steps discussed in the previous chapter were implemented and the thermal analysis of the obtained powder showed that the precautions taken to avoid oxidation were effective and reduced the % mass loss significantly.
- Also, after application of the optimization steps, the obtained particles exhibited an average saturation magnetization of 104-183 emu/g with the highest belonging to the stoichiometric batch of the open system and the lowest belonging to the stoichiometric batch of the closed system, which pleasantly revealed a 9-fold increase in magnetization values and a coercivity range of 20-100 Oe.
- High-temperature magnetic measurements revealed that obtained samples are stable ferromagnets up to 795 K at 10 kOe, as no transition temperature (T_c) was observed.
- Cobalt-Titanium-Boron based composite nanostructures were successfully synthesized in a single-step process after the reaction of $CoCl_2$-$TiCl_4$-$NaBH_4$ at 850 °C, via a sealed reactor under autogenic pressure.

- The reaction of stoichiometric excess amounts of $CoCl_2$-$TiCl_4$-$NaBH_4$ at 850 °C resulted in crystalline CoB, TiB_2 and, unstable TiBx phases.
- The reaction of stoichiometric amounts of $CoCl_2$-$TiCl_4$-$NaBH_4$ at 850 °C resulted in the complete conversion of chloride precursors to crystalline CoB-TiB_2 composite powders with an average particle size of 300-500 nm.
- Particles obtained from the reaction of the stoichiometric amounts of $CoCl_2$-$TiCl_4$-$NaBH_4$, exhibited two distinctive morphologies: CoB particles formed agglomerates with an average size distribution of 450 nm without any sign of surface oxidation where TiB_2 particles possessed a homogenous distribution and an average particle size of 60 nm which were prone to oxidation due to the affinity of Titanium to oxygen.
- Bulk samples were fabricated via the SLM method using Ti6Al4V powder as matrix and synthesized CoB-TiB_2 composite powder, in-house synthesized TiB_2, and CP-TiB_2 powders as reinforcement particles.
- With addition of 1 wt. % of reinforcement particles, both the hardness and compressive strength of the bulk samples were enhanced as a result of grain boundary hardening and dislocation motion prevention by the reinforcement particles.
- It was observed that samples reinforced with CoB-TiB_2 particles exhibited the highest hardness and compressive strength values being 506 Hv and1682 MPa, respectively. In comparison, the hardness and compressive strength values for the unreinforced sample (pure Ti6Al4V) were 410 Hv and 1320 MPa, while they were 420 Hv and 1605 MPa for the CP-TiB_2 and, 497 Hv and 1617 MPa for the S-TiB_2, respectively.
- Considering the amount of the incorporated reinforcement particles (1 wt. %), it could be anticipated that addition of the higher amounts of composite CoB-TiB_2 particles can significantly enhance the mechanical properties of the host matrix.

Appendix A

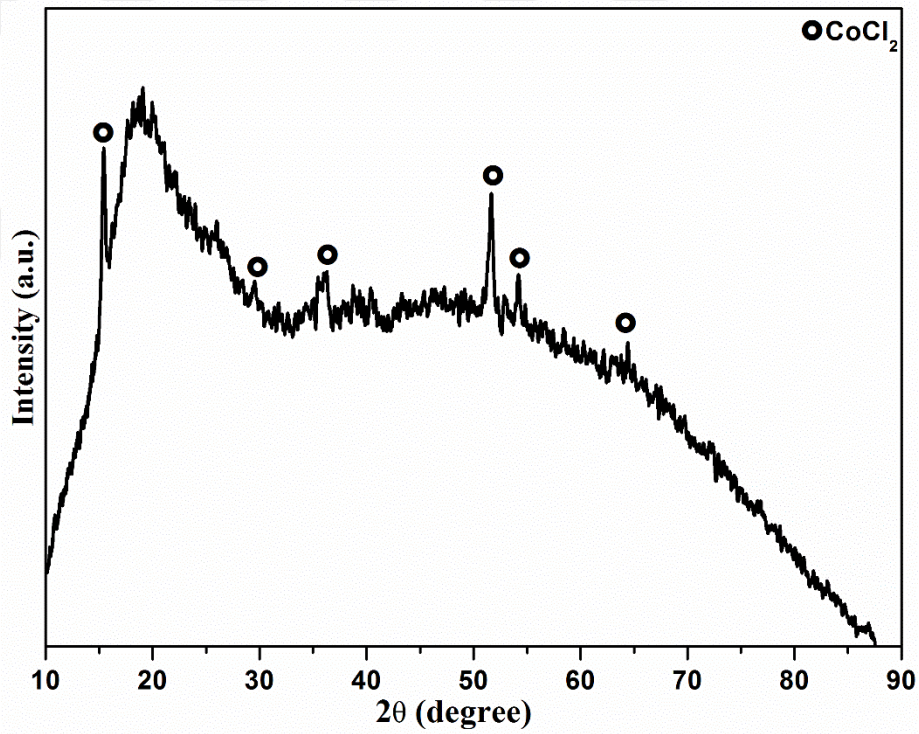

(a)

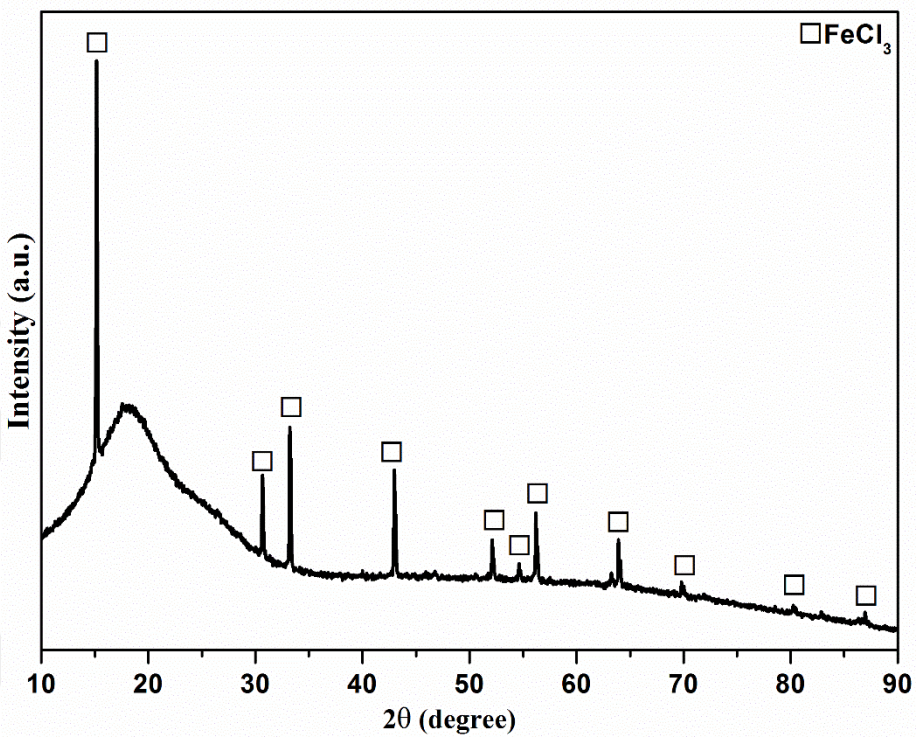

(b)

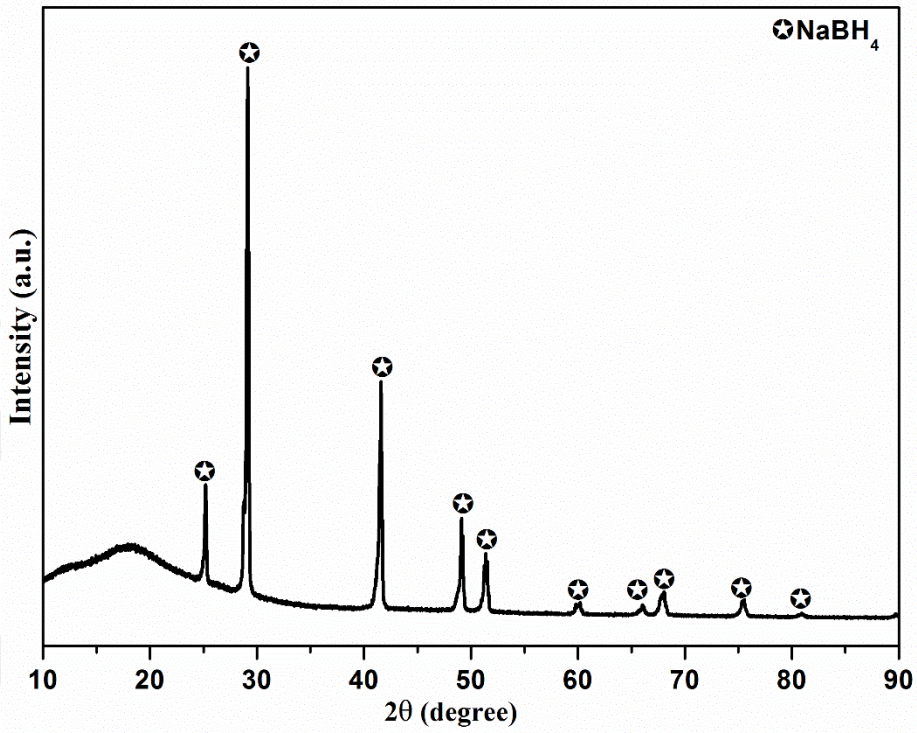

(c)

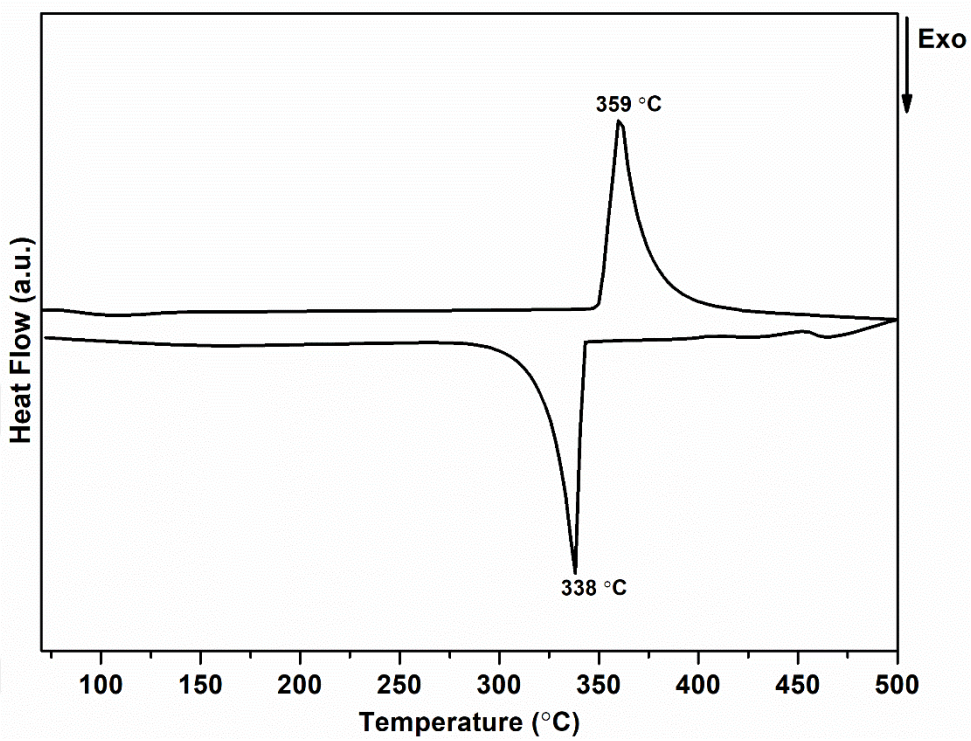

(d)

Figure A1. XRD patterns of a) $CoCl_2$, b) $FeCl_3$, c) $NaBH_4$ powders and d) DSC heating and cooling curve of LiCl/KCl eutectic mixture.

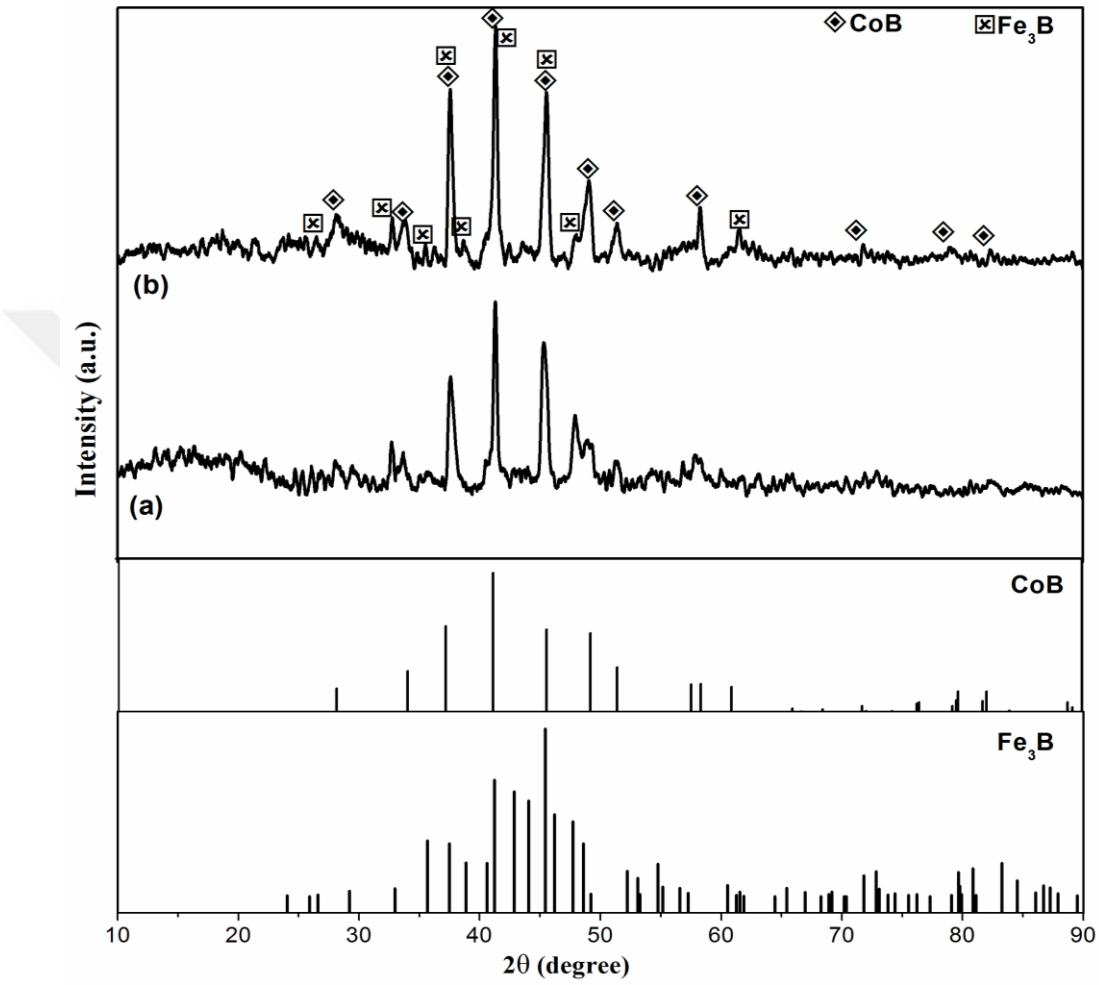

Figure A2. XRD patterns of the powders obtained by reaction of a mixture of $CoCl_2$-$FeCl_3$-$NaBH_4$ at 850 °C in the close system: (a) without eutectic salt mixture and (b) with eutectic salt mixture.

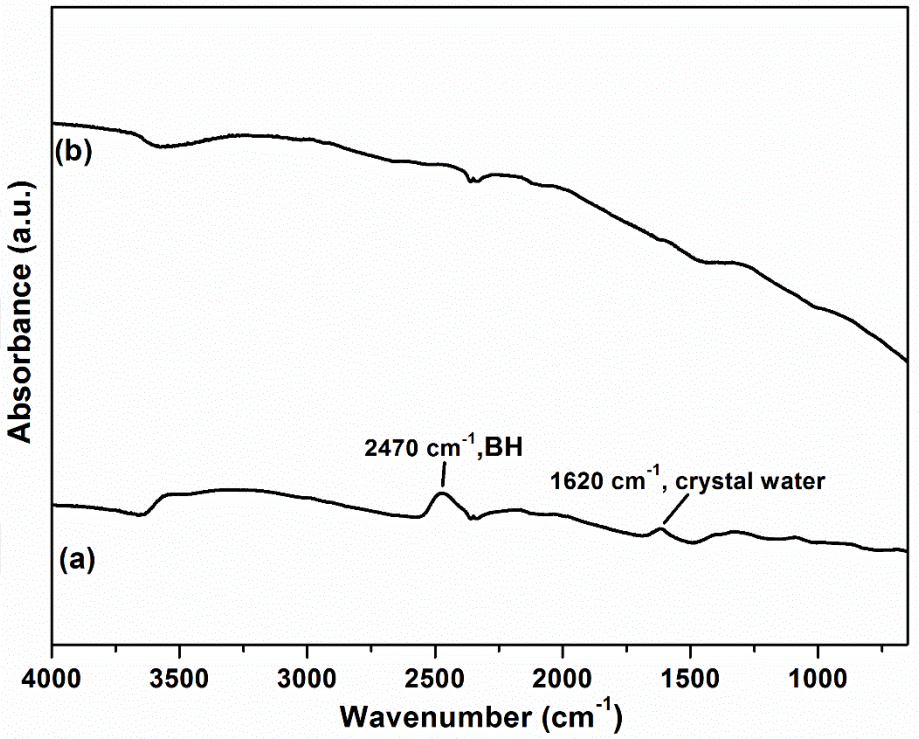

Figure A3. FTIR analysis of powders obtained by reaction of $CoCl_2$-$FeCl_3$-$NaBH_4$ in the close system at 850 °C: sample (a) without eutectic salt mixture and (b) with eutectic salt mixture environment.

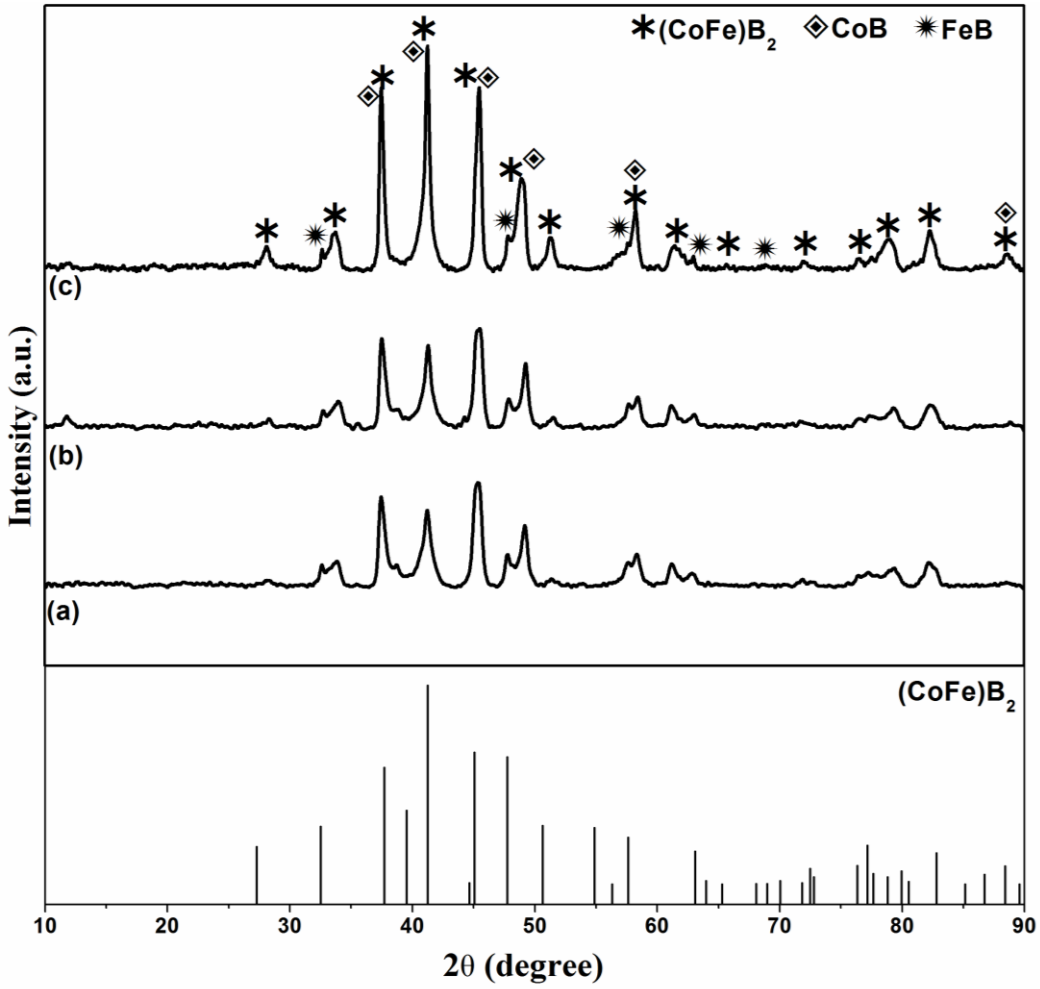
*(CoFe)B2 ◈CoB ✹FeB
(c)
(b)
(a)
Intensity (a.u.)
(CoFe)B2
10
20
30
40
50
60
70
80
90
2θ (degree)

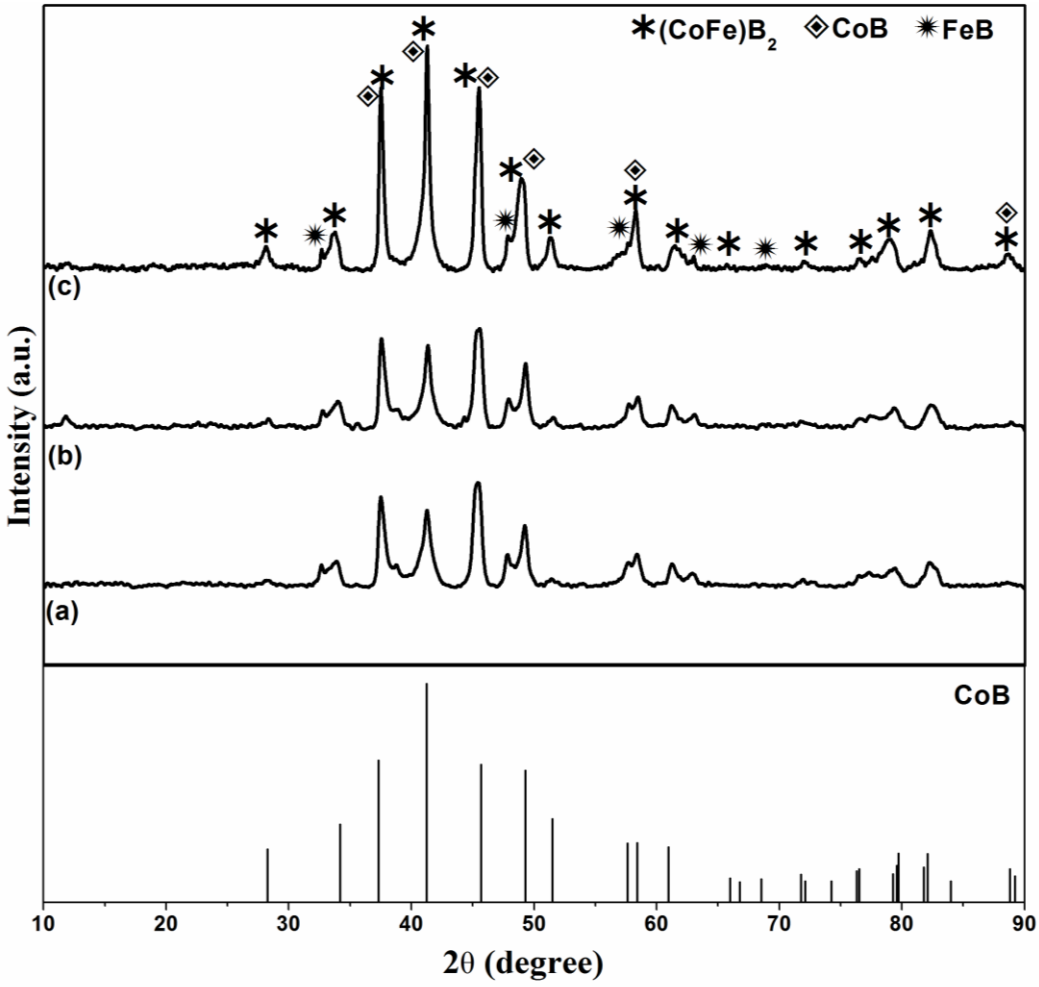
(CoFe)B2
CoB
FeB
(c)
(b)
(a)
Intensity (a.u.)
CoB
10
20
30
40
50
60
70
80
90
2θ (degree)

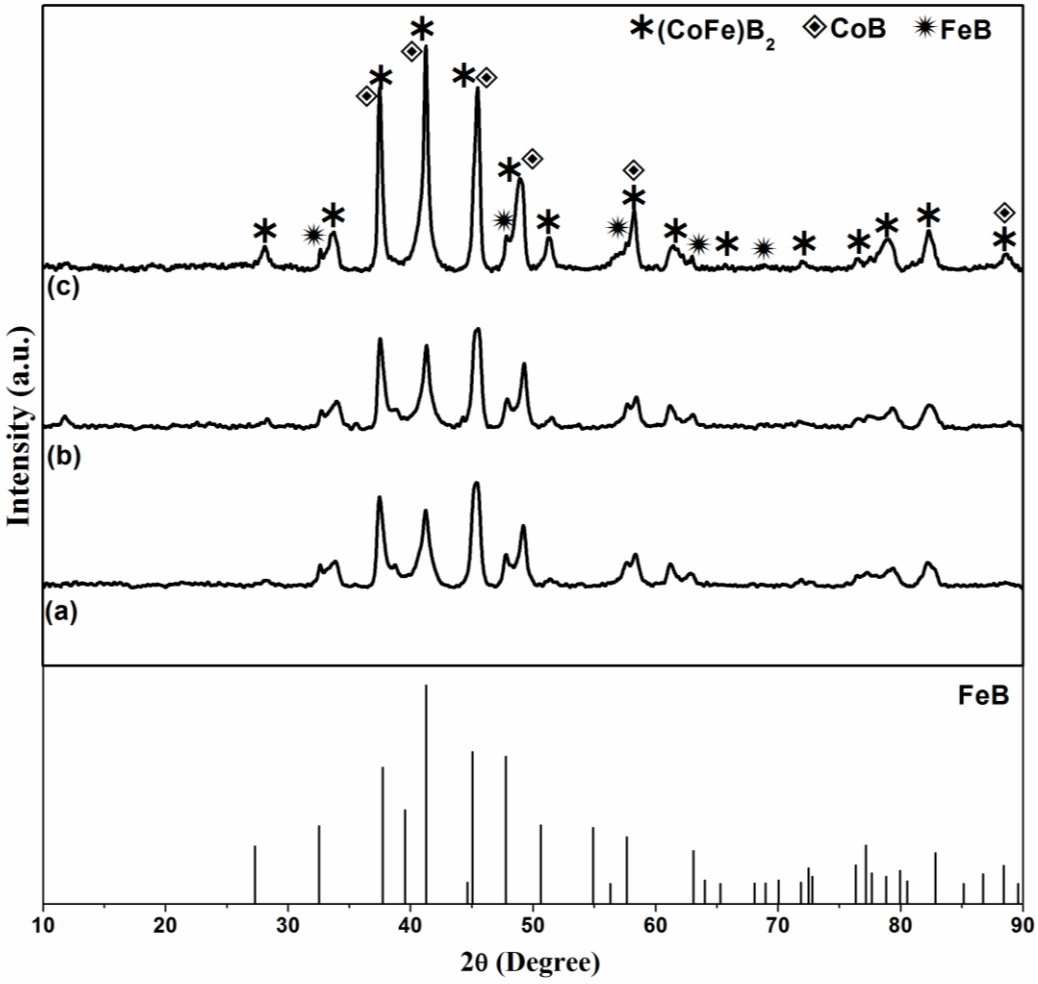

Figure A4. XRD patterns of the powders obtained from reaction of $CoCl_2$-$FeCl_3$-$NaBH_4$ (with eutectic salt mixture in the open system) at: (a) 650, (b) 750 and (c) 850 °C.

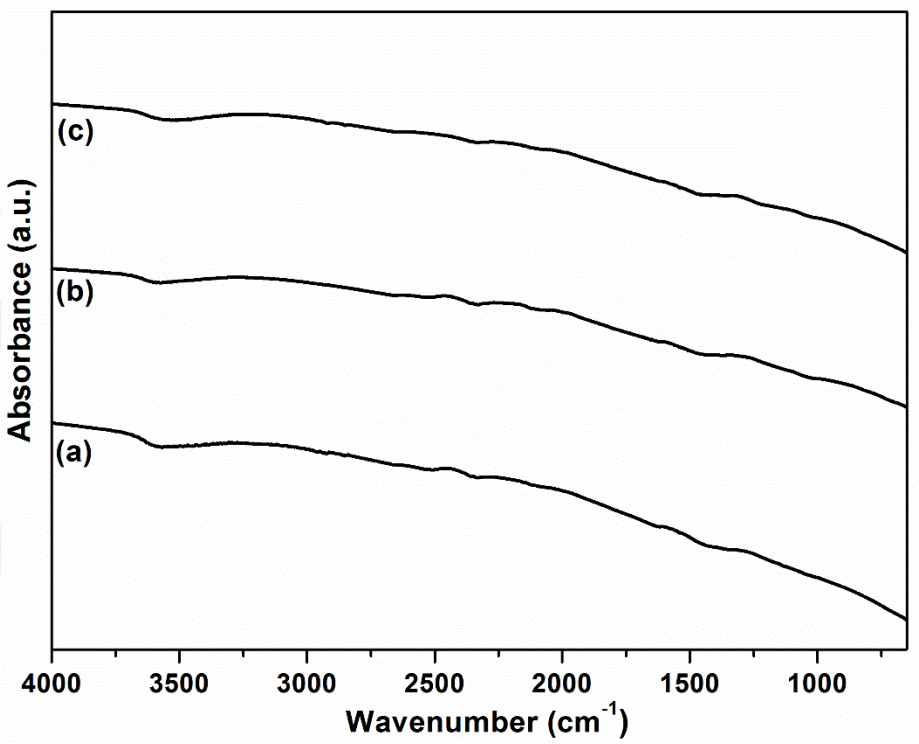

Figure A5. FTIR analysis of powders obtained by reaction of $CoCl_2$-$FeCl_3$-$NaBH_4$ (with eutectic salt mixture in the open system) at: (a) 650, (b) 750 and (c) 850 °C.

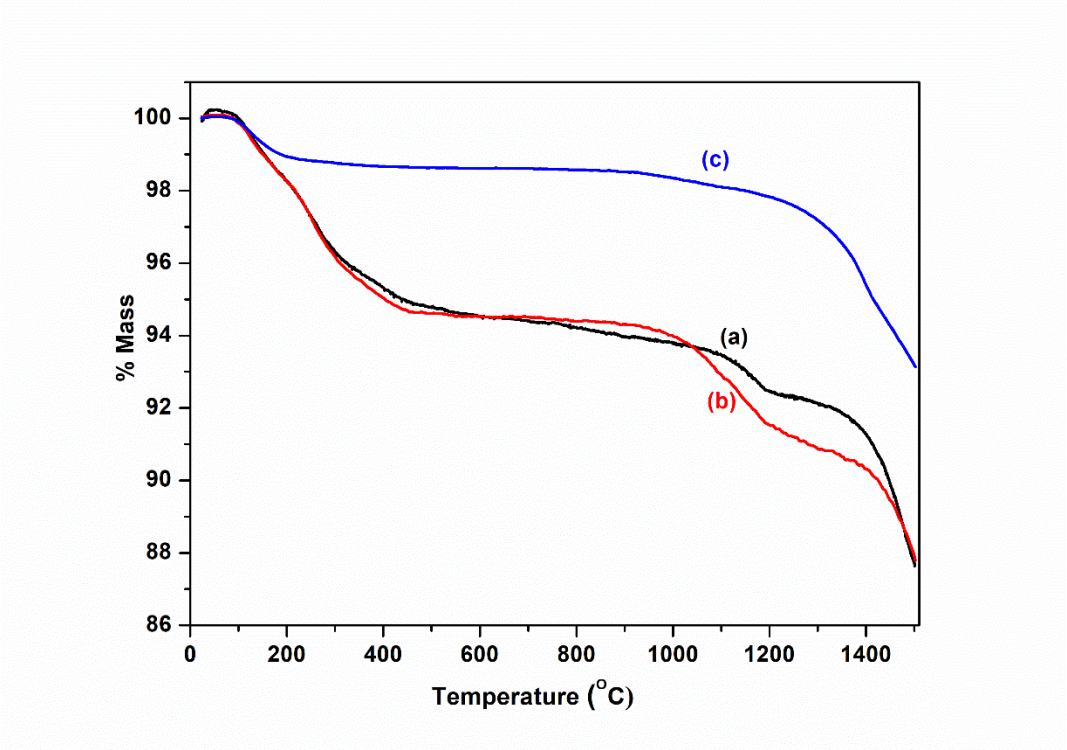

Figure A6. TG curves of powders obtained by reaction of $CoCl_2$-$FeCl_3$-$NaBH_4$ (with eutectic salt mixture in the open system) at: (a) 650, (b) 750 and (c) 850 °C.

B-Co

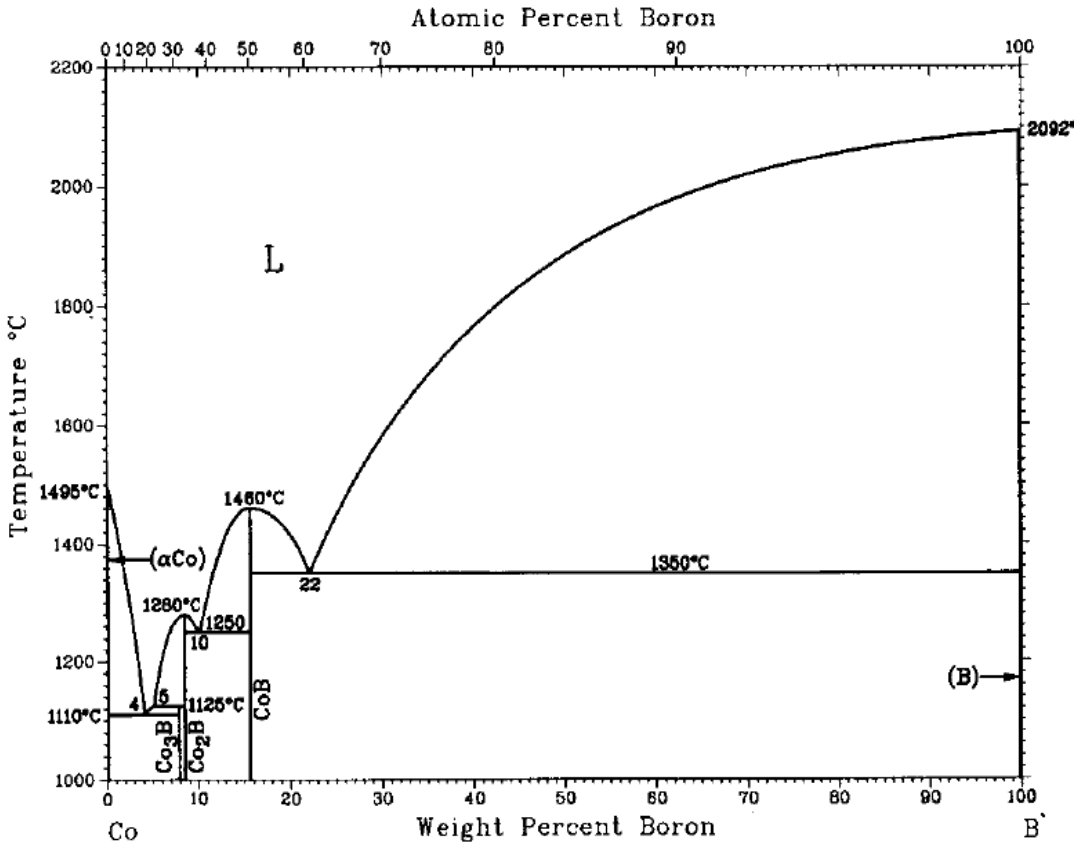
Atomic Percent Boron
0 10 20 30 40 50 60 70 80 90 100
2200
2000
1800
1600
1400
1200
1000
Temperature °C
L
2092°
1495°C
1460°C
(αCo)
1350°C
22
1280°C
1250
10
4
5
1125°C
1110°C
Co3B
Co2B
CoB
(B)
0 10 20 30 40 50 60 70 80 90 100
Co
Weight Percent Boron
B

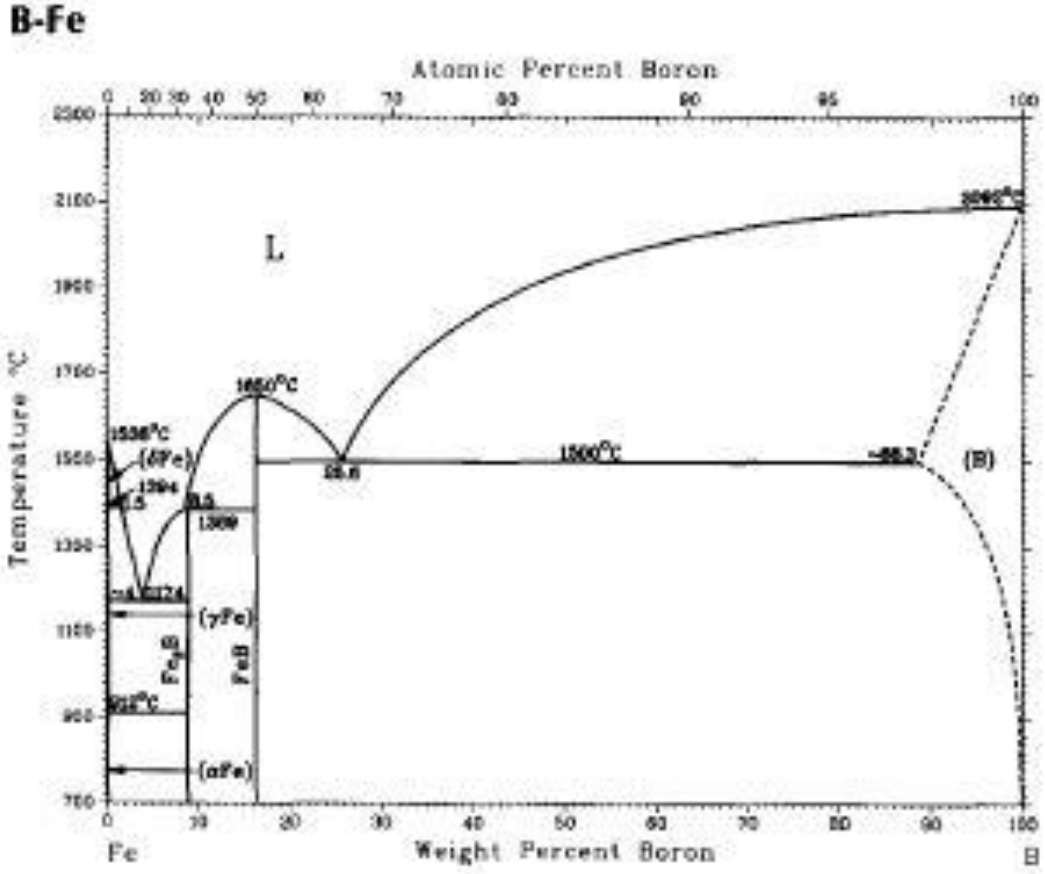
B-Fe
Atomic Percent Boron
Temperature °C
Weight Percent Boron
Fe
B
L
(δFe)
(γFe)
(αFe)
(B)
1665°C
1500°C
1389
1394
Fe2B
FeB

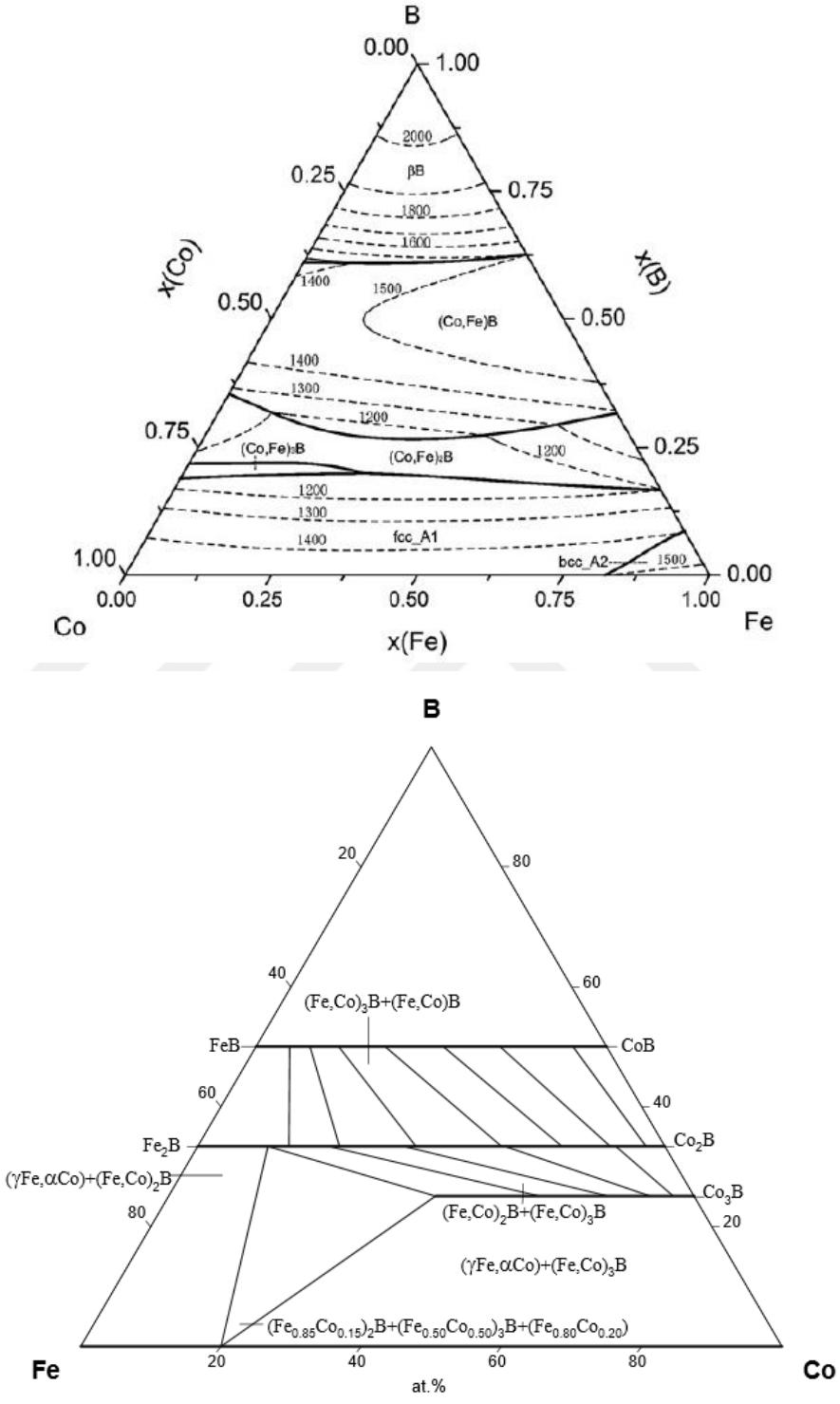

Figure A7. Binary and Ternary phase diagrams of Fe-B, Co-B and, Co-Fe-B (Top: different temperatures – Bottom: Isotherm at 1000 C).

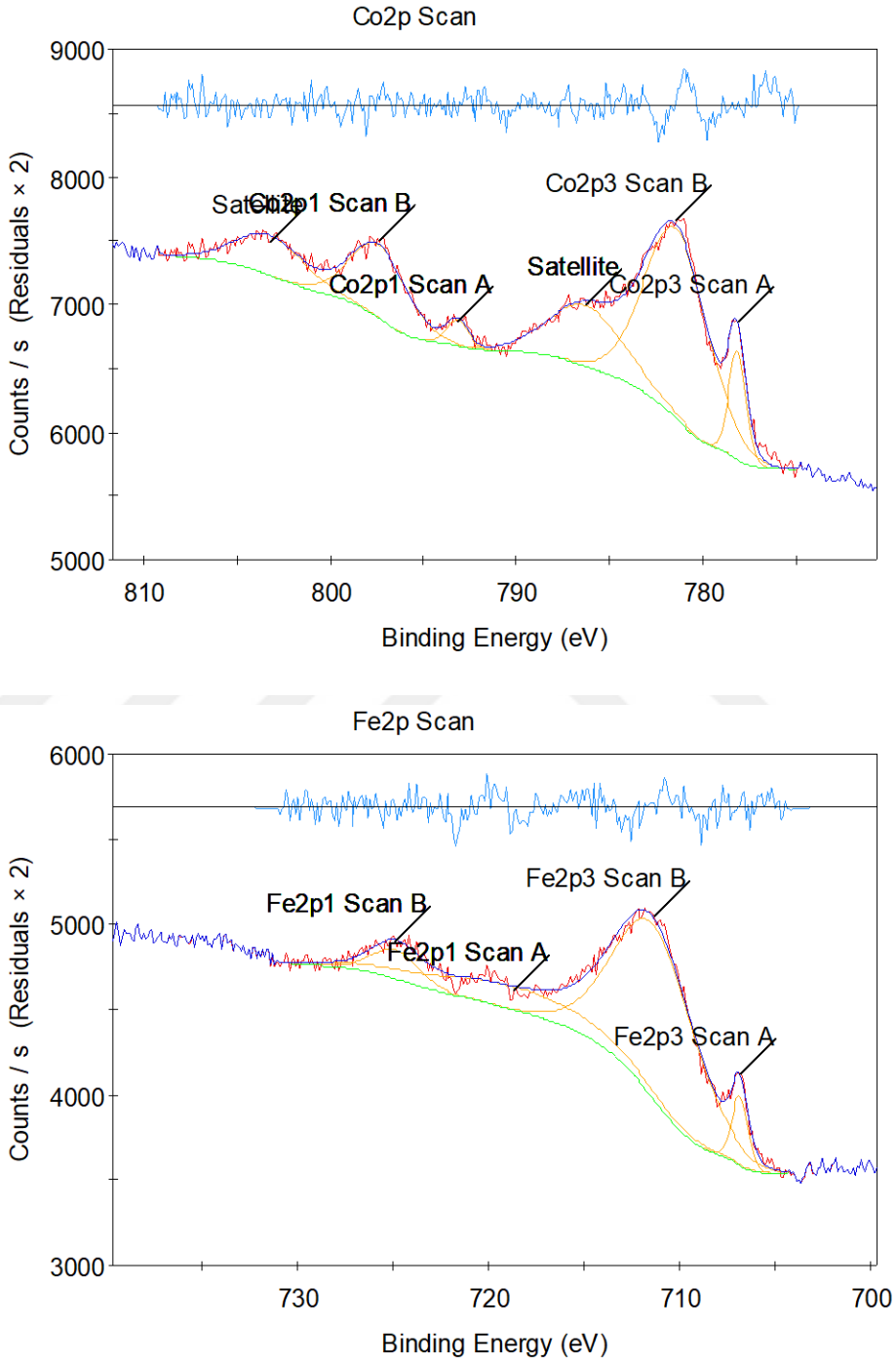

Figure A8. 2p regions for Fe and Co elements showing the Cobalt (II) and Iron (II) peaks at 780 and 712 eV, respectively.

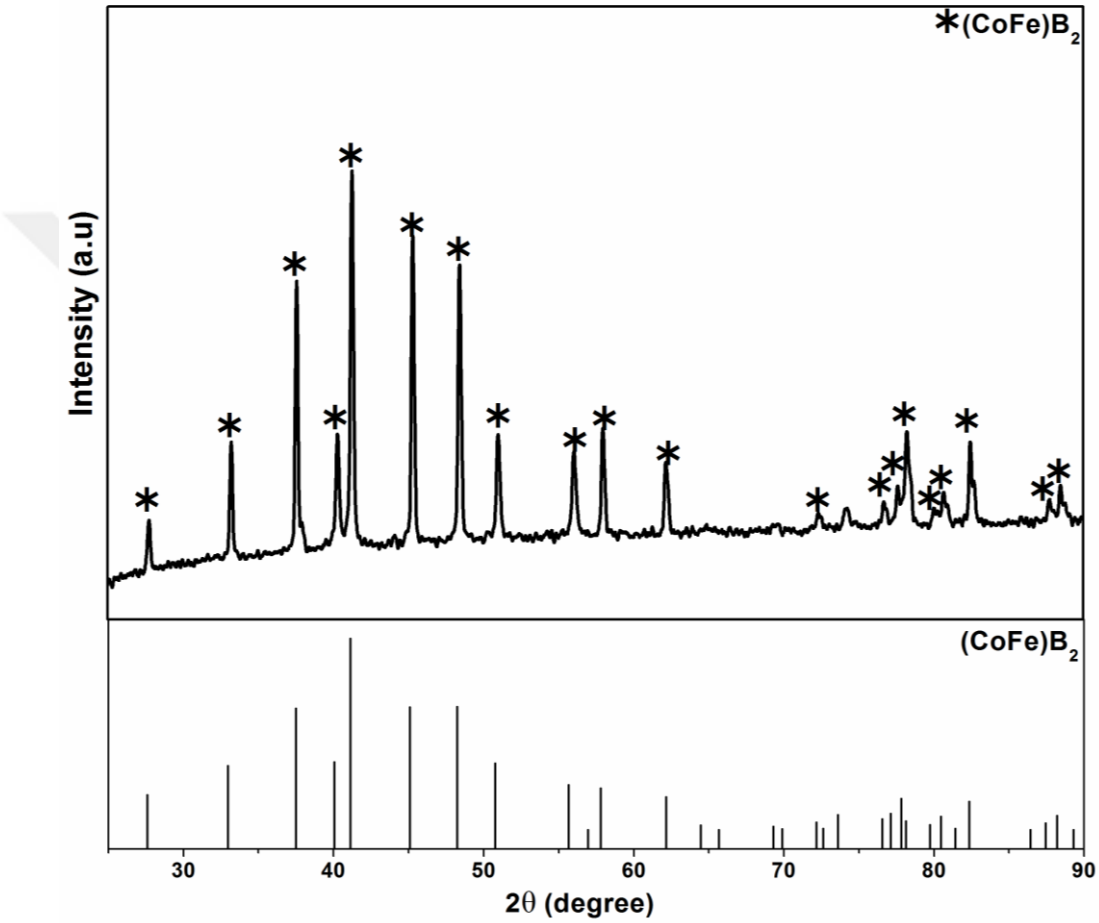

Figure A9. XRD pattern of the powders obtained by reaction of $CoCl_2$-$FeCl_3$-$NaBH_4$ (with eutectic salt mixture in open system at 850 °C) and annealed at 1100 °C.

Appendix B

Table B1. Theoretical and refined lattice parameters for the obtained phases both in open and closed system.

				a	b	c
Open System	1:1	Fe_3B Orthorhombic	Theoretical	5.43	6.69	4.43
			Refined	5.424(2)	6.699(3)	4.439(3)
		Co_2B Tetragonal	Theoretical	5.015		4.22
			Refined	5.017(1)		4.220(1)
	1:2	$(CoFe)B_2$ Orthorhombic	Theoretical	5.430	2.985	4.020
			Refined	5.436(2)	2.981(1)	4.025(2)
		(CoFe)B Tetragonal	Theoretical	5.09		4.24
			Refined	5.091 (3)		4.237 (1)
Close system	1:1	(CoFe)B Tetragonal	Theoretical	5.09		4.24
			Refined	5.100(2)		4.238(3)
		$Fe_{0.71}Co_{0.29}$ Cubic	Theoretical	2.86		
			Refined	2.864(2)		
		$Co_3B_7ClO_{13}$ Rhombohedral	Theoretical	8.54		20.96
			Refined	8.578(3)		20.973(2)
	1:2	(CoFe)B Tetragonal	Theoretical	5.09		4.24
			Refined	5.079(4)		4.227(2)
		$Fe_{0.71}Co_{0.29}$ Cubic	Theoretical	2.86		
			Refined	2.862(1)		
		$Fe_3B_7ClO_{13}$ Rhombohedral	Theoretical	8.623		21.050
			Refined	8.608(2)		20.999(2)

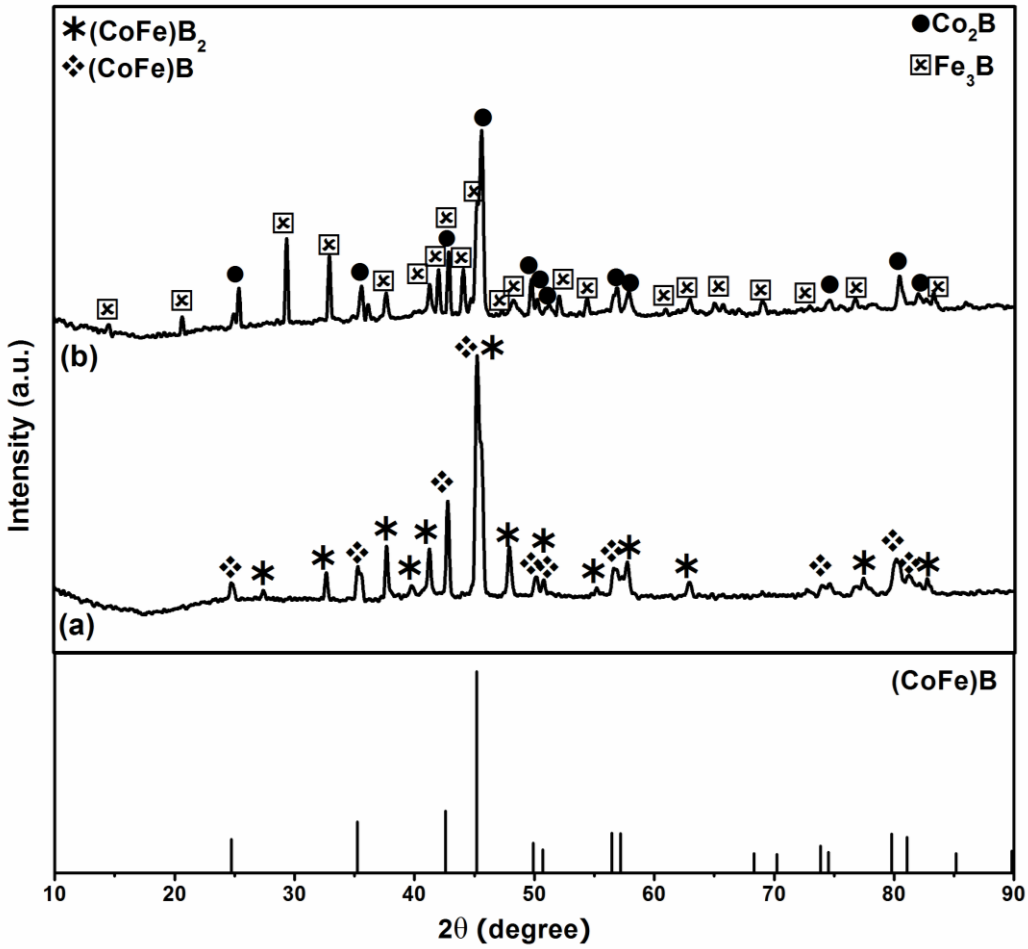
✱(CoFe)B2
❖(CoFe)B
●Co2B
⊠Fe3B
(b)
(a)
(CoFe)B
Intensity (a.u.)
10
20
30
40
50
60
70
80
90
2θ (degree)

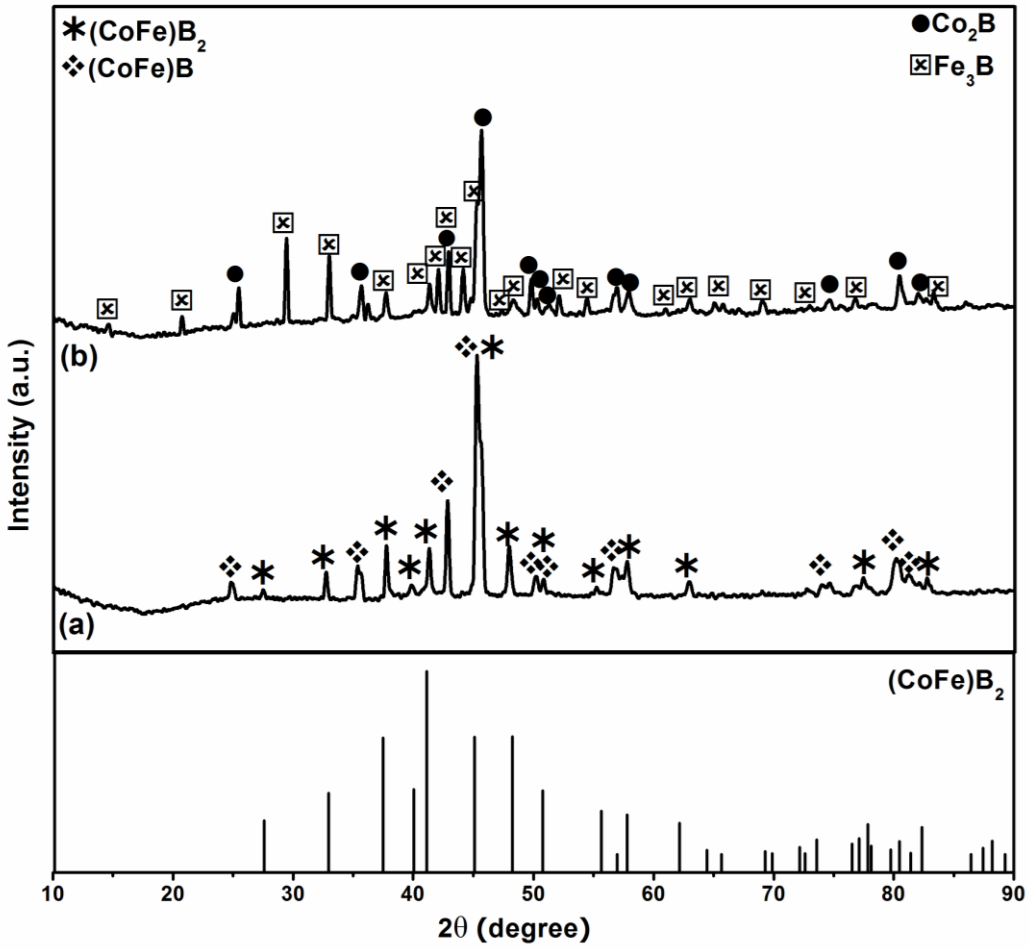
✱(CoFe)B2
❖(CoFe)B
●Co2B
⊠Fe3B
(b)
(a)
(CoFe)B2
Intensity (a.u.)
10
20
30
40
50
60
70
80
90
2θ (degree)

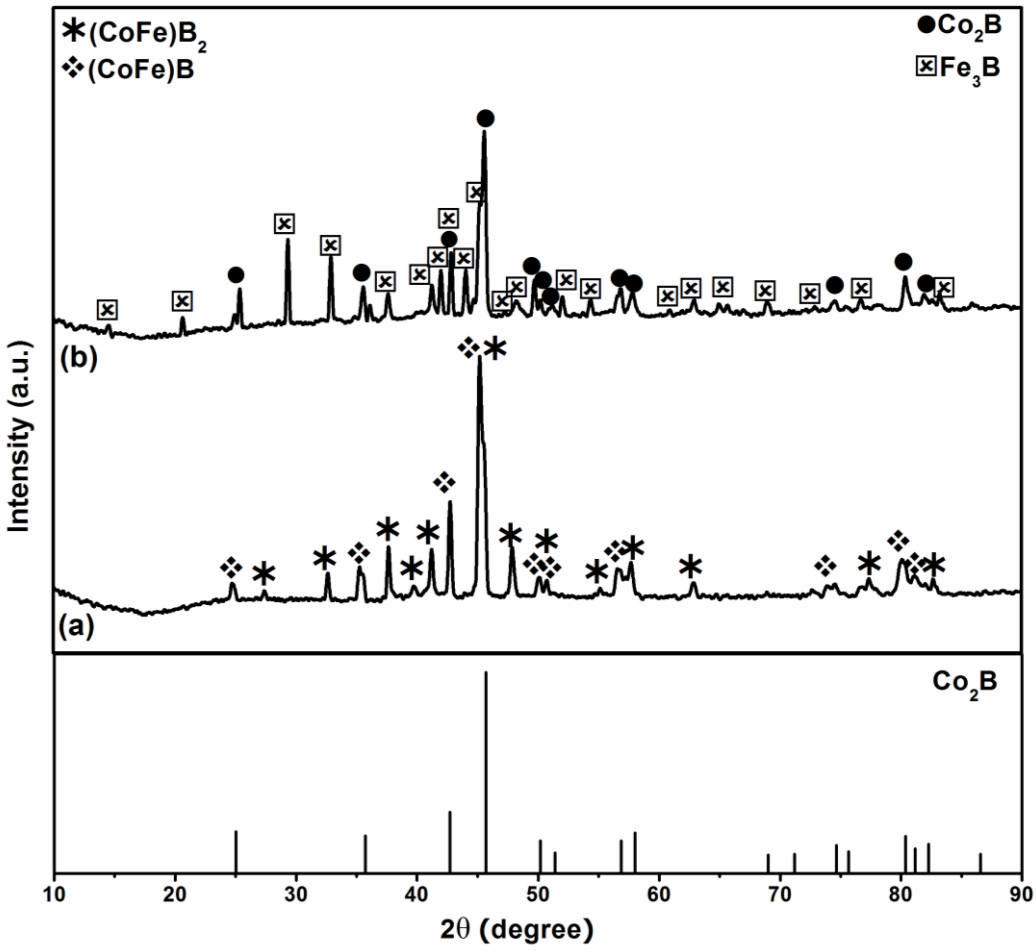
(CoFe)B2
(CoFe)B
Co2B
Fe3B
(b)
(a)
Co2B
Intensity (a.u.)
10
20
30
40
50
60
70
80
90
2θ (degree)

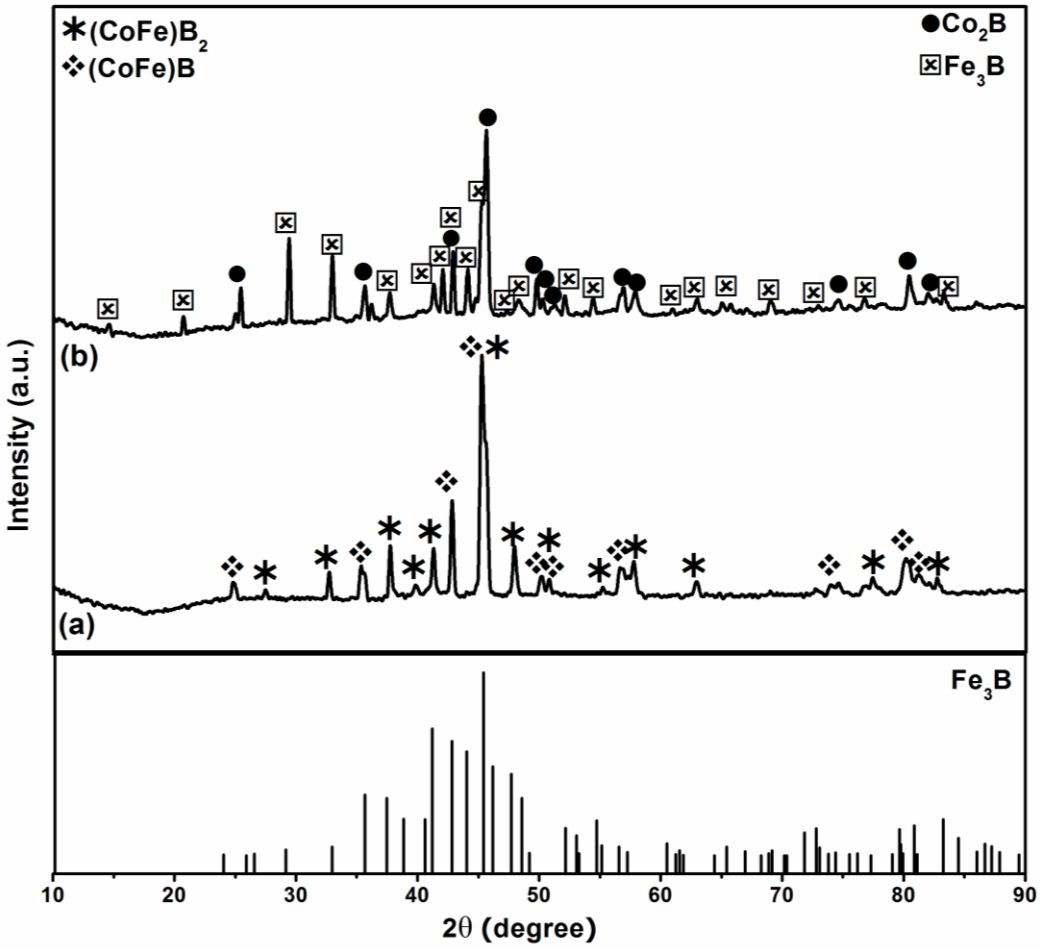

Figure B1. XRD patterns of the synthesized powders in the open system: (a) 1:2 and (b) 1:1 batch.

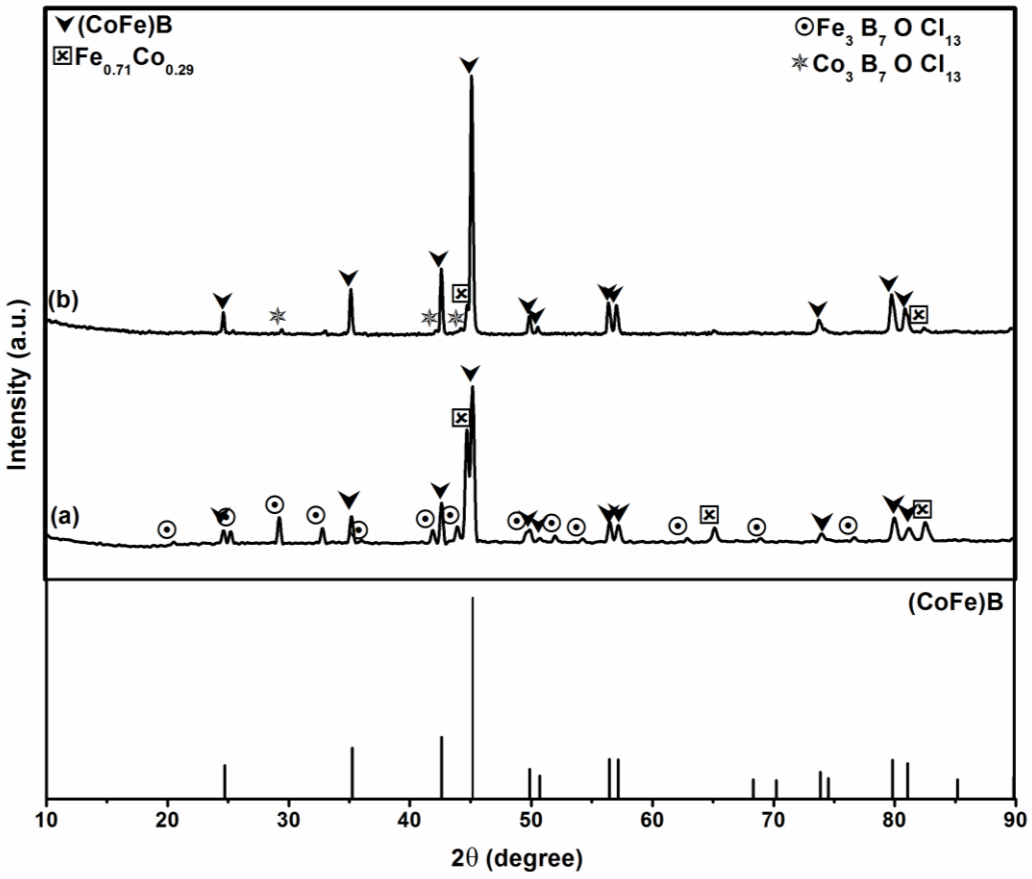
(CoFe)B
Fe0.71Co0.29
Fe3 B7 O Cl13
Co3 B7 O Cl13
(b)
(a)
(CoFe)B
Intensity (a.u.)
10
20
30
40
50
60
70
80
90
2θ (degree)

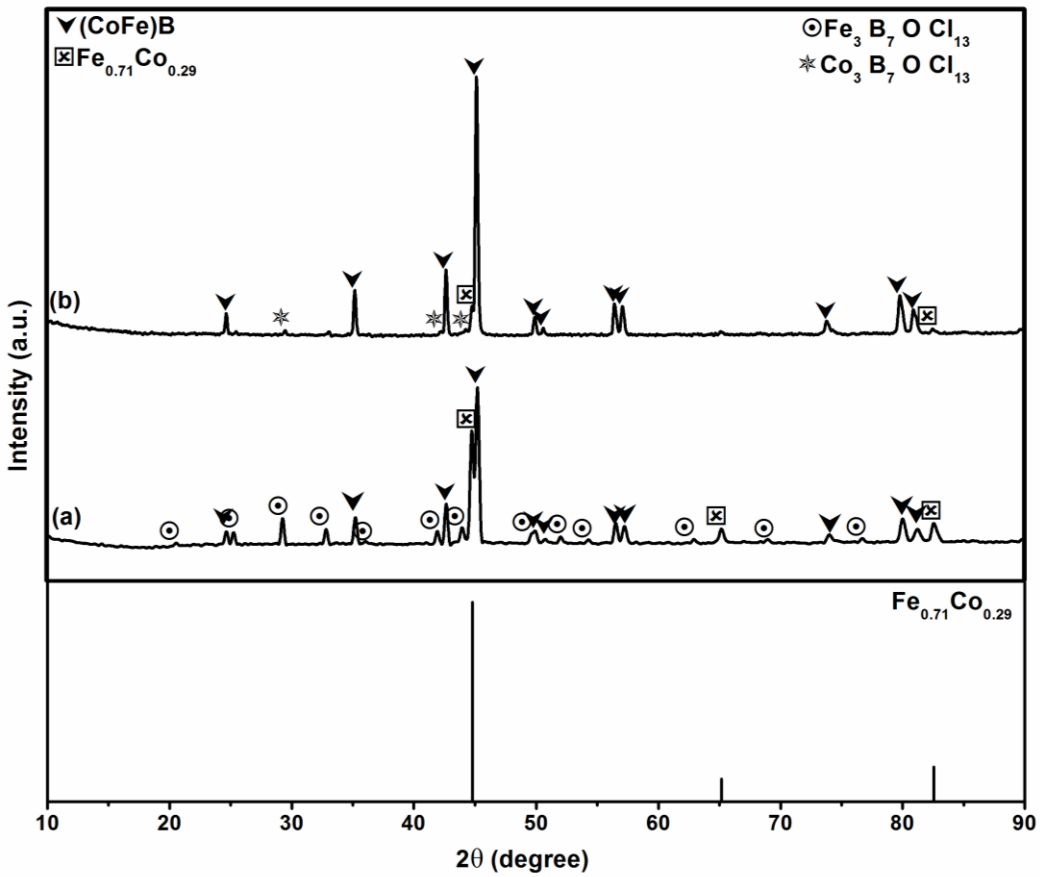
(CoFe)B
Fe0.71Co0.29
Fe3 B7 O Cl13
Co3 B7 O Cl13
(b)
(a)
Fe0.71Co0.29
Intensity (a.u.)
10
20
30
40
50
60
70
80
90
2θ (degree)

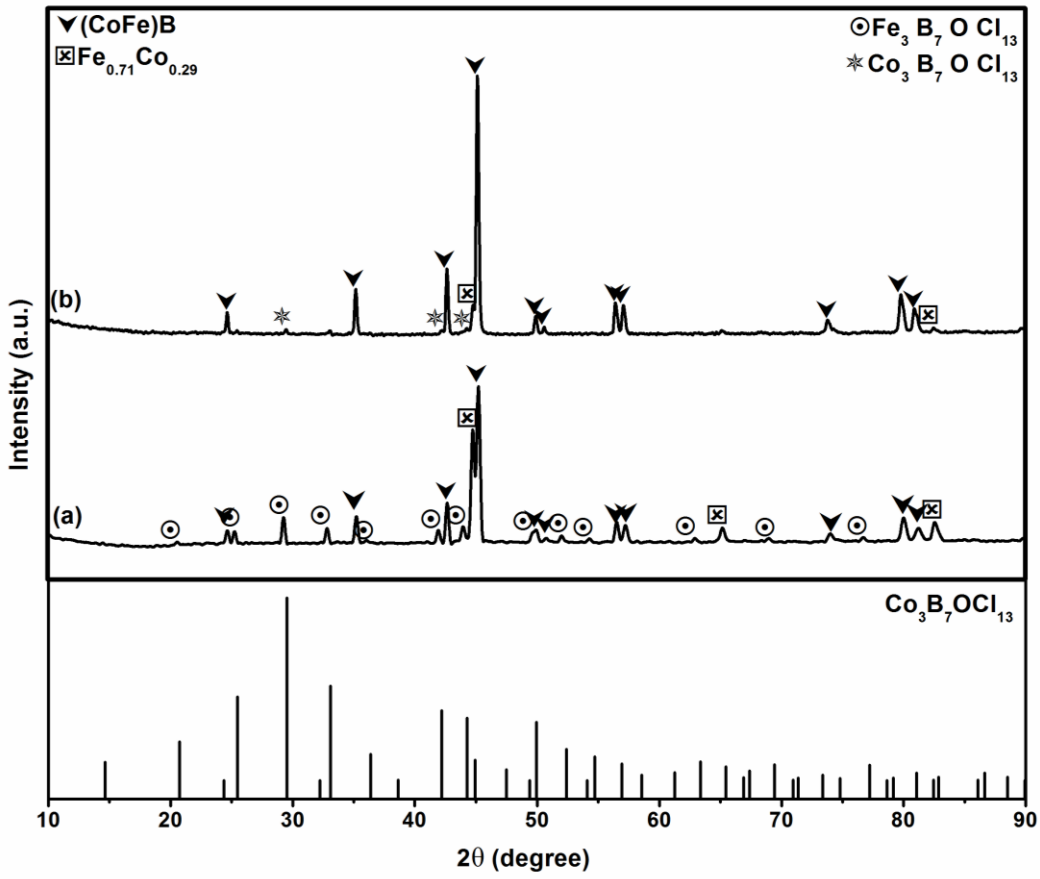
(CoFe)B
Fe0.71Co0.29
Fe3 B7 O Cl13
Co3 B7 O Cl13
(b)
(a)
Intensity (a.u.)
Co3B7OCl13
10
20
30
40
50
60
70
80
90
2θ (degree)

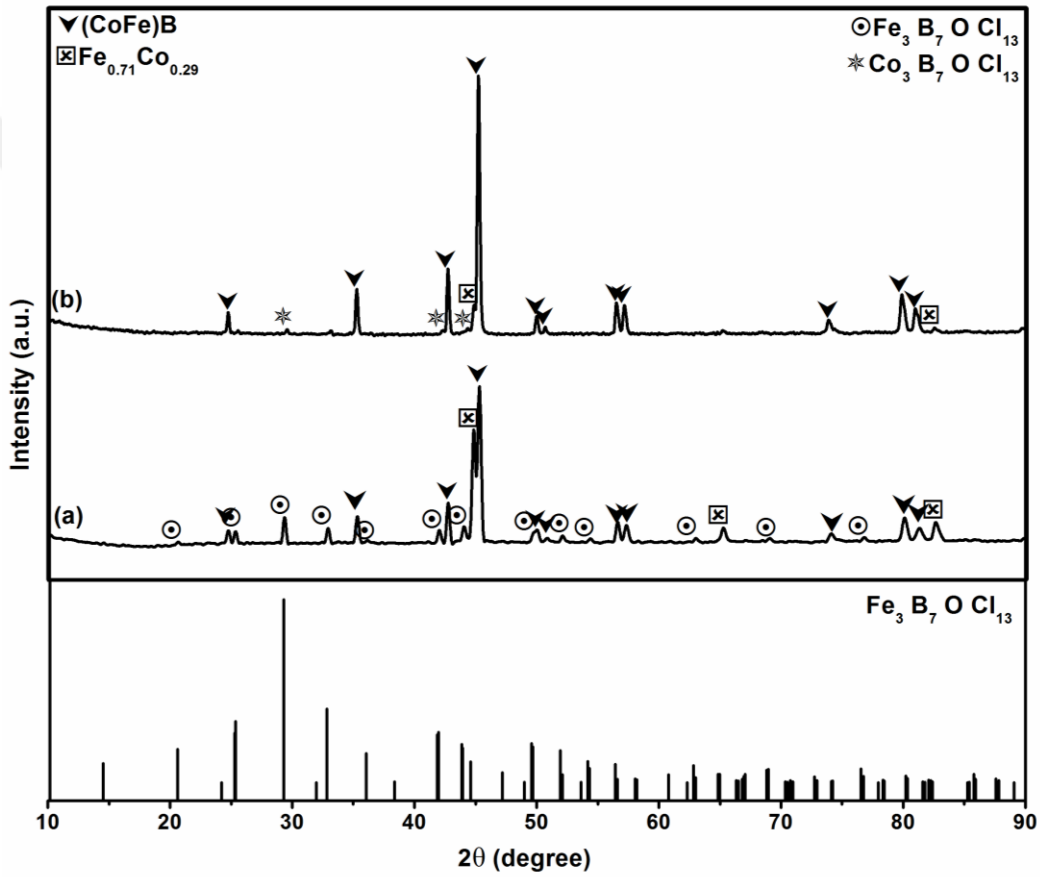

Figure B2. XRD patterns of the synthesized powders in the closed system: (a) 1:2 and (b) 1:1 batch.

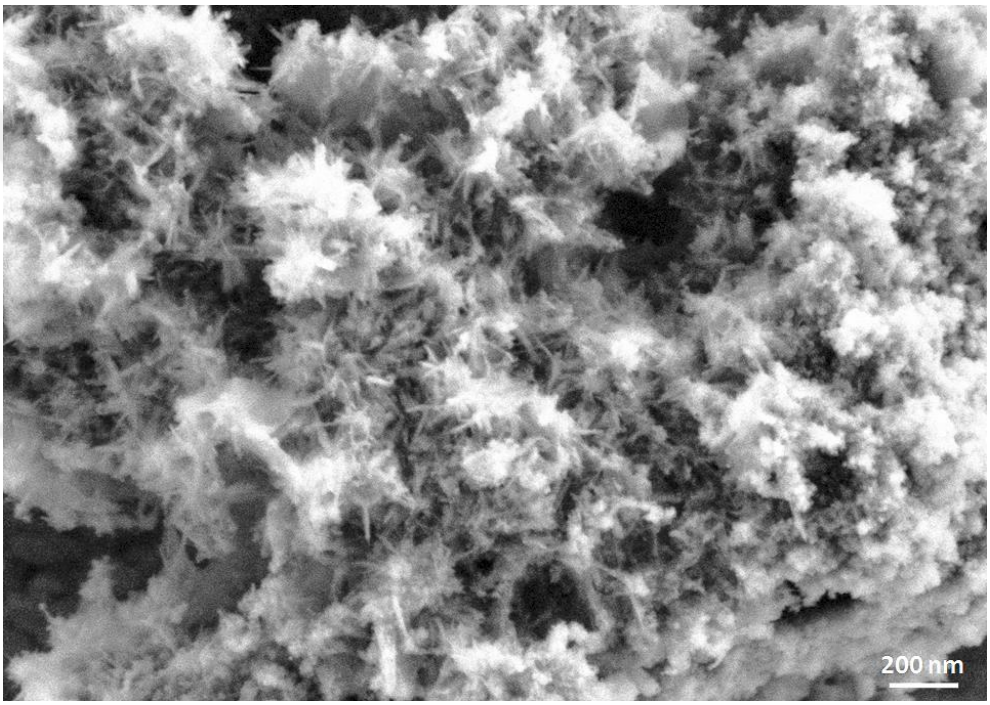

Figure B3. High magnification SEM image of the needle-shaped morphology of the 1:1 batch of the open system.

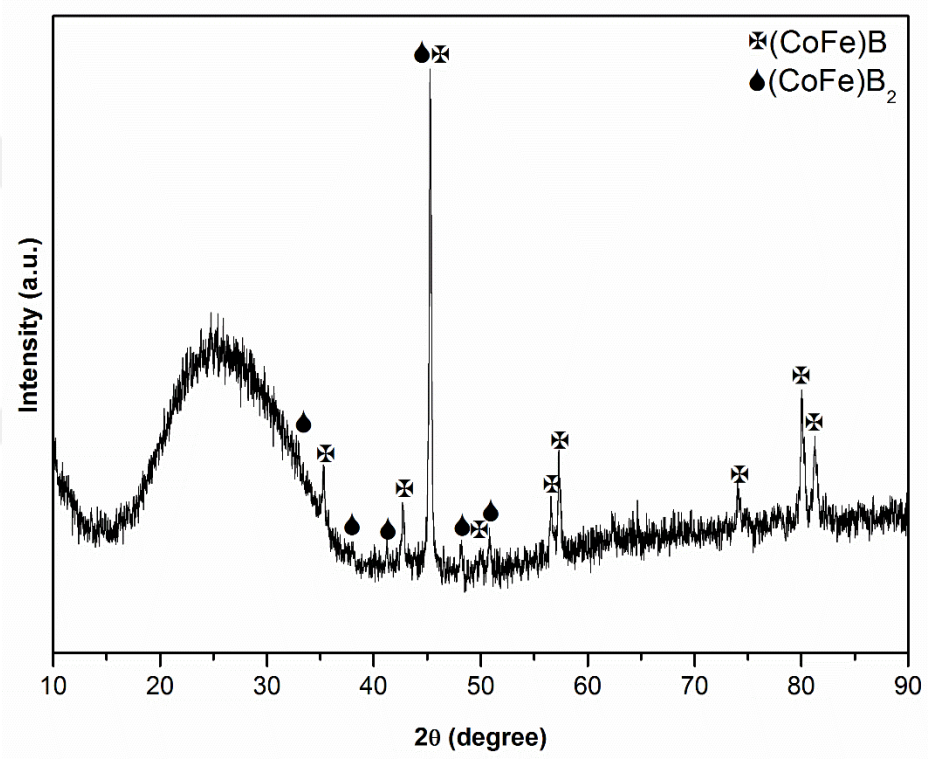

Figure B4. XRD pattern of the obtained powder from the 1:2 batch in the open system, after DTA.

Definition of the mathematical expected value:

In probability theory, the expected value of a random variable X, denoted E(X) or E[X], is a generalization of the weighted average, and is intuitively the arithmetic mean of a large number of independent realizations of X. The expected value is also known as the expectation, mathematical expectation, mean, average, or first moment. Expected value is also a key concept in economics, finance, and many other subjects.

By definition, the expected value of a constant random variable X=c is c. The expected value of a random variable X with equiprobable outcomes $\{c_1,\ldots,c_n\}$ is defined as the arithmetic mean of the terms c_i. If some of the probabilities P_r $(X=c_i)$ of an individual outcome c_i are unequal, then the expected value is defined to be the probability-weighted average of the c_i, that is, the sum of the n products c_i*P_r $(X = c_i)$.

Appendix C

Table C1. Comparison of various synthesis methods on the feasibility of the method (▪ is an indicator showing lowest amount of the discussed quality with ▪ and highest amount with ▪▪▪▪▪).

Method	***Reactant Price***	***Synthesis Condition Temp., etc.***	***Product Purity***	***Post Processing***	***Ref***
Arc Melting	▪▪▪▪▪	▪▪▪▪▪	▪▪▪▪▪	▪	[77,123,131,138,139]
Hot Pressing	▪▪▪▪▪	▪▪▪▪	▪▪	▪▪▪	[151]
Induction Furnace Melting	▪▪▪▪▪	▪▪▪▪▪	▪▪▪	▪▪	[152–154]
Spark Plasma Sintering (SPS)	▪▪▪▪▪	▪▪▪	▪▪▪▪	▪▪	[77,123,134,273]
Self-Propagating High Temperature Synthesis (SHS)	▪▪▪▪▪	▪	▪▪▪	▪▪▪	[161]
Carbothermal Reduction	▪▪▪	▪▪▪▪	▪▪	▪▪▪▪	[162]
Borocarbothermal Reduction	▪▪▪▪	▪▪▪	▪	▪▪▪▪▪	[163]
Boron Carbide Reduction	▪▪▪▪	▪▪▪▪	▪▪▪▪	▪▪	[166]
Borothermal Reduction	▪▪▪	▪▪▪	▪▪▪	▪▪▪	[163,164]
Chemical Vapor Deposition	▪▪▪▪	▪▪▪▪	▪▪▪▪▪	▪▪▪▪▪	[168,170,171]
Metallothermal Reduction	▪▪▪	▪▪▪	▪▪▪	▪▪▪▪	[166,167]
Low Temperature Synthesis	▪	▪▪	▪▪▪	▪▪▪	This work, [257]

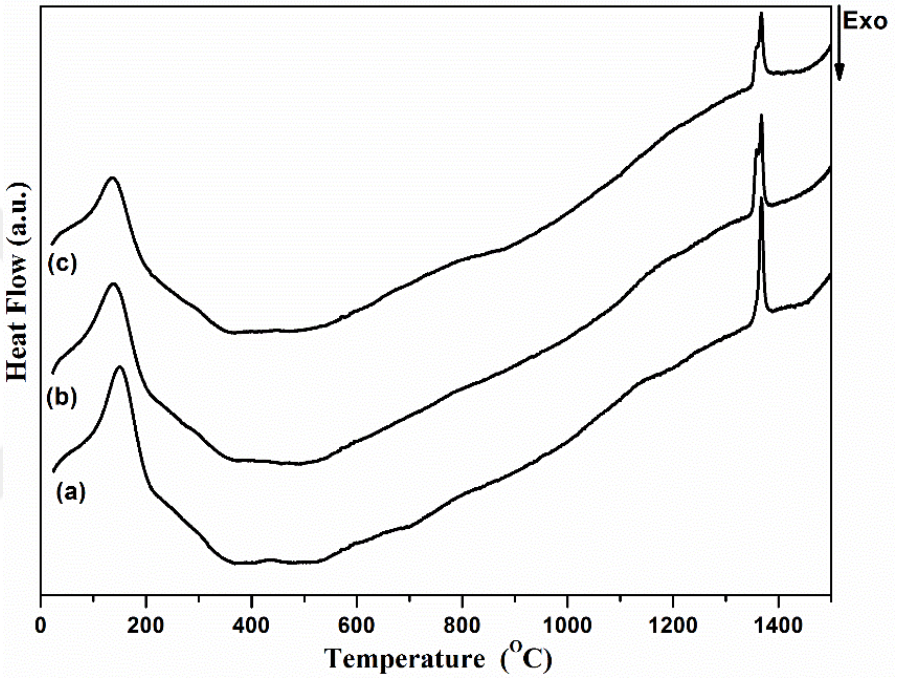

Figure C1. DTA curves of the powders obtained from reaction of $CoCl_2$-$TiCl_4$-$NaBH_4$ at 850 ˚C: (a) stoichiometric, (b) 50% excess $NaBH_4$ and (c) 50% excess $TiCl_4$.

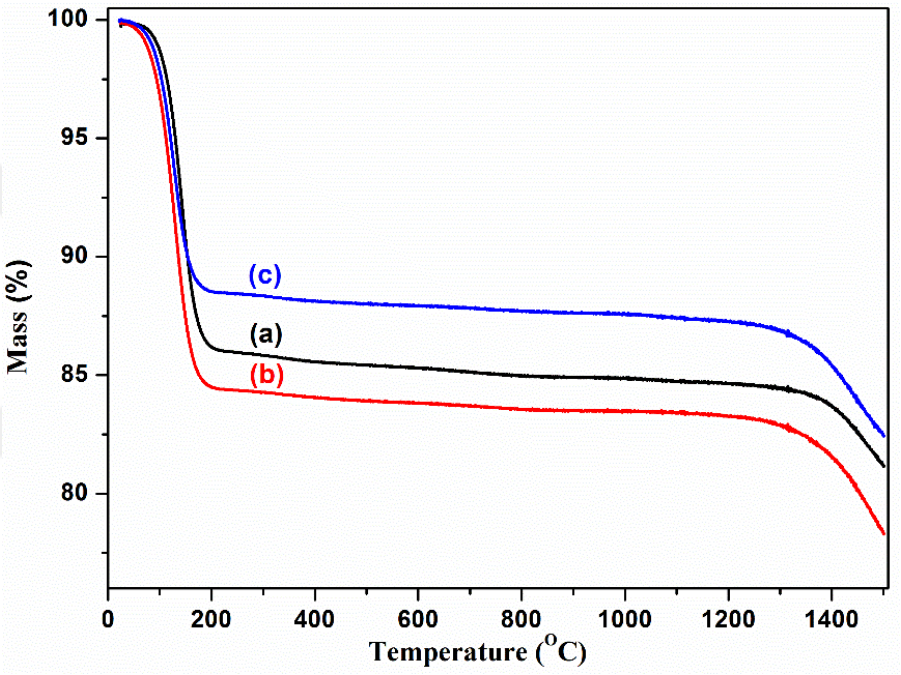

Figure C2. TG curves of the powders obtained from reaction of $CoCl_2$-$TiCl_4$-$NaBH_4$ at 850 ˚C: (a) stoichiometric, (b) 50% excess $NaBH_4$ and (c) 50% excess $TiCl_4$.

B-Co

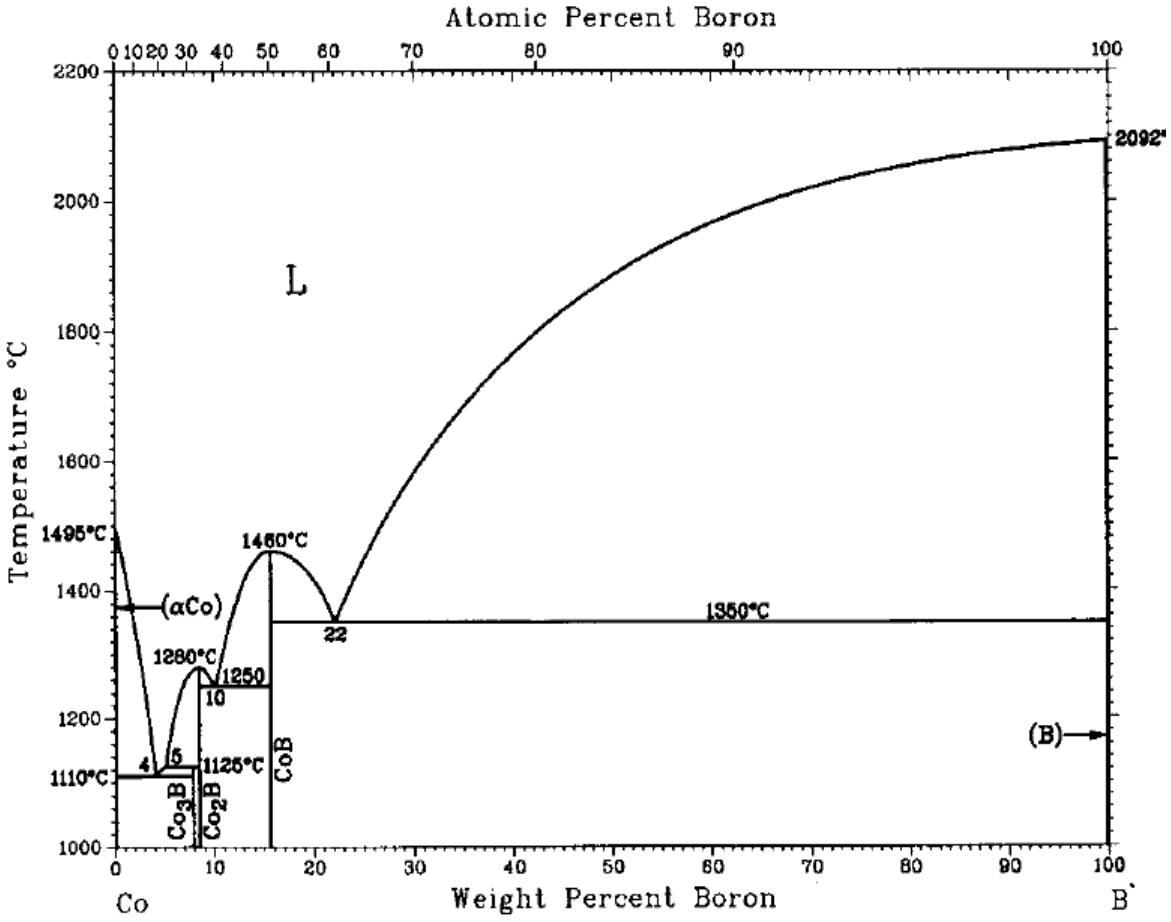
Atomic Percent Boron
0 10 20 30 40 50 60 70 80 90 100
2200
2000
1800
1600
1400
1200
1000
Temperature °C
L
2092°
1495°C
1460°C
(αCo)
1350°C
22
1280°C
1250
10
4
5
1126°C
1110°C
Co3B
Co2B
CoB
(B)
0 10 20 30 40 50 60 70 80 90 100
Co
Weight Percent Boron
B

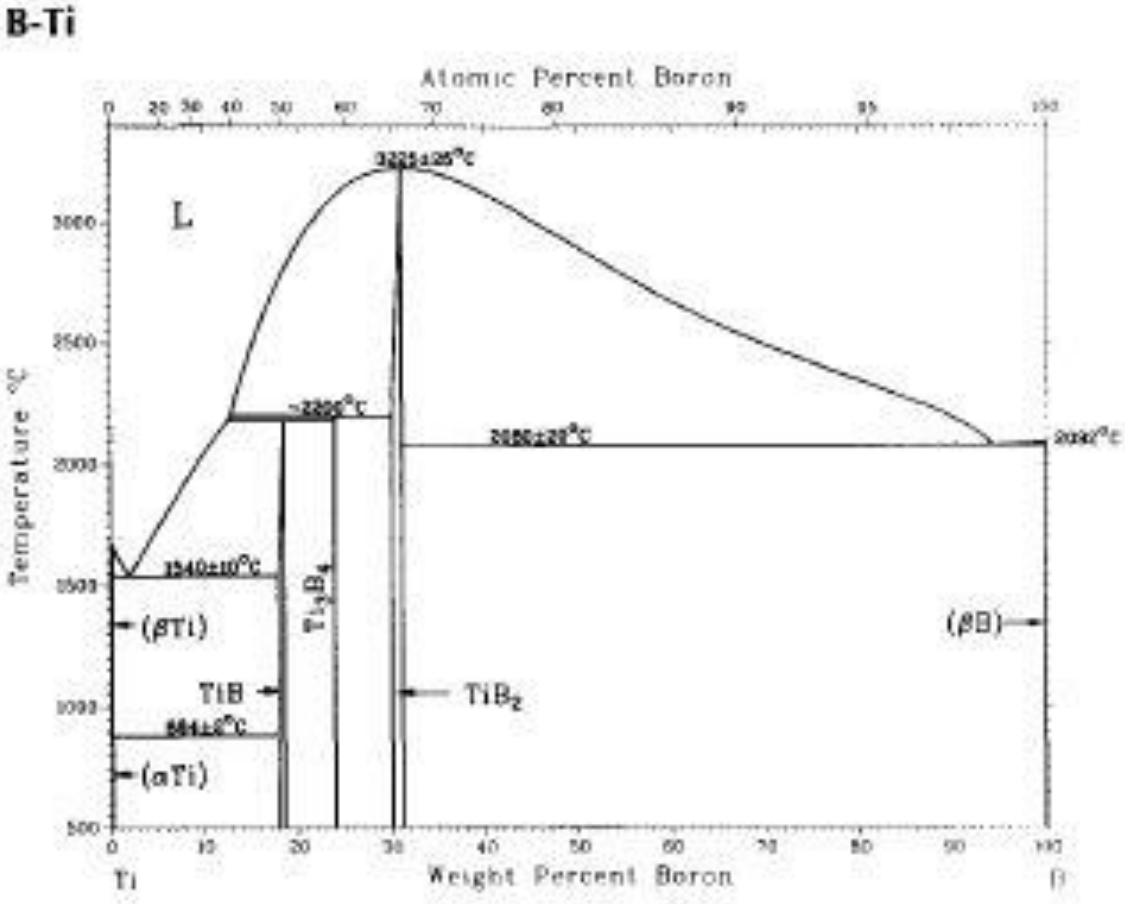

Figure C3. Binary phase diagrams of Co-B and Ti-B

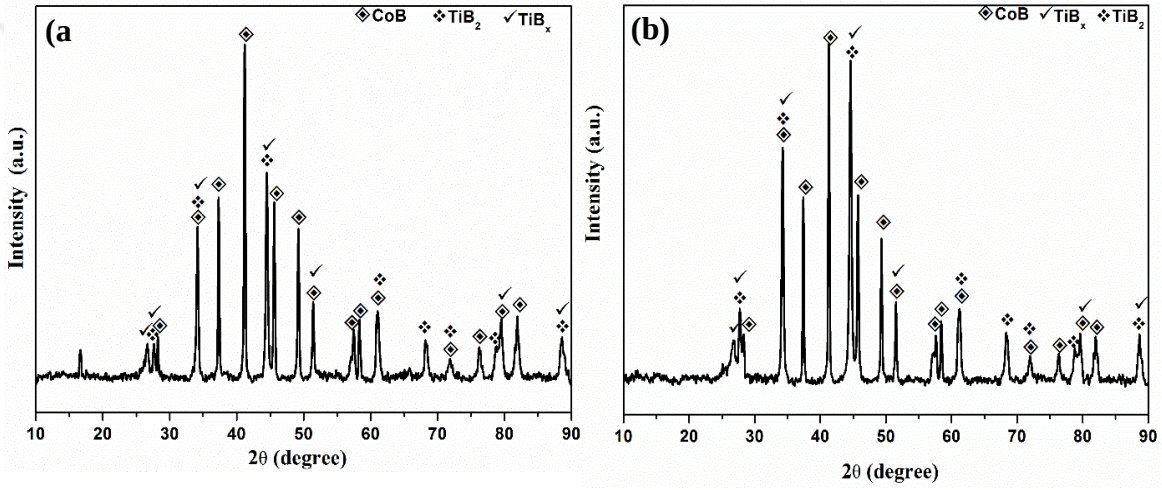

Figure C4. XRD patterns of powders after annealing at 1100 ˚C: (a) 50% excess $NaBH_4$ and (b) 50% excess $TiCl_4$ containing mixture.

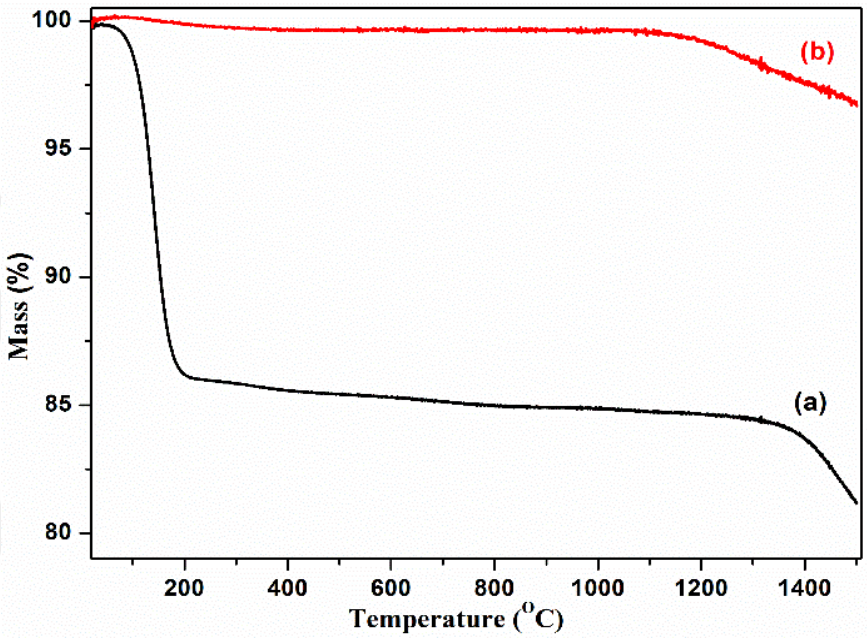

Figure C5. TG curves of the stoichiometric powders: (a) obtained at 850 ˚C and (b) after annealing at 1100 ˚C.

Table C2. Average particle size measurement of the different phases in the powders after annealing with comparison to the particle size distribution of the powders before annealing. (Powders obtained from the stoichiometric reaction of $CoCl_2$-$TiCl_4$-$NaBH_4$ and subsequent annealing).

Average particle size of TiB_2 phase after annealing	***Average particle size of CoB phase after annealing***	***Particle size distribution of the powders before annealing***
60 nm	450 nm	300 – 500 nm

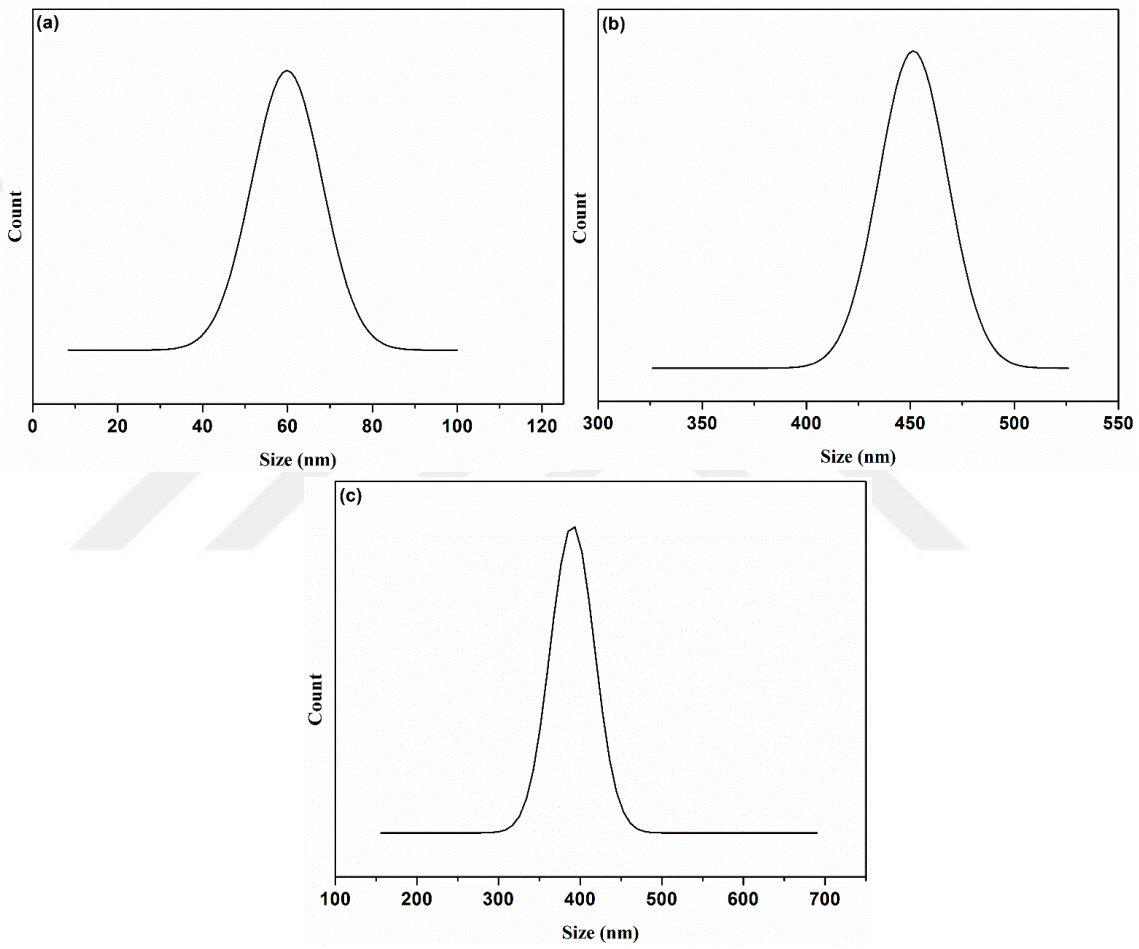

Figure C6. Average particle size distribution graphs for: (a) TiB_2 phase after annealing, (b) CoB phase after annealing and, (c) powders before annealing.

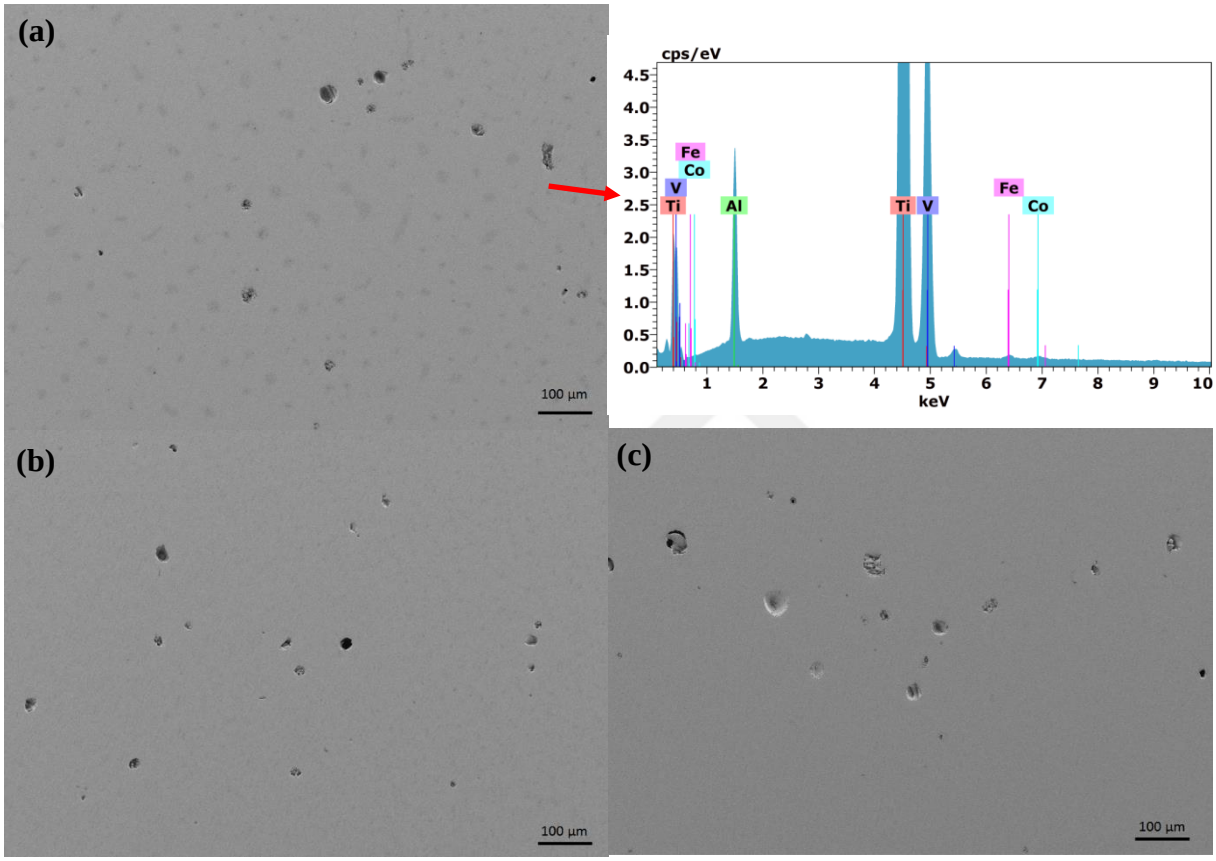

Figure C7. SEM analyses (Secondary electron images and EDS analysis) of the bulk SLM fabricated samples of Ti6Al4V matrix reinforced with a) Synthesized CoB-TiB_2 composite powder, b) Synthesized TiB_2 and c) CP-TiB_2.

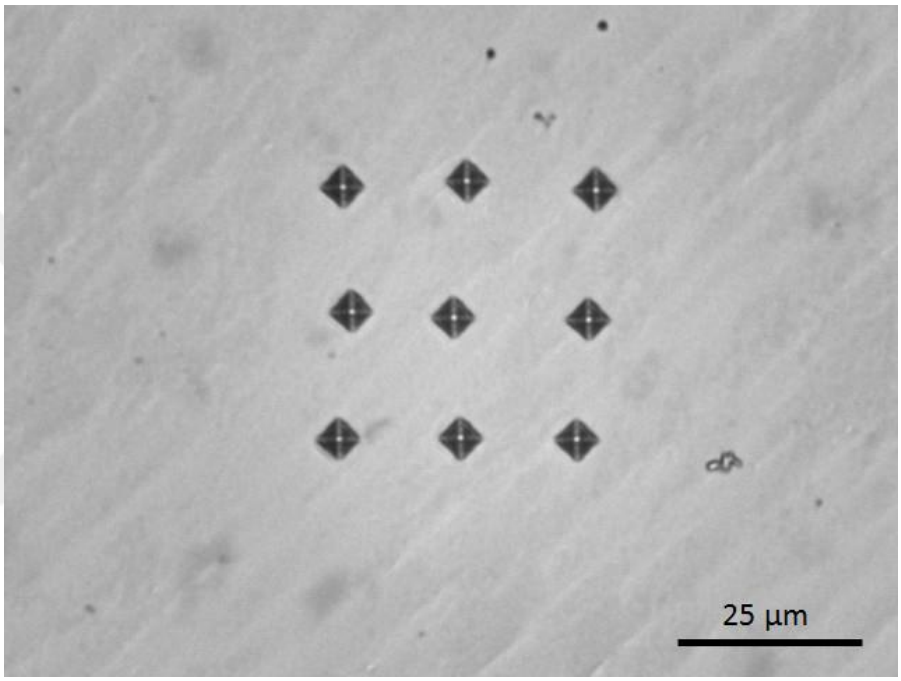

Figure C8. Indentation map carried out on the CoB-TiB_2 reinforced sample.

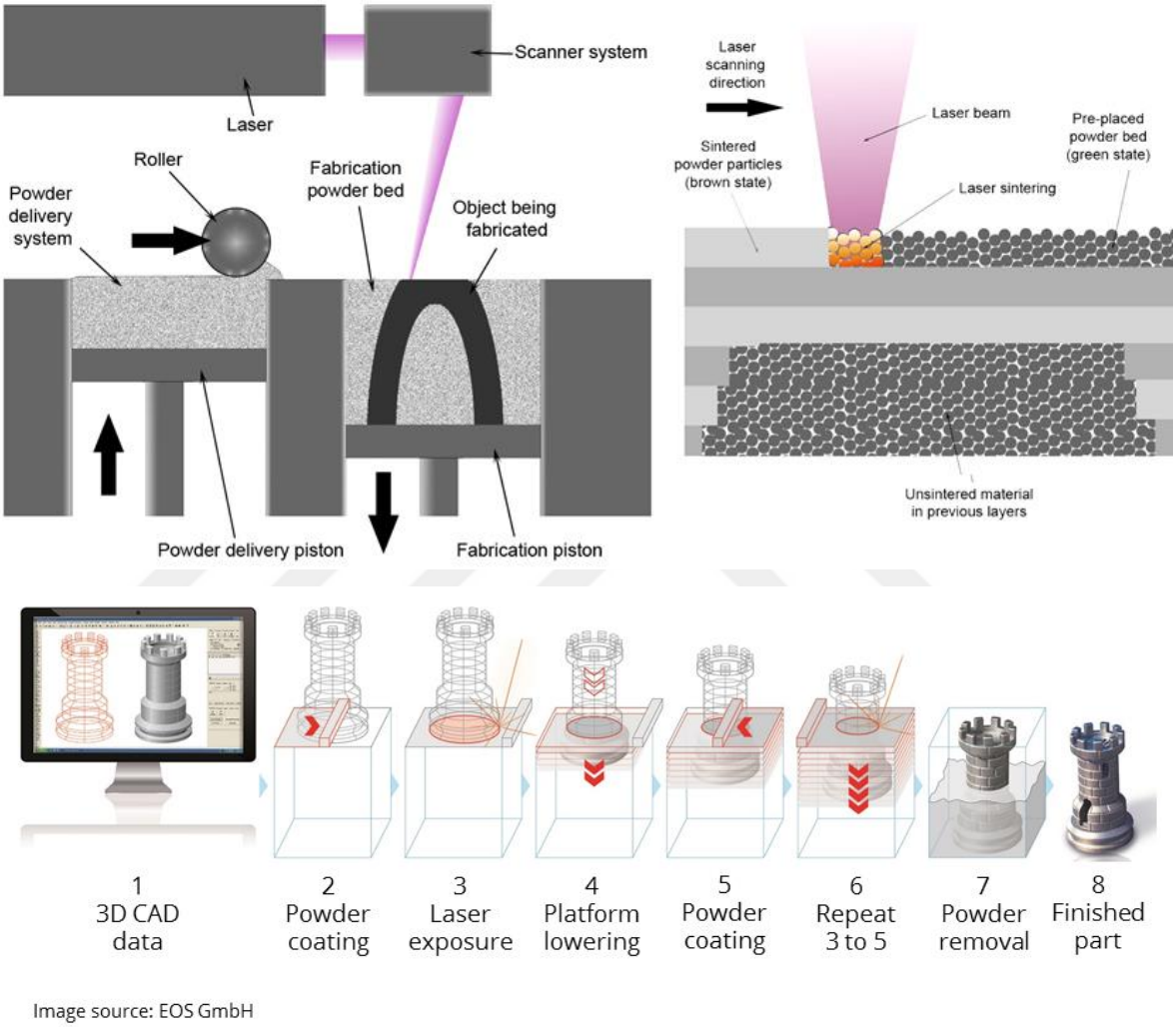

Figure C9. Schematic of the SLM procedure and sample fabrication steps.

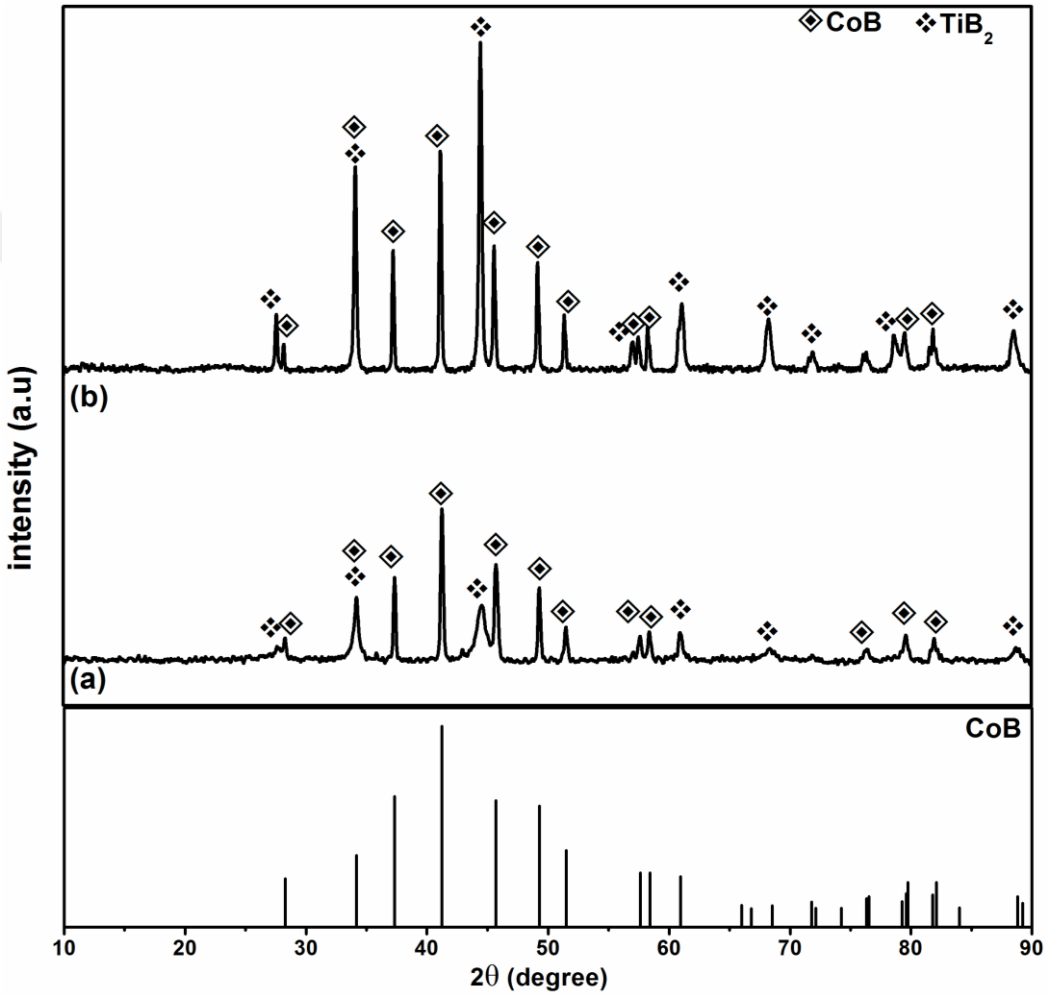
CoB
TiB2
(b)
(a)
CoB
intensity (a.u)
10
20
30
40
50
60
70
80
90
2θ (degree)

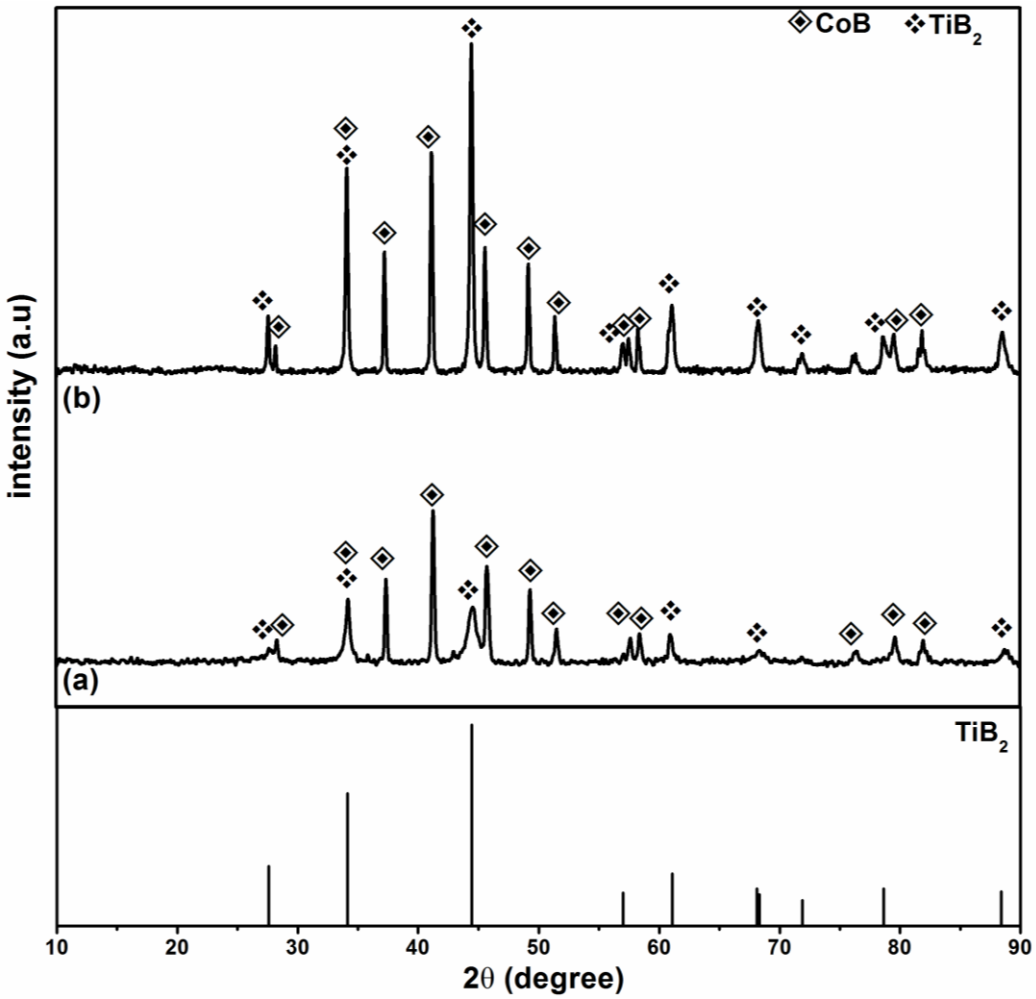

Figure C10. XRD patterns of the powders obtained from the stoichiometric reaction of $CoCl_2$-$TiCl_4$-$NaBH_4$: (a) obtained at 850 ˚C and (b) after annealing at 1100 ˚C.

References

[1] D.B. Sullenger, C.H.L. Kennard, Boron crystals, Sci. Am. 215 (1966) 96–107. https://www.scientificamerican.com/article/boron-crystals/.

[2] J. Nagamatsu, N. Nakagawa, T. Muranaka, Y. Zenitani, J. Akimitsu, Superconductivity at 39 K in magnesium diboride, Nature. 410 (2001) 63–64. doi:10.1038/35065039.

[3] H. Zhang, Q. Zhang, J. Tang, L.-C. Qin, Single-Crystalline LaB6 Nanowires, J. Am. Chem. Soc. 127 (2005) 2862–2863. doi:10.1021/ja043512c.

[4] L. Schlapbach, A. Züttel, Hydrogen-storage materials for mobile applications, Nature. 414 (2001) 353–358. doi:10.1038/35104634.

[5] A. Masago, K. Shirai, H. Katayama-Yoshida, Crystal stability of α- and β- boron, Phys. Rev. B. 73 (2006) 104102. doi:10.1103/PhysRevB.73.104102.

[6] M.J. van Setten, M.A. Uijttewaal, G.A. de Wijs, R.A. de Groot, Thermodynamic Stability of Boron: The Role of Defects and Zero Point Motion, J. Am. Chem. Soc. 129 (2007) 2458–2465. doi:10.1021/ja0631246.

[7] U. Wannagat, Holleman-Wiberg: Lehrbuch der Anorganischen Chemie. Begründet von A. F. Holleman, fortgesetzt von E. Wiberg. 91.–100. verbesserte und stark erweiterte Auflage von N. Wiberg. Walter de Gruyter, Berlin 1985. XXI, 1451 S., geb. DM 120.00. – ISBN 3-11-007511-, Angew. Chemie. 99 (1987) 604–605. doi:10.1002/ange.19870990634.

[8] A.R. Oganov, J. Chen, C. Gatti, Y. Ma, Y. Ma, C.W. Glass, Z. Liu, T. Yu, O.O. Kurakevych, V.L. Solozhenko, Ionic high-pressure form of elemental boron, Nature. 457 (2009) 863–867. doi:10.1038/nature07736.

[9] V.L. Solozhenko, O.O. Kurakevych, A.R. Oganov, On the hardness of a new boron phase, orthorhombic γ-B28, J. Superhard Mater. 30 (2008) 428–429.

doi:10.3103/S1063457608060117.

[10] J.L. Gay-Lussac, L.J. Thénard, Sur la décomposition et la recomposition de l'acide boracique, Ann. Chim. Phys. 68 (1808) 169–174.

[11] H. Moissan, Etude du bore amorphe, Ann. Chim. Phys. 6 (1895) 296–304.

[12] G.K. Gaule, W.F. Nye, J.A. Kohn, Boron: Synthesis, Structure, and Properties: Proceedings of the Conference on Boron, in: Conf. Boron, 1960: pp. 110–115.

[13] L. V McCarty, J.S. Kasper, F.H. Horn, B.F. Decker, A.E. Newkirk, A NEW CRYSTALLINE MODIFICATION OF BORON, J. Am. Chem. Soc. 80 (1958) 2592–2592. doi:10.1021/ja01543a066.

[14] E. Amberger, W. Dietze, Zur Bildung von α-rhomboedrischem, rotem Bor, Zeitschrift Für Anorg. Und Allg. Chemie. 332 (1964) 131–139. doi:10.1002/zaac.19643320304.

[15] H. Werheit, Die Halbleitereigenschften des Bors BT - Festkörperprobleme 10: Plenary Lectures of the Professional Groups "Semiconductor Physics", "Low Temperature Physics", "Thermodynamics", "Metal Physics" of the German Physical Society Freudenstadt, April 6–11, 197, in: O. Madelung (Ed.), Springer Berlin Heidelberg, Berlin, Heidelberg, 1970: pp. 189–226. doi:10.1007/BFb0108435.

[16] D.E. Sands, J.L. Hoard, RHOMBOHEDRAL ELEMENTAL BORON, J. Am. Chem. Soc. 79 (1957) 5582–5583. doi:10.1021/ja01577a072.

[17] F.H. Horn, Zone-Refined Boron, J. Appl. Phys. 30 (1959) 1612–1613. doi:10.1063/1.1735011.

[18] J.L. Hoard, S. Geller, R.E. Hughes, ON THE STRUCTURE OF ELEMENTARY BORON1, J. Am. Chem. Soc. 73 (1951) 1892–1893. doi:10.1021/ja01148a555.

[19] J.L. Hoard, R.E. Hughes, D.E. Sands, The Structure of Tetragonal Boron1, J. Am. Chem. Soc. 80 (1958) 4507–4515. doi:10.1021/ja01550a019.

[20] F. Liu, W.J. Liang, Z.J. Su, J.X. Xia, S.Z. Deng, J. Chen, J.C. She, N.S. Xu, J.F. Tian, C.M. Shen, H.-J. Gao, Fabrication and field emission properties of boron nanowire bundles, Ultramicroscopy. 109 (2009) 447–450. doi:https://doi.org/10.1016/j.ultramic.2008.12.010.

[21] W. Xing-Jun, T. Ji-Fa, B. Li-Hong, Y. Tian-Zhong, H. Chao, L. Fei, S. Cheng-Min, X. Ning-Sheng, G. Hong-Jun, Formation and photoluminescence properties of boron nanocones, Chinese Phys. B. 17 (2008) 3827–3835. doi:10.1088/1674-1056/17/10/048.

[22] W. Hayami, S. Otani, Surface Energy and Growth Mechanism of β-Tetragonal Boron Crystal, J. Phys. Chem. C. 111 (2007) 10394–10397. doi:10.1021/jp072594z.

[23] W. Hayami, S. Otani, The Role of Surface Energy in the Growth of Boron Crystals, J. Phys. Chem. C. 111 (2007) 688–692. doi:10.1021/jp065680s.

[24] D. Gabel, Bor-Neutroneneinfangtherapie von Tumoren, Chemie Unserer Zeit. 31 (1997) 235–240. doi:10.1002/ciuz.19970310505.

[25] D. Gabel, Y. Endo, Boron Clusters in Medical Applications, Mol. Clust. Main Gr. Elem. (2004) 95–125. doi:doi:10.1002/3527602445.ch2b.

[26] B. Albert, K. Hofmann, Metal Borides: Versatile Structures and Properties, in: Handb. Solid State Chem., Wiley-VCH Verlag GmbH & Co. KGaA, Weinheim, Germany, 2017: pp. 435–453. doi:10.1002/9783527691036.hsscvol1011.

[27] B. Albert, H. Hillebrecht, Boron: Elementary Challenge for Experimenters and Theoreticians, Angew. Chemie Int. Ed. 48 (2009) 8640–8668. doi:10.1002/anie.200903246.

[28] M. Ade, D. Kotzott, H. Hillebrecht, Synthesis and crystal structures of the new metal-rich ternary borides Ni12AlB8, Ni12GaB8 and Ni 10.6Ga0.4B6-examples for the first B 5 zig-zag chain fragment, J. Solid State Chem. 183 (2010) 1790–1797. doi:10.1016/j.jssc.2010.05.009.

[29] B.P.T. Fokwa, Transition-Metal-Rich Borides – Fascinating Crystal Structures and Magnetic Properties, Eur. J. Inorg. Chem. 2010 (2010) 3075–3092. doi:10.1002/ejic.201000116.

[30] M. Tillard, C. Belin, New Nickel Gallium Boride, B14Ga3Ni27: Synthesis and Crystal Structure, Inorg. Chem. 50 (2011) 3907–3912. doi:10.1021/ic102212n.

[31] Z.P. Malik, O. Sologub, A. Grytsiv, G. Giester, P.F. Rogl, Crystal Structure of Novel

Ni–Zn Borides: First Observation of a Boron–Metal Nested Cage Unit: B20Ni6, Inorg. Chem. 50 (2011) 7669–7675. doi:10.1021/ic2007167.

[32] D. Portehault, S. Devi, P. Beaunier, C. Gervais, C. Giordano, C. Sanchez, M. Antonietti, A general solution route toward metal boride nanocrystals, Angew. Chemie - Int. Ed. 50 (2011) 3262–3265. doi:10.1002/anie.201006810.

[33] Z.L. Schaefer, X. Ke, P. Schiffer, R.E. Schaak, Direct Solution Synthesis, Reaction Pathway Studies, and Structural Characterization of Crystalline Ni3B Nanoparticles, J. Phys. Chem. C. 112 (2008) 19846–19851. doi:10.1021/jp8082503.

[34] J. Ma, Y. Gu, L. Shi, L. Chen, Z. Yang, Y. Qian, Reduction–boronation route to chromium boride (CrB) nanorods, Chem. Phys. Lett. 381 (2003) 194–198. doi:https://doi.org/10.1016/j.cplett.2003.09.128.

[35] J. Ma, Y. Du, M. Wu, G. Li, Z. Feng, M. Guo, Y. Sun, W. Song, M. Lin, X. Guo, A simple inorganic-solvent-thermal route to nanocrystalline niobium diboride, J. Alloys Compd. 468 (2009) 473–476. doi:https://doi.org/10.1016/j.jallcom.2008.01.021.

[36] Y. Gu, Y. Qian, L. Chen, F. Zhou, A mild solvothermal route to nanocrystalline titanium diboride, J. Alloys Compd. 352 (2003) 325–327. doi:https://doi.org/10.1016/S0925-8388(02)01173-8.

[37] J.W. Kim, J.-H. Shim, J.-P. Ahn, Y.W. Cho, J.-H. Kim, K.H. Oh, Mechanochemical synthesis and characterization of TiB2 and VB2 nanopowders, Mater. Lett. 62 (2008) 2461–2464. doi:https://doi.org/10.1016/j.matlet.2007.12.022.

[38] V.G. Pol, S. V Pol, A. Gedanken, Dry Autoclaving for the Nanofabrication of Sulfides, Selenides, Borides, Phosphides, Nitrides, Carbides, and Oxides, Adv. Mater. 23 (2011) 1179–1190. doi:10.1002/adma.201001210.

[39] S. Carenco, D. Portehault, C. Boissière, N. Mézailles, C.C. Sanchez, C. Boissière, N. Mézailles, C.C. Sanchez, Nanoscaled metal borides and phosphides: Recent developments and perspectives, Chem. Rev. 113 (2013) 7981–8065. doi:10.1021/cr400020d.

[40] N. Orlovskaya, M. Lugovy, Boron rich solids: Sensors, ultra high temperature

ceramics, thermoelectrics, armor, Springer, Dordrecht, The Netherlands, 2010.

[41] K.A. Gschneidner, J.C.G. Bunzli, V.K. Pecharsky, Handbook on the physics and chemistry of rare earths: optical spectroscopy, Elsevier, Amsterdam, 2007.

[42] R. Caputo, F. Guzzetta, A. Angerhofer, Room-Temperature Synthesis of Nickel Borides via Decomposition of NaBH4 Promoted by Nickel Bromide, Inorg. Chem. 49 (2010) 8756–8762. doi:10.1021/ic100896a.

[43] G. Akopov, M.T. Yeung, R.B. Kaner, Rediscovering the Crystal Chemistry of Borides, Adv. Mater. 29 (2017). doi:10.1002/adma.201604506.

[44] X.L. Chen, Q.Y. Tu, M. He, L. Dai, L. Wu, The bond ionicity of MB2(M = Mg, Ti, V, Cr, Mn, Zr, Hf, Ta, Al and Y), J. Phys. Condens. Matter. 13 (2001) L723–L727. doi:10.1088/0953-8984/13/29/105.

[45] J.K. Burdett, E. Canadell, G.J. Miller, Electronic structure of transition-metal borides with the AlB2 structure, J. Am. Chem. Soc. 108 (1986) 6561–6568. doi:10.1021/ja00281a020.

[46] J.K. Burdett, E. Canadell, Chromium boride (CrB4) and manganese boride (MnB4): electronic structures of two unusual systems containing the tetragonal carbon net, Inorg. Chem. 27 (1988) 4437–4444. doi:10.1021/ic00297a021.

[47] A.L. Ivanovskii, Mechanical and electronic properties of diborides of transition 3d–5d metals from first principles: Toward search of novel ultra-incompressible and superhard materials, Prog. Mater. Sci. 57 (2012) 184–228. doi:https://doi.org/10.1016/j.pmatsci.2011.05.004.

[48] C.T. Zhou, J.D. Xing, B. Xiao, J. Feng, X.J. Xie, Y.H. Chen, First principles study on the structural properties and electronic structure of X2B (X=Cr, Mn, Fe, Co, Ni, Mo and W) compounds, Comput. Mater. Sci. 44 (2009) 1056–1064. doi:https://doi.org/10.1016/j.commatsci.2008.07.035.

[49] D.R. Armstrong, P.G. Perkins, E.A. Cetina V, The electronic structures and bonding of some transition-metal monoborides, Theor. Chim. Acta. 64 (1983) 41–55. doi:10.1007/BF00554152.

[50] P. Mohn, D.G. Pettifor, The calculated electronic and structural properties of the transition-metal monoborides, J. Phys. C Solid State Phys. 21 (1988) 2829–2839. doi:10.1088/0022-3719/21/15/015.

[51] B.T. Matthias, T.H. Geballe, K. Andres, E. Corenzwit, G.W. Hull, J.P. Maita, Superconductivity and Antiferromagnetism in Boron-Rich Lattices, Science (80-.). 159 (1968) 530 LP – 530. doi:10.1126/science.159.3814.530.

[52] J.F. Herbst, J.J. Croat, F.E. Pinkerton, W.B. Yelon, Relationships between crystal structure and magnetic properties in Nd2Fe14B, Phys. Rev. B. 29 (1984) 4176–4178. doi:10.1103/PhysRevB.29.4176.

[53] C.B. Shoemaker, D.P. Shoemaker, R. Fruchart, The structure of a new magnetic phase related to the sigma phase: iron neodymium boride Nd2Fe14B, Acta Crystallogr. Sect. C. 40 (1984) 1665–1668. doi:10.1107/S0108270184009094.

[54] P.K. Deheri, S. Shukla, R. V Ramanujan, The reaction mechanism of formation of chemically synthesized Nd2Fe14B hard magnetic nanoparticles, J. Solid State Chem. 186 (2012) 224–230. doi:https://doi.org/10.1016/j.jssc.2011.11.022.

[55] C. Saiyasombat, N. Petchsang, I.M. Tang, J.H. Hodak, Preparation of iron boride–silica core–shell nanoparticles with soft ferromagnetic properties, Nanotechnology. 19 (2008) 85705. doi:10.1088/0957-4484/19/8/085705.

[56] C.W. Kim, Y.H. Kim, U. Pal, Y.S. Kang, Facile synthesis and magnetic phase transformation of Nd–Fe–B nanoclusters by oxygen bridging, J. Mater. Chem. C. 1 (2013) 275–281. doi:10.1039/C2TC00083K.

[57] A. Mustapic, Mislav; Pajic, Damir; Novosel, Nikolina; Babic, Emil; Zadro, Kreso; Cindric, Marina; Horvat, Joseph; Skoko, Zeljko; Bijelic, Mirjana; Shcherbakov, Synthesis, structural characterization and magnetic properties of iron boride nanoparticles with or without silicon dioxide coating, Croat. Chem. Acta. 83 (2010) 275–282.

[58] P.H. Gaskell, Similarities in amorphous and crystalline transition metal–metalloid alloy structures, Nature. 289 (1981) 474–476. doi:10.1038/289474a0.

[59] P.K. Deheri, V. Swaminathan, S.D. Bhame, Z. Liu, R. V Ramanujan, Sol−Gel Based Chemical Synthesis of Nd2Fe14B Hard Magnetic Nanoparticles, Chem. Mater. 22 (2010) 6509–6517. doi:10.1021/cm103148n.

[60] A.B. Dávila-Ibáñez, J.L. Legido-Soto, J. Rivas, V. Salgueirino, Amorphous tunable-size Co–B magnetic nanoparticles from the cobalt-catalyzed NaBH4 hydrolysis, Phys. Chem. Chem. Phys. 13 (2011) 20146–20154. doi:10.1039/C1CP21988J.

[61] M.A. Hamayun, M. Abramchuk, H. Alnasir, M. Khan, C. Pak, S. Lenhert, L. Ghazanfari, M. Shatruk, S. Manzoor, Magnetic and magnetothermal studies of iron boride (FeB) nanoparticles, J. Magn. Magn. Mater. 451 (2018) 407–413. doi:10.1016/j.jmmm.2017.11.088.

[62] E. Medvedovski, Formation of Corrosion-Resistant Thermal Diffusion Boride Coatings, Adv. Eng. Mater. 18 (2016) 11–33. doi:10.1002/adem.201500102.

[63] H. Li, P. Wen, Q. Li, C. Dun, J. Xing, C. Lu, S. Adhikari, L. Jiang, D.L. Carroll, S.M. Geyer, Earth-Abundant Iron Diboride (FeB2) Nanoparticles as Highly Active Bifunctional Electrocatalysts for Overall Water Splitting, Adv. Energy Mater. 7 (2017) 1700513. doi:10.1002/aenm.201700513.

[64] C. Wang, C.H. Bartholomew, Preparation and adsorption, chemical and catalytic properties of iron boride fischer-tropsch catalysts, Appl. Catal. 62 (1990) 221–251. doi:https://doi.org/10.1016/S0166-9834(00)82249-6.

[65] S. Ma, Z. Huang, J. Xing, G. Liu, Y. He, H. Fu, Y. Wang, Y. Li, D. Yi, Effect of crystal orientation on microstructure and properties of bulk Fe2B intermetallic, J. Mater. Res. 30 (2015) 257–265. doi:DOI: 10.1557/jmr.2014.383.

[66] S. Ma, J. Xing, H. Fu, Y. He, Y. Bai, Y. Li, Y. Bai, Interface characteristics and corrosion behaviour of oriented bulk Fe2B alloy in liquid zinc, Corros. Sci. 78 (2014) 71–80. doi:https://doi.org/10.1016/j.corsci.2013.08.033.

[67] J. Legrand, S. Gota, M.-J. Guittet, C. Petit, Synthesis and XPS Characterization of Nickel Boride Nanoparticles, Langmuir. 18 (2002) 4131–4137. doi:10.1021/la0117247.

[68] W.G. Fahrenholtz, G.E. Hilmas, I.G. Talmy, J.A. Zaykoski, Refractory Diborides of Zirconium and Hafnium, J. Am. Ceram. Soc. 90 (2007) 1347–1364. doi:10.1111/j.1551-2916.2007.01583.x.

[69] J.B. Levine, S.H. Tolbert, R.B. Kaner, Advancements in the Search for Superhard Ultra-Incompressible Metal Borides, Adv. Funct. Mater. 19 (2009) 3519–3533. doi:10.1002/adfm.200901257.

[70] A.L. Ivanovskii, The search for novel superhard and incompressible materials on the basis of higher borides of s, p, d metals, J. Superhard Mater. 33 (2011) 73–87. doi:10.3103/S1063457611020018.

[71] Y.B. Paderno, A.A. Adamovskii, A.B. Lyashchenko, V.N. Paderno, V.B. Fillipov, Y. V Naydich, Zirconium Dodecaboride-based cutting material, Powder Metall. Met. Ceram. 43 (2004) 546–548. doi:10.1007/s11106-005-0019-0.

[72] E. Svanidze, T. Besara, M.F. Ozaydin, C.S. Tiwary, J.K. Wang, S. Radhakrishnan, S. Mani, Y. Xin, K. Han, H. Liang, T. Siegrist, P.M. Ajayan, E. Morosan, High hardness in the biocompatible intermetallic compound β-Ti3Au, Sci. Adv. 2 (2016) e1600319. doi:10.1126/sciadv.1600319.

[73] R.A. Andrievski, Superhard materials based on nanostructured high-melting point compounds: achievements and perspectives, Int. J. Refract. Met. Hard Mater. 19 (2001) 447–452. doi:https://doi.org/10.1016/S0263-4368(01)00023-3.

[74] A. Chatterjee, N. Kumar, J.R. Abelson, P. Bellon, A.A. Polycarpou, Nanowear of Hafnium Diboride Thin Films, Tribol. Trans. 53 (2010) 731–738. doi:10.1080/10402001003753341.

[75] A. Chatterjee, N. Kumar, J.R. Abelson, P. Bellon, A.A. Polycarpou, Nanoscratch and nanofriction behavior of hafnium diboride thin films, Wear. 265 (2008) 921–929. doi:https://doi.org/10.1016/j.wear.2008.02.002.

[76] A. Rinaldi, M.A. Correa-Duarte, V. Salgueirino-Maceira, S. Licoccia, E. Traversa, A.B. Dávila-Ibáñez, P. Peralta, K. Sieradzki, Elastic properties of hard cobalt boride composite nanoparticles, Acta Mater. 58 (2010) 6474–6486.

doi:10.1016/j.actamat.2010.08.009.

[77] K.I. Portnoi, V.M. Romashov, L.N. Burobina, Constitution diagram of the system zirconium-boron, Sov. Powder Metall. Met. Ceram. 9 (1970) 577–580.

[78] K. Upadhya, J.M. Yang, W.P. Hoffman, Advanced materials for ultrahigh temperature structural applications above 2000° C, Am. Ceram. Soc. Bull. 76 (1997) 51–56.

[79] M.M. Opeka, I.G. Talmy, J.A. Zaykoski, Oxidation-based materials selection for 2000°C + hypersonic aerosurfaces: Theoretical considerations and historical experience, J. Mater. Sci. 39 (2004) 5887–5904. doi:10.1023/B:JMSC.0000041686.21788.77.

[80] J.E. Kunzler, E. Buehler, F.S.L. Hsu, J.H. Wernick, Superconductivity in Nb3Sn at High Current Density in a Magnetic Field of 88 kgauss, Phys. Rev. Lett. 6 (1961) 89–91. doi:10.1103/PhysRevLett.6.89.

[81] S.L. Bud'ko, G. Lapertot, C. Petrovic, C.E. Cunningham, N. Anderson, P.C. Canfield, Boron Isotope Effect in Superconducting MgB2, Phys. Rev. Lett. 86 (2001) 1877–1880. doi:10.1103/PhysRevLett.86.1877.

[82] H.J. Choi, D. Roundy, H. Sun, M.L. Cohen, S.G. Louie, The origin of the anomalous superconducting properties of MgB2, Nature. 418 (2002) 758–760. doi:10.1038/nature00898.

[83] C. Buzea, T. Yamashita, Review of the superconducting properties of MgB2, Supercond. Sci. Technol. 14 (2001) R115–R146. doi:10.1088/0953-2048/14/11/201.

[84] E.E. Havinga, H. Damsma, J.M. Kanis, Compounds and pseudo-binary alloys with the CuAl2 (C16)-type structure IV. Superconductivity, J. Less Common Met. 27 (1972) 281–291. doi:https://doi.org/10.1016/0022-5088(72)90060-4.

[85] J.-Y. Wang, Y.-Y. Kang, H. Yang, W.-B. Cai, Boron-Doped Palladium Nanoparticles on Carbon Black as a Superior Catalyst for Formic Acid Electro-oxidation, J. Phys. Chem. C. 113 (2009) 8366–8372. doi:10.1021/jp900349g.

[86] H. Werheit, Optical properties of the crystalline modifications of boron and boron-rich borides, Prog. Cryst. Growth Charact. 16 (1988) 179–223.

doi:https://doi.org/10.1016/0146-3535(88)90018-4.

[87] S. Labov, S. Bowyer, G. Steele, Boron and silicon: filters for the extreme ultraviolet, Appl. Opt. 24 (1985) 576–578. doi:10.1364/AO.24.000576.

[88] L. Wang, L. Xu, Z. Ju, Y. Qian, A versatile route for the convenient synthesis of rare-earth and alkaline-earth hexaborides at mild temperatures, CrystEngComm. 12 (2010) 3923. doi:10.1039/c001167c.

[89] Q. Yang, J. Sha, X. Ma, Y. Ji, D. Yang, Aligned single crystal MgB 2 nanowires, Supercond. Sci. Technol. 17 (2004) L31–L33. doi:10.1088/0953-2048/17/8/L01.

[90] R. Ma, Y. Bando, T. Mori, D. Golberg, Direct Pyrolysis Method for Superconducting Crystalline MgB 2 Nanowires, Chem. Mater. 15 (2003) 3194–3197. doi:10.1021/cm021823l.

[91] Y. Wang, C. Zhuang, J. Gao, X. Shan, J. Zhang, Z. Liao, H. Xu, D. Yu, Q. Feng, MgB2 Superconducting Whiskers Synthesized by Using the Hybrid Physical−Chemical Vapor Deposition, J. Am. Chem. Soc. 131 (2009) 2436–2437. doi:10.1021/ja8087828.

[92] J. Sung, D.M. Goedde, G.S. Girolami, J.R. Abelson, Remote-plasma chemical vapor deposition of conformal ZrB2 films at low temperature: A promising diffusion barrier for ultralarge scale integrated electronics, J. Appl. Phys. 91 (2002) 3904–3911. doi:10.1063/1.1436296.

[93] H. Zhang, J. Tang, Q. Zhang, G. Zhao, G. Yang, J. Zhang, O. Zhou, L.-C. Qin, Field Emission of Electrons from Single LaB6 Nanowires, Adv. Mater. 18 (2006) 87–91. doi:10.1002/adma.200500508.

[94] J.Q. Xu, Y.M. Zhao, Q.Y. Zhang, Enhanced electron field emission from single-crystalline LaB6 nanowires with ambient temperature, J. Appl. Phys. 104 (2008) 124306. doi:10.1063/1.3048547.

[95] D. Emin, Icosahedral Boron-Rich Solids, Phys. Today. 40 (1987) 55–62. doi:10.1063/1.881112.

[96] I. Gunjishima, T. Akashi, T. Goto, Thermoelectric Properties of Single Crystalline

B4C Prepared by a Floating Zone Method, Mater. Trans. 42 (2001) 1445–1450. doi:10.2320/matertrans.42.1445.

[97] U. Kuhlmann, H. Werheit, T. Dose, T. Lundström, Influence of interstitially soluted iron on structural, optical and electrical properties of β-rhombohedral boron, J. Alloys Compd. 186 (1992) 187–200. doi:10.1016/0925-8388(92)90004-S.

[98] H. Werheit, R. Schmechel, V. Kueffel, T. Lundström, On the electronic properties of β-rhombohedral boron interstitially doped with 3d transition metal atoms, J. Alloys Compd. 262–263 (1997) 372–380. doi:10.1016/S0925-8388(97)00414-3.

[99] S. Maruyama, Y. Miyazaki, K. Hayashi, T. Kajitani, T. Mori, Excellent p-n control in a high temperature thermoelectric boride, Appl. Phys. Lett. 101 (2012) 152101. doi:10.1063/1.4758297.

[100] M. Gürsoy, M. Takeda, B. Albert, High-pressure densified solid solutions of alkaline earth hexaborides (Ca/Sr, Ca/Ba, Sr/Ba) and their high-temperature thermoelectric properties, J. Solid State Chem. 221 (2015) 191–195. doi:10.1016/j.jssc.2014.10.001.

[101] B. Ganem, J.O. Osby, Synthetically useful reactions with metal boride and aluminide catalysts, Chem. Rev. 86 (1986) 763–780. doi:10.1021/cr00075a003.

[102] R. Paul, P. Buisson, N. Joseph, Catalytic Activity of Nickel Borides, Ind. Eng. Chem. 44 (1952) 1006–1010. doi:10.1021/ie50509a029.

[103] H.I. Schlesinger, H.C. Brown, A.E. Finholt, J.R. Gilbreath, H.R. Hoekstra, E.K. Hyde, Sodium Borohydride, Its Hydrolysis and its Use as a Reducing Agent and in the Generation of Hydrogen1, J. Am. Chem. Soc. 75 (1953) 215–219. doi:10.1021/ja01097a057.

[104] J.F. Deng, J. Yang, S.S. Sheng, H.G. Chen, G.X. Xiong, The Study of Ultrafine Ni-B and Ni-P Amorphous Alloy Powders as Catalysts, J. Catal. 150 (1994) 434–438. doi:https://doi.org/10.1006/jcat.1994.1362.

[105] Z. Wu, W. Li, M. Zhang, K. Tao, Advances in chemical synthesis and application of metal-metalloid amorphous alloy nanoparticulate catalysts, Front. Chem. Eng. China. 1 (2007) 87–95. doi:10.1007/s11705-007-0018-4.

[106] H. Li, H. Li, W.-L. Dai, W. Wang, Z. Fang, J.-F. Deng, XPS studies on surface electronic characteristics of Ni–B and Ni–P amorphous alloy and its correlation to their catalytic properties, Appl. Surf. Sci. 152 (1999) 25–34. doi:https://doi.org/10.1016/S0169-4332(99)00294-9.

[107] H. Li, H. Yang, H. Li, Highly active mesoporous Co–B amorphous alloy catalyst for cinnamaldehyde hydrogenation to cinnamyl alcohol, J. Catal. 251 (2007) 233–238. doi:https://doi.org/10.1016/j.jcat.2007.07.022.

[108] H. Li, H. Li, W. Dai, M. Qiao, Preparation of the Ni-B amorphous alloys with variable boron content and its correlation to the hydrogenation activity, Appl. Catal. A Gen. 238 (2003) 119–130. doi:https://doi.org/10.1016/S0926-860X(02)00342-3.

[109] G. Bai, L. Niu, M. Qiu, F. He, X. Fan, H. Dou, X. Zhang, Liquid-phase selective hydrogenation of benzophenone over ultrasonic-assisted Ni–La–B amorphous alloy catalyst, Catal. Commun. 12 (2010) 212–216. doi:https://doi.org/10.1016/j.catcom.2010.09.021.

[110] M.-H. Qiao, S.-H. Xie, W.-L. Dai, J.-F. Deng, Ultrafine Ni–Co–W–B amorphous alloys and their activities in benzene hydrogenation to cyclohexane, Catal. Letters. 71 (2001) 187–192. doi:10.1023/A:1009047003259.

[111] H. Okamoto, B−Mg (Boron-Magnesium), J. Phase Equilibria Diffus. 27 (2006) 428–428. doi:10.1007/s11669-006-0028-9.

[112] H. Okamoto, M.E. Schlesinger, E.M. Mueller, Binary Alloy Phase Diagrams, in: H. Okamoto, M.E. Schlesinger, E.M. Mueller (Eds.), Alloy Phase Diagrams, ASM International, 2016: pp. 89–89. doi:10.31399/asm.hb.v03.a0006247.

[113] P. Blum, F. Bertaut, Contribution à l'étude des borures à teneur élevée en bore, Acta Crystallogr. 7 (1954) 81–86. doi:10.1107/S0365110X54000151.

[114] M.L. Whittaker, R.A. Cutler, Effect of synthesis atmosphere, wetting, and compaction on the purity of AlB2, J. Solid State Chem. 201 (2013) 93–100. doi:10.1016/j.jssc.2013.02.027.

[115] J.A. Kohn, D.W. Eckart, Crystallographic Data. 188. Aluminum Boride. AlB12, Anal.

Chem. 32 (1960) 296–298. doi:10.1021/ac60158a052.

[116] T. Tanaka, S. Otani, Y. Ishizawa, Preparation of single crystals of YB66, J. Cryst. Growth. 73 (1985) 31–36. doi:10.1016/0022-0248(85)90326-4.

[117] G.H. Olsen, A.V. Cafiero, Single-crystal growth of mixed (La, Eu, Y, Ce, Ba, Cs) hexaborides for thermionic emission, J. Cryst. Growth. 44 (1978) 287–290. doi:10.1016/0022-0248(78)90027-1.

[118] P.K. Liao, K.E. Spear, M.E. Schlesinger, The B-Ce (Boron-Cerium) system, J. Phase Equilibria. 18 (1997) 280. doi:10.1007/BF02647853.

[119] M.K. Blomberg, M.J. Merisalo, M.M. Korsukova, V.N. Gurin, Single-crystal X-ray diffraction study of NdB6, EuB6 and YbB6, J. Alloys Compd. 217 (1995) 123–127. doi:10.1016/0925-8388(94)01313-7.

[120] B.F. Decker, J.S. Kasper, The crystal structure of TiB, Acta Crystallogr. 7 (1954) 77–80. doi:10.1107/S0365110X5400014X.

[121] R.G. Fenish, PART V - Communications - A New Intermediate Compound in the Titanium-Boron System, Ti3B4, Trans. Metall. Soc. AIME. 236(5) (1966) 804.

[122] G. Akopov, L.E. Pangilinan, R. Mohammadi, R.B. Kaner, Perspective: Superhard metal borides: A look forward, APL Mater. 6 (2018) 070901. doi:10.1063/1.5040763.

[123] K.I. Portnoi, V.M. Romashov, I.V. Romanovich, Y.V. Levinskii, S.A. Prokof'ev, PHASE DIAGRAM OF THE SYSTEM Hf--B, Inorg. Mater. (USSR) (Engl. Transl.). 7 (1971) 1769–72.

[124] L. PK, S. KE, M. TB, Binary alloy phase diagrams, ASM Int. Mater. Park. Ohio. 1 (1990) 557–559.

[125] R.M. Peçanha, F. Ferreira, G.C. Coelho, C.A. Nunes, B. Sundman, Thermodynamic modeling of the Nb–B system, Intermetallics. 15 (2007) 999–1005. doi:10.1016/j.intermet.2006.10.054.

[126] R. Kiessling, N. Norman, L.G. Sillén, A Method for Preparing Boron of High Purity., Acta Chem. Scand. 2 (1948) 707–712. doi:10.3891/acta.chem.scand.02-0707.

[127] S. Okada, K. Kudou, I. Higashi, T. Lundström, Single crystals of TaB, Ta5B6, Ta3B4

and TAB2, as obtained from high-temperature metal solutions, and their properties, J. Cryst. Growth. 128 (1993) 1120–1124. doi:https://doi.org/10.1016/S0022-0248(07)80109-6.

[128] S. Okada, T. Atoda, I. Higashi, Structural investigation of Cr2B3, Cr3B4, and CrB by single-crystal diffractometry, J. Solid State Chem. 68 (1987) 61–67. doi:10.1016/0022-4596(87)90285-4.

[129] H. Klesnar, T.L. Aselage, B. Morosin, G.H. Kwei, The diboride compounds of molybdenum: MoB2−x and Mo2B5−y, J. Alloys Compd. 241 (1996) 180–186. doi:10.1016/0925-8388(96)02294-3.

[130] H. Duschanek, P. Rogl, Critical assessment and thermodynamic calculation of the binary system boron-tungsten (B-W), J. Phase Equilibria. 16 (1995) 150–161. doi:10.1007/BF02664852.

[131] A.T. Lech, C.L. Turner, R. Mohammadi, S.H. Tolbert, R.B. Kaner, Structure of superhard tungsten tetraboride: A missing link between MB2 and MB12 higher borides, Proc. Natl. Acad. Sci. 112 (2015) 3223 LP – 3228. doi:10.1073/pnas.1415018112.

[132] H. Okamoto, B-Mn (boron-manganese), J. Phase Equilibria. 14 (1993) 121–122. doi:10.1007/BF02652172.

[133] H.-Y. Chung, M.B. Weinberger, J.B. Levine, A. Kavner, J.-M. Yang, S.H. Tolbert, R.B. Kaner, Synthesis of Ultra-Incompressible Superhard Rhenium Diboride at Ambient Pressure, Science (80-.). 316 (2007) 436 LP – 439. doi:10.1126/science.1139322.

[134] K.I. Portnoi, V.M. Romashov, Phase diagram of the system rhenium-boron, Sov. Powder Metall. Met. Ceram. 7 (1968) 112–114. doi:10.1007/BF00774302.

[135] P.K. Liao, K.E. Spear, The B−Co (Boron-Cobalt) system, Bull. Alloy Phase Diagrams. 9 (1988) 452–457. doi:10.1007/BF02881866.

[136] L.-E. Tergenius, T. Lundström, The crystal structure of Pd2B, J. Solid State Chem. 31 (1980) 361–367. doi:10.1016/0022-4596(80)90100-0.

[137] E. Hassler, T. Lundström, L.-E. Tergenius, The crystal chemistry of platinum metal borides, J. Less Common Met. 67 (1979) 567–572. doi:10.1016/0022-5088(79)90042-0.

[138] M. Xie, B. Winkler, Z. Mao, R.B. Kaner, A. Kavner, S.H. Tolbert, Raman scattering from superhard rhenium diboride under high pressure, Appl. Phys. Lett. 104 (2014) 11904. doi:10.1063/1.4858410.

[139] L.G. Bodrova, M.S. Koval'chenko, T.I. Serebryakova, Preparation of tungsten tetraboride, Sov. Powder Metall. Met. Ceram. 13 (1974) 1–3. doi:10.1007/BF00790675.

[140] R. Mohammadi, M. Xie, A.T. Lech, C.L. Turner, A. Kavner, S.H. Tolbert, R.B. Kaner, Toward Inexpensive Superhard Materials: Tungsten Tetraboride-Based Solid Solutions, J. Am. Chem. Soc. 134 (2012) 20660–20668. doi:10.1021/ja308219r.

[141] T. Lundström, B. Lönnberg, I. Westman, A study of the microhardness in the homogeneity ranges of NbB2 and TaB2, J. Less Common Met. 96 (1984) 229–235. doi:https://doi.org/10.1016/0022-5088(84)90199-1.

[142] M.T. Yeung, J. Lei, R. Mohammadi, C.L. Turner, Y. Wang, S.H. Tolbert, R.B. Kaner, Superhard Monoborides: Hardness Enhancement through Alloying in W1−xTaxB, Adv. Mater. 28 (2016) 6993–6998. doi:10.1002/adma.201601187.

[143] G. Akopov, M.T. Yeung, C.L. Turner, R. Mohammadi, R.B. Kaner, Extrinsic Hardening of Superhard Tungsten Tetraboride Alloys with Group 4 Transition Metals, J. Am. Chem. Soc. 138 (2016) 5714–5721. doi:10.1021/jacs.6b02676.

[144] R. Mohammadi, A.T. Lech, M. Xie, B.E. Weaver, M.T. Yeung, S.H. Tolbert, R.B. Kaner, Tungsten tetraboride, an inexpensive superhard material, Proc. Natl. Acad. Sci. 108 (2011) 10958 LP – 10962. doi:10.1073/pnas.1102636108.

[145] G. Akopov, M.T. Yeung, C.L. Turner, R.L. Li, R.B. Kaner, Stabilization of HfB12 in Y1–xHfxB12 under Ambient Pressure, Inorg. Chem. 55 (2016) 5051–5055. doi:10.1021/acs.inorgchem.6b00627.

[146] S.T. Renosto, L.E. Corrêa, M.S. da Luz, P.F.S. Rosa, Z. Fisk, J. Albino-Aguiar, A.J.S.

Machado, Superconductivity in the Th0.93Zr0.07B12 compound with UB12 prototype structure, Phys. Lett. A. 379 (2015) 2498–2501. doi:https://doi.org/10.1016/j.physleta.2015.07.018.

[147] R.W. Mar, N.D. Stout, High Temperature Enthalpies of Binary Dodecaborides, J. Chem. Phys. 57 (1972) 5342–5349. doi:10.1063/1.1678228.

[148] J.-O. Carlsson, T. Lundström, The solution hardening of β-rhombohedral boron, J. Less Common Met. 22 (1970) 317–320. doi:https://doi.org/10.1016/0022-5088(70)90081-0.

[149] J.L. Hoard, D.B. Sullenger, C.H.L. Kennard, R.E. Hughes, The structure analysis of β-rhombohedral boron, J. Solid State Chem. 1 (1970) 268–277. doi:https://doi.org/10.1016/0022-4596(70)90022-8.

[150] O. Sologub, L.P. Salamakha, H. Michor, E. Bauer, B. Stöger, P.F. Rogl, Incorporation of platinum atoms in a silicon-free boride of the YB50-type structure, J. Alloys Compd. 675 (2016) 99–103. doi:https://doi.org/10.1016/j.jallcom.2016.03.015.

[151] G.A. Slack, C.I. Hejna, M. Garbauskas, J.S. Kasper, X-ray study of transition-metal dopants in β-boron, J. Solid State Chem. 76 (1988) 64–86. doi:https://doi.org/10.1016/0022-4596(88)90193-4.

[152] H. Werheit, V. Filipov, K. Shirai, H. Dekura, N. Shitsevalova, U. Schwarz, M. Armbrüster, Raman scattering and isotopic phonon effects in dodecaborides, J. Phys. Condens. Matter. 23 (2011) 65403. doi:10.1088/0953-8984/23/6/065403.

[153] S.M. Richards, J.S. Kaspar, The crystal structure of YB66, Acta Crystallogr. Sect. B. 25 (1969) 237–251. doi:10.1107/S056774086900207X.

[154] A. Leithe-Jasper, A. Sato, T. Tanaka, Refinement of the crystal structure of zirconium dodecaboride, ZrB12, at 140 K and 293 K, ZEITSCHRIFT FUR Krist. Cryst. Struct. 217 (2002) 319–320.

[155] J.B. Levine, S.L. Nguyen, H.I. Rasool, J.A. Wright, S.E. Brown, R.B. Kaner, Preparation and Properties of Metallic, Superhard Rhenium Diboride Crystals, J. Am. Chem. Soc. 130 (2008) 16953–16958. doi:10.1021/ja804989q.

[156] A. Knappschneider, C. Litterscheid, J. Kurzman, R. Seshadri, B. Albert, Crystal Structure Refinement and Bonding Patterns of CrB4: A Boron-Rich Boride with a Framework of Tetrahedrally Coordinated B Atoms, Inorg. Chem. 50 (2011) 10540–10542. doi:10.1021/ic2018083.

[157] A. Knappschneider, C. Litterscheid, J. Brgoch, N.C. George, S. Henke, A.K. Cheetham, J.G. Hu, R. Seshadri, B. Albert, Manganese Tetraboride, MnB4: High-Temperature Crystal Structure, p–n Transition, 55Mn NMR Spectroscopy, Solid Solutions, and Mechanical Properties, Chem. – A Eur. J. 21 (2015) 8177–8181. doi:10.1002/chem.201406631.

[158] J. Qin, D. He, J. Wang, L. Fang, L. Lei, Y. Li, J. Hu, Z. Kou, Y. Bi, Is Rhenium Diboride a Superhard Material?, Adv. Mater. 20 (2008) 4780–4783. doi:10.1002/adma.200801471.

[159] J. Cueilleron, G. Lahet, F. Thevenot, R.A. Pâris, Nouvelle methode d'obtention de borures metalliques, J. Less Common Met. 24 (1971) 317–322. doi:https://doi.org/10.1016/0022-5088(71)90112-3.

[160] M. İpekçi, S. Acar, M. Elmadağlı, J. Hennicke, Ö. Balcı, M. Somer, Production of TiB2 by SHS and HCl leaching at different temperatures: Characterization and investigation of sintering behavior by SPS, Ceram. Int. 43 (2017) 2039–2045. doi:https://doi.org/10.1016/j.ceramint.2016.10.174.

[161] O.K. Lepakova, L.G. Raskolenko, Y.M. Maksimov, Titanium borides prepared by self-propagating high-temperature synthesis, Inorg. Mater. 36 (2000) 568–575. doi:10.1007/BF02757955.

[162] P.M. McKenna, Tantalum Carbide its Relation to other Hard Refractory Compounds, Ind. Eng. Chem. 28 (1936) 767–772. doi:10.1021/ie50319a004.

[163] B. Post, D. Moskowitz, F.W. Glaser, Borides of Rare Earth Metals, J. Am. Chem. Soc. 78 (1956) 1800–1802. doi:10.1021/ja01590a007.

[164] T.I. Serebryakova, É. V Marek, Conditions of preparation of calcium and barium hexaboride powders, Sov. Powder Metall. Met. Ceram. 8 (1969) 608–612.

doi:10.1007/BF00775416.

[165] G.V. Samsonov, T.I. Kovenskaya, B.A. Serebryakova, E.Y. Tel'nikov, Thermal conductivity of diborides of group IV--VI transition metals, High Temp. (Engl. Transl.). 10 (1972) 1324–1326.

[166] G. SAMSONOV, L. MARKOVSKII, KHIMIYA BORIDOV, Usp. Khim. 25 (1956) 190–241.

[167] L.Y. Markovskii, N. V Vekshina, E.T. Bezruk, G.E. Sukhareva, T.K. Voevodskaya, A magnesium-thermic method for the preparation of metal borides, Sov. Powder Metall. Met. Ceram. 8 (1969) 350–354. doi:10.1007/BF00776606.

[168] P. Peshev, Preparation of crystalline titanium diboride by a vapor deposition process, in: Proc. Inst. Gen. Inorg. Chem. Bulg. Acad. Sci., 1966: pp. 53–67.

[169] R.A. Huggins, Thermodynamic considerations relating to the use of electrochemical techniques for the growth of single crystals of borides, Mater. Res. Bull. 5 (1970) 391–401. doi:https://doi.org/10.1016/0025-5408(70)90077-2.

[170] F. Galasso, J. Pinto, Metal borides in boron fiber cores. Identification of MoB4, Trans. Metall. Soc. AIME. 242 (1968) 754–755.

[171] R. Bakish, C.A. Gellor, I. Marinow, Vapor-phase metallurgy and ceramics, J. Met. 14 (1962) 770–774.

[172] Ö. Balcı, D. Ağaoğulları, İ. Duman, M.L. Öveçoğlu, Synthesis of CaB6 powders via mechanochemical reaction of Ca/B2O3 blends, Powder Technol. 225 (2012) 136–142. doi:10.1016/j.powtec.2012.03.051.

[173] D. Ağaoğulları, Ö. Balcı, N. Akçamlı, İ. Duman, M.L. Öveçoğlu, Effects of different milling conditions on the properties of lanthanum hexaboride nanoparticles and their sintered bodies, Ceram. Int. 45 (2019) 18236–18246. doi:10.1016/j.ceramint.2019.06.034.

[174] E.G. Gillan, R.B. Kaner, Synthesis of Refractory Ceramics via Rapid Metathesis Reactions between Solid-State Precursors, Chem. Mater. 8 (1996) 333–343. doi:10.1021/cm950232a.

[175] R.W. Cumberland, M.B. Weinberger, J.J. Gilman, S.M. Clark, S.H. Tolbert, R.B. Kaner, Osmium Diboride, An Ultra-Incompressible, Hard Material, J. Am. Chem. Soc. 127 (2005) 7264–7265. doi:10.1021/ja043806y.

[176] S. Choi, L.D.S.S. Lapitan, Y. Cheng, T. Watanabe, Synthesis of cobalt boride nanoparticles using RF thermal plasma, Adv. Powder Technol. 25 (2014) 365–371. doi:10.1016/j.apt.2013.06.002.

[177] G. Gouget, D.P. Debecker, A. Kim, G. Olivieri, J.J. Gallet, F. Bournel, C. Thomas, O. Ersen, S. Moldovan, C. Sanchez, S. Carenco, D. Portehault, In Situ Solid-Gas Reactivity of Nanoscaled Metal Borides from Molten Salt Synthesis, Inorg. Chem. 56 (2017) 9225–9234. doi:10.1021/acs.inorgchem.7b01279.

[178] S. Dutz, R. Müller, D. Eberbeck, I. Hilger, M. Zeisberger, Magnetic nanoparticles adapted for specific biomedical applications, Biomed. Tech. 60 (2015) 405–416. doi:10.1515/bmt-2015-0044.

[179] X. Li, C. Wang, X. Han, Y. Wu, Surfactant-free synthesis and electromagnetic properties of Co-Ni-B composite particles, Mater. Sci. Eng. B Solid-State Mater. Adv. Technol. 178 (2013) 211–217. doi:10.1016/j.mseb.2012.10.039.

[180] H. Euchner, P.H. Mayrhofer, Designing thin film materials — Ternary borides from first principles, Thin Solid Films. 583 (2015) 46–49. doi:10.1016/j.tsf.2015.03.035.

[181] D. Kotzott, M. Ade, H. Hillebrecht, Single crystal studies on Co-containing τ-borides Co23-xMxB6(M=Al, Ga, Sn, Ti, V, Ir) and the boron-rich τ-boride Co12.3Ir8.9B10.5, J. Solid State Chem. 182 (2009) 538–546. doi:10.1016/j.jssc.2008.10.036.

[182] M. Mustapić, J. Horvat, M.S. Hossain, Z. Sun, Ž. Skoko, D.R.G. Mitchell, S.X. Dou, Novel synthesis of superparamagnetic Ni-Co-B nanoparticles and their effect on superconductor properties of MgB2, Acta Mater. 70 (2014) 298–306. doi:10.1016/j.actamat.2014.02.040.

[183] M. Mustapić, J. Horvat, Ž. Skoko, M.S. Al Hossain, S.X. Dou, Interplay between boron precursors and Ni-Co-B nanoparticle doping in the fabrication of MgB2superconductor with improved electromagnetic properties, Acta Mater. 80

(2014) 457–467. doi:10.1016/j.actamat.2014.08.030.

[184] S. Klemenz, J. Schuch, S. Hawel, A.M. Zieschang, B. Kaiser, W. Jaegermann, B. Albert, Synthesis of a Highly Efficient Oxygen-Evolution Electrocatalyst by Incorporation of Iron into Nanoscale Cobalt Borides, ChemSusChem. 11 (2018) 3150–3156. doi:10.1002/cssc.201801547.

[185] N. Patel, R. Fernandes, A. Miotello, Promoting effect of transition metal-doped Co-B alloy catalysts for hydrogen production by hydrolysis of alkaline NaBH4solution, J. Catal. 271 (2010) 315–324. doi:10.1016/j.jcat.2010.02.014.

[186] G. Ababei, M. Gaburici, L.C. Budeanu, M. Grigoras, M. Porcescu, N. Lupu, H. Chiriac, Influence of the chemically synthesis conditions on the microstructure and magnetic properties of the Co-Fe-B nanoparticles, J. Magn. Magn. Mater. 451 (2018) 565–571. doi:10.1016/j.jmmm.2017.11.110.

[187] J. Wells, J.H. Lee, R. Mansell, R.P. Cowburn, O. Kazakova, Controlled manipulation of domain walls in ultra-thin CoFeB nanodevices, J. Magn. Magn. Mater. 400 (2016) 219–224. doi:10.1016/j.jmmm.2015.07.047.

[188] S. l. Wang, Electroless deposition of Ni-Co-B alloy films and influence of heat treatment on the structure and the magnetic performances of the film, Thin Solid Films. 515 (2007) 8419–8423. doi:10.1016/j.tsf.2007.05.066.

[189] Y. Zhang, W. Mi, X. Wang, Z. Guo, Scaling of anomalous Hall effect in amorphous CoFeB films with accompanying quantum correction, Solid State Commun. 215–216 (2015) 5–11. doi:10.1016/j.ssc.2015.05.001.

[190] I.H. Lee, T.Y. Lee, C.W. Chung, Etch characteristics of CoFeB magnetic thin films using high density plasma of a H2O/CH4/Ar gas mixture, Vacuum. 97 (2013) 49–54. doi:10.1016/j.vacuum.2013.03.018.

[191] Z. Liu, W.L. Li, P.P. Jin, W.D. Fei, Magnetic anisotropy transformation of Co – Fe – B nanowire arrays synthesized under the magnetic fi eld, J. Magn. Magn. Mater. 345 (2013) 96–99. doi:10.1016/j.jmmm.2013.06.043.

[192] M. Ciureanu, F. Beron, L. Clime, P. Ciureanu, A. Yelon, T.A. Ovari, R.W. Cochrane,

F. Normandin, T. Veres, Magnetic properties of electrodeposited CoFeB thin films and nanowire arrays, Electrochim. Acta. 50 (2005) 4487–4497. doi:10.1016/j.electacta.2005.02.011.

[193] H. Nowotny, P. Rogl, Ternary Metal Borides, in: Boron Refract. Borides, 1977. doi:10.1007/978-3-642-66620-9_23.

[194] M. Baris, T. Simsek, A. Akkurt, Mechanochemical synthesis and characterization of pure Co2B nanocrystals, Bull. Mater. Sci. 39 (2016) 1119–1126. doi:10.1007/s12034-016-1231-x.

[195] H. Sharifi, S. Rabiei Faradonbeh, M. Tayebi, Production and characterization of cobalt/vanadium boride nanocomposite powder by mechanochemical method, Mater. Chem. Phys. 202 (2017) 251–257. doi:10.1016/j.matchemphys.2017.09.015.

[196] Y. Wei, Z. Liu, S. Ran, A. Xia, T.F. Yi, Y. Ji, Synthesis and properties of Fe-B powders by molten salt method, J. Mater. Res. 32 (2017) 883–889. doi:10.1557/jmr.2017.38.

[197] M. Mohammadi, A. Ghasemi, M. Tavoosi, Mechanochemical synthesis of nanocrystalline Fe and Fe–B magnetic alloys, J. Magn. Magn. Mater. 419 (2016) 189–197. doi:10.1016/j.jmmm.2016.06.037.

[198] T. Hyeon, Chemical synthesis of magnetic nanoparticles, Chem. Commun. 3 (2003) 927–934. doi:10.1039/b207789b.

[199] S. Rades, A. Kornowski, H. Weller, B. Albert, Wet-Chemical Synthesis of Nanoscale Iron Boride , XAFS Analysis and Crystallisation to a -FeB **, (2011) 1756–1760. doi:10.1002/cphc.201001072.

[200] J. Abenojar, F. Velasco, J.M. Mota, M.A. Martínez, Preparation of Fe/B powders by mechanical alloying, J. Solid State Chem. 177 (2004) 382–388. doi:10.1016/j.jssc.2003.01.001.

[201] T. Simsek, M. Baris, B. Kalkan, Mechanochemical processing and microstructural characterization of pure Fe2B nanocrystals, Adv. Powder Technol. 28 (2017) 3056–3062. doi:10.1016/j.apt.2017.09.017.

[202] K.I. Takagi, Y. Yamasaki, M. Komai, High-Strength Boride Base Hard Materials, J. Solid State Chem. 133 (1997) 243–248. doi:10.1006/jssc.1997.7449.

[203] Y. Yamasaki, M. Nishi, K.I. Takagi, Development of very high strength Mo2NiB2complex boride base hard alloy, J. Solid State Chem. 177 (2004) 551–555. doi:10.1016/j.jssc.2003.03.008.

[204] J.-F. Deng, H. Li, W. Wang, Progress in design of new amorphous alloy catalysts, Catal. Today. 51 (1999) 113. doi:doi: 10.1016/S0920-5861(99)00013-9.

[205] I. Campos-Silva, D. Bravo-Bárcenas, H. Cimenoglu, U. Figueroa-López, M. Flores-Jiménez, O. Meydanoglu, The boriding process in CoCrMo alloy: Fracture toughness in cobalt boride coatings, Surf. Coatings Technol. 260 (2014) 362–368. doi:10.1016/j.surfcoat.2014.07.092.

[206] G. Gouget, P. Beaunier, D. Portehault, C. Sanchez, New route toward nanosized crystalline metal borides with tuneable stoichiometry and variable morphologies, Faraday Discuss. 191 (2016) 511–525. doi:10.1039/c6fd00053c.

[207] D. Ihiawakrim, Y. Le Godec, O. Ersen, C. Chanéac, O.O. Kurakevych, S. Delacroix, G. Gouget, D. Portehault, P. Beaunier, R. Grosjean, A high pressure pathway toward boron-based nanostructured solids, Dalt. Trans. 47 (2018) 7634–7639. doi:10.1039/c8dt00932e.

[208] Y. Li, E. Tevaarwerk, R.P.H. Chang, Ferromagnetic iron boride (Fe 3B) nanowires, Chem. Mater. 18 (2006) 2552–2557. doi:10.1021/cm060068z.

[209] S. Kumar, A. Singh, K. Nakajima, A. Jain, H. Miyaoka, T. Ichikawa, G.K. Dey, Y. Kojima, Improved hydrogen release from magnesium borohydride by ZrCl4additive, Int. J. Hydrogen Energy. 42 (2017) 22342–22347. doi:10.1016/j.ijhydene.2016.12.090.

[210] F.J. Humphreys, Recrystallization mechanisms in two-phase alloys, Met. Sci. 13 (1979). doi:10.1179/msc.1979.13.3-4.136.

[211] F.J. Humphreys, Particle stimulated nucleation of recrystallization at silica particles in nickel, Scr. Mater. 43 (2000) 591–596. doi:10.1016/S1359-6462(00)00442-5.

[212] F.J. Humphreys, Grain Boundary Migration and Zener Pinning in Particle-Containing Copper Crystals, Acta Mater. 44 (1996) 2717–2727.

[213] T. Haibach, M.A. Estermann, A. Cervellino, W. Steurer, Phase transitions in quasicrystals - the example of decagonal Al-Co-Ni, Mater. Sci. Eng. A. 294–296 (2000) 17–22. doi:10.1016/S0921-5093(00)01147-3.

[214] J.P. Davis, E.H. Majzoub, J.M. Simmons, K.F. Kelton, Ternary phase diagram studies in Ti-Zr-Ni alloys, Mater. Sci. Eng. A. 294 (2000) 104–107. doi:10.1016/S0921-5093(00)01093-5.

[215] J.D. Robson, D.T. Henry, B. Davis, Particle effects on recrystallization in magnesium-manganese alloys: Particle pinning, Mater. Sci. Eng. A. (2011). doi:10.1016/j.msea.2011.02.030.

[216] T.A. Bennett, R.H. Petrov, L.A.I. Kestens, L.Z. Zhuang, P. de Smet, The effect of particle-stimulated nucleation on texture banding in an aluminium alloy, Scr. Mater. 63 (2010) 461–464. doi:10.1016/j.scriptamat.2010.04.028.

[217] W. Xu, M. Ferry, J.M. Cairney, F.J. Humphreys, Three-dimensional investigation of particle-stimulated nucleation in a nickel alloy, Acta Mater. 55 (2007) 5157–5167. doi:10.1016/j.actamat.2007.05.045.

[218] W. Xu, M. Ferry, F.J. Humphreys, Spatial morphology of interfacial voids and other features generated at coarse silica particles in nickel during cold rolling and annealing, Scr. Mater. 60 (2009) 862–865. doi:10.1016/j.scriptamat.2009.01.034.

[219] C. Schäfer, J. Song, G. Gottstein, Modeling of texture evolution in the deformation zone of second-phase particles, Acta Mater. 57 (2009) 1026–1034. doi:10.1016/j.actamat.2008.10.052.

[220] S. Kobayashi, T. Takasugi, Grain refinement of a Fe3Al-based alloy using κ-Fe3AlC precipitate particles stimulating nucleation of recrystallization, Intermetallics. 15 (2007) 1659–1665. doi:10.1016/j.intermet.2007.07.012.

[221] D. Fruchart, P. Chaudouet, R. Fruchart, A. Rouault, J.P. Senateur, Etudes structurales de compose´s de type ce´mentite: Effet de l'hydroge`ne sur Fe3C suivi par diffraction

neutronique. Spectrome´trie Mössbauer sur FeCo2B et Co3B dope´s au57Fe, J. Solid State Chem. (1984). doi:10.1016/0022-4596(84)90340-2.

[222] M.B. Weinberger, J.B. Levine, H.Y. Chung, R.W. Cumberland, H.I. Rasool, J.M. Yang, R.B. Kaner, S.H. Tolbert, Incompressibility and hardness of solid solution transition metal diborides: Os1-xRuxB2, Chem. Mater. 21 (2009) 1915–1921. doi:10.1109/ICIP.2014.7025097.

[223] A.T. Lech, C.L. Turner, J. Lei, R. Mohammadi, S.H. Tolbert, R.B. Kaner, Superhard Rhenium/Tungsten Diboride Solid Solutions, J. Am. Chem. Soc. 138 (2016) 14398–14408. doi:10.1021/jacs.6b08616.

[224] S. Rades, S. Kraemer, R. Seshadri, B. Albert, Size and Crystallinity Dependence of Magnetism in Nanoscale Iron Boride, α ‑ FeB, (2014) 24–27. doi:10.1021/cm403167a.

[225] Y.Q. Liu, X.S. Zhao, J. Yang, J.Y. Shen, Thermodynamic optimization of the boron-cobalt-iron system, J. Alloys Compd. 509 (2011) 4805–4810. doi:10.1016/j.jallcom.2011.01.170.

[226] M. Vignolo, G. Romano, C. Bernini, A. Martinelli, A.S. Siri, A novel process to produce amorphous nano-sized B useful for MgB2 phase synthesis, IEEE Trans. Appl. Supercond. 22 (2012) 0–5.

[227] R.W. Cahn, Binary Alloy Phase Diagrams-Second edition. T. B. Massalski, Editor-in-Chief; H. Okamoto, P. R. Subramanian, L. Kacprzak, Editors. ASM International, Materials Park, Ohio, USA. December 1990. xxii, 3589 pp., 3 vol., hard- back. $995.00 the set, Adv. Mater. 3 (1991) 628–629. doi:10.1002/adma.19910031215.

[228] J.C. Ingersoll, N. Mani, J.C. Thenmozhiyal, A. Muthaiah, Catalytic hydrolysis of sodium borohydride by a novel nickel-cobalt-boride catalyst, J. Power Sources. 173 (2007) 450–457. doi:10.1016/j.jpowsour.2007.04.040.

[229] P. Krishnan, S.G. Advani, A.K. Prasad, Cobalt oxides as Co2B catalyst precursors for the hydrolysis of sodium borohydride solutions to generate hydrogen for PEM fuel cells, Int. J. Hydrogen Energy. 33 (2008) 7095–7102.

doi:10.1016/j.ijhydene.2008.09.026.

[230] C. Wu, F. Wu, Y. Bai, B. Yi, H. Zhang, Cobalt boride catalysts for hydrogen generation from alkaline NaBH4solution, Mater. Lett. 59 (2005) 1748–1751. doi:10.1016/j.matlet.2005.01.058.

[231] S. Li, X. Yang, H. Zhu, X. Wei, Y. Liu, Ultrafine amorphous Co-W-B alloy as the anode catalyst for a direct borohydride fuel cell, Int. J. Hydrogen Energy. 38 (2013) 2884–2888. doi:10.1016/j.ijhydene.2012.11.148.

[232] D. Mu, C. Yang, B. luo Shen, H. Jiang, Oxidation resistance of borided pure cobalt, J. Alloys Compd. 479 (2009) 629–633. doi:10.1016/j.jallcom.2009.01.015.

[233] A.R. Trueman, D.P. Schweinsberg, G.A. Hope, A study of the effect of cobalt additions on the corrosion of tungsten carbide/carbon steel metal matrix composites, Corros. Sci. 41 (1999) 1377–1389. doi:10.1016/S0010-938X(98)00193-0.

[234] C. Petit, M.P. Pileni, Cobalt Nanosized Particles Organized in a 2D Superlattice: Synthesis, Characterization, and Magnetic Properties, J. Phys. Chem. B. 103 (1999) 1805–1810. doi:10.1021/jp982755m.

[235] Y. Bao, M. Beerman, K.M. Krishnan, Controlled self-assembly of colloidal cobalt nanocrystals mediated by magnetic interactions, J. Magn. Magn. Mater. 272–276 (2004) 1367–1368. doi:10.1016/j.jmmm.2003.12.219.

[236] V. Salgueiriño-Maceira, M.A. Correa-Duarte, M. Farle, M.A. López-Quintela, K. Sieradzki, R. Diaz, Synthesis and characterization of large colloidal cobalt particles, Langmuir. 22 (2006) 1455–1458. doi:10.1021/la0526885.

[237] B.M. Goortani, P. Proulx, S. Xue, N.Y. Mendoza-Gonzalez, Controlling nanostructure in thermal plasma processing: Moving from highly aggregated porous structure to spherical silica nanoparticles, Powder Technol. 175 (2007) 22–32. doi:10.1016/j.powtec.2007.01.014.

[238] J. Szépvölgyi, I. Mohai, Z. Károly, L. Gál, Synthesis of nanosized ceramic powders in a radiofrequency thermal plasma reactor, J. Eur. Ceram. Soc. 28 (2008) 895–899. doi:10.1016/j.jeurceramsoc.2007.09.034.

[239] S. Samal, D.-W. Park, Nano-particle synthesis of titanium oxides from ilmenite in a thermal plasma reactor, Chem. Eng. Res. Des. 90 (2012) 548–554. doi:10.1016/j.cherd.2011.08.011.

[240] M. Mustapic, D. Pajic, N. Novosel, E. Babic, K. Zadro, M. Cindric, J. Horvat, Z. Skoko, M. Bijelic, A. Shcherbakov, Synthesis, Structural Characterization and Magnetic Properties of Iron Boride Nanoparticles with or without Silicon Dioxide Coating, Croat. Chem. Acta. 83 (2010) 275–282.

[241] S.E. Skrabalak, K.S. Suslick, On the Possibility of Metal Borides for Hydrodesulfurization, Chem. Mater. 18 (2006) 3103–3107. doi:10.1021/cm060341x.

[242] S. Khoshsima, Z. Altintas, M. Somer, Ö. Balci, Synthesis of Cobalt-Nickel-Boron based composite powders using metal chloride powder blends, in: 27th Int. Conf. Metall. Mater., TANGER LTD, KELTICKOVA 62, SLEZSKA, OSTRAVA 710 00, CZECH REPUBLIC, Brno, Czech Republic, 2018: pp. 1563–1568. http://www.scopus.com/inward/record.url?eid=2-s2.0-85059371798&partnerID=MN8TOARS.

[243] X.P. Gao, H.X. Yang, Multi-electron reaction materials for high energy density batteries, Energy Environ. Sci. 3 (2010) 174–189. doi:10.1039/b916098a.

[244] H. Park, A. Encinas, J.P. Scheifers, Y. Zhang, B.P.T. Fokwa, Boron-Dependency of Molybdenum Boride Electrocatalysts for the Hydrogen Evolution Reaction, Angew. Chemie Int. Ed. 56 (2017) 5575–5578. doi:10.1002/anie.201611756.

[245] D.M. Wang, Y.F. Hou, Z.Z. Tian, A novel high-torque magnetorheological brake with a water cooling method for heat dissipation, Smart Mater. Struct. 22 (2013) 25019. doi:10.1088/0964-1726/22/2/025019.

[246] G. Schinteie, P. Palade, L. Vekas, N. Iacob, C. Bartha, V. Kuncser, Volume fraction dependent magnetic behaviour of ferrofluids for rotating seal applications, J. Phys. D. Appl. Phys. 46 (2013) 395501. doi:10.1088/0022-3727/46/39/395501.

[247] J.-R. Lin, R.-F. Lu, M.-C. Lin, P.-Y. Wang, Squeeze film characteristics of parallel circular disks lubricated by ferrofluids with non-Newtonian couple stresses, Tribol.

Int. 61 (2013) 56–61. doi:https://doi.org/10.1016/j.triboint.2012.12.001.

[248] P. Zu, C. Chiu Chan, T. Gong, Y. Jin, W. Chang Wong, X. Dong, Magneto-optical fiber sensor based on bandgap effect of photonic crystal fiber infiltrated with magnetic fluid, Appl. Phys. Lett. 101 (2012) 241118. doi:10.1063/1.4772017.

[249] J.K. Oh, J.M. Park, Iron oxide-based superparamagnetic polymeric nanomaterials: Design, preparation, and biomedical application, Prog. Polym. Sci. 36 (2011) 168–189. doi:https://doi.org/10.1016/j.progpolymsci.2010.08.005.

[250] K.M. Krishnan, Biomedical nanomagnetics: A spin through possibilities in imaging, diagnostics, and therapy, IEEE Trans. Magn. 46 (2010) 2523–2558. doi:10.1109/TMAG.2010.2046907.

[251] J. Dobson, TOPICAL REVIEW : Progress in applications of magnetic nanoparticles in biomedicine Progress in applications of magnetic nanoparticles in biomedicine, 224001 (2009). doi:10.1088/0022-3727/42/22/224001.

[252] D. Ortega, Q.A. Pankhurst, Magnetic hyperthermia, in: 2012: pp. 60–88. doi:10.1039/9781849734844-00060.

[253] K.J. Widder, R.M. Morris, G. Poore, D.P. Howard, A.E. Senyei, Tumor remission in Yoshida sarcoma-bearing rts by selective targeting of magnetic albumin microspheres containing doxorubicin, Proc. Natl. Acad. Sci. 78 (1981) 579 LP – 581. doi:10.1073/pnas.78.1.579.

[254] C. Alexiou, W. Arnold, R.J. Klein, F.G. Parak, P. Hulin, C. Bergemann, W. Erhardt, S. Wagenpfeil, A.S. Lübbe, Locoregional Cancer Treatment with Magnetic Drug Targeting, Cancer Res. 60 (2000) 6641 LP – 6648. http://cancerres.aacrjournals.org/content/60/23/6641.abstract.

[255] C. Alexiou, R. Tietze, E. Schreiber, R. Jurgons, H. Richter, L. Trahms, H. Rahn, S. Odenbach, S. Lyer, Cancer therapy with drug loaded magnetic nanoparticles—magnetic drug targeting, J. Magn. Magn. Mater. 323 (2011) 1404–1407. doi:https://doi.org/10.1016/j.jmmm.2010.11.059.

[256] Y. Shimada, Y. Endo, M. Yamaguchi, S. Okamoto, O. Kitakami, Y. Imano, H.

Matsumoto, S. Yoshida, Production of Magnetically Soft Submicron Particles From Aqueous Solutions and Characterization, IEEE Trans. Magn. 45 (2009) 4298–4301. doi:10.1109/TMAG.2009.2024951.

[257] S. Khoshsima, Z. Altıntaş, M. Schmidt, M. Bobnar, M. Somer, Ö. Balcı, Crystalline Co–Fe–B nanoparticles: Synthesis, microstructure and magnetic properties, J. Alloys Compd. 805 (2019) 471–482. doi:10.1016/j.jallcom.2019.07.079.

[258] N.N. Greenwood, R. V. Parish, P. Thornton, Metal borides, Q. Rev. Chem. Soc. 20 (1966) 441. doi:10.1039/qr9662000441.

[259] P. Martelli, R. Caputo, A. Remhof, P. Mauron, A. Borgschulte, A. Zu, Stability and Decomposition of NaBH 4, J. Phys. Chem. C. 114 (2010) 7173–7177.

[260] S. Orimo, Y. Nakamori, A. Züttel, Material properties of MBH4 (M = Li, Na, and K), Mater. Sci. Eng. B Solid-State Mater. Adv. Technol. 108 (2004) 51–53. doi:10.1016/j.mseb.2003.10.045.

[261] H. Frydrych, A. Romański, J. Konstanty, The influence of iron content and powder metallurgy processing route on microstructure and mechanical properties of cobalt-iron materials, Arch. Metall. Mater. 49 (2004) 973–980.

[262] T. Massalski, P. Submanian, H. Okamoto, Binary Alloy Phase Diagrams 2nd ed. (ASM International Materials Park, OH), 1998. doi:10.1007/BF02869318.

[263] G. Suresh, D. Rajan Babu, A simple wet-chemical approach to synthesize shape controlled high magnetic moment Fe71–Co29 nanocrystals, J. Alloys Compd. 509 (2011) 10145–10149. doi:10.1016/j.jallcom.2011.08.064.

[264] P.R. Jothi, K. Yubuta, B.P.T. Fokwa, A Simple, General Synthetic Route toward Nanoscale Transition Metal Borides, Adv. Mater. 30 (2018). doi:10.1002/adma.201704181.

[265] G. Pradelli, C. Gianoglio, E. Quadrini, The cobald-iron-boron system in the presence of liquid, Metall. Ital. 73 (1981) 351–355.

[266] M. Mustapic, D. Pajic, N. Novosel, E. Babic, K. Zadro, M. Cindric, J. Horvat, Z. Skoko, M. Bijelic, A. Shcherbakov, M. Mustapić, D. Pajić, N. Novosel, E. Babić, K.

Zadro, M. Cindrić, J. Horvat, Ž. Skoko, M. Bijelić, A. Shcherbakov, M. Mustapic, D. Pajic, N. Novosel, E. Babic, K. Zadro, M. Cindric, J. Horvat, Z. Skoko, M. Bijelic, A. Shcherbakov, Synthesis, Structural Characterization and Magnetic Properties of Iron Boride Nanoparticles with or without Silicon Dioxide Coating, Croat. Chem. Acta. 83 (2010) 275–282.

[267] T. Oguchi, Theory of Magnetism in CoCl 2 ·2H 2 O, J. Phys. Soc. Japan. 20 (1965) 2236–2243. doi:10.1143/JPSJ.20.2236.

[268] H. Wan, X.-W.W. Liu, M. Qing, J.-J.J. Liu, Y. Zhang, S. Liu, H. Wang, X.-D.D. Wen, Y. Yang, Y.-W.W. Li, Insight into the magnetic moment of iron borides: theoretical consideration from the local coordinative and electronic environment, Dalt. Trans. 49 (2020) 2168–2175. doi:10.1039/C9DT04193A.

[269] P. Villars, K. Cenzual, eds., Co3B7O13Cl orthorhombic (Co3B7ClO13 ht3) Crystal Structure: Datasheet from ``PAULING FILE Multinaries Edition -- 2012'' in SpringerMaterials (https://materials.springer.com/isp/crystallographic/docs/sd_1310063), (n.d.). https://materials.springer.com/isp/crystallographic/docs/sd_1310063.

[270] F. Habashi, Handbook of extractive metallurgy, vol. 2, Wiley-VCH, Heidelberg, Germany, 1997. doi:10.1002/cphc.201500601.

[271] A.W. Weimer, Carbide, Nitride and Boride Materials Synthesis and Processing, Springer, London, United Kingdom, 1997.

[272] R.G. Munro, Material properties of titanium diboride, J. Res. Natl. Inst. Stand. Technol. 105 (2000) 709. doi:10.6028/jres.105.057.

[273] V.I. Matkovich, Boron and refractory borides, Springer-Verlag, 1977. https://books.google.com.tr/books?id=xd_vAAAAMAAJ.

[274] C. Subramanian, T.S.R.C. Murthy, A.K. Suri, Synthesis and consolidation of titanium diboride, Int. J. Refract. Met. Hard Mater. 25 (2007) 345–350. doi:10.1016/j.ijrmhm.2006.09.003.

[275] A.K. Khanra, L.C. Pathak, S.K. Mishra, M.M. Godkhindi, Effect of NaCl on the

synthesis of TiB2powder by a self-propagating high-temperature synthesis technique, Mater. Lett. 58 (2004) 733–738. doi:10.1016/j.matlet.2003.06.003.

[276] V. Sundaram, K. V. Logan, R.F. Speyer, Reaction path in the magnesium thermite reaction to synthesize titanium diboride, J. Mater. Res. 12 (1997) 2657–2664. doi:10.1557/JMR.1997.0355.

[277] P. Foroughi, A. Rabiei Baboukani, A. Franco Hernandez, C. Wang, Z. Cheng, Phase control during synthesis of nanocrystalline ultrahigh temperature tantalum-hafnium diboride powders, J. Am. Ceram. Soc. 101 (2018) 5745–5755. doi:10.1111/jace.15783.

[278] M. Shibuya, Y. Yamamoto, M. Ohyanagi, Simultaneous densification and phase decomposition of TiB2-WB2solid solutions activated by cobalt boride addition, J. Eur. Ceram. Soc. 27 (2007) 307–312. doi:10.1016/j.jeurceramsoc.2006.05.084.

[279] G.A. Rodríguez-castro, C.D. Reséndiz-calderon, L.F. Jiménez-tinoco, A. Meneses-amador, Surface & Coatings Technology Micro-abrasive wear resistance of CoB / Co 2 B coatings formed in CoCrMo alloy, Surf. Coat. Technol. 284 (2015) 258–263. doi:10.1016/j.surfcoat.2015.06.081.

[280] Z. Wang, B. Xie, W. Zhou, G. Shi, Z. Wu, Thermophysical properties of TiB2-SiC ceramics from 300 ˚C to 1700 ˚C, Int. J. Refract. Met. Hard Mater. 41 (2013) 609–613. doi:10.1016/j.ijrmhm.2013.08.001.

[281] S.E. Bates, W.E. Buhro, C.A. Frey, S.M.L. Sastry, K.F. Kelton, Synthesis of titanium boride TiB2 nanocrystallites by solution-phase processing, J. Mater. Res. 10 (1995) 2599–2612. doi:DOI: 10.1557/JMR.1995.2599.

[282] Ö. Balcı, U. Burkhardt, M. Schmidt, J. Hennicke, M. Barış Yağcı, M. Somer, Densification, microstructure and properties of TiB2 ceramics fabricated by spark plasma sintering, Mater. Charact. 145 (2018) 435–443. doi:10.1016/j.matchar.2018.09.010.

[283] E.W. Neuman, H.J. Brown-Shaklee, G.E. Hilmas, W.G. Fahrenholtz, Titanium diboride–silicon carbide–boron carbide ceramics with super-high hardness and

strength, J. Am. Ceram. Soc. 101 (2018) 497–501. doi:10.1111/jace.15201.

[284] M. Rafiei, M. Salehi, M. Shamanian, Formation mechanism of B4C–TiB2–TiC ceramic composite produced by mechanical alloying of Ti–B4C powders, Adv. Powder Technol. 25 (2014) 1754–1760. doi:https://doi.org/10.1016/j.apt.2014.07.003.

[285] S. Rizaneh, G.H. Borhani, M. Tavoosi, Synthesis and characterization of Al (Al2O3–TiB2/Fe) nanocomposite by means of mechanical alloying and hot extrusion processes, Adv. Powder Technol. 25 (2014) 1693–1698. doi:https://doi.org/10.1016/j.apt.2014.06.016.

[286] N.N. Greenwood, R. V Parish, P. Thornton, Some reactions of metal borides, J. Chem. Soc. (1965) 545–549. doi:10.1039/JR9650000545.

[287] A. Sabahi Namini, M. Azadbeh, M. Shahedi Asl, Effect of TiB2 content on the characteristics of spark plasma sintered Ti–TiBw composites, Adv. Powder Technol. 28 (2017) 1564–1572. doi:https://doi.org/10.1016/j.apt.2017.03.028.

[288] Z. Wang, W. Han, Q. Kuang, Q. Fan, Y. Zhao, Low-temperature synthesis of CeB6 nanowires and nanoparticles as feasible lithium-ion anode materials, Adv. Powder Technol. 31 (2020) 595–603. doi:https://doi.org/10.1016/j.apt.2019.11.014.

[289] V. Jindal, A. Sarda, A. Degnah, K.S. Ravi Chandran, Effect of iron & boron content on the Spark Plasma Sintering of Ti-B-Fe alloys, Adv. Powder Technol. 30 (2019) 423–427. doi:https://doi.org/10.1016/j.apt.2018.11.021.

[290] S. Ehtemam-Haghighi, K.G. Prashanth, H. Attar, A.K. Chaubey, G.H. Cao, L.C. Zhang, Evaluation of mechanical and wear properties of TixNb7Fe alloys designed for biomedical applications, Mater. Des. 111 (2016) 592–599. doi:10.1016/j.matdes.2016.09.029.

[291] Y. Liu, L.F. Chen, H.P. Tang, C.T. Liu, B. Liu, B.Y. Huang, Design of powder metallurgy titanium alloys and composites, Mater. Sci. Eng. A. 418 (2006) 25–35. doi:10.1016/j.msea.2005.10.057.

[292] E.O. Ezugwu, Z.M. Wang, Titanium alloys and their machinability - A review, J.

Mater. Process. Technol. 68 (1997) 262–274. doi:10.1016/S0924-0136(96)00030-1.

[293] D. Gu, Laser Additive Manufacturing of High-Performance Materials, Springer Berlin Heidelberg, Berlin, Heidelberg, 2015. doi:10.1007/978-3-662-46089-4.

[294] J.A. Wollmershauser, B.N. Feigelson, E.P. Gorzkowski, C.T. Ellis, R. Goswami, S.B. Qadri, J.G. Tischler, F.J. Kub, R.K. Everett, An extended hardness limit in bulk nanoceramics, Acta Mater. 69 (2014) 9–16. doi:10.1016/j.actamat.2014.01.030.

[295] K. J-P., Binding mechanisms in selective laser sintering and selective laser melting, Rapid Prototyp. J. 11 (2005) 26–36. doi:10.1108/13552540510573365.

[296] W.G. Fahrenholtz, E.J. Wuchina, W.E. Lee, Y. Zhou, Ultra-High Temperature Ceramics, John Wiley & Sons, Inc, Hoboken, NJ, 2014. doi:10.1002/9781118700853.

[297] B. Basu, G.B. Raju, A.K. Suri, Processing and properties of monolithic TiB 2 based materials, Int. Mater. Rev. 51 (2006) 352–374. doi:10.1179/174328006X102529.

[298] G.B. Raju, B. Basu, Development of High Temperature TiB2-Based Ceramics, Key Eng. Mater. 395 (2009) 89–124. doi:10.4028/www.scientific.net/KEM.395.89.

[299] A. Kulpa, T. Troczynski, Oxidation of TiB2 powders below 900˚C, J. Am. Ceram. Soc. 79 (1996) 518–520.

[300] P. Foroughi, C. Zhang, A. Agarwal, Z. Cheng, Controlling phase separation of TaxHf1−xC solid solution nanopowders during carbothermal reduction synthesis, J. Am. Ceram. Soc. 100 (2017) 5056–5065. doi:10.1111/jace.15065.

[301] K. Morsi, V. V. Patel, S. Naraghi, J.E. Garay, Processing of titanium-titanium boride dual matrix composites, J. Mater. Process. Technol. 196 (2008) 236–242. doi:10.1016/j.jmatprotec.2007.05.047.

[302] W. Liu, J.N. Dupont, In-situ reactive processing of nickel aluminides by laser-engineered net shaping, Metall. Mater. Trans. A. 34 (2003) 2633–2641. doi:10.1007/s11661-003-0022-3.

[303] D.D. Gu, W. Meiners, K. Wissenbach, R. Poprawe, Laser additive manufacturing of metallic components, 57 (2013) 133–164. doi:10.1179/1743280411Y.0000000014.

[304] M. Agarwala, D. Bourell, J. Beaman, H. Marcus, J. Barlow, Direct selective laser

sintering of metals, Rapid Prototyp. J. 1 (1995) 26–36. doi:10.1108/13552549510078113.

[305] A.. Sergueeva, V.. Stolyarov, R.. Valiev, A.. Mukherjee, Advanced mechanical properties of pure titanium with ultrafine grained structure, Scr. Mater. 45 (2001) 747–752. doi:10.1016/S1359-6462(01)01089-2.

[306] W.D. Callister, Materials science and engineering: An introduction (2nd edition), 1991. doi:10.1016/0261-3069(91)90101-9.

[307] H. Attar, M. Calin, L.C. Zhang, S. Scudino, J. Eckert, Manufacture by selective laser melting and mechanical behavior of commercially pure titanium, Mater. Sci. Eng. A. 593 (2014) 170–177. doi:10.1016/j.msea.2013.11.038.

Vita

Sina Khoshsima received his B.S degree in Mechanical Engineering from Azad University, Tabriz, in 2011. He then started his M.S degree in department of Biomedical Science and Engineering at Middle East Technical University. After completion of his studies, he started his PhD degree at Koç University and under supervision of Prof. Dr. Mehmet S. Somer in February 2015.

List of Publications

[1] S. Khoshsima, Z. Altıntaş, M. Schmidt, M. Bobnar, M. Somer, Ö. Balcı, Crystalline Co–Fe–B nanoparticles: Synthesis, microstructure and magnetic properties, J. Alloys Compd. 805 (2019) 471–482. doi:10.1016/j.jallcom.2019.07.079.

[2] Z. Altıntaş, S. Khoshsima, M. Schmidt, M. Bobnar, U. Burkhardt, M. Somer, Ö. Balcı, Evolution of magnetic properties of crystalline cobalt-iron boride nanoparticles via optimization of synthesis conditions using hydrous metal chlorides, J. Magn. Magn. Mater. (n.d.).

[3] S. Khoshsima, Z. Altıntaş, U. Burkhardt, M. Schmidt, K.G. Prashanth, M. Somer, Ö. Balcı, CoB-TiB2 crystalline powders: Synthesis, microstructural analysis and their utilization as reinforcement agent, Adv. Powder Technol. 31 (2020) 2964–2972. doi:10.1016/j.apt.2020.05.026.

[4] S. Khoshsima, Z. Altintas, M. Somer, Ö. Balci, Synthesis of Cobalt-Nickel-Boron based composite powders using metal chloride powder blends, in: 27th Int. Conf. Metall. Mater., TANGER LTD, KELTICKOVA 62, SLEZSKA, OSTRAVA 710 00, CZECH REPUBLIC, Brno, Czech Republic, 2018: pp. 1563–1568. http://www.scopus.com/inward/record.url?eid=2-s2.0-85059371798&partnerID=MN8TOARS.

[5] Z. ALTINTAŞ, S. KHOSHSİMA, M. SOMER, Ö. BALCI, The synthesis of binary and ternary cobalt based metal borides by inorganic molten salt technique, J. Boron. 5 (2020) 12–22. doi:10.30728/boron.613117.

[6] S. Khoshsima, B. Yilmaz, A. Tezcaner, Z. Evis, Structural, mechanical and biological properties of hydroxyapatite-zirconia-lanthanum oxide composites, Ceram. Int. 42 (2016). doi:10.1016/j.ceramint.2016.07.041.

[7] S. Khoshsima, A. Alshemary, A. Tezcaner, S. Surdem, Z. Evis, Impact of B2O3 and La2O3 addition on structural, mechanical and biological properties of hydroxyapatite, Process. Appl. Ceram. 12 (2018) 143–152. doi:10.2298/PAC1802143K.

[8] A. Paksoy, S.F. Kurtoğlu, A. Dizaji Khodadadi, Z. Altıntaş, S. Khoshsima, A. Uzun, Ö. Balcı, Nanocrystalline cobalt–nickel–boron-based metal boride catalysts for efficient hydrogen production from the hydrolysis of sodium borohydride, J. Hyrogen Energy. (2020).

[9] S. Khoshsima, S. Mertdinç, Z. Altıntaş, A. Motallebzadeh, D. Ağaoğulları, Ö. Balcı, Enhanced microstructural and mechanical properties of Al-based metal matrix composites reinforced with hybrid metal boride particles, (2021).